Title
Advances in nearly-magnetic superconductivity

Author
Maksimovic, Nikola

Publication Date
2022

Peer reviewed|Thesis/dissertation

Advances in Nearly-Magnetic Superconductivity

by

Nikola Maksimovic

A dissertation submitted in partial satisfaction of the

requirements for the degree of

Doctor of Philosophy

in

Physics

in the

Graduate Division

of the

University of California, Berkeley

Committee in charge:

Professor James G. Analytis, Chair
Professor Ehud Altman
Assistant Professor Kwabena Bediako

Spring 2022

Advances in Nearly-Magnetic Superconductivity

Abstract

Advances in Nearly-Magnetic Superconductivity

by

Nikola Maksimovic

Doctor of Philosophy in Physics

University of California, Berkeley

Professor James G. Analytis, Chair

Many-body systems present some of the deepest challenges in physics. The interactions between a large number of objects can give rise to phenomena which are unprecedented from the standpoint of the individual objects themsleves. In many-body quantum systems, such as the electron fluid in metals, an effective single-particle description for modeling their properties has been successfully developed and tested. One of the central open questions in the study of many-body quantum physics lies in systems where the particles interact with each other strongly enough that the conventional description in terms of effectively individual particles fails. This problem is prevalent in metals which are on the verge of magnetism — for example, when perturbed by external stress, magnetic field, or electric field, they spontaneously become magnetic. Notably, some of these metals achieve superconductivity, a collective electron phase which exhibits zero electrical resistance, at remarkably high temperatures. This text focuses on experimentally addressing fundamental open questions regarding strongly-interacting electrons in such metals. It is divided into separate sections on nearly-antiferromagnetic iron-based superconductors, a novel layered ferromagnetic superconducting compound, and a cerium-based alloy hosting an interplay between magnetism and the spontaneous localization of electrons to their host atoms.

Dedicated to my family.
Thank you James for the mentorship and guidance. I've certainly become a better scientist and person in the time that I've known you.

Contents

List of Figures

List of Tables

Acknowledgments

Thank you to all of the wonderful people whom I had the great fortune of meeting and interacting with over these past six years. This list is not exhaustive. There are more whom, in the interest of space, I have not included here.

First of all, I would like to thank James. In many ways, I was an unmanageable student, yet you stuck with me. I often found it difficult to appreciate the high points of graduate school in the moment, but now I look back on these years very fondly and will probably continue to do so for a long time. Your patience and empathy helped me get here.

To Ian and Sooyoung for bringing me into the world of correlated electrons and for their guidance when I was just a first year without a clue. Sylvia, your positive attitude kept me going during my rebellious graduate student phase. Very glad to have shared the title of messiest desk in the office with you. Special thanks to John Singleton. None of the work in this thesis would have been possible without you.

To Vikram, my graduate school brother, whom I've grown up with. I've shared many memories with you (probably shared beds one too many times for our own good, but that's ok). I appreciate how much you've patiently listened to me complain. We're both gonna make it someday. To Robert for his welcoming attitude, and for always being a person to talk to with my problems. Holy Diver will forever live on in the halls of the 5th floor of Birge. Looking forward to shredding the slopes with you in the future. To Danny, Kayla, Shannon, and Roger. The DnD sessions let me get my insanity out in a healthy medium (for the most part). To Shannon for being one of my best friends and colleagues, and supporting me during some of the most difficult moments of my life. I hope I was able to do the same for you. To Eran for being a mentor, a friend, and a role model for years. I'm very glad that things worked out for you and your family — someday I'll visit the beaches of Israel to see you and Noam and your kids. To Ryan for showing me that you can both be productive and also be a kind and generous person with a life. I won't soon forget those moments of stillness (you know what I'm talking about) — running up a hill while you ask me whether I would rather eat toenail clippings or a lard bar full of toe hairs. To Ella, thanks for wading through the hell of the 16T with me. There is exactly zero data in this thesis taken on that system, but I wouldn't trade those memories for anything. To Daria for breathing life into every situation. Although we only overlapped for a short time, I'll remember you for a while. Thanks for the pickleball with the legendary Sasha. To Alex and Jon. You're both too cool to be graduate students, but I'm very lucky to have overlapped with you. To Luke, the best low temperature experimentalist that I know, and an inspiration. You are often right, but you are wrong about one thing. Hershey's is better.

To the legendary physcal soccer team for giving me a setting to take my frustration out on a ball. Some seasons we won miraculously. Some we didn't do so great, but it was always a blast. Special tribute to Andy, my fearless leader and tall German drinking buddy.

To the places that made these last six years special. Molo. The Hotsy Totsy 5K. El parasol. The Northroad Inn. Shattuck house. The Francisco St apartment. Taco tuesdays. Wednesday night trivia at Bobby G's. The list goes on. I will forever remember these places.

To Wendy, Andie, and Zeyu. You've shown me the great things that students can go on to do. To Carlos Bustamante and Jon Deasy. We couldn't have asked for friendlier people to do the most important jobs in the physics department. My PhD would have taken twice as long if it weren't for you guys.

Chapter 1

Introduction to metals, superconductivity, and magnetic quantum criticality

Usually quantum coherent phenomena, i.e. entanglement and wavefunction interference, are observed in extremely controlled conditions — maybe in a few hundred atoms within a laser-cooled apparatus. There are only a few examples of natural phenomena where quantum coherent properties manifest on a macroscopic scale; one of these is superconductivity in metals. A superconductor could be just a piece of metal, say lead, which is not particularly carefully prepared, and is then dunked in a bath of liquid cryogen. The free electrons in the piece of lead become quantum entangled spontaneously, all on their own, without any extra help from the experimentalist.

For the average person, perhaps the most striking characteristic of superconductivity in metals is that below a certain critical temperature, the electrical resistance of the metal drops to exactly zero. Of course, one can imagine that this property has enormous technological value — lossless generators [29], power transmission [64], energy storage [201], powerful electromagnets [109], magnetic levitation [73], and so on. Unfortunately, the applicability of superconducting materials is limited by their very low critical temperatures, typically just a few degrees Kelvin above absolute zero — one needs expensive cryogenic cooling techniques to achieve such temperatures, meaning that superconductors are cost ineffective for the majority of applications where they might have otherwise found value. All this is to say that one of the motivations for studying superconductivity in metals is to understand what sets the superconducting critical temperature of a given metal. The ultimate goal is to engineer and/or create superconducting materials that operate at higher temperatures. So as to not set the reader's expectations too high, we must admit that we leave this ultimate goal largely untouched in this text.

1.1 Conventional and unconventional superconductors

"Stay away from magnetism" — Rule 4 of B. Matthias' rules for discovering new superconductors

Fortunately, there are a huge number of superconductors which have already been discovered and characterized. Motivating the search for new superconducting materials and formulating general guiding questions in this field is made significantly easier by this large body of previous work. Starting from the most direct goal and working our way to more specific questions is usually a good strategy, so let's say we would like to discover a room temperature superconductor. What are the challenges associated with this goal?

Because superconductivity is a quantum coherent state, we immediately expect it to be sensitive to temperature — thermal fluctuations that get stronger with increasing temperature on general grounds tend to destroy quantum coherence. The spatial coherence between separated quantum wavefunctions, say two wavepackets, can be enhanced by increasing the spatial overlap of the wavefunctions. This admittedly naive intuition has more rigorous backing in the study of Bose-Einstein condensation, where bosons at finite temperature spontaneously fall into the same quantum state [117]. The temperature of Bose condensation increases with the density of particles ($T_c \sim n^{2/3}$, where n is the particle density and T_c is the condensation temperature).

With this intuition, it seems favorable to increase the density of the electron fluid to make superconductivity in metals more robust to temperature fluctuations. It might be useful to test this intuitive backing using real-world material examples. In Fig. 1.1 we plot the value of T_c versus the electron Fermi temperature (T_F, a proxy for the electron density) in a number of superconducting materials. Systems which lie further in the upper left of the plot tend to be 'stronger' superconductors in the sense that for a given electron density, their superconducting transition temperature is higher. Likewise superconductors in the lower right portion of the plot are 'weaker'. Some readers may recognize Fig. 1.1 as a representation of the Uemura plot for superconductors [207]. The original motivation for this plot was more precise than the arguments given above, but at least we have interrogated an interesting argument that leads us to notice some important correlations.

First of all, the electrons in a metal appear to be much less susceptible to condensation than a boson gas — almost all of the data points in Fig. 1.1 lie below the expected value predicted for Bose-Einstein condensates (BEC). This is perhaps to be expected, because electrons are fermions, and their condensation relies on an attractive interaction to transform them into bosonic pairs of electrons. Such a mechanism was established by Bardeen, Cooper, and Schrieffer almost half a century after the observation of superconductivity in mercury at about 4.2 degrees Kelvin [21]. Based on the "BCS" theory, the electrons of a metal are attracted to one another through quantized vibrations of their ionic lattices (phonons), which results in the bosonization of electrons through the formation of electron pairs, and ultimately their condensation into a superconducting state. BCS theory gives a prediction

for the superconducting critical temperature based on microscopic parameters

$$T_c \propto E_D e^{-1/N(\epsilon_F)V}. \tag{1.1}$$

Here E_D is a characteristic frequency of lattice vibrations. $N(\epsilon_F)$ is the density of electron states, and V is the effective electron-phonon coupling potential. The critical temperature is enhanced by increasing any of these values. The expected trend of superconducting transition temperature as a function of electron density according to this BCS prediction is shown in Fig. 1.1.

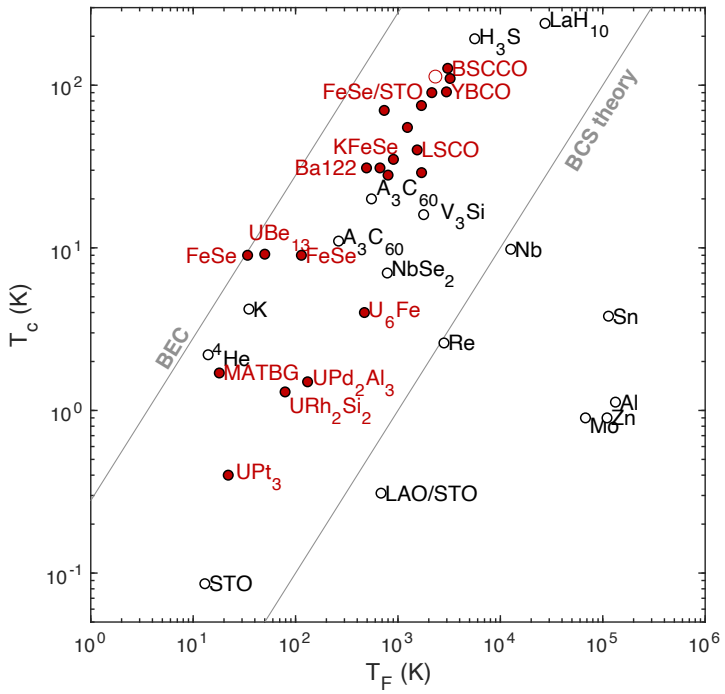

Figure 1.1: **Comparison of transition temperatures and Fermi temperature in various superconductors** The red points are superconductors in which the superconducting phase is close to a magnetic phase. The grey lines delineate the predicted trend based on BCS theory of electron-phonon coupling superconductivity, and the Bose-einstein condensate (BEC) expectation assuming that all of the fermions in the electron gas become bosons.

According to Eq. 1.1, one of the ways to increase the superconducting temperature is by increasing the density of states (or equivalently the density of electrons). In this way, the superconducting condensation temperature is enhanced by particle density much like the Bose-Einstein condensation temperature, but the overall scale of the superconducting transition temperature is lower because the electrons need to overcome the hurdle of becoming bosons in order to condense. The strategy of enhancing the density of states in

electron-phonon coupling superconductors has achieved greatest success in materials like Nb_3Sn, which are often used in superconducting electromagnet applications [173]. Unfortunately, the strategy of simply increasing the free electron density falls apart for one main reason. In materials where the density of electrons is too high, like gold, copper, silver, the electrons tend to have very low coupling constants with the phonons because the high density of itinerant charge screens the electrons from the underlying ions in the lattice. In fact, many high carrier density metals are not observed to superconduct at any measurable temperature. So while increasing the density of states has achieved some success as a strategy to improve superconducting materials, it has its limits. There seems to be a 'sweet spot' in terms of electron density where the electron-phonon coupling strength and density of states are both optimized. With these restrictions in mind, electron-phonon coupling superconductivity is apparently limited to rather low temperatures, as shown by the 'BCS' delimiting line in Fig. 1.1, and many real materials which are presumably electron-phonon coupling superconductors like Sn, Al, and Zn tend to underperform compared to the prediction of BCS theory.

Another idea is to enhance the phonon frequency by constructing a metallic material made from light atoms that can vibrate a lot. This direction achieved great success in materials like C_{60} and MgB_2, with critical temperatures up to 40K, among the highest known critical temperatures in electron-phonon coupling superconductors. More recently hydrogen-based superconductors under enormous hydrostatic pressure have been shown to have superconducting transition temperatures close to room temperature [47]. It has been argued that the very high energy vibrational modes of hydrogen (the lightest element) induce electron-phonon coupling superconductivity in these materials at unusually high temperatures [18], albeit at ridiculously high pressures.

The final idea is to increase the value of E_D, the phonon energy prefactor, by leveraging BCS-like pairing mechanisms which go beyond electron-phonon interactions. For example, with BCS-like mechanisms following Eq. 1.1, but where the pairing is induced by electron-electron interactions rather than electron-phonon. In this scenario, E_D would be replaced by some characteristic electronic energy scale with typical interaction scales on the order of $\sim$1 eV in many metals such that transition temperatures in theory up to 200K would be possible even with relatively weak coupling strengths [155]. This idea potentially puts room-temperature superconductivity at ambient conditions within reach. Interestingly, such an effectively attractive electron-electron interaction could also result in the formation of other electronic instabilities (antiferromagnetism, ferromagnetism, structural distortions, and charge density waves) in analogy to soft phonons inducing structural instabilities [155]. So in materials where superconductivity can be mediated by an electronic attractive potential, we might expect to see electronic or magnetic order in close proximity or competing with a superconducting phase. By this logic, it is probably no coincidence that some of the materials that completely outperform BCS theory — materials like $YBa_2Cu_3O_7$, and tetramethyltetraselenafulvalene (TMTSF) among others — are nearly-magnetic superconductors, as seen in Fig. 1.1. That is, their superconducting state exists in proximity to a magnetic phase; for example, either under applied pressure, strain, magnetic field, or

chemical substitution, they turn from superconductors into magnetically-ordered materials or vice versa. It is believed that magnetic fluctuations near a magnetic phase boundary can induce a pairing interaction between the electrons. As a result, such 'unconventional' (non-electron-phonon coupling) superconductivity that exists in proximity to magnetism sometimes exhibits remarkably high transition temperatures compared to that expected of the more 'conventional' electron-phonon mechanism. Note that in many cases, magnetism is not the only phase present in proximity to superconductivity, as strong electron-electron interactions tend to induce a complicated ground state landscape, which will be the subject of further discussion later.

Perhaps a more important problem to physicists who study many-body systems is the basic description of the electrons in such materials. What has been discovered, and is a central topic of this thesis, is that many of the metals in Fig. 1.1 that seem to host 'nearly-magnetic' superconductivity also exhibit unconventional properties in many other ways. In particular, as a consequence of the strong interelectron interactions in such materials, the behavior of their electronic properties tends to challenge very well-established theories that describe the electronic and thermodynamic properties of the majority of metals (like copper, lead, silver, etc). And, before a theory of nearly-magnetic superconductivity analogous to BCS theory is developed, a description of strongly-interacting electron fluids needs to be more firmly developed and tested by experiments. Why is such a fundamental understanding important? With a full understanding of electron-phonon coupling in superconductors, and the relevant parameters that go into it, tremendous success was achieved in enhancing the performance of electron-phonon coupling superconductors. Essentially, this followed from optimizing the parameters going into Eq. 1.1. If an analogous theory to BCS theory is developed for nearly-magnetic superconductors, we might expect to see short-term order of magnitude improvements in their properties with a more directed approach to materials engineering and discovery. This line of thought provides motivation for studying nearly-magnetic metals, not only for their superconducting performance, but also from a fundamental perspective.

This text is broadly outlined as follows. First, we will build up the basic concepts behind understanding electrons in conventional metals (the materials that generally fall beneath the 'BCS' line in Fig. 1.1). Then we will go into more detail about how, and to what extent certain metals violate the conventional tools used to understand the behavior of electrons in solids. With some examples, experiments, and a bit of theory, an explanation is put forward for certain properties of nearly-magnetic metals, and some insight is provided about others.

1.2 Fermi liquid theory and Luttinger's theorem

"Most important part of physics is the knowledge of approximation" — Lev Landau

The workflow for the theory of electrons in solids is to start from the simplest approximation, the free electron model. From the point of view of the free electron model, all metals are basically the same aside from possible variations in the density of electrons between different materials. The ionic lattice in such a picture is assumed to produce a uniform background of

charge, which essentially has no effect on the properties of the electrons. The effects of the lattice can be included more rigorously as a weak perturbation to the free electron model in the "nearly free electron model", which decorates each metal, semiconductor, and band insulator with its own unique electronic properties. Electron-electron interactions can be considered in the "somewhat free electron model" (aka Fermi liquid theory). Fermi-liquid theory is the most complete description of electrons in solids at the moment, and, for various reasons which will be described, Fermi liquid theory has been observed to fall short in a number of real circumstances.

For most solid state applications, the nearly free electron model is essentially used as a working theory of metals and semiconductors. That being said, the reason that the nearly free electron model works at all is explained by concepts developed in Fermi liquid theory, so even though Fermi liquid theory is seldom explicitly referenced, it essentially underlies all of our modern understanding of electrons in solids. As such, we choose to first present the free electron model, then discuss Fermi liquid theory, which in principle applies to weakly-interacting electron gases that are not in a periodic lattice potential. Then we will discuss the effects of the periodic potential of the ionic lattice, and its implications for some of the results of Fermi liquid theory including most importantly the effects of symmetry-broken order in Fermi liquids.

Free electron model

Everything in this text deals with solid state materials, which consist of a set of ions locked into a lattice whose positions may fluctuate slightly on relatively slow timescales due to thermal vibrations, and sea of electrons that are relatively much faster moving [206]. To consider the simplest approximation of the system, assume the electrons to be a gas of completely non-interacting fermions. Of course, a metal is charge neutral, so we need to consider also the influence of positively charged ions in the lattice. Let us at the moment assume that the ions simply meld together into a sea of uniform positively charged background, inducing a constant electrical potential. This "free electron model" is at first glance a ridiculously simple approximation, but starting from this point gives some useful insight, and the complexity of the model can be built upon.

Electrons are fermions, and as such, no two electrons can occupy the same state. For example, no two electrons can have the exact same momentum and spin. From this constraint alone, we can already tell that the electrons will fill up some set of available quantized energy levels — which in this case can be labeled by their momenta — until some characteristic momentum value which is determined by the number of particles. This characteristic momentum is called the 'Fermi' momentum, which is related to the 'Fermi' energy through the Hamiltonian, which for this scenario basically only consists of the electron kinetic energy ($\hat{H} = \frac{\hat{p}^2}{2m} + V_{ions}$). In this approximation, V_{ions} is simply a constant.

In order to make these statements more precise, and to obtain some more information about the phase space structure of the quantum states in the free electron model, we should solve the Schrodinger equation with boundary conditions. Consider the edges of the sample

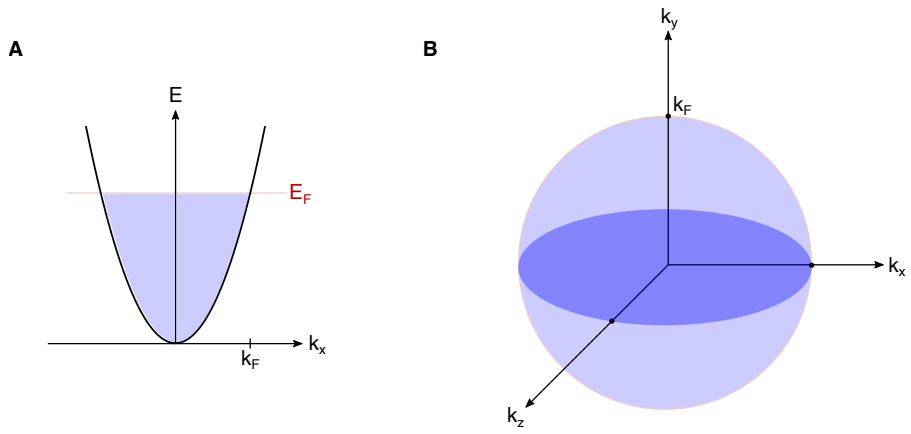

Figure 1.2: **Electronic spectrum and Fermi surface of free electrons A** Energy spectrum of available momentum states, with k_x taken as an example, although for the free electron gas, the spectrum would like identical to this no matter which linear momentum direction were selected. The states below the Fermi energy, E_F, are filled. The Fermi momentum is labeled on the x-axis. **B** The locus of filled quantum states in momentum space, which trace out an isotropic sphere with radius equal to the Fermi momentum.

as an infinite potential barrier such that electrons have no hope of escaping. The solutions to the Schrodinger equation produce an energy spectrum in a cube of sample of length L,

$$E = \frac{\pi^2\hbar^2}{2mL^2}(n_x^2 + n_y^2 + n_z^2) \tag{1.2}$$

The resulting ground state consists of a filled surface of quantum states in momentum space, a Fermi surface, with a sharp boundary at the Fermi energy ($E_F = \hbar k_F$). Note that these energy states are discretized, as n_x, n_y, and n_z are integers, but because of the enormous number of electrons in a typical sample of a metal, the surface can be well-approximated as a smooth sphere for all intents and purposes (this approximation is not appropriate for extremely small samples, where the discretization of energy levels becomes apparent!).

We have not yet considered the effects of finite temperature. Fundamentally, every gas of electrons is quantum mechanical. That is, the particles in the gas obey Fermi statistics, giving rise to a Fermi energy. But, there are some gases that can be modeled quite well with classical Maxwell-Boltzmann statistics, say dilute plasmas [153]. No explicit reference to a Fermi energy is made in these systems. What is the difference?

If temperature is sufficiently high relative to the Fermi energy, there are many states available to each electron, and the Fermi surface becomes so smeared out that it is essentially not a surface — electrons rarely overlap in state space or in real space, and can thus be treated as essentially independent particles (Fig. 1.3A). This leads to a recovery of Maxwell-Boltzmann statistics, which is essentially a high-temperature limiting form of Fermi-Dirac

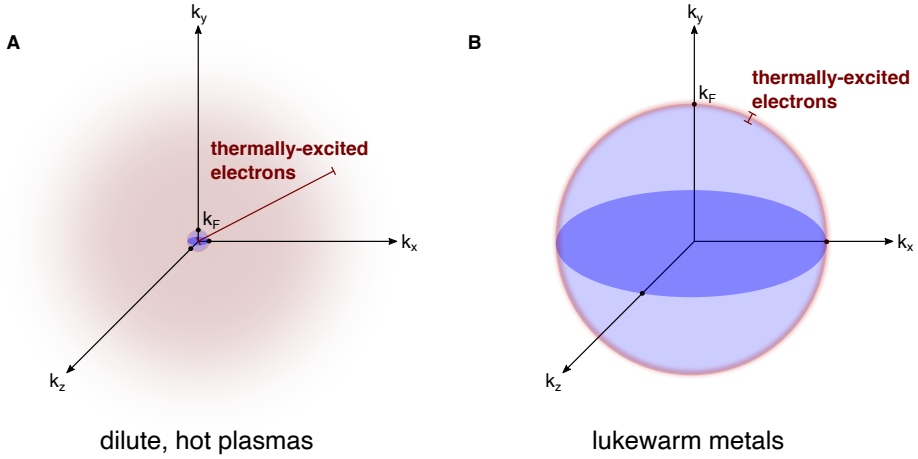

Figure 1.3: **Fermi surfaces with thermally excited states**. A comparison between classical and quantum electron gases **A** A classical electron gas, in which the temperature is much greater than the Fermi energy. Excited states are distributed well outside the boundary of the Fermi surface, and their motion and thermodynamic properties are not influenced by their interactions with each other, or the existence of an underlying Fermi surface. **B** A quantum gas where the temperature is much less than the Fermi energy. Excited states exist in a narrow shell around the Fermi energy, and the the presence of a Fermi surface strongly affects the available energy levels that excited states have access to.

statistics. If the temperature is well below the Fermi energy, the Fermi surface severely constrains the states available to the electrons (Fig. 1.3B). This is a consequence of the real space picture in which the effective width of each particle's wavefunction is comparable or much greater than the spacing between electrons. Their quantum statistics become relevant in this regime.

In many metals, the concept of the Fermi surface is crucial to modeling the properties of the electrons. If we take crystalline copper as an example, the calculated Fermi temperature of its electrons based on their density is on the order of 80,000 Kelvin. Therefore, these electrons comprise a degenerate Fermi gas in basically every conceivable circumstance where copper appears in nature ($T \ll T_F$). Based on low-temperature heat capacity data [24], the specific heat of the Fermi gas of electrons in a sample of copper can be determined to be close to 0.7 mJ/molK^2 (Fig. 1.4). Interestingly, if we calculate the expected specific heat capacity coefficient of a completely free electron gas with the same density as that of the electrons in copper, we find that the expected value is 0.5 mJ/molK^2. Therefore, the non-interacting electron gas picture turns out to be remarkably accurate for estimating the thermodynamic properties of copper, and indeed those of most metals.

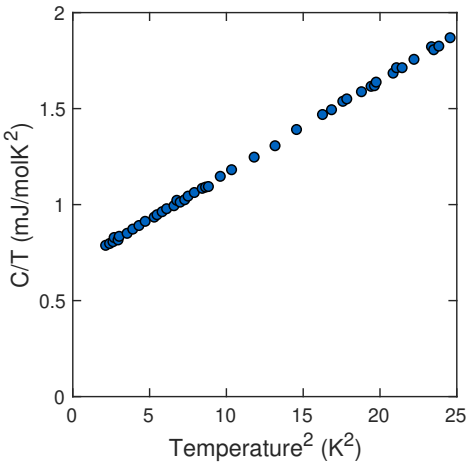

Figure 1.4: **Heat capacity of copper at low temperature** On this scale, the heat capacity of copper clearly has a linear contribution at low temperature (a zero-temperature intercept of about 0.7 mJ/molK^2 on the C/T vs T^2 scale). This indicates a contribution from a degenerate fermion gas of electrons. The T^3 contribution is understood as originating from the phonon contribution of the lattice of ions.

Fermi liquid theory

While the general thermodynamic properties of metals are pretty well-described by the free electron model, dynamical properties like transition rates between states (useful for things like absorption coefficients, heat and charge transport coefficients, magnetism, etc), as well as more precise predictions of thermodynamic coefficients, require a more precise treatment, which includes the effect of electron-electron interactions. This requires us to employ the most accurate model of interacting fermion gases to date — Fermi liquid theory.

Let us consider incorporating electron-electron interactions into the free electron model. In principle, the Hamiltonian now includes a sum of all interaction potentials between an enormous number of electrons. The problem of determining the ground state and eigenstates becomes almost infinitely more complicated, and virtually impossible to solve exactly. Luckily, we have at our disposal the principal of adiabatic continuity, one of the most powerful concepts in physics. Lev Landau popularized the method of applying adiabatic continuity to the interacting fermion gas [39], originally for the study of liquid ^{3}He, which is why Fermi liquid theory is sometimes called Landau's theory of the Fermi liquid. The principle of adiabatic continuity states that the good quantum numbers associated with the stationary states of a given Hamiltonian remain unchanged by a perturbation provided that the perturbation is sufficiently 'weak'. This argument has been put on more rigorous ground previously based on consideration of the time-dependent Schrodinger equation as a perturbation is turned on over some time [90]. The broad conclusion of these arguments is that the spectra of

two Hamiltonians can be adiabatically connected provided that there is no ambiguity in the ordering of their energy levels, i.e. degeneracies or level crossings are not introduced by the perturbation.

We will first discuss a concrete example to give more intuitive meaning behind this concept. Then, we will describe how the adiabatic principle can be applied to the interacting gas of electrons in a metal.

Adiabatic continuity and symmetry breaking

As a simple example, consider a particle in a quartic potential well ($V(x) = x^4$); perhaps we can draw an analogy between this scenario and the potential of a single ion in a crystal lattice. The energy spectrum can be solved, where each stationary state solution to the Schrodinger equation looks basically like part of a sinusoidal wave that decays on either end (Fig. 1.5A). Each successive energy level has a wavefunction that includes one extra node compared to the one below it. Therefore, one can say that the 'good' quantum number labeling each state in this case are the number of nodes in the wavefunction. The zeroth energy level has zero nodes, the first has one node, etc. There are no degeneracies. We can now consider deforming the background potential into a slightly more complicated shape by adding a bump to the center of the well ($V_{perturbation} = -2x^2$). This might be one way that the 'turning on' of electron interactions in a metal could manifest; for example, if there are two electrons in the well that repel each other, the total potential landscape could be crudely modeled by adding a bump to the well potential. Luckily the Schrodinger equation is easy enough to solve numerically for the potentials shown in Fig. 1.5A, and we can draw the wavefunctions and energy spectrum from the numerical solution. Notice that, with the addition of a weak bump in the potential well, although the level spacings change slightly, and the precise shapes of the wavefunctions change, there are some things that didn't change. The number of nodes per sine wave in each energy level stayed the same under the perturbation, so the good quantum numbers are left unaffected. There are no level crossings, and no degeneracies are introduced by this weak perturbation. This is an example of the adiabatic principle at play — as long as the deformation to the potential is sufficiently weak, the system can be adiabatically connected to the bare potential such that the labels of the quantum states are robust to the perturbation.

But as the bump perturbation to the potential well becomes stronger, the characteristics of the wavefunctions and their energy spacings change qualitatively. Consider the rightmost panel of Fig. 1.5A, which involves a very strong bump perturbation to the quartic potential well. When this perturbation is applied, the lowest two energy levels approach degeneracy. This is also true of the next two highest energy levels, and the next two. As the bump becomes larger, pairs of successive wavefunctions with even and odd numbers of nodes start becoming degenerate. In this sense, an infinitely strong bump perturbation to the background potential cannot be adiabatically connected to the bare potential because the quantum numbers for the stationary states fundamentally change due to the ambiguity introduced by energy levels becoming degenerate. The effects on the ground state wavefunction are explored further in

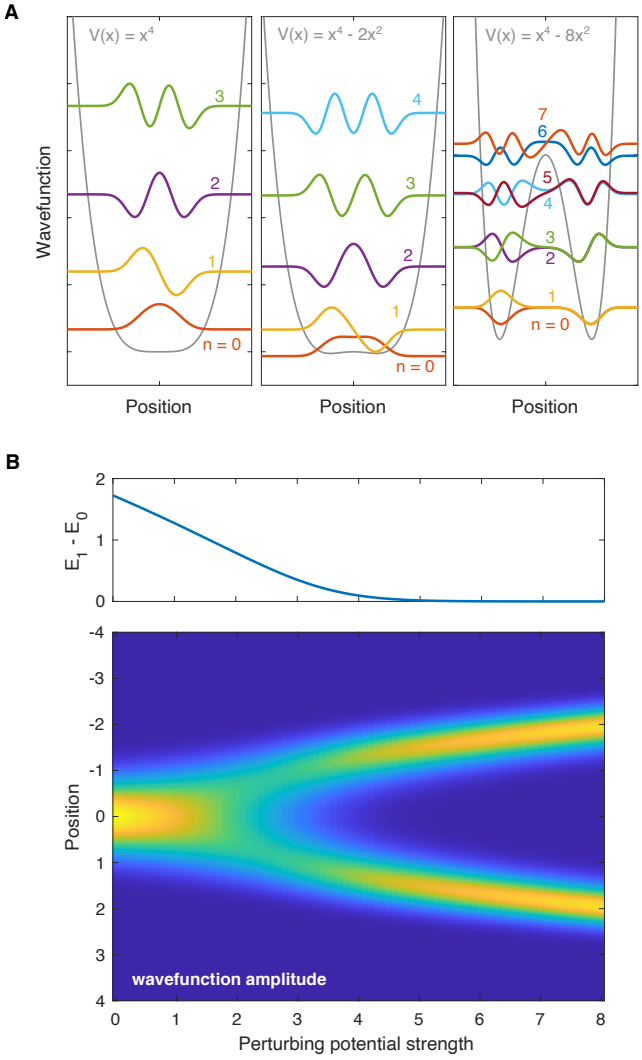

Figure 1.5: **Perturbations to a potential well**. **A** The background potential (grey line) evolves from left to right as a "bump" is introduced to a double-well potential. The wavefunctions are shown and offset in proportion to their energies. When the bump perturbation becomes strong enough, the energy levels start becoming degenerate. States with even and odd numbers of nodes begin pairing up into approximately degenerate levels. **B** Color plot of how the ground state wavefunction amplitude evolves as the size of the bump perturbation increases. As the perturbation becomes stronger, the wavefunction changes qualitatively in character. The panel above shows the energy splitting between ground and excited states approach zero as the perturbation is turned on. This occurs at the same perturbation strength at which the ground state wavefunction amplitude splits from one lobe into two.

Fig. 1.5B. As the perturbation is introduced, the level spacing between the ground state and first excited states approaches zero. At the same time, the qualitative shape of the ground state wavefunction changes from being concentrated to the center of the well to being separately concentrated in the right and left wells.

Another way to look at this situation is from the perspective of symmetry. Consider the parity operator which inverts the position across the center of the well. In the ground state of the unperturbed and weakly-perturbed systems, the ground state is even under the parity operation, and the first excited state is odd. However, as the strength of the bump perturbation increases, the energy gap between the even and odd states approaches zero (Fig. 1.5B). Therefore, as the bump becomes stronger, the wavefunction's symmetry under the parity operation no longer uniquely determines its energy. In the limit of an infinitely strong bump, the ground state is doubly degenerate where the respective wavefunctions are concentrated fully in either the right or left sides of the well — these stationary states don't respect parity [128]. Thus, although the Hamiltonian of a double well potential commutes with the parity operator, the resulting wavefunctions in the limit of an infinitely strong bump do not respect parity. This is one example of spontaneous symmetry-breaking, and it is a direct consequence of the degeneracy introduced between even and odd eigenstates by an infinitely strong bump perturbation. It is no coincidence that symmetry-breaking coincides with a change of the good quantum numbers because there is a direct relationship between symmetry and degeneracy in quantum systems [127, 128].

The central takeaway from the toy model discussed in this section is that the spectrum of a bare potential and a perturbed potential cannot be adiabatically connected to one another if a symmetry is spontaneously broken by the introduction of the perturbation. We will discuss this more later in the context of the symmetry-breaking potential induced by a lattice, and symmetry-broken phases in the electron fluid. These phenomenon can lead to a breakdown of the adiabatic principle, and therefore of Fermi liquid theory, in the interacting electron fluid.

Adiabatic continuity applied to weakly interacting electron gases

Consider again the metal. The principle of adiabatic continuity applies not only to simple Hamiltonians like the one shown in Fig. 1.5, but also more complicated ones like the many body electron gas. According to the adiabatic principle the labels for the good quantum states remain the same as the interactions between the electrons are included, provided that the interactions are not 'too strong' (what is meant by 'too strong' in this context is very important, and is most easily defined in terms of the lifetime of the states, as we will discuss later). But with this caveat in mind, we can still describe the low-energy excitations of the interacting gas as states each with the same good quantum numbers — spin, charge, and momentum — as the electrons in the free Fermi gases described in the previous sections. Generally speaking in most metals, the electron-electron interactions are relatively weak because they are mutually screened from one another, as will be discussed more in Chapter 2. Thus, the ground state excitations of the electron liquid in most metals 'look'

like electrons in the sense that they have the same spin and charge as electrons in a vacuum. However, they are *not* electrons but 'quasi'particles — collective excitations of the electron fluid, which in some sense can be considered wavepackets composed of a superposition of independent-particle wavefunctions. As a result of the preservation of the good quantum numbers, the general thermodynamic properties of the Fermi liquid are the same as the free electron gas. However, there are two key differences between Fermi liquid quasiparticles and non-interacting electrons. First, because quasiparticles are collective excitations, there is an inertial backflow when the quasiparticles move. Thus, their dynamical properties are renormalized by the response of the surrounding fluid (for example the bare electron mass m is renormalized to a different value m^*, which in principle could be several orders of magnitude larger than the bare electron mass! [11]). Second, quasiparticles are not exact eigenstates of the interacting Hamiltonian, and therefore the quasiparticles have finite lifetimes. The latter statement essentially defines the conditions of adiabaticity in an interacting Fermi liquid. If the lifetime is too short, the quasiparticle loses meaning as a well-defined excitation.

To see what 'well-defined excitation' means more directly, and define the conditions of adiabaticity in an interacting electron gas, it is useful to reference the spectral function. In the most precise language possible, the spectral function is a probability distribution that an electron (a *normal* electron, not a quasiparticle) in a particular basis state, say momentum k, can be found at energy ω. More intuitively, the spectral function essentially shows us how similar the interacting excitations are to bare electrons, and whether they can be adiabatically connected to one another. Incidentally, it is quite a useful tool in photoemission measurements, where quasiparticle excitations are excited out of the material by electromagnetic radiation, and then become normal electrons in the vacuum which are then detected with momentum resolution. In the non-interacting case the spectral function is a delta function at the energy $\epsilon_k^0 = \frac{k^2}{2m}$ (as shown in Fig. 1.6) because there is a one-to-one correspondence between momentum and energy for each non-interacting electron wavefunction. As electron-electron interactions are cranked up in a Fermi liquid, the electron wavefunctions lose their 'eigen-ness', and so an electron with a given momentum may take part in a number of energy eigenstates. In the Fermi liquid, there may still be a peak at a certain energy determined by the renormalized mass ($\epsilon_k = \frac{k^2}{2m^*}$), as seen in Fig. 1.6, but the peak has some width, and part of the spectral weight is transferred to an incoherent continuum. The peak in the interacting spectral function defines the quasiparticle. The height and width of this peak are related, and determined by the quasiparticle weight Z, which is proportional to the lifetime of the quasiparticle τ. Essentially, the interacting spectral function tells us how related a quasiparticle is to a bare electron; the sharper and taller it is ($Z \to 1$), the more similar it is to a delta function, i.e. a bare electron.

Another way to view the interacting Fermi liquid is with the electron distribution function n_k. In the non-interacting electron gas, the distribution function at zero temperature just looks like a step function with a step at the Fermi momentum, as seen in Fig. 1.6. As the interactions are turned on, there is still a step at the Fermi momentum with also some electron-hole excitations that smear out the distribution function, as shown in the Fermi liquid distribution function in Fig. 1.6. The height of the step at the Fermi momentum

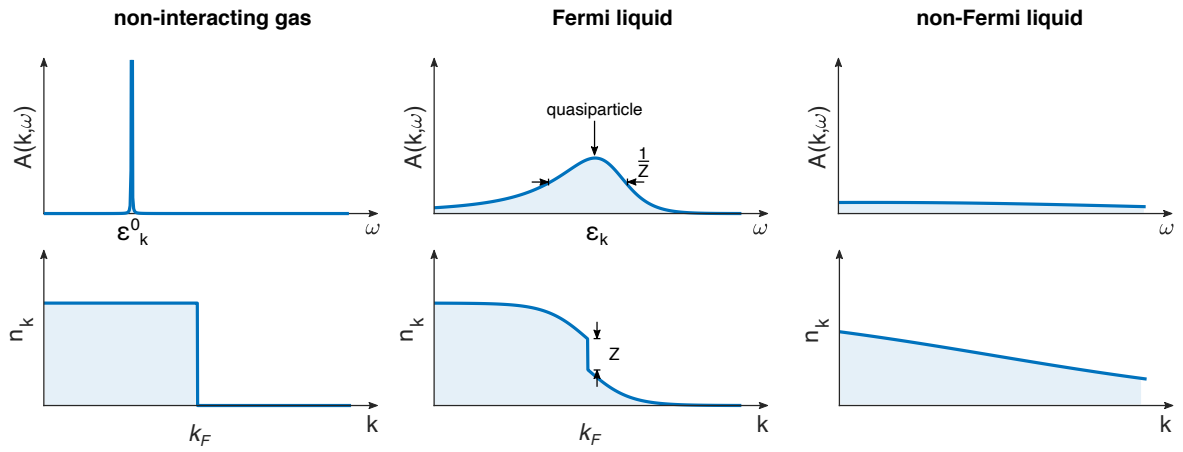

Figure 1.6: **Spectral $A(k,\omega)$ and distribution (n_k) functions of a free (or nearly free) electron gas, an interacting Fermi liquid, and a strongly interacting non-Fermi liquid** Moving from left to right in the above graphs, the electron-electron interactions become stronger. The spectral function $A(k,\omega)$ determines the distribution of bare electron states as a function of energy for a given momentum. In the non-interacting gas it is a delta function at an energy determined by $\epsilon_k^0 = \frac{\hbar^2 k^2}{2m}$. In the interacting Fermi liquid, its position is renormalized to $\epsilon_k = \frac{\hbar^2 k^2}{2m*}$, and it becomes broadened and shrunk in accordance with the finite quasiparticle lifetime, parametrized by the quasiparticle weight Z. In a non-Fermi liquid, the quasiparticle peak is indistinguishable from the broad incoherent background, or in other words $Z \to 0$. In the bottom plots the distribution function of non-interacting electrons at zero temperature are shown. As the quasiparticle weight Z decreases with the strength of the electron-electron interactions, the well-defined step of the Fermi-Dirac distribution becomes progressively smeared out into a continuous lineshape.

in this case is determined by the quasiparticle weight, Z, the same weight that defines the width of the quasiparticle peak in the spectral function.

Now, we can imagine a situation where the interactions are so strong that it becomes impossible to define a quasiparticle in terms of bare electrons. These scenarios are shown in the 'non-Fermi liquid' graphs in Fig. 1.6. In these cases, there is no contrast between the peak of the spectral function and the incoherent background, and the similarity between the interacting and non-interacting cases becomes zero ($Z \to 0$). In addition, the distribution function at zero temperature can look like a smooth continuum. This is how it looks when the adiabatic condition is violated when moving from the non-interacting electron gas to the interacting electron fluid. Now we can ask the question: what are the physical conditions that give rise to a non-Fermi liquid? Or, in other words, is there some sort of stability criterion for a Fermi liquid?

The principle of adiabaticity in an interacting electron gas boils down to the lifetime of the quasiparticle excitations, because $Z \sim \tau$. So if the lifetime τ is very short, then $Z \to 0$ and the quasiparticle loses meaning as a coherent excitation. The quasiparticle lifetime in a Fermi liquid can be derived from energy conservation. This argument has been rewritten several times in the literature [174], and will be rewritten for clarity again here (especially because this argument is so important to the concepts in Chapter 3). Say there is an excited quasiparticle at energy ϵ above the Fermi surface. The quasiparticle can undergo a transition to a state with lower energy while at the same time another quasiparticle is excited with equivalent energy exchange. Fermi's golden rule tells us the rate $(1/\tau)$ at which this process happens (see Ref. [174])

$$\frac{1}{\tau} \sim \frac{\pi}{\hbar}|V|^2 g_F^2 \epsilon^2, \tag{1.3}$$

where g_F is the density of states at the Fermi surface, and $|V|$ is the scattering matrix element between initial and final states. Both of these are assumed to be constant for the duration of the transition, so the decay rate of excited quasiparticles in the Fermi liquid is proportional to their energy squared. For quasiparticles near the Fermi surface, $\epsilon > \epsilon^2$, so that quasiparticles are well-defined in the sense that their decay rate is slower than their energy; of course, this result only applied to excitations close to the Fermi level where ϵ is small. The condition that the lifetime is smaller than ϵ is equivalent to the result that $Z > 0$. In the zero-temperature limit, we can make an equivalence between temperature and energy ($\epsilon \sim T$). This leads to the conclusion that in a Fermi liquid, the quasiparticle decay rate goes as T^2 in the low temperature limit and for excitations close to the Fermi level. If the quasiparticle excitation decay faster than T^2, say as T, then the principle of adiabaticity is violated.

One of the firm criteria here is that the quasiparticle decay rate due to electron-electron transitions in a Fermi liquid is essentially limited to be slower than T^2 (or ϵ^2 if energy is input in a way other than raising the temperature). If the decay rate of electronic excitations satisfies the above inequality, then the system is a Fermi liquid, and the adiabatic condition is satisfied. Consequently, the rate of momentum dissipation (i.e. the resistivity) in the limit of zero temperature in a Fermi liquid should go as T^2. There are a number of assumptions involved in mapping the quasiparticle decay rate from electron-electron transitions to a resistivity. The primary assumption, as far as we are concerned experimentally, is that the temperature needs to be sufficiently low that all other sources of momentum relaxation are absent. It is often difficult to independently verify that this is the case, as sources of momentum relaxation aside from electron-electron scattering events can in some cases persist to remarkably low temperatures, as will be discussed in Chapter 3. Another complication is that electron-electron collisions actually conserve momentum, and superficially should not lead to a resistivity, but the combination of electron-electron scattering and Umklapp scattering events associated with a change in the crystal momentum, results in dissipation [113].

Luttinger's theorem

"You can't just jump from little to big things" — Nadia Comăneci

Fermi liquid theory, while elegant, is in some ways shrouded in layers of abstraction. The notion of 'adiabatic continuity' is a rather difficult concept to wrap one's head around intuitively for a single particle in a potential, let alone when one also tries to keep count of the mutual potential between trillions upon trillions of electrons. With such a seemingly simple conclusion, there is a tendency to wonder what is surprising about the results of Fermi liquid theory. We are motivated to consider whether there are some more concrete results.

One of the most profound is the Luttinger-Ward theorem, the simple statement of which is that the integrated volume of the Fermi surface of a Fermi liquid is proportional to the density of electrons. This result is independent of the strength of the interaction between the electrons, provided that the adiabatic principle of Fermi liquid theory is not violated by these interactions. This theorem was initially proved by considering a perturbative expansion of the electron-electron interactions [118], and later on proven non-perturbatively [143]. In the case of non-interacting electrons, Luttinger's theorem is a direct result of the Pauli exclusion principle, but the fact that it applies to the quasiparticles even as the interactions are included is remarkable. The momentum states available to quasiparticle excitations in a Fermi liquid is essentially a conserved quantity, which can only be changed by physically adding *regular* electrons to, or removing regular electrons from, the system. This serves as quite a powerful framework given that quasiparticle excitations can be composed of hundreds or thousands of individual electrons.

Finally, it is worth noting that the Fermi liquid state is inherently unstable. So far we have mainly been considering repulsive interactions between electrons — this is rather natural because Coulomb interactions between single electrons are repulsive. However, in the presence of even a weak attractive potential between electron quasiparticles, they are susceptible to pair up with each other and condense into a superconducting state. The low energy excitations of the superconductor do not bear resemblance to single electrons; they are composed of pairs of electrons. In this sense, an attractive interaction, especially between quasiparticles of opposite momenta, is a non-adiabatic perturbation to the Fermi gas. There are several arguments given in the literature regarding the instability of the Fermi liquid to an attractive potential. One very general argument relies on renormalization group analysis [156]. The interested reader can also look at Chapter 10.3 of Ref. [82] for specific arguments. It is worth noting that the low-energy description of a superconducting state of electrons is one of the few instances in which the solution to a non-adiabatic perturbation to the Fermi gas has been determined.

As discussed in the introduction, by far the most well-understood mechanism for the formation of an attractive potential between electrons is through an interaction mediated by the quanta of lattice vibrations, i.e. phonons. The intuitive picture is the following. After an electron moves through a region of the lattice, it leaves a wave of positive charge as the ions of the lattice cluster in its wake. This wake of positive charge can attract a different electron that comes into the region. An attractive interaction results from this mechanism

in second order perturbation theory [21]. Such a mechanism is fairly generic, which makes superconductivity a surprisingly common phenomenon in metals at low temperature.

Effects of the symmetry-breaking periodic lattice potential

"I don't remember. I don't remember, in fact, that Sommerfeld was worried about electrons being free. But to me, Bloch was essential." — Hans Bethe

Certainly we expect the structure of the underlying ionic lattice to have some sort of effect on the electron wavefunction in metals, and the resulting physical properties such as directional-dependent conductivity, response to polarized light, etc. In addition, the free electron model cannot account for the insulating properties of solids.

To account for these situations, we must consider the effect of the periodic electric potential induced by the ions in the underlying crystal lattice. The reason we chose to present the results of Fermi liquid theory first is to emphasize that Fermi liquid theory is a rather general result for weakly-interacting fermion gases (originally it was developed for liquid helium, a fluid in free space). The potential induced by the periodic lattice of a crystal can be considered a perturbation applied to the Fermi liquid, and the fact that the lattice is a translation symmetry-breaking potential turns out to have some interesting implications from the perspective of Luttinger's theorem. This will set the stage for discussing other types of symmetry-broken order in electron fluids.

By Bloch's theorem [15], the wavefunction of the electrons (or quasiparticles if we are starting with a Fermi liquid in free space) becomes modulated by a periodic term with the same periodicity as the crystal lattice.

$$\psi(\mathbf{r}) = e^{i\mathbf{k}\cdot\mathbf{r}}u(\mathbf{r}), \tag{1.4}$$

where $u(\mathbf{r}) = u_k(\mathbf{r}+\mathbf{a})$ is determined by the periodic potential of the lattice and has the same spatial periodicity as the crystal lattice. $\mathbf{a}$ is the lattice translation vector. These electron wavefunctions are called Bloch states, which extend over the entire crystal and give rise to familiar properties like electrical conductivity. Note that Bloch states can still be considered single-particle states.

One can calculate the dispersion of these states by treating the periodic potential as a perturbation of the Fermi liquid dispersion in free space [15]. A cartoon of the resulting electronic structure is shown in Fig. 1.7. The single-particle spectrum is repeated every $2\pi/a$ units in momentum space. Gaps arise at the level crossings because their degeneracy is lifted by the periodic potential. Microscopically, these gaps in the energy spectrum arise because wavefunctions of electrons that are free to move about in the vacuum begin to destructively interfere with each other at these momenta in the periodic potential. If the number of electrons in the system places the Fermi energy within one of these gaps, then the itinerant states that existed in the vacuum disappear after the periodic potential is turned on. More generally, depending on the location of the Fermi energy, which is set by the number of electrons that existed in the vacuum, the number of itinerant states left over after

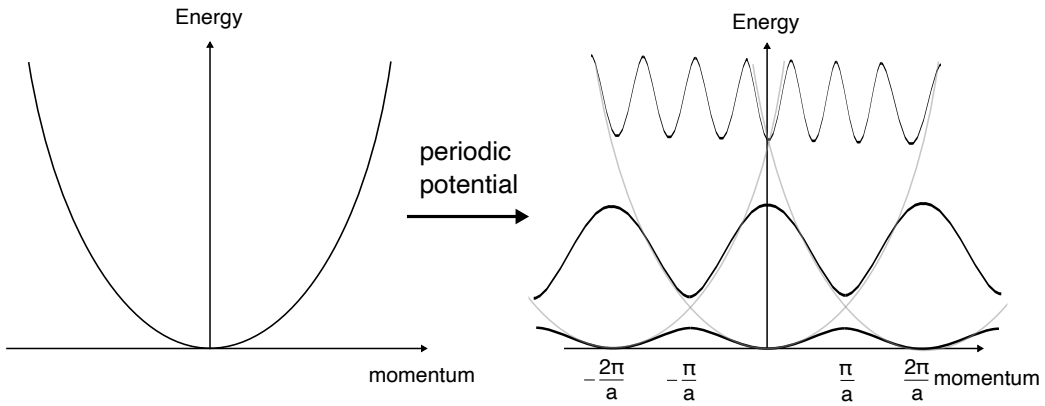

Figure 1.7: **Periodic perturbation to a gas of fermions** The free electron (or Fermi liquid) quadratic dispersion is modified by the presence of a periodic potential of periodicity a. The dispersion is repeated in momentum space (grey lines), and depending on the strength of the periodic potential, a gap opens at points where the dispersion crosses itself. This results in a reconstruction of the electronic spectrum into different "bands" of energy with occupied states that may be separated by gaps.

the periodic perturbation is turned on could in principle be different from the number of electrons that made up the Fermi liquid in vacuum.

Note the following important point from the perspective of Luttinger's theorem; the periodic potential of ions is a non-adiabatic deformation of the original potential because it breaks the continuous translational symmetry of the vacuum. Thus, Luttinger's theorem places no constraints on the relative volumes of the Fermi surfaces before and after the lattice potential is considered. This isn't to say that Fermi liquid theory does not apply in the case of electrons confined to a lattice, but that the Fermi liquid in the periodic potential cannot be adiabatically connected to the Fermi liquid in vacuum.

1.3 Beyond Fermi liquid theory: quantum critical nearly-magnetic metals

"It is hard to imagine describing the physics of metals without beginning with the electron" — Andrew Schofield

Although Fermi liquid theory has proven to be surprisingly robust in describing the properties of most metals, there are some metals where the principle of adiabatic continuity breaks down, and the systems exhibit non-Fermi liquid behavior. Typically, these cases coincide with proximity to some sort of symmetry-broken phase of the electron fluid, of-

ten magnetism. This text is focused on three distinct situations in which non-Fermi liquid physics can arise, with a chapter dedicated to each. All three non-Fermi liquid scenarios can be described, at least in part, as metals near magnetism. What is particularly notable about non-Fermi liquids is that the electrons, rather than remain in their non-Fermi liquid state down to zero temperature, often prefer to reorganize themselves into more stable collective phases like superconductivity, for example. Thus, all of the non-Fermi liquids described in this text have the potential to exhibit, and often do exhibit, nearly-magnetic superconductivity (or in some cases nearly-magnetic superconductivity which is also in proximity to other ordered phases). In other words, the reason that superconductivity happens and the reason that non-Fermi liquid physics happens might be the same. In this section, we will briefly introduce the topics which will be explored further in the chapters of this text.

Nearly-ferromagnetic metals

In no particular order, the first situation where the Fermi liquid description can break down is in metals close to the zero-temperature intercept of a ferromagnetic phase boundary (Chapter 4). A good example of this phenomenon occurs in MnSi, where the low-temperature resistivity is observed to vary as $T^{3/2}$ when the material is subject to pressures high enough to suppress the ferromagnetic transition temperature to zero [163] (recall that a low-temperature electron relaxation faster than quadratic in temperature is indicative of a breakdown of the adiabatic principle central to Fermi liquid theory); the phase diagram of this material is presented in Fig. 1.8. Superconductivity sometimes, but not always, appears in nearly-ferromagnetic metals, as seen for example in UGe_2 under pressure (see Fig. 1.8) [172].

The source of non-Fermi liquid behavior in weakly- or nearly-ferromagnetic metals was originally explained in a picture by Hertz, Millis, and Moriya [133] (see also Ref. [39] chapter 13). The general idea is that at zero temperature, the system undergoes a symmetry-breaking transition between magnetically ordered and magnetically disordered — a quantum phase transition. If this transition is continuous, it is associated with the development of long-range magnetic modes in analogy to the way that long-range fluctuations drive thermal phase transitions. These long-range modes increase the strength of interactions between the Fermi liquid quasiparticles, and in principle can be a source of an electron-electron interaction that is a non-adiabatic perturbation to the non-interacting electron gas. The conventional method to treat such a problem is to consider the Fermi liquid continuum of quasiparticles weakly coupled to a bath of bosonic fluctuations associated with the symmetry-breaking order parameter [129]. There has been reasonable success in deriving scaling exponents of various physical quantitites based on these theories [132]. In practice, in metals near ferromagnetism, the transition often becomes first-order when the phase boundary approaches zero [95]. This issue will be discussed more in Chapter 4.4. Nevertheless, non-Fermi liquid physics can be observed at the zero-temperature endpoint of a ferromagnetic phase as has been seen in MnSi [163].

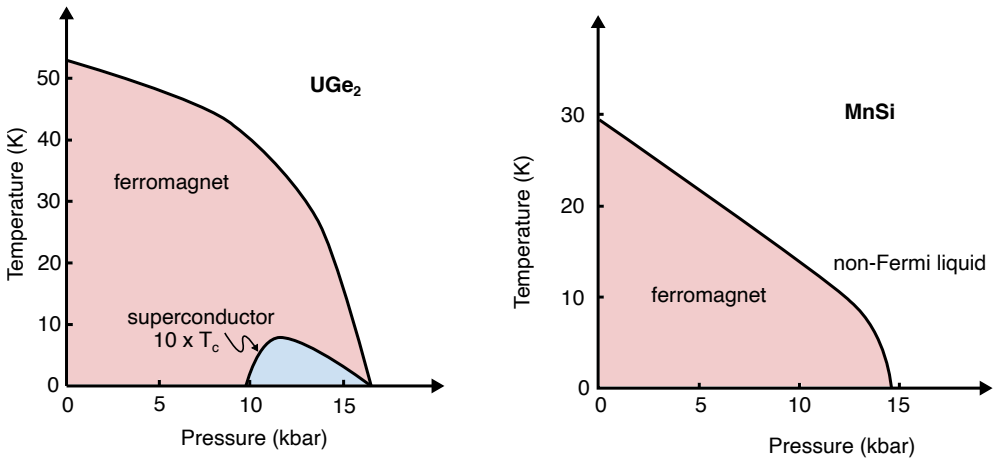

Figure 1.8: **Phase diagrams of some nearly-ferromagnetic metals** Both superconductivity and non-Fermi liquid behavior can be observed near the zero-temperature endpoint of a ferromagnetic phase [172, 163].

Nearly-antiferromagnetic metals

The second situation where non-Fermi liquid behavior commonly occurs is in metals near the zero-temperature intercept of an antiferromagnetic phase boundary, where superconductivity is frequently observed as well. This situation, discussed more in Chapter 3, is perhaps more well-studied than that of nearly-ferromagnetic metals, largely because there are more material examples that exhibit nearly-antiferromagnetic superconductivity — many iron-based superconductors [35], heavy fermion superconductors [67], organics [197], and copper-oxide ceramics [214] are nearly-antiferromagnetic metals with qualitatively similar phase diagrams to one another, as shown in Fig. 1.11.

The essential physics of these systems is that of a metal which undergoes an antiferromagnetic instability — the same electrons which are part of the itinerant conduction sea become magnetically ordered. While this complicates the situation somewhat if the electronic degrees of freedom are very strongly coupled to the magnetic degrees of freedom, it seems to be the case that certain properties of nearly-antiferromagnetic metals can be described by so-called weak coupling picture [2], where the magnetic fluctuations are treated as a perturbation to the electronic system (sort of analogous to the way in which electron-phonon interactions are treated in metals). This scenario is similar to the weak-coupling picture of ferromagnetic quantum critical metals discussed in the previous section — the main difference between ferromagnets and antiferromagnets is the energy-momentum dispersion relation of the magnetic modes, and where they overlap with the Fermi liquid continuum of electronic excitations [133].

Near the endpoint of the antiferromagnetic phase, the magnetic fluctuations become ‘soft’

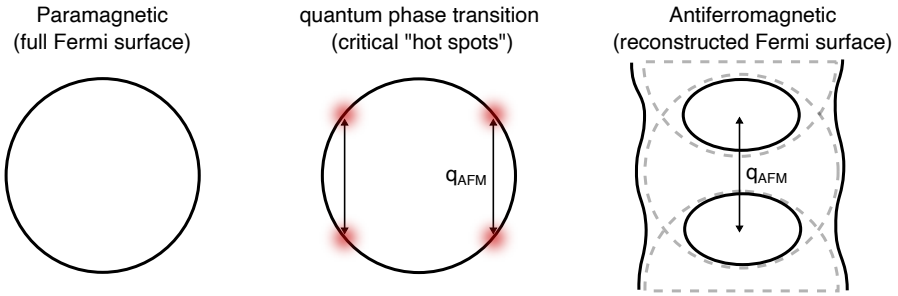

Figure 1.9: **Fermi surfaces of an antiferromagnetic quantum phase transition in a metal** The paramagnetic state has a circular Fermi surface, as shown on the left hand side. In the antiferromagnetic state, shown on the right, the Fermi surface reconstructs. States that coincide with the ordering vector of the antiferromagnetism (q_{AFM}) are gapped by the interference effect caused by Bragg diffraction from the electron spins in their ordered state. At the critical point between these two phases, points on the Fermi surface which would have been connected by q_{AFM} are strongly influenced by fluctuations of the antiferromagnetic order parameter. These red regions of the Fermi surface are expected to exhibit non-Fermi liquid behavior. This diagram is recreated from Ref. [40].

in the sense that their dispersion has a relatively small gap. Because antiferromagnetic order breaks translational symmetry, it is associated with a well-defined crystal momentum. These magnetic fluctuations therefore induce strong electron-electron interactions in very localized regions of the Fermi surface which are connected by the momentum of the antiferromagnetic modes. Such a situation is shown from the Fermi surface perspective in Fig. 1.9. We emphasize again that the above arguments should only pertain to the weak-coupling scenario, though there is a school of thought that this treatment can be extended to more general situations [2]. In addition, although antiferromagnetic fluctuations should only affect localized regions of momentum space, it is often the case that such materials exhibit non-Fermi liquid behavior in their bulk properties, as will be discussed more extensively throughout Chapter 3. For example, the heat capacity near the antiferromagnetic phase boundary of cerium-gold-copper alloys at a critical concentration seems to logarithmically diverge at low temperatures (e.g. 1.10B) [174]. The behavior of thermodynamic properties around such a magnetic quantum phase transition can be decently described through the derivation of critical exponents based on the Hertz-Millis-Moriya models of magnetic quantum criticality [133]. Many of the outstanding questions in the study of nearly-antiferromagnetic metals focus on explaining their bulk transport properties, which superficially should not be affected significantly by very localized scattering from antiferromagnetic modes at “hot spots” (Fig. 1.9), but in reality often experimentally exhibit strong deviations from the expectations of Fermi liquid theory in bulk measurements. Resolving this discrepancy is an experimental and theoretical challenge which is discussed more in Chapter 3 of this text.

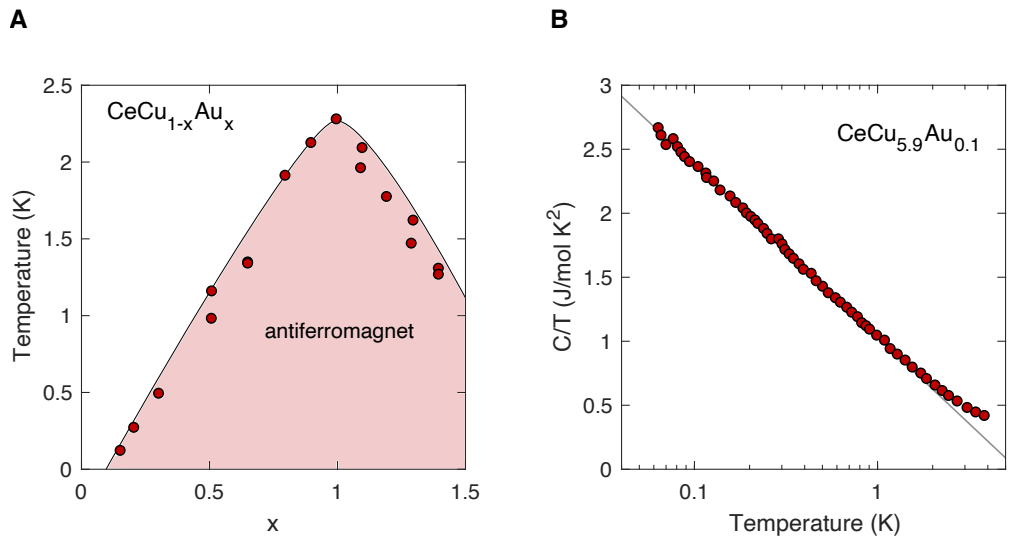

Figure 1.10: **Non-Fermi liquid properties in a nearly-antiferromagnetic metal A** An alloy of cerium, gold, and copper exhibits a transition from antiferromagnetic to magnetically disordered at zero temperature as a function of gold concentration. When the gold concentration in the sample is controlled such that the material is close to the zero-temperature endpoint of the antiferromagnetic phase, non-Fermi liquid physics is observed. **B** The low-temperature heat capacity coefficient logarithmically diverges at a critical concentration of gold. In a typical Fermi liquid, this value would be expected to be temperature-independent at low temperatures.

It is also important to address the validity of Luttinger's theorem around such a zero-temperature phase transition. The Fermi surface in the antiferromagnetic phase reconstructs due to the expansion of the unit cell. A gap can open up on certain points on the Fermi surface which intersect the magnetic Brillouin zone as a result of Bragg diffraction of the electrons from the spins of the antiferromagnetic order parameter, as seen in Fig. 1.9. In this sense, some itinerant electron states that are present in the magnetically disordered phase actually disappear in the antiferromagnetic phase because of interactions between the electrons and the symmetry-breaking antiferromagnetic order parameter. Thus, the zero-temperature transition between antiferromagnet and paramagnet in such materials typically does not conserve Fermi volume, just as the introduction of the periodic lattice potential of ions also does not conserve Fermi volume. The central difference between the lattice potential and an antiferromagnetic phase is that in this case the symmetry-breaking potential is induced by the antiferromagnetic order parameter in the spin degrees of freedom rather than the ionic potential of the crystal lattice. That being said, neither the antiferromagnetic phase nor the paramagnetic phase are incompatible with Luttinger's theorem because the states on either side of the critical point cannot be adiabatically connected to one another. As

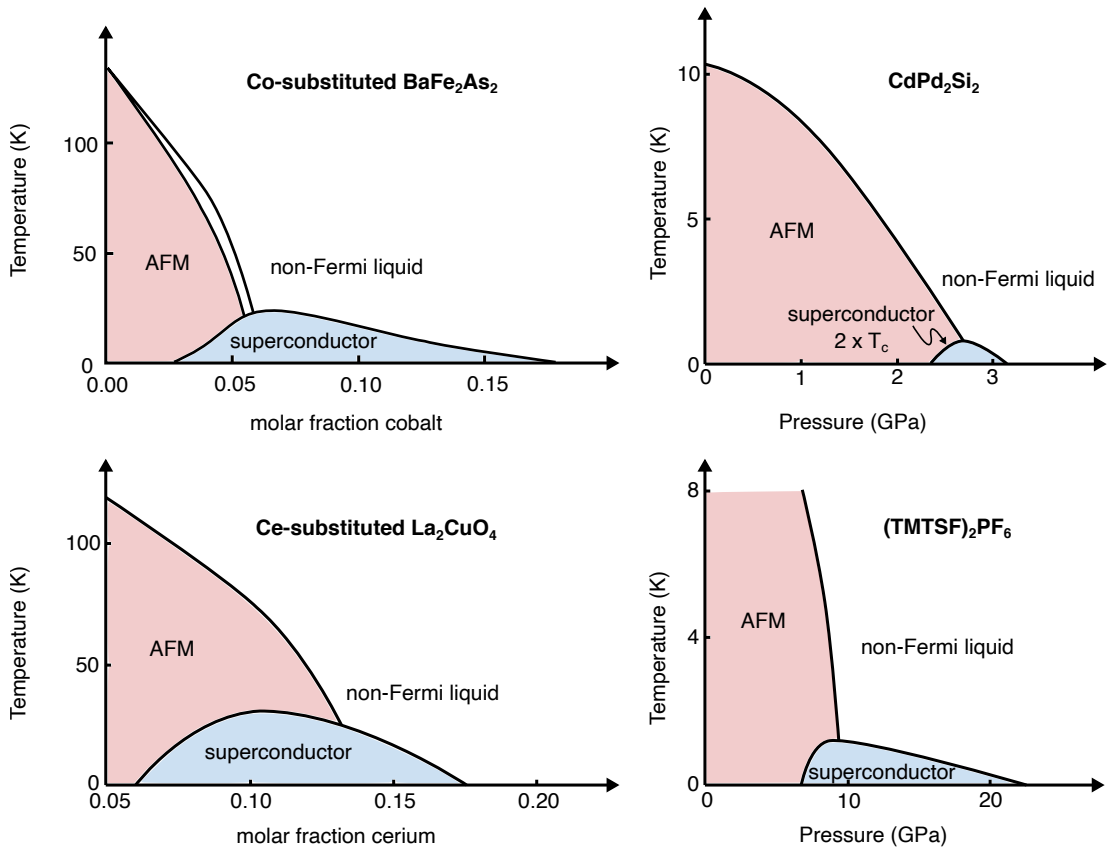

Figure 1.11: **Phase diagrams of some nearly-antiferromagnetic metals** Antiferromagnetic (AFM) phases suppressed to zero temperature tend to catalyze a 'dome' of superconductivity in the phase diagram, sometimes at relatively high temperature. A few examples are shown including $BaFe_2As_2$ [35], an iron-based superconductor, $CePd_2Si_2$ [67], a heavy fermion superconductor, La_2CuO_4 [214], a copper-oxide ceramic, and $(TMTSF)_2PF_6$ [197], an organic superconductor. All of them show qualitatively similar phase diagrams, as well as putative non-Fermi liquid behavior near the zero-temperature endpoint of the AFM phase.

a consequence, Luttinger's theorem has nothing to say about their relative Fermi volumes. Conventionally, then, near such a metallic antiferromagnetic quantum critical point it is believed that the ground state phases on either side are well-described by Fermi liquid theory. It is only at the critical point itself, or maybe a region of phase space at finite temperature above the critical point, where Fermi liquid theory may be violated by the interaction of electrons with critical magnetic modes.

Nearly-antiferromagnetic, nearly-charge localized metals

The third, and perhaps most complicated, situation where non-Fermi liquid behavior resides is in metals where the Coulomb interactions between the electrons are relatively strong, even strong enough to localize electrons which would have otherwise contributed to the density of the Fermi liquid. Antiferromagnetism, or even more complex charge and spin ordered phases, can also occur in such systems when the charges become localized. This scenario will be discussed in Chapter 2.

There are two major research thrusts in this category of materials. The first thrust is to characterize the ground state of the phase where charges are localized due to their mutual Coulomb repulsion — a scenario which, if not accompanied by a symmetry-breaking phase transition, apparently violates Luttinger's theorem [46]. One proposal is that if the electron-electron interactions in an electron fluid become strong enough, the fundamental excitations are different from Fermi liquid quasiparticles. An example is the 'Luttinger' liquid characterized by separate spin- and charge-carrying quasiparticles [177], completely different from the Fermi liquid quasiparticles which each carry both spin and charge. The spin excitations remain itinerant while the charged excitations become gapped, resulting in an insulating state with a sharply defined Fermi surface of charge neutral excitations. In this sense the Luttinger's theorem conserving the volume of the Fermi surface in the weakly-interacting Fermi liquid is conserved even when the interactions are cranked up to the point where the electrons localize. The Luttinger liquid scenario has been theoretically well-established in one-dimensional systems [126], and to some extent experimentally demonstrated for materials where the electronic structure is one-dimensional [85, 92]. However, it is not clear if such a description applies to the charge localized state of two- or three-dimensional systems. A related possibility is that of Anderson's resonant valence bond model [10], where quantum entanglement persists over long length scales in the charge localized state. Another possibility is a phenomenological description known as the 'marginal' Fermi liquid [210], which primarily seeks to describe the properties of the electrons close to the localization transition. On the other hand, there are other ways that Luttinger's theorem can be circumvented in such charge localized systems, namely by symmetry-breaking phase transitions which coincide with the reduction of Fermi surface volume. In this case, it would be no issue that the Fermi surface disappears in the strongly-interacting electron fluid because a symmetry is broken at the same time. This would be analogous to the introduction of the symmetry-breaking potential of the ionic lattice or of an antiferromagnetic order parameter as discussed previously; the Fermi liquid with and without symmetry breaking cannot be adiabatically

connected to one another and are therefore unconstrained by Luttinger's theorem. It may be that there is a fundamental reason that strongly interacting electron fluids, as exemplified by high-temperature superconductors and f-electron metals, seem to be generically unstable to symmetry-broken order.

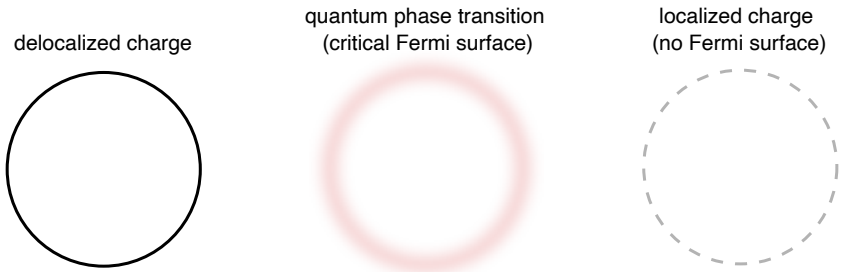

Figure 1.12: **Fermi surface of a charge localization transition** The Fermi surface of the itinerant metal in the delocalized case becomes 'critical' at the transition point to the localized case. In the localized case, there is no well-defined Fermi surface of itinerant electron states. Such a transition apparently violated Luttinger's theorem for Fermi liquids, and it is unclear how to describe the fluctuations of a critical Fermi surface.

Therefore, a second main research thrust is to characterize the transition between a charge localized state and a delocalized state, i.e. characterize the metal which is "nearly-localized" — such metals often exhibit non-Fermi liquid behavior, as well as other forms of symmetry-broken order (like antiferromagnetism) induced by the strong electron interactions. Unlike in nearly-antiferromagnetic metals as discussed in the previous section, where antiferromagnet order destabilizes the Fermi liquid in localized regions of momentum space associated with antiferromagnetic ordering, the localization of charges at a quantum phase transition is expected to result in the disappearance of an entire Fermi surface, as shown schematically in Fig. 1.12. Sometimes, this localized insulator is also antiferromagnetic. Therefore, in these systems, not only are antiferromagnetic fluctuations potentially relevant at the quantum phase transition, but charge fluctuations associated with the dissolution of the Fermi liquid may be relevant as well. It remains to be seen how to even describe such a 'critical Fermi surface' [177]. It also remains an open question whether symmetry-breaking is a universal phenomenon in systems where the electron-electron interactions are strong enough to cause a loss of itinerant states.

Part of the reason that this topic is given urgency is that the high-temperature superconducting copper-oxide ceramics, in compositions where superconductivity is strongest, are believed to be metals close to a charge localization-delocalization transition [114]. Some argue that the Luttinger liquid physics of spin-charge separation is relevant to superconductivity in these materials [7]. On the other hand, as mentioned earlier, nearly charge localized materials are also very often nearly-magnetic (charge localization can coincide with antifer-

romagnetic order developing in the same electrons that localize as is the case in $YbRh_2Si_2$ and $CeRhIn_5$, and also in a region of the cuprate phase diagram), so in addition to the potential presence of spin-charge separation, and charge order fluctuations [114, 76, 68, 211, 59, 42], spin fluctuations associated with nearby antiferromagnetism are present as well [114, 4, 111, 80]. For these reasons, the mechanism for high-temperature superconductivity in copper-oxide ceramics is unsettled with some arguing that spin-charge separation plays the key role, some arguing that nearly-antiferromagnetic physics plays the key role, and others arguing that proximity to some other form of charged order (such as charge density waves, or the enigmatic pseudogap) plays the key role. In reality, it is probably the case that all of these qualities are important to the development of high-temperature superconductivity in cuprates. But, the focus of this thesis is not explaining high-temperature superconductivity in cuprates. Instead, we focus on accumulating evidence for a phase transition between a charge-localized state and a charge-delocalized state in a quasi-two dimensional metal $CeCoIn_5$ away from a symmetry-broken phase. We also provide indirect evidence of Luttinger liquid physics including spin-charge separation associated with this transition, giving a potential starting point for describing the critical modes associated with the 'critical' Fermi surface that connects the delocalized metal to the charge-localized state. Phenomenological similarities between $CeCoIn_5$ and copper-oxide ceramics lead us to speculate that Luttinger liquid physics may be relevant to certain physical properties of high-temperature superconductors.

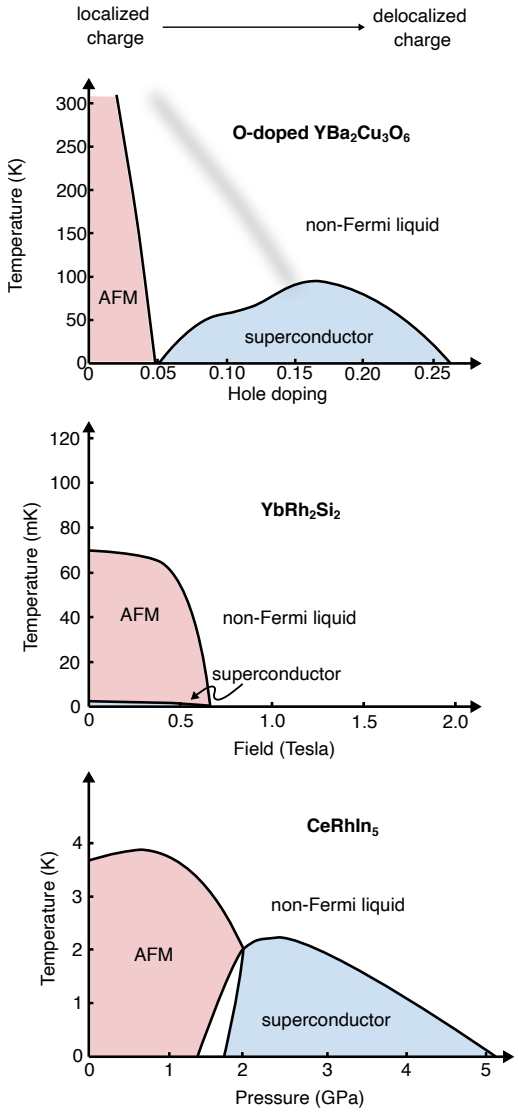

Figure 1.13: **Phase diagrams of some nearly-charge localized systems with antiferromagnetism (AFM)** Each of these systems appears to exhibit some sort of charge delocalization transition. YBCO ($YBa_2Cu_3O_7$) begins in an insulating antiferromagnetic state. The antiferromagnetic order is suppressed as the system is doped with excess oxygen [159]. There is evidence that the charges are localized at higher doping levels, and only delocalize between 0.15-0.20 doping levels [17] where superconductivity is strongest and non-Fermi liquid behavior is observed. The fuzzy black line indicates a possible 'pseudogap' phase transition of unclear origin [91]. In $YbRh_2Si_2$, the application of magnetic field delocalizes the Yb f-level valence electrons at the same time that antiferromagnetism is suppressed to zero temperature, giving rise to a non-Fermi liquid phase [179]. In $CeRhIn_5$, the cerium f-level valence electrons undergo a localization-delocalization transition, perhaps concomitant with the zero temperature endpoint of the AFM phase boundary [96]. Superconductivity tends to appear somewhere in the phase diagram of these systems.

Chapter 2

Nearly-charge localized systems and spin-charge separation

"I was able to explain most of the experimental data about layered cuprates ... As a result I can state that the so called 'mystery' of high-T_c superconductivity does not exist." — Alexei Abrikosov"

The work in this chapter was based on previously published work in Ref. [122]. Sections 2.1, 2.2, 2.3, 2.4, and 2.7 are original to this text. The other section were copied from Ref. [122] with certain parts rewritten to fit into the broader structure of this text. The present author performed crystal growth and measurements of the quantum oscillation data, Hall effect measurements, analysis, and conceived of the experiments. Permission to include published work was obtained from the coauthors of Ref. [122].

At a charge localization quantum phase transition, all momenta of the Fermi surface are affected. The Fermi surface itself becomes unstable and disappears. In these situations, antiferromagnetism can appear 'incidentally' when the Fermi surface is destroyed, or in a nearby region of the phase diagram. Certainly, our expectation is that spin fluctuations play a key role in such systems in much the same way as in other nearly-antiferromagnetic metals. However, in addition to spin fluctuations, we may expect to see new physics associated with the localization of charge induced by electron-electron interactions. The central questions brought up by a 'Fermi volume collapse' type of critical point are: How do we describe the phases on either side of a Fermi surface instability? How do we reconcile this scenario with Luttinger's theorem, which protects the volume of a Fermi surface? What are the low-energy excitations in the phase where Luttinger's theorem is apparently violated? And, ultimately, because many high-temperature superconductors are nearly-charge localized materials, what is the relevance of all of these phenomena to promoting superconductivity?

Clearly, there are many questions remaining in the study of high-temperature superconductivity, and certainly almost none of them will be definitively answered in this text, or indeed for the next several decades if at all. The point of this section is to broadly introduce concepts which are thought to be relevant to certain unconventional superconductors, and to search for avenues to begin to understand the high-level physical picture of their phase

diagrams.

2.1 Mott insulators and antiferromagnetism

"The physical origin of a Mott insulator is understandable to any child" — Branislav Nikolić

In Chapter 1, we discussed several of the implications of Fermi liquid theory, and the conditions under which it holds. To summarize, Fermi liquid theory successfully describes the gross properties of most metals. The central result of Fermi liquid theory is that the interactions between the electrons lead to renormalized dynamical properties of single particles (which essentially behave in many ways like electrons). The central assumption is that the interactions between electrons are not 'too strong' in the sense that the lifetime of the single particle states is longer than their characteristic energy. Physically, one of the reasons that this is true, even though Coulombic interactions between electrons are in general quite strong, is that in most metals the itinerant electrons screen their mutual Coulomb interactions.

This effect is known as Thomas-Fermi screening in quantum degenerate electron gases — also known as Debye screening in classical plasmas at finite temperature. The effectiveness of Thomas-Fermi screening depends on the density of the electron gas in a metal — at high electron densities, the electrons are screened from their mutual Coulomb potentials very effectively. However, under certain regimes of electron density, mutual interactions between the electrons in the gas become strong enough that stable bound states can be formed. Charges might prefer to localize to their host atoms under these circumstances, and this is the essence of a Mott insulator.

A breakdown of Thomas-Fermi screening

To make the screening argument a little more rigorous, imagine adding a single charge of q to a nearly-free electron gas. This is equivalent to adding a local perturbing potential $\delta U(r)$ (the following argument is taken from slides by B.K. Nikolić). The task now is to find the induced electric potential distribution taking into account the screening effects of the free electrons. The density of electrons in the near vicinity of the perturbing charge will change in order to keep the chemical potential constant $\delta n(r) = eD(\epsilon_F)\delta U(r)$, where $D(\epsilon_F)$ is the density of states at the Fermi level. Assuming that the electrical potential near the perturbation charge is determined by the space charge distribution, we can solve the Poisson equation. $\nabla^2 \delta U(r) = -\frac{e\delta U(r)}{\epsilon_0}$. The result is

$$\delta U(r) = \frac{q}{4\pi\epsilon_0}\frac{e^{-r/\lambda_{TF}}}{r}. \tag{2.1}$$

This is the familiar Yukawa potential, which is the name given to the screened Coulomb potential. In this case, $\lambda_{TF} = \sqrt{\frac{\epsilon_0}{e^2 D(\epsilon_F)}}$, is the screening length. In the context of solid-state

physics, it is referred to as the Thomas-Fermi screening length (in the context of plasmas at finite temperature the same quantity is called the Debye screening length). λ_{TF} gives a measure of length scale over which the Coulomb potential of a point charge will be screened in the electron gas. Plugging in the expression for the density of states in three dimensions, we arrive at an equation for the characteristic screening length in terms of the electron density

$$\lambda_{TF} = \frac{\hbar^2 \epsilon_0}{m} \left(\frac{\pi}{3n}\right)^{1/3} \approx \frac{1}{4} \frac{a_0}{n^{1/3}}. \tag{2.2}$$

In the second approximation, we have substituted the value of the Bohr radius. A general qualitative, but rather satisfying, argument is that if $\lambda_{TF}^2 < a_0^2$, then the electrons on each site do not 'see' each other — they are screened over a length scale which is smaller than the average distance between the electrons. In typical metals, let's say copper, this condition is satisfied easily, which is part of the reason that the electrons in copper can be so well described as a Fermi liquid at low temperature.

At low values of electron density, by the above arguments the screening between electrons is relatively ineffective, and the interaction potential between the electrons can be strong enough to form a bound state such that electrons prefer to remain localized to their host atoms ($\lambda_{TF}^2 > a_0^2$). This state would be insulating (a Mott insulator!) in the sense that the charges are localized by their mutual repulsion with each other and the system does not conduct electricity. Thus, the itinerant quasiparticle states that are expected to exist from the Fermi liquid theory perspective actually disappear (they are no longer itinerant states) because of a process driven entirely by the interactions between the constituent electrons. Therefore, we have a loss of Fermi volume due to electron-electron interactions; as such, Luttinger's theorem is apparently violated by this configuration. Consequently, the adiabatic principle is also violated because the Fermi liquid quasiparticle is clearly not an accurate description of the low-energy excitations. There is certainly no overlap between this phase and the Fermi gas.

Antiferromagnetism in Mott insulators

It is often the case that real Mott insulators (e.g. La_2CuO_4) also undergo an antiferromagnetic transition either concomitant with or in proximity to their charge localized phases. Anderson, Mott, and others developed a theory describing how an antiferromagnetic 'superexchange' interaction can develop between the electrons localized into a Mott insulating state [107, 8, 9, 63].

The full perturbation theory calculation will not be presented here, but some qualitative arguments will be presented relevant to the proceeding discussion. A. Schofield gives a clear intuitive explanation for the antiferromagnetic superexchange interaction that arises when electrons are localized into a Mott state in his review on non-Fermi liquids [174]:

> "no electron really likes to be fixed on a single site — it is like being held in a small box and its kinetic energy is high. This can be lowered if the electron

> made 'virtual' tunnelling hops onto the neighbouring occupied sites and back. This the electron can only do if the neighbouring site has the opposite spin (the Pauli principle remains absolute). So we see that the interactions also favour the antiferromagnetic arrangement of spins..."

What is meant by 'virtual' tunneling here is really just the result of a second order perturbation calculation, where the term which lowers the overall energy involves an intermediate transition from an energy level localized to one site to one localized on a neighboring site.

Mott localization-delocalization transitions

The origin of a Mott insulator is understandable qualitatively. There are of course remaining questions in the Mott insulator — specifically, what is the ground state and what are the low-energy excitations? Clearly, a Fermi liquid description is inadequate because there are no itinerant fermion quasiparticles. Within this landscape, there are several proposals that have existed for some time, including Anderson's resonant valence bond solid picture [10], and others.

However, with these questions about the Mott insulating state in mind, perhaps one of the most puzzling aspects of Mott insulator or charge localized systems is a description of their basic properties when the charges undergo a delocalization transition when the system is perturbed by pressure, charge doping, etc. Say, for example, the electron density is increased such that screening effects become strong enough such that the Fermi liquid is restored. Or, the density of electrons is reduced so that there is some room for electrons to hop from site to site. One straightforward model for these effects is to include the hopping of electrons from site to site as a term in the Hamiltonian (the second term in Eq. 2.3), which competes with the onsite Coulomb repulsion between electrons (first term in Eq. 2.3). Strictly speaking, we don't need to write down the Hubbard model because we will not delve deeply into theoretical approaches to solve it, but it is useful to bring up now in order to contrast to other comparable models later on.

$$H = U \sum_{i,\sigma} \hat{n}_{i\uparrow}\hat{n}_{i\downarrow} - t \sum_{i,\sigma} \left(\hat{c}^{\dagger}_{i,\sigma}\hat{c}_{i+1,\sigma} + \hat{c}^{\dagger}_{i+1,\sigma}\hat{c}_{,\sigma} \right). \tag{2.3}$$

Here, i labels the lattice site and σ labels the electron spin. If t becomes comparable or much greater than U, then the system tends towards delocalization. Both theoretically, and in the real-world examples where such a delocalization transition occurs, this is a challenging problem to address. From a theory point of view, such a quantum phase transition itself represents a slightly different paradigm compared to 'conventional' quantum phase transitions with a thermodynamic order parameter. More specifically, unlike in the case of say an antiferromagnetic quantum phase transition, where electrons are coupled to long-wavelength fluctuations of a bosonic order parameter (which at least under certain circumstances can be considered 'weakly-coupled' to the electrons), in the case of a such a delocalization transition,

the electrons are coupled to fluctuations of electrons themselves because the Fermi liquid itself is disappearing. In other words, the order parameter that is vanishing is the quasiparticle weight itself. What makes this even more challenging theoretically is that there are no small parameters in the problem — the kinetic and interaction potential energies are comparable, and perturbation theory is relatively ineffective. Experimentally, one of the reasons that this problem is so challenging is that there is a tendency for nearly-charge localized systems to rearrange themselves into other strongly correlated phases like charge density waves or superconductivity (or sometimes more enigmatic 'pseudo'-gapped states, where it is unclear if there is some sort of thermodynamic order). The proximity of Mott insulating states to antiferromagnetic order also raises questions about the role of antiferromagnetic fluctuations. So around such a localization-delocalization quantum critical point, there may be charge fluctuations, magnetic fluctuations, and other order parameters in close proximity. Experimentally disentangling these different contributions, and their effects on physical properties like charge transport or relevance to the development of superconductivity, is a monumental task, one which has withstood nearly four decades of concerted research effort in the case of the hole-doped cuprates.

In this text, we will focus on a specific and fundamental question about charge delocalization transitions. What is the mechanism by which the Fermi liquid (in the delocalized state) disintegrates when the system moves into the localized state? More specifically, Luttinger's theorem conserving Fermi volume is apparently violated by such a quantum phase transition, and our interest is in answering exactly how Luttinger's theorem fails around such a transition, or if there is a way to reconcile charge localization with Luttinger's theorem. The answer to this question provides an indirect means to characterize the ground state phases on either side of a Mott localization-delocalization transition without necessarily needing to sort through all of the complicated electronic phases that may form in real samples. The goal of this is to provide a 'high-level' picture of the phase diagram of a Mott localization-delocalization transition, and then perhaps examine whether such a high level view is capable of predicting or explaining some of the resulting physical properties such as charge transport and thermodynamics, some of which are rather remarkable and unique to systems near Mott localization-delocalization.

2.2 Heavy fermion metals as model Mott insulators

"The Heavy Fermions would make a great band name" — Steve Kivelson

In some ways, heavy fermions — a name usually applied to metal alloys containing an element in the lanthanide or actinide series with a partially occupied $4f$ or $5f$ level — are like 'quantum simulators' of other correlated electron systems, where the interactions are well-understood and some of their fundamental physical properties have a close correspondence with those of other systems of quantum correlated matter. This type of 'quantum simulation' using heavy fermion metals has been a common theme in the history of correlated quantum matter. For example, heavy fermion materials provided some of the strictest tests of Fermi

liquid theory, where the notion of renormalized quasiparticles is taken to an extreme — the materials often show effective masses of order 10-1000 times the free electron mass, hence their name. Interestingly, the heavy fermion metal $CeAl_3$ was one of the first materials where Fermi liquid electron-electron scattering was unambiguously observed in low-temperature resistivity measurements [11]. Some of the first known unconventional superconductors, discovered in the 1970s, were heavy fermion materials [192]. The study of conventional quantum criticality in metals was initially carried out almost exclusively on heavy fermion compounds. And finally, some of the best examples of nearly-ferromagnetic supeconductivity occur in uranium-based metals. The above isn't meant to be an exhaustive list of heavy fermions, but to give examples of where heavy fermion metals have been extremely useful in the study of correlated electron physics. We take a similar approach in attempting to gain insight on the Mott delocalization phase transition. In particular, the main question we are trying to answer is how to reconcile a transition between a Mott insulator and a delocalized metal with the constraints imposed by Luttinger's theorem. To this end, the heavy fermions are a useful platform, and in particular the '115' materials, $CeCoIn_5$ and $CeRhIn_5$ are particularly useful.

In metals like $CeCoIn_5$, each cerium atom, of which there is one per crystallographic unit cell, hosts one f level valence electron. The $4f$ orbital is one of the most strongly localized of any atomic orbital ($5f$ is a close second) because the large nuclear charge, and relatively weak screening of the nuclear charge in the $4f$ wavefunction, pulls the electron wavefunction close to the nucleus [39]. Thus, at the simplest level this $4f$ electron can be considered a localized spin-1/2 moment. These local moments coexist with a sea of itinerant conduction electrons from d, p, and s orbitals. If there were no interaction between the f-electrons and the conduction electrons, the f-electrons would be in an insulating state as a result of their strong relative Coulomb repulsion. Such a state can be considered a Mott insulating state of the f-electrons.

But, there is an interaction between the electrons in the f-level and those in the more itinerant conduction electrons of the d, p, and s orbitals. This interaction is essentially what makes f-electron metals so interesting to low-temperature physicists. A hybridization term, known as the 'Kondo' interaction — a name taken from the study of isolated magnetic impurities in metallic hosts — describes the antiferromagnetic contact interaction between the f-electron moments and those of the conduction electrons. Now, there are basically two ways to take into account the Coulomb repulsion between f-electrons. On the one hand, the Anderson lattice model includes the f-electrons as a separate band from the conduction electrons, and an exchange interaction U between neighboring f-electrons:

$$H = \sum_{k\sigma} \epsilon_k c^\dagger_{k\sigma} c_{k\sigma} + E_0 \sum_{i\sigma} f^\dagger_{i\sigma} f_{i\sigma} + V \sum_{i\sigma} (c^\dagger_{i\sigma} f_{i\sigma} + c.c.) + U \sum_i n^\uparrow_{fi} n^\downarrow_{fi}, \tag{2.4}$$

where ϵ_k is the dispersion relation for the conduction electrons. E_0 is the Fermi energy of the localized f electrons. The third term describes the hybridization between the f electrons and the conduction band. The last term describes the onsite Coulomb repulsion U between the f-electrons.

The second way to consider the f electrons is the 'Kondo' limit of the Anderson lattice, where it is assumed that the energy of the f electrons E_0 is much larger than any other energy scale in the system:

$$H = \sum_{k\sigma} \epsilon_k c^\dagger_{k\sigma} c_{k\sigma} + J_K \sum_i s_i \cdot S_i, \tag{2.5}$$

where J_K is the Kondo contact interaction between the conduction and f electron spins. The transformation from the Anderson to Kondo lattices yields $J_K = V^2 \left[-\frac{1}{E_0} + \frac{1}{E_0+U} \right]$ [40].

Luttinger's theorem for f-electron metals

Right away we can draw some comparisons between the Hubbard model for Mott insulators, and the Kondo lattice model for f-electron metals. In the Kondo lattice, the 'Mott-like' part of the system is included explicitly — i.e. by construction the Kondo lattice Hamiltonian has f-electrons which are localized by their Coulomb repulsion. The Kondo lattice can thus be thought of as a Mott insulator in the f band with conduction electrons coupled to it by the Kondo exchange interaction. As such, we can (at least indirectly) begin to answer the question of what the ground state of a Mott insulator is, by asking what is the ground state of a Kondo lattice.

It is natural in the context of the Kondo lattice is ask whether the Mott-insulating f-electrons should become part of the Fermi volume when the Kondo contact interaction is turned on. Unlike in the Mott insulator, this problem has actually been solved in the case of the Kondo or Anderson lattices. The answer, due to Oshikawa [143], is that in the conventional metallic ground state of the Kondo lattice, the f-electrons appear to become an integral part of the itinerant metal. In particular, they join the conduction electrons, contributing their full share to the Fermi volume. The Kondo lattice therefore obeys a type of Luttinger theorem, where the conserved Fermi volume includes both the f-electron density and the conduction electron density. The results of Oshikawa's theorem are non-perturbative. From a more microscopic perspective, the f-electrons join the Fermi volume through the formation of Kondo singlet correlations between the local f moments and the conduction electrons, which effectively hybridize the f-level with the conduction bands. This mechanism is what gives heavy fermions their name — the hybridization between the f-electron and conduction band results in a very weakly dispersing hybridized band with a high effective mass, where the quasiparticles are composed of conduction electrons and f-electrons that are strongly interacting. In principle, this mechanism has been known for a long time — long before Oshikawa came up with his theorem. But Oshikawa first noticed that, not only do f-electron *typically* hybridize into the Fermi surface, but strictly speaking they are actually *required* to.

Energy scales in the Kondo lattice applied to real materials

With Oshikawa's theorem, and the overall f/conduction hybridization mechanism in mind, we give here some background on the temperature-dependent properties of heavy Fermi liquid metals. This section isn't completely necessary for the following arguments of our text, but there is some useful insight to be gained by considering the energy scales involved in f-electron metals, and how they manifest in physical properties. The reader can skip this section without losing much context for the following sections.

For a $4f^1$ electron, the spin-orbit coupling is usually much stronger than the crystal field splitting. So, we use $J = L + S$ as the good quantum number; $L = 3, S = 1/2$ for an f-orbital electron. Hund's rule implies that the lowest energy state is $J = |L - S| = 5/2$. So we have a 6-fold degenerate manifold with m_J values spanning between -5/2 and +5/2. Crystal field splitting, in this instance octahedral splitting, results in a low-lying doublet according to Hund's rules. This state has a total angular momentum of $J = 5/2$, giving an expected magnetic moment of $2.54\mu_B/Ce$.

Generally speaking, in the limit of high temperature, thermal fluctuations quench the f/conduction electron hybridization, and the system can be treated as paramagnetically fluctuating localized moments (the f-electron moments), weakly coupled to an itinerant sea of conduction electrons. At high temperature, therefore, the f-electrons induce a Curie-Weiss paramagnetic susceptibility with an expected fluctuating moment of $2.54\mu_B/Ce$ based on the arguments above. Indeed, using $CeCoIn_5$ as an example, we do observe a paramagnetic $\sim 1/T$ susceptibility, which corresponds to a fluctuating moment of $2.97\mu_B/Ce$, in fairly good agreement with the expected value of a free Ce^{3+} ion (Fig. 2.1A). As the temperature decreases and the system approaches its ground state, the spin-spin interaction between the f and conduction electrons kicks in. One of the key energy scales is the crystal field splitting between the lowest Kramer's doublet and the next energy level. The Kondo/Anderson lattice models described above are only valid in the limit where the f-electrons are concentrated in the lowest energy level, otherwise thermal vibrations are energetic enough to induce hopping between sites via the first excited doublet. Therefore, the models described in the previous section are only expected to apply to the temperature regime below the field crystal field splitting. This picture is consistent with the tendency of the magnetic susceptibility to saturate, an indication of screening of the fluctuating moments, in $CeCoIn_5$ below about 35K. This temperature roughly corresponds to the crystal field splitting between ground and first excited states in $CeCoIn_5$ [31]. Below about 10K, another divergence in the paramagnetic susceptibility occurs upon decreasing temperature further — the origin of this behavior is not clear, but might have to do with itinerant spin fluctuations present in the material.

One of the other physical properties of heavy fermion materials that tends to show a number of interesting features is the temperature-dependent resistivity (Fig. 2.1B). The resistivity of the sample upon cooling actually increases logarithmically. This is understood as a proliferation of scattering from the localized magnetic moments [100, 99]. In the case of a Kondo impurity, a single magnetic adatom in a metallic host, the resistivity would continue increasing until it saturates at low temperature [218]. In the case of a Kondo lat-

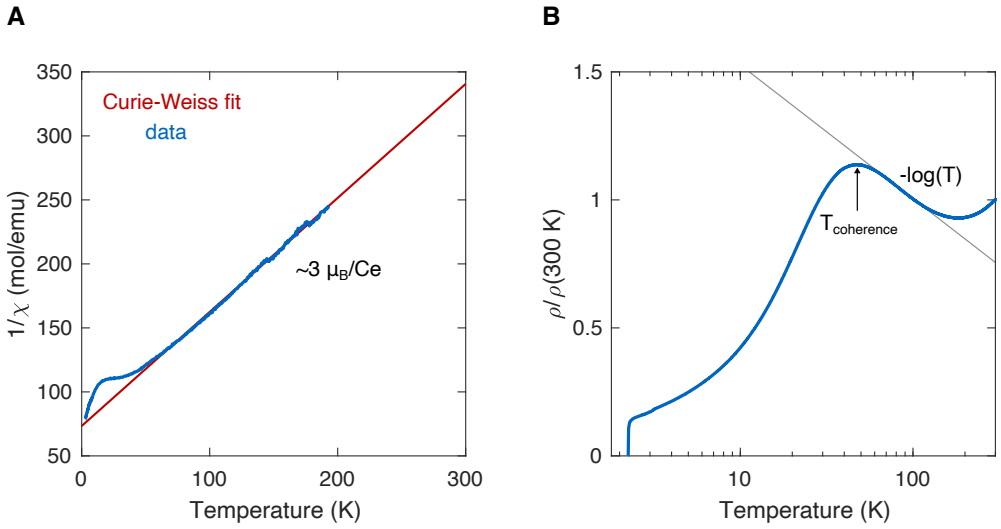

Figure 2.1: **Temperature-dependent physical and magnetic properties of $CeCoIn_5$** **A** Inverse magnetic susceptibility (H/M) measured in an applied field of 500 Oe. The linear trend at high temperatures can be fit to the Curie-Weiss law, from which a fluctuating moment of about $3\mu_B$/Ce ion is obtained. This gives decent agreement with the expected value of a free Ce ion ($2.54\mu_B$), as discussed in the text. The inverse susceptbility shows a tendency to saturate below about 35K. **B** Resistivity of $CeCoIn_5$ normalized to the room temperature value. A logarithmic upturn occurs over a broad temperature range at higher temperatures, followed by a pronounced peak at about 45K. Below the peak, the resistance precipitously drops and the sample ultimately becomes superconductivity at about 2.3K.

tice, the resistivity peaks and drops when the sample is cooled below a certain temperature. This behavior is often taken as an indication for the partial formation of 'coherent' singlet correlations between the f and conduction electrons, in which the local moments transition from scattering centers to components of an entangled wavefunction which includes the conduction electrons. It should be noted that in reality the peak in the resistance has the characteristics of a broad crossover regime, which has more in common with a percolation transition of f/conduction electron singlets than it does with a sharp phase transition [86, 32]. Experimentally, evidence has been found for singlet correlations developing well above the coherence temperature, and in heavy fermion metals with a Fermi liquid ground state, the Fermi liquid forms well below the coherence temperature [86]. Sometimes these experimental observations are described with a phenomenological two-fluid model, where the population of singlets compared to the population of localized moments evolves continuously with decreasing temperature [140]. Interestingly, in $CeCoIn_5$, the experimentally determined coherence temperature is about 45K — pretty close to the temperature below which the susceptibility starts to show saturation, and the energy scale of crystal field splitting between

the ground and excited crystal field states.

Because we are primarily concerned with the ground state of the Kondo lattice, these topics will only be addressed tangentially from now on. Perhaps the important takeaway here is that the presence of a coherence temperature in the resistivity should not be taken as evidence that a heavy Fermi liquid state has formed, or that it will eventually form even well below the coherence temperature. A straightforward example is $YbRh_2Si_2$, in which a coherence temperature is present [204], but the f-electrons are thought to be fully localized at the lowest measurable temperatures [147]. Certainly, the temperature-dependent formation of a coherent f/conducton electron state is an understudied topic both theoretically and experimentally, and probably one which should be explored further in future work.

Taking the above discussion at face value, we can see that in a typical f-electron metal with a Fermi liquid ground state, the Fermi volume of the metal actually increases when going from high to low temperature — the f-electrons are localized at high temperature, and join the Fermi surface only at low temperature apparently as a result of an electron-electron (Kondo) interaction. Is this a violation of Luttinger's theorem? The answer is no, simply because Luttinger's theorem only applies to the ground state of a metal.

Quantum phase transitions out of the heavy Fermi liquid: f-electron localization and critical Fermi surfaces

"This is all just a fantasy" — Chandra Varma

We are now prepared to address the problem of the Mott localization-delocalization transition from the perspective of f-electron localization. Unfortunately, Oshikawa's theorem tells us that no matter how small the Kondo coupling is, the ground state of the system is a Fermi liquid with the f-electrons as part of the Fermi volume. So in order to see how the f-electrons behave when they are decoupled from the conduction electrons, we would have to reduce the Kondo coupling to zero. In practice, this isn't possible in real materials. Luckily, in most Kondo lattice-like materials, there is an interaction which competes with the Kondo coupling called the RKKY (Ruderman–Kittel–Kasuya–Yosida) interaction. This is an antiferromagnetic exchange interaction between the f-electrons mediated by the conduction electrons, which tends to force the f-electrons to localize and antiferromagnetically order.

$$H_{RKKY} = \sum_{rr'} J_H(r, r') \overrightarrow{S}_r \cdot \overrightarrow{S}_{r'}. \tag{2.6}$$

Here $J_H(r, r')$ is the antiferromagnetic exchange between two f-electron spins at positions r and r', respectively. The exchange J_H is determined by the contact interaction between the conduction and f-electron spins, as well as the density of conduction electrons.

By tuning the relative strengths of the Kondo and RKKY interaction, for example by changing the density of conduction electrons, we can induce a quantum phase transition potentially into a Mott insulating state of the f-electrons. Observing and characterizing such a transition would give us insight into two aspects of Mott-like localization. First, we can

see how to reconcile such a transition with Luttinger's theorem (or in this case Oshikawa's theorem). Second, we can develop an understanding of the low-energy excitations of the Mott insulating ground state. This interaction has a tendency to destabilize the heavy Fermi liquid, allowing us to study possible f-electron localization transitions.

Characterizing a possible zero-temperature transition in which the f-electrons withdraw from the Fermi volume and recover their localized character in the *ground state* has been a long-standing problem. Theoretically, it has been established that there are essentially three different scenarios, where the interplay between f-electron charge localization and antiferromagnetic order in the f-electrons occurs in distinct ways.

The three possible QCPs in heavy fermion metals are summarized in Fig. 2.2. A ground state phase diagram has been theoretically developed. It is reprinted in Fig. 2.2 from Ref. [185]. The J_K parameter is the Kondo coupling constant, which tends to push the system towards a phase with delocalized f-electrons (a 'large' Fermi surface), as discussed in the previous sections. G is a parameter which characterizes the degree of 'frustration' in the system. For example, this could be geometrical frustration, by inducing significant next-nearest-neighbor interactions, or it could be enhanced with quantum frustration by making the system more two-dimensional (in two-dimensions quantum fluctuations tend to be stronger than in three dimensions). When a physical perturbation is applied to a system, i.e. hydrostatic pressure, both J_K and G would tend to change, and the perturbation will trace out different trajectories in the ground state phase diagram. Depending on the degree of frustration inherent in the material, broadly speaking three different permutations of antiferromagnetism and charge delocalization quantum phase transitions are present.

In scenario II, the charge localization transition occurs inside of the antiferromagnetic phase, as seen for example in $CeIn_3$ at high magnetic fields [175]. This transition between localized and itinerant AFM may be associated with a change in symmetry of the AFM order parameter such that Luttinger's theorem is not violated. A separate transition out of antiferromagnetic order occurs at a later point in the phase diagram after the f-electrons are already delocalized. The antiferromagnetic transition in this case corresponds to heavy quasiparticles weakly coupled to a bath of AFM fluctuations — this is the situation that appears to describe $CePd_2Si_2$, for example [185]. Such a transition can be considered a more or less 'conventional' AFM QCP, in that the physics of critical spin fluctuations in nearly-antiferromagnetic metals seems to well-describe many of the properties of the materials that are thought to fall into scenario II.

In the scenario I, the antiferromagnetic phase is destroyed at the same critical point where the heavy electron are formed and the f-electrons undergo a localization-delocalization transition. While there is a change in Fermi volume in this scenario, it is accompanied by a symmetry-breaking transition. In principle, this scenario does not violate Luttinger's theorem because Luttinger's theorem does not apply to cases where symmetry breaking occurs. Such a description is thought to apply to the field-induced antiferromagnetic transition/f-electron localization transition in $YbRh_2Si_2$ [147]. The physics of charge delocalization and magnetic quantum criticality are present simultaneously.

In scenario III, there is a separation between the antiferromagnetic phase and the charge

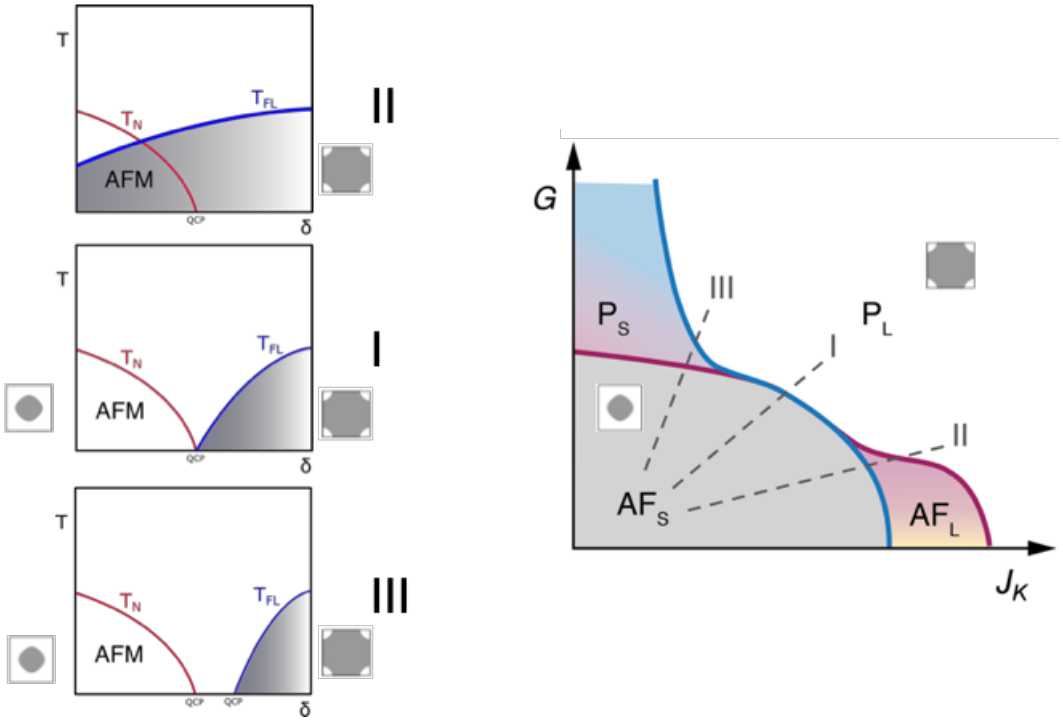

Figure 2.2: **Phase diagrams in the Kondo lattice problem** On the right is the theoretically constructed ground state phase diagram of the Kondo lattice [186]. J_K is the Kondo coupling constant, and G quantifies the degree of 'frustration' — either geometrical or quantum frustration (i.e. reduced dimensionality). Phases labeled by subscript S have a 'small' Fermi surface with localized f-electrons, whereas phases labeled by L have delocalized f-electrons with a 'large' Fermi surface. The small boxes are example Fermi surface of the small and large cases. There are three different scenarios for ground state trajectories as a non-thermal parameter δ is tuned (say pressure or chemical composition). Each scenario is depicted as a function of temperature in the plots on the left. In scenario I, the antiferromagnetic transition coincides with the charge delocalization transition. In scenario II, there is a transition between different antiferromagnetic states associated with charge delocalization, and then a separate AFM quantum critical point of itinerant antiferromagnetism. In scenario III, the AFM transition and charge delocalization occur at separate points, with a paramagnetic phase with localized f-electron charge (called P_S) between them.

localization point. An intermediate paramagnetic phase with localized f-electron charge separates the two. Superficially, if the f-electrons localize without some sort of spontaneous symmetry breaking, the remaining Fermi volume without f-electrons is in apparent violation of Luttinger's theorem (recall that Oshikawa showed that the Luttinger count in a Kondo lattice includes the f-electrons). Thus, scenario III is quite similar to the Mott localization transition described in the introduction, where charges seem to localize solely because of their mutual interaction.

The only established theoretical possibility in which scenario III satisfies Oshikawa's theorem is for an ordered phase to form — however, it is not a conventional symmetry broken phase. Rather, it is a topologically ordered phase known as a fractionalized Fermi liquid [176]. In this phase, the f-electron charge localizes to the cerium site, while the spin 1/2 degree of freedom remains itinerant. This f-electron phase is different from a conventional magnetic insulator in that the spin-carrying quasiparticles are spin-1/2 fermions (spinons) rather than integer-spin bosons (magnons). The presence of spinful, but charge neutral fermions manifests as a sharp Fermi surface of neutral fermions, which conserves the overall Fermi volume even when charges appear to localize. This Fermi surface has all of the thermodynamic and thermal transport properties of normal electrons, but is largely inert to external electric fields for example, or any other perturbations which couple to charge. Thus, this phase could be considered analogous to the spin-charge separated one-dimensional Luttinger liquid, but in a quasi two-dimensional crystal for example. In the Kondo lattice model, this fractionalized f-electron Fermi liquid would coexist with the normal electron contribution coming from the d, p, and s conduction electrons of the metallic background. $YbRh_2Si_2$ doped with Ir may fall into this category [185], as could YbAgGe [203], but scenario III is largely under-explored.

Already, we can imagine parallels with the phase transition in scenario III, and the qualitative structure of the phase diagram of hole-doped cuprate superconductors, which begin in the parent state as Mott insulators where the charge appears to delocalize at a critical oxygen doping level without clear accompanying signatures of a broken symmetry state in proximity (the 'pseudogap' phase of the cuprates may host broken symmetry, but this is still up for debate). Characterizing such a Mott-like localization transition without symmetry breaking in a Kondo lattice material may provide considerable insight into possibly related transitions in cuprate superconductors, and in its own right would present opportunities to study new physics, including fractionalized quasiparticles and critical charge fluctuations.

2.3 Phase diagram of doped $CeCoIn_5$

"$CeCoIn_5$ is an oxymoron" — Bill Steele, Cornell Chronicle

It is pretty well-established that in $CeRhIn_5$, the charge delocalization transition and accompanying Fermi surface reconstruction occur at the same point in the phase diagram as the antiferromagnetic quantum critical point (putting $CeRhIn_5$ into the scenario I class discussed in the previous section) [182]. The experiments were done on $CeRhIn_5$ under

pressure — where pressure is analogous to the control parameter in Fig. 2.2 that enhances the strength Kondo interaction relative to the RKKY interaction. Interestingly, $CeCoIn_5$ has a slightly more two-dimensional crystal structure than $CeRhIn_5$. The c-axis lattice constant is larger in the Co version, and the f-level ground state wavefunction appears to be more compressed in the Co version than the Rh one [196]. In addition, the electronic energy spectrum is overall more two-dimensional in the Co version compared to the Rh one [178]. Therefore, we might expect the degree of quantum frustration to be enhanced in the Co version than in the Rh version, and thus for the factor G (of Fig. 2.2) to be larger, perhaps inducing some separation in the AFM and charge delocalization transitions as in scenario III. Such a separation may allow us to probe the physical properties associated with charge localization of a Mott insulator without an accompanying antiferromagnetic phase transition. In the following sections, we establish evidence that $CeCoIn_5$ does indeed host a quantum phase transition of the scenario III type.

$CeCoIn_5$ in particular has notable qualitative similarities to high-temperature cuprate superconductors, for example in crystal structure, transport properties, and unconventional superconducting state. Like many other unconventional superconductors, $CeCoIn_5$ exhibits signatures of a nearby QCP, including a logarithmically diverging specific heat capacity at low temperature [23] and a diverging Gruneissen constant [202]. $CeCoIn_5$ itself is not antiferromagnetic, but it is certainly close to AFM. Doping with Cd induces longe-range antiferromagnetism, as depicted in Fig. 2.3. In Fig. 2.3, however, one of the main questions is whether there is an f-electron delocalization transition in this material as in $CeRhIn_5$. And, in addition, if there is an f-electron delocalization transition, does it coincide with the zero-temperature endpoint of the antiferromagnetic phase boundary or occur at a separate point in the ground state phase diagram?

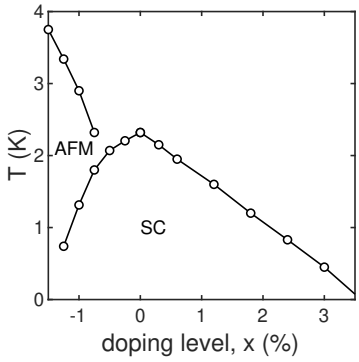

Figure 2.3: **Phase diagram of doped $CeCoIn_5$.** Positive doping corresponds to electron-doping (Sn substitution of the indium site). Negative doping corresponds to hole-doping (Cd substitution of the indium site). Antiferromagnetic order abruptly ends at cadmium doping levels of 0.6%. A superconducting dome is present and centered at zero doping. The phase diagram is reproduced from Ref. [31].

2.4 Low-temperature carrier density measurements: evidence for an f-electron delocalization transition

"You are always a little bit wrong" — Hank Green

In some sense, the net carrier density of a metal at very low temperature is a measurement of the volume of the Fermi surface. And thus, if we are in search of Fermi volume-changing transitions, carrier density measurements are extremely valuable. In a more specific language to $CeCoIn_5$ in particular, the localized or itinerant nature of f-electrons can be probed by carrier density measurements. If the f-electrons are localized, the measured carrier density will reflect that of the d, p, and s conduction bands alone. On the other hand, if the f-electrons are itinerant, the total carrier density will be enhanced commensurate with the number of f-electrons per unit volume (e.g. in $CeCoIn_5$ there is one cerium f-electron per unit cell). To this end, we can probe the carrier density with Hall effect measurements across the phase diagram of $CeCoIn_5$. We will first go through how to convert the measured Hall voltage into a carrier density, and the various caveats associated with this conversion.

Hall effect theory

Single carrier type

The Hall effect refers to the transverse voltage generated by a magnetic field in the presence of applied current (see also Chapter 3, where we discuss details about semiclassical transport theory). If there is only one type of charge carrier, this voltage increases linearly with magnetic field with a constant of proportionality that is inversely related to the density of charge carriers. This relation can be derived with a simple force balance in the steady-state, with the constraint that current does not flow in the transverse direction ($qV_{xy} = F_{lorentz}$). Assuming current is flowing along x, and field is applied along z, then

$$\begin{aligned} V_{xy} &= v_x B_z t_z, \\ V_{xy} &= \frac{I_x B_z}{nte} \end{aligned} \tag{2.7}$$

where t_z is the thickness of the sample in the z direction.

Multiple carriers

The Hall effect is a deceptively complicated quantity in real metals in part because there need not be only one carrier type. In the case of multiple carrier types, the interplay of carrier densities and mobilities from each species gives rise to a nonlinear-in-field Hall voltage signal, making it difficult to determine the carrier density unless specific details about carrier mobilities are known independently.

Luckily, in the limit of high fields the Hall effect recovers a linear dependence on field which is inversely proportional to the *net* carrier density. That is, the sum of the carrier densities of each species. This result is independent of the detailed mobility balance between different carrier types, as shown in Fig. 2.4.

Note also that in the low-field limit (as $B \to 0$) the Hall coefficient is proportional to the density of the highest-mobility carriers. This is shown in Fig. 2.4D, where the amount of higher-mobility electrons is varied, while the number of lower-mobility holes is kept constant. At low fields, the value of ρ_{xy}/B is the same in every instance, proportional to the inverse carrier density of the higher-mobility electrons. At high fields, the value asymptotically approaches a value which depends on the relative number of carriers, and is independent of the relative mobility of carriers.

A second complication is that the above formulas, strictly speaking, assume that the Fermi surface is isotropic for each carrier type. This of course need not be the case, and a more general formula is required to deal with these details using the Shockley tube integral (which is discussed more in Chapter 3). However, in many situations one can model an anisotropic Fermi surface as a parallel contribution of different carriers with varying mobilities or carrier densities. Thus, the arguments described above using the simple isotropic carrier models for the most part carry over to generalized Fermi surfaces. The main result here is that, regardless of the shape and scattering time on each Fermi surface, or the number of different Fermi surfaces, the Hall voltage in the limit of ultra high fields recovers a linear dependence which is simply proportional to the net carrier density, i.e. the volume enclosed by the Fermi surface. The only assumption here is that the quasiparticles can be described as electrons, i.e. the Fermi liquid approximation, and that the sources of scattering randomize the momentum of the quasiparticles, i.e. the relaxation time approximation.

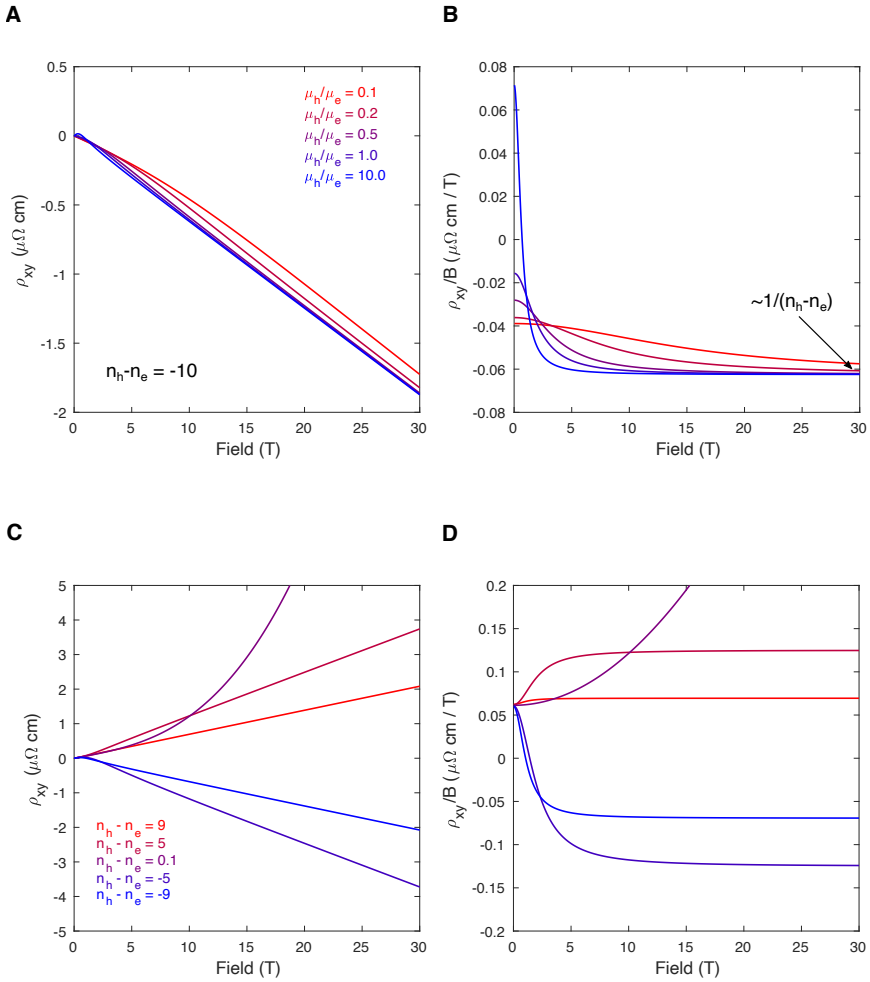

Figure 2.4: **Simulated semiclassical two-band Hall resistivity. A** Transverse resistivity for a fixed number of hole and electron carriers, where the relative mobility of the two carriers is varied. **B** Hall resistivity divided by field, with the same conditions as in panel A. The value in all cases approaches a similar constant at high fields, because the high-field limiting Hall effect only becomes proportional to the net carrier density $1/(n_h - n_e)$ independent of their relative mobilities. **C** Hall resistivity where the mobility ratio is kept fixed, while the relative carrier density is varied. **D** The Hall resistivity divided by field approaches a different constant in each case as the net carrier density is varied. Note that at zero field, the value in all cases is the same and is proportional only to the carrier density of the most mobile carriers — in this case the holes.

Hall effect measurements

"The experiments were hastily and roughly made, but are sufficiently accurate" — Edwin H. Hall

Now that we've discussed some Hall effect theory and how to extract the carrier density from Hall effect measurements, we are prepared to probe the localized or itinerant nature of the f-electrons (i.e. the total Fermi volume) in $CeCoIn_5$ across the phase diagram using Hall effect measurements. As discussed in the introduction to this section, what we would like to do is compare the measured carrier density of $CeCoIn_5$, where in principle the f-electron could be a carrier, to the expected carrier density of the conduction electrons of the other non-f bands in the material. That is, the d, p, and s bands from indium and cobalt. In principle, we could use ab initio methods to calculate the carrier density of the non-f bands alone, but generally Fermi volume calculations coming from density functional theory calculations need to be supplemented by more direct Fermi surface measurements. A more accurate, and more straightforward method, is to measure the carrier density of $LaCoIn_5$. The difference between $CeCoIn_5$ and $LaCoIn_5$ is that lanthanum has a completely empty f shell while cerium has one f-electron in the $4f$ shell.

Carrier density of $LaCoIn_5$: the non-f analogue of $CeCoIn_5$

$LaCoIn_5$ is a metal with both hole- and electron-like carriers. From the electronic structure determined by published photoemission measurements and ab initio calculations, we expect the carrier density of the electrons to be higher than that of the holes [33], but we don't necessarily have a priori information about their relative mobilities. In Fig. 2.5, we show Hall resistivity measurements of $LaCoIn_5$ samples. We find that the Hall resistivity at the lowest temperatures is non-linear at low fields, but approaches a linear dependence on field at high fields. The data can be well-fitted by a simple two-carrier model — that is, in the semiclassical relaxation time approximation, and assuming a single average mobility for each carrier type respectively. The equation for the Hall resistivity in this model is (see also chapter 3 for additional details)

$$\rho_{xy} = \frac{B}{e}\frac{(n_h\mu_h^2 - n_e\mu_e^2) + (n_h - n_e)\mu_h^2\mu_e^2B^2}{(n_h\mu_h + n_e\mu_e)^2 + (n_h - n_e)^2\mu_h^2\mu_e^2B^2}, \tag{S1}$$

where $n_{h,e}$ are the carrier densities of the electrons and holes, and $\mu_{h,e}$ are their respective mobilities. The mobilities of the two carriers are plotted in Fig. 2.5C. The mobility of the electrons is higher than that of the holes, with both increasing as a function of decreasing temperature and saturating at low temperature. This behavior is broadly speaking consistent with expectations of metallic transport, where the mobility saturates at low temperature as the role of temperature-independent scattering dominates at low temperature. Scattering from thermal vibrations picks up as temperature increases, leading to a decrease in the mobilities of both carriers. The two-carrier model yields a net carrier density of $9.7\pm1\times10^{21}/\mathrm{cm}^3$.

As a simple check, we can compare the value of the net carrier density extracted from fits to the two-carrier model to the value of ρ_{xy}/B at the highest accessible field (recall that the net carrier density in semiclassical transport theory is given by the high-field limit of the Hall coefficient $n_{net} = 1/(e(n_h - n_e))$. Note that in Fig. 2.5A, the value of ρ_{xy}/B and the slope of ρ_{xy} are similar at the highest accessible field of 14 Tesla. The net carrier density extracted from this analysis is $9.5\pm0.6\times10^{21}/\text{cm}^3$ (uncertainty primarily arises from the uncertainty in the thickness measurement of the sample), giving good agreement with the two-carrier model described above. From these estimated mobility values, it appears that μB for electrons and holes attains a value of roughly 8 and 13 respectively at a magnetic field of 5T and 1.8K. Thus, the ρ_{xy} measurement at 1.8K and 14 Tesla is well into the high-field limit of $\omega_c\tau \gg 1$ for both carrier types, and consequently the Hall coefficient approaches a regime of field-independence above 5T as seen in Fig. 2.5. This gives confidence that the value of ρ_{xy}/B at our highest accessible field and lowest temperature is representative of the net carrier density of the sample.

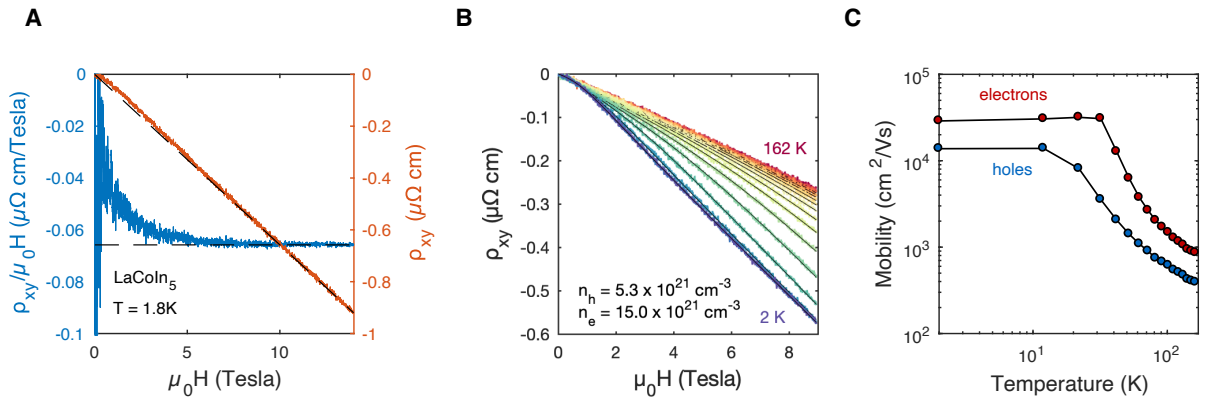

Figure 2.5: **Carrier density measurements of A** Hall resistivity, and Hall resistivity divided by field, in $LaCoIn_5$ at 1.8K. The slope of the Hall resistivivity and $\rho_{xy}/\mu_0 H$ both saturate at high field, indicated by the dashed lines. This suggests that the Hall coefficient at high fields measures the net carrier density. From this measurement $n_{tot} = 9.5 \pm 0.6 \times 10^{21}/\text{cm}^3$. **B** Temperature-dependent Hall resistivity of $LaCoIn_5$ including fits (black lines) using a two-band transport model on a second sample. The carrier densities were constrained to be temperature-independent and the mobility was allowed to vary. The carrier densities of the hole and electron carriers extracted from these fits are shown in the panel. The net carrier density ($n_{tot} = 9.7 \pm 1 \times 10^{21}/\text{cm}^3$) agrees well with the carrier density determined in panel A. **C** Mobility of the hole and electron carriers from the fits in panel B as a function of temperature.

Carrier density of doped $CeCoIn_5$

"Just like the old days, last day of the last week of magnet time!" — James Analytis

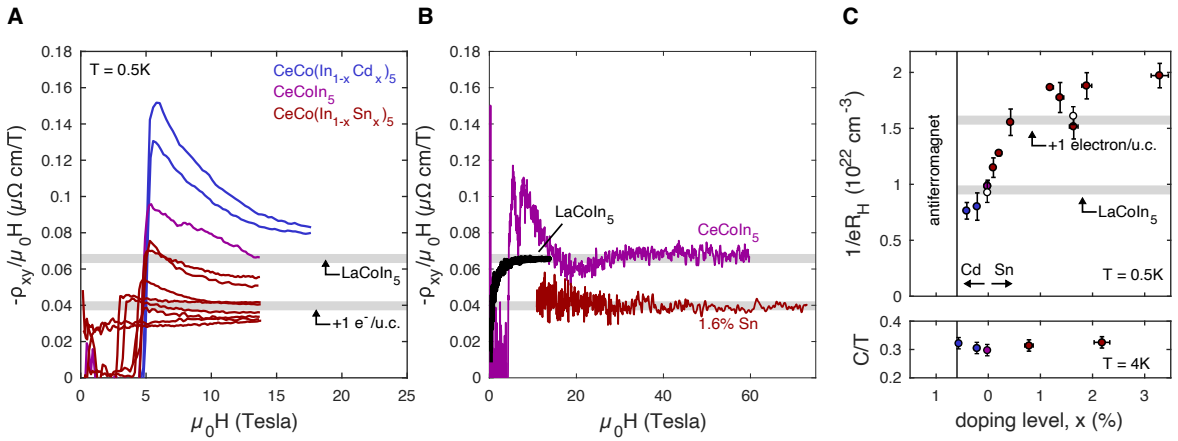

Figure 2.6: **Carrier density measurements in doped $CeCoIn_5$** **A** Hall coefficient as a function of field in doped $CeCoIn_5$ with Cd concentrations 0.2% and 0.4%, and Sn concentrations 0.11%, 0.22%, 0.33%, 0.44%, 1.2%, 1.39%, 1.65%, 1.9%, and 3.3%. As discussed in the main text, the inverse of the Hall coefficient ($\rho_{xy}/\mu_0 H$) in the high-field limit can be used to approximate the net carrier density. Grey lines denote the high-field Hall coefficient of the non-f analogue $LaCoIn_5$ and the calculated value including one additional electron per unit cell. **B** Pulsed field Hall resistivity of $CeCoIn_5$ (T = 0.66K) and Sn-doped $CeCoIn_5$ (T = 0.5K) overlaid on the continuous field Hall resistivity of $LaCoIn_5$ (1.8K). **C** Inverse high-field Hall coefficient of $CeCoIn_5$ at 0.5K as a function of doping level, including measurements in continuous field up to 14T or 18T (filled circles) and pulsed field up to 73T (open circles). With Sn-substitution, the apparent carrier density of $CeCoIn_5$ increases by about one electron per unit cell above that of $LaCoIn_5$. This trend provides evidence that Sn-substitution delocalizes the single cerium f-electron per unit cell in $CeCoIn_5$. The value of $1/eR_H$ in some Sn-doped samples lies above the calculated +1 electron line, likely because the Hall coefficient has not completely saturated in these samples at 14T. At higher fields the value of $1/eR_H$ seems to saturate at the +1 electron value as seen in the 1.6% Sn-doped sample at 70T. The lower panel shows the 4 Kelvin heat capacity (units of mJ/mol K^2) across this doping series.

Fig. 2.6A presents low-temperature measurements of the Hall resistivity, ρ_{xy}, versus magnetic field, H, for $CeCoIn_5$ samples with varying levels of cadmium (hole-doping) or tin (electron-doping), both of which substitute indium. The Hall coefficient, $R_H = \rho_{xy}/\mu_0 H$ can be used to estimate the net carrier density enclosed by the Fermi surface according to the

formula [154]

$$n_{net} = \frac{1}{eR_H(H \to \infty)}. \tag{2.8}$$

where n_{net} is the net carrier density — electrons minus holes. In multiple band metals such as $CeCoIn_5$, Eq. 2.8 only applies in the limit where high fields eliminate the effects of carrier mobility misbalances, or anisotropy in the quasiparticle spectrum and scattering time, and R_H becomes field-independent. For each sample, we measure the high-field value of R_H at 0.5K in order to approximate the net carrier density. Many of the traces shown in Fig. 2.6A appear to saturate at high fields, Fig. 2.7 shows that evaluation of the high-field slope of ρ_{xy} is in good agreement with the high-field value of $\rho_{xy}/\mu_0 H$, suggesting that at these temperatures and fields the Hall coefficient is close to field-independent. In addition, select samples were measured in pulsed magnetic fields up to 75T, as shown in Fig. 2.6B, where the Hall coefficient is field-independent over an extended field range; the extracted Hall coefficients from pulsed and continuous fields are in good agreement for these samples (Fig. 2.6C). Finally, our Hall coefficient measurements on pure $CeCoIn_5$ agree well with measurements at 20mK where the Hall resistivity is completely linear in field [188]. These facts together give confidence that our extracted Hall coefficient values can be interpreted as an approximate measurement of the net carrier density as described by Eq. 2.8.

Fig. 2.6C shows the value of $1/eR_H$, approximating the net carrier density, extracted for samples with different levels of chemical substitution in continuous and pulsed magnetic fields. The carrier density of this material excluding the f-electron can be established using Hall resistivity measurements of $LaCoIn_5$ shown in Fig. 2.6B (its Hall coefficient is field-independent above 5T at 1.8K. See also Fig. 2.5); $LaCoIn_5$ can be thought of as $CeCoIn_5$ without the f-electron. We find that the Hall coefficient of $CeCoIn_5$, evaluated either up to 60 Tesla or up to 14 Tesla at 0.5K, is close to that of $LaCoIn_5$ (Fig. 2.6C). This suggests that the two materials have similar net carrier densities, implying that the f-electrons are close to localized in $CeCoIn_5$. With cadmium-substitution $1/eR_H$ remains close to that of $LaCoIn_5$, but with tin substitution increases to a value consistent with the addition of one itinerant electron per unit cell. Identifying the additional electron as the single cerium f-electron suggests that Sn-substitution induces a delocalization transition of the f-electrons. None of these samples show a finite-temperature phase transition other than superconductivity. Only in Cd substitution levels higher than 0.6% is an antiferromagnetic phase observed (Fig. 2.3) [152].

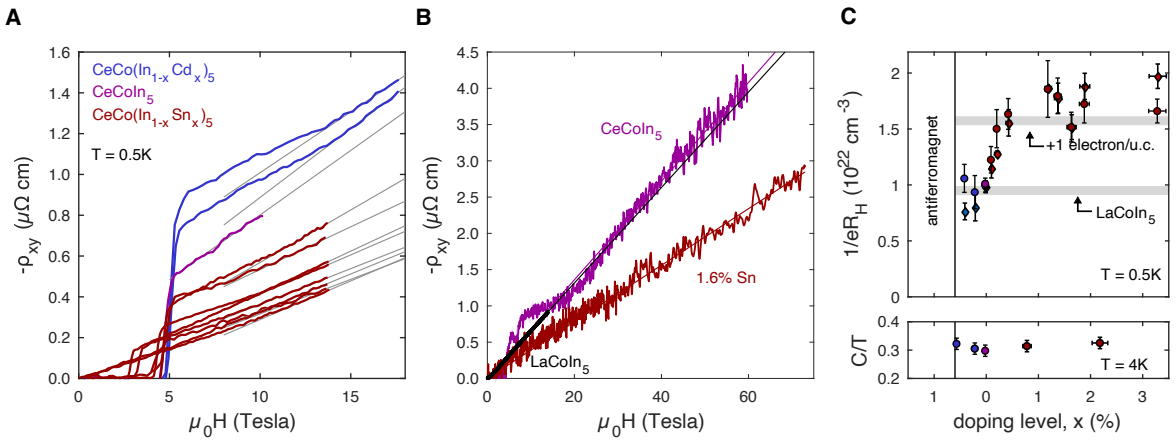

Figure 2.7: **Hall resistivity of doped $CeCoIn_5$.** **A** Continuous field measurements at low temperature, where the Hall coefficient is extracted with a linear fit to the high-field slope of the Hall resistivity. **B** Both devices measured in pulsed field exhibit an extended regime of linear dependence with zero intercept. The Hall coefficient of the Sn-doped sample is considerable lower than that of pure $CeCoIn_5$. **C** Comparison of the Hall coefficient determined from the slope of $\rho_{xy}(B)$ (circles), and that determined from the high-field value of $\rho_{xy}/\mu_0 H$ (diamonds). Good agreement is found between these two methods of evaluating the Hall coefficient, suggesting that these measurements are in the high-field limit where the Hall resistivity is characterized by a single slope proportional to inverse the net carrier density.

2.5 Evidence for a Fermi surface reconstruction without symmetry breaking

"Consider, for example, those portions of the Fermi surface known as 'monsters' " — Brian Pippard

The Hall effect measurements suggest that the Fermi volume changes when the material is doped with tin. Such a transition should be associated with a Fermi surface reconstruction. Here we present density functional theory (DFT) calculations predicting the structure of the rather complicated Fermi surfaces of $CeCoIn_5$ in both the localized and delocalized f-electron scenarios. The results of the calculations are compared to direct measurements of the Fermi surface in the form of de Haas-van Alphen (dHvA) oscillations and angle-resolved photoemission (ARPES).

Density Functional Theory calculations

"The code that will be used is not the same one as we used 15 years ago" — Peter Oppeneer

The results of the DFT calculations are shown in Fig. 2.10. The first calculation is performed under the assumption that the f-electrons are core-level electrons (localized). The second assumes that the f-electrons are delocalized. Both calculations are performed within the local-density approximation of the exchange correlation energy.

In the case of localized f-electrons, there are three Fermi surface sheets. The electron-like Fermi surfaces labeled α and β are predominantly two-dimensional cylinders centered at the zone corners. The last is a more complicated three-dimensional hole-like γ Fermi surface. According to the calculations, f-electron delocalization causes the extended γ surface to disconnect into small ellipsoidal pockets at the Brillouin zone center and edge, and the γ pocket at the zone top (labeled γ_Z) to disappear. Also, large extended surfaces α_Z and β_Z appear at the zone top, and the α and β cylinders expand slightly. In pure $CeCoIn_5$, previous angle-resolved photoemission (ARPES) data at 10-20K are in better qualitative agreement with the localized f-electron model as α_Z and β_Z are absent, and γ_Z is present [33, 31]. However, the volumes of the α and β cylinders are slightly larger than those of the localized model [33, 31, 98], and the smaller γ Fermi surface seems to exhibit features of both the delocalized and localized models, being potentially disconnected (suggesting delocalized) but retaining γ_Z (suggesting localized) [86, 31, 33, 58]. These characteristics may point to a partially delocalized f-electron character in pure $CeCoIn_5$. This interpretation is also promoted by previous magnetic resonance [43] and photoemission studies [56, 32, 33]. Note that our Hall effect measurements suggest that the f-electrons only weakly contribute to the Fermi volume of $CeCoIn_5$ even at 0.5K, consistent with partially localized f-electrons in the low-temperature limit.

de Haas-van Alphen oscillations

"What is the meaning of life?" — Vikram Nagarajan

De Haas-van Alphen (dHvA) oscillations measure extremal areas of the Fermi surface perpendicular to the field direction, giving a probe of the Fermi surface structure at low temperatures [77]. Quantization of Landau orbits causes oscillations in the density of states as a function of magnetic field (actually they are periodic in inverse magnetic field). Quantum oscillations in transport properties are called Shubnikov-de Haas oscillations whereas oscillations in thermodynamic properties are called de Haas-van Alphen. In this case, we opted to measure de Haas-van Alphen oscillations in the sample's magnetization. This was done using a piezoresistive torque cantilever, which bends in proportion to the magnetic torque that the sample experiences in a magnetic field, due to the sample's dipole moment ($\mathbf{M}$) induced by the magnetic field ($\mathbf{H}$). Through this measurement, dHvA oscillations in the sample's magnetization are observable in the measured torque on the sample.

$$\tau = \mathbf{M} \times \mathbf{H} \tag{2.9}$$

A picture of the piezoresistive cantilever used in these experiments is shown in Fig. 2.8B. Because the round-trip resistance of the cantilever itself is around 600 Ω, small changes in the resistance of this element induced by bending of the cantilever are best detected through a differential measurement. Essentially, two different cantilevers are used, with the sample being placed on one while the other is used as a dummy. The changes in the cantilever resistance are measured using lock-in detection techniques through a Wheatstone bridge circuit as shown in Fig. 2.8A. The principle of the Wheatstone bridge is that the voltage across the two nodes of the bridge induced by a current run through the other two nodes should be zero if all of the resistances are equal. A voltage is generated if the resistance of one resistor changes with respect to its neighbor. In this way, very small changes in the 600 Ω cantilever resistance can be detected with respect to the resistance of another 600 Ω dummy cantilever which does not bend in magnetic field. Note that in practice, a potentiometer is wired in series with the dummy cantilever to adjust for small variations in the resistance of different manufactured cantilevers, or the temperature-dependence of the cantilever's resistance.

The sample is mounted to the active cantilever using vacuum grease, and the voltage through the Wheatstone bridge generated by an AC excitation was measured using standard lock-in detection techniques. The experiments were performed at the milliKelvin facility at the National High Magnetic Field lab in Tallahassee, Florida. Fig. 2.9 shows an example of the magnetic torque signal as a function of magnetic field induced by the torque that the external field exerts on a sample of doped $CeCoIn_5$ mounted on the cantilever. The superconducting critical field of the sample around 5 Tesla is clearly observed in this measurement. The stage on which the cantilever is mounted can then be rotated in the magnetic field to perform angle-resolved magnetization measurements up to 18 Tesla and at 20 mK.

Background subtraction was performed on the measured signal by subtracting a smoothed version of the data from the original trace. Various smoothing windows were checked to ensure that the peaks observed in the frequency domain were not a spurious result of the background subtraction method. The background subtracted oscillations are visible as a function of inverse field (see for example Fig. 2.10B inset), where the periodicity on this scale is indicative of the k-space area of a Fermi surface orbit (see Ref. [184]). By performing angle-dependent measurements, a map of the Fermi surface structures can be obtained. The oscillations in magnetic torque as a function of inverse field were zero padded and then either a hattop or Hanning window was applied. The resulting arrays were put through a fast Fourier transform algorithm to obtain power spectra [45].

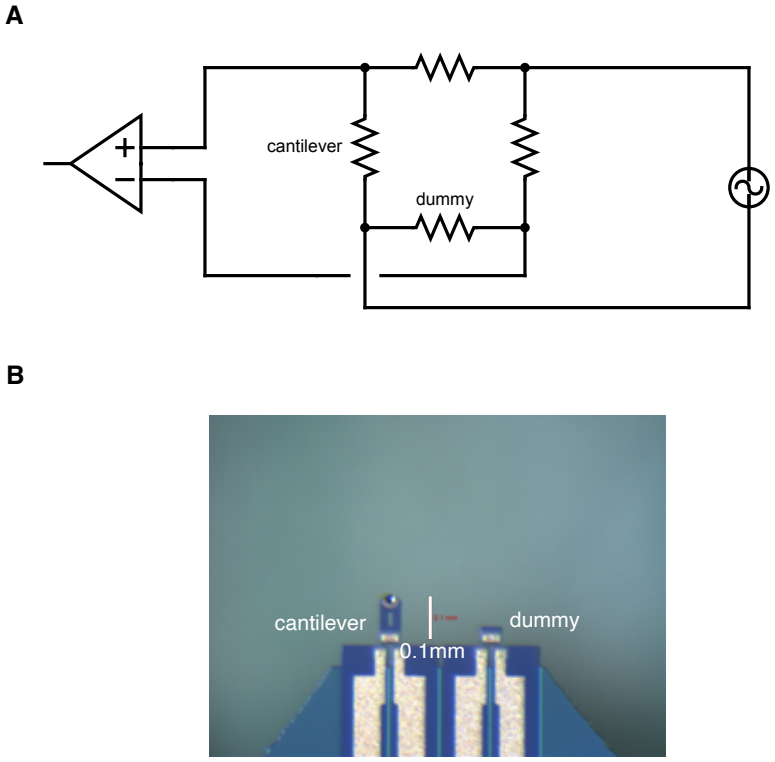

Figure 2.8: **Magnetic torque measurement circuit and picture of piezoresistive cantilever A** The measurement circuit in which the dummy and cantilever are opposite resistors as part of a wheatstone bridge. An AC excitation current is sent through two nodes and the resulting voltage is lock-in detected at the other two nodes. The signal is proportional to the cantilever resistance with respect to the dummy. **B** A picture of the piezoresistive cantilever and dummy cantilever on a single chip.

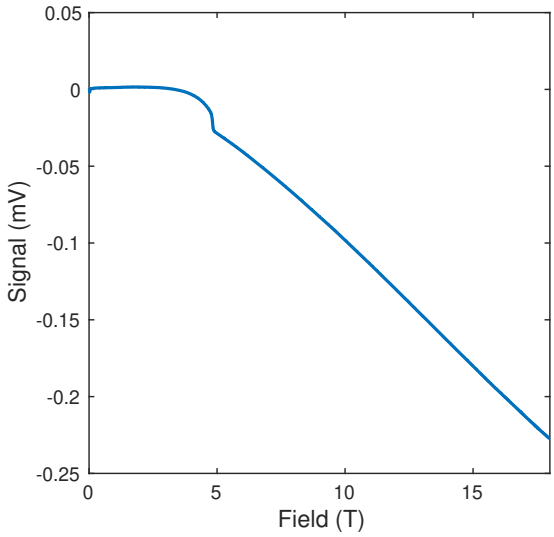

Figure 2.9: **Magnetic torque measured using a wheatstone bridge** The signal is detected through standard lock-in amplification techniques using a frequency of 177 Hz, and an excitation current of 100μA through a wheatstone bridge as described in the text. The signal is generated by the resistance imbalance between the piezoresistive cantilever with the sample on it, and a dummy cantilever without a sample. Mounted on this cantilever is a sample of Sn-doped $CeCoIn_5$ at 20mK with magnetic field parallel to the crystallographic c-axis. The superconducting critical field of about 5 Tesla is clearly visible in the measured torque. Oscillations in the magnetization at high field are visible after background subtraction, as discussed in the text.

Here we discuss the fermiology of these compositions as measured by dHvA measurements [178]. As seen in Table 2.5 and Fig. 2.10C, the sizes of the α and β cylinder orbits in pure $CeCoIn_5$ are more consistent with the delocalized model, implying that f-electrons incorporate into these Fermi surface sheets. However, there do not appear to be additional frequencies associated with the α_Z and β_Z sheets of the delocalized model. Perhaps more notably, orbit β_2 increases as a function of tilt angle away from [001] (Fig. 2.10C), suggesting that the β cylinder is fully connected in better qualitative agreement with the localized model, i.e. the Fermi surface called β_Z is not present in the Fermi surface of pure $CeCoIn_5$. This conclusion is in agreement with previous photoemission data on pure $CeCoIn_5$ as discussed in the previous section.

In the Sn-substituted sample, the sizes of the α cylinders change slightly compared to in pure $CeCoIn_5$ (Table 1). In addition, an oscillation of about 16kT appears for two field angles near [001]. This oscillation does not appear to be harmonically related to the α_{1-3} branches, and its frequency and angle-dependence agree well with a predicted orbit on α_Z of our delocalized model calculations. This suggests that the α_Z Fermi surface is present in

the Sn-doped sample, while it has not been reported in previous dHvA measurements on the pure compound.

Examining the β sheets, we notice that part of the electron-like β Fermi surface actually shrinks upon electron-doping, suggesting that the change in volume of the β Fermi surface cannot be attributed to a straightforward shift in the Fermi level. It seems that the β_1 cylinder orbit shrinks to accommodate the presence of the large interconnected β_Z sheet. The first piece of evidence for this interpretation is that, when compared to the DFT calculations, the 1.2kT and 2kT frequencies for field angles near [001] are evidence of holes in the β cylinder (Fig. 2.10A) consistent with the presence of β_Z. The second piece of evidence is that a branch of the β_2 cylinder orbit appears to decrease as a function of tilt angle from [001] in better agreement with the delocalized model (Fig. 2.6C), suggesting that holes develop in the β cylinder due to the interconnected β_Z Fermi surface.

Finally, possible low frequency oscillations < 800T at several angles, which seem to be present in pure $CeCoIn_5$ over certain angular ranges as well, are most naturally assigned to small γ-ellipsoids (Fig. 2.10C), but could also originate from the γ_Z sheet. Table 2.5 summarizes the frequency assignments based on comparison to DFT calculations, which suggests that the α_Z and β_Z sheets are present in the Fermi surface of the Sn-substituted sample. From dHvA, it is not possible to conclusively say whether these sheets are absent in pure $CeCoIn_5$ at low temperature because the orbit frequencies on α_Z and β_Z are sensitive to the precise structure of these Fermi surfaces (although the increase of β_2 with increasing tilt angle in pure $CeCoIn_5$ certainly provides strong evidence that β_Z is absent from its Fermi surface). Nevertheless, the comparison shown in Table 2.5 is indicative of a Fermi surface reconstruction induced by Sn-substitution. To summarize, the reconstruction is reflected in slight changes in the volumes of the existing α and β cylinders, and also the appearance of Fermi surfaces α_Z and β_Z, which are unique to the delocalized f-electron model.

At zero degree tilt angle, a sweep was taken at a higher temperature of 50mK. Many of the β orbits seem to disappear into the noise floor at the higher temperature consistent with large effective masses. The strength of the α_{1-3} oscillations and their harmonics seem to depend non-monotonically on temperature. Similar behavior is observed at 12 degree tilt angle as discussed later on. The α_4 orbit is repeatable at the higher temperature and also appears at two tilt angles. While the value of α_4 is very close to $3\alpha_1$, there are a few reasons that α_4 is unlikely to be harmonically related to α_1. First, the strength of the α_4 oscillation is greater than that of the $2\alpha_1$ oscillation. Second, as the tilt angle increases away from [001], α_4 increases by a few 100T while α_1 stays constant between 0 and 5 degrees.

Candidate peaks in Fourier spectra were checked by band-pass filtering the data and examining the field-evolution of various oscillatory components. Fig. 2.12 shows the time-series filtered data for various oscillations at zero degree tilt angle for example. The oscillations become stronger as field increases.

The most complete temperature-dependent data was taken at a field angle of 12 degrees from the [001] axis towards the [100] axis. Fig. 2.13 shows the temperature-induced suppression of the main alpha orbits along with estimates of their effective masses using an attempted Lifshitz-Kosevich fit. There are two notable peculiarities in the temperature-dependent data

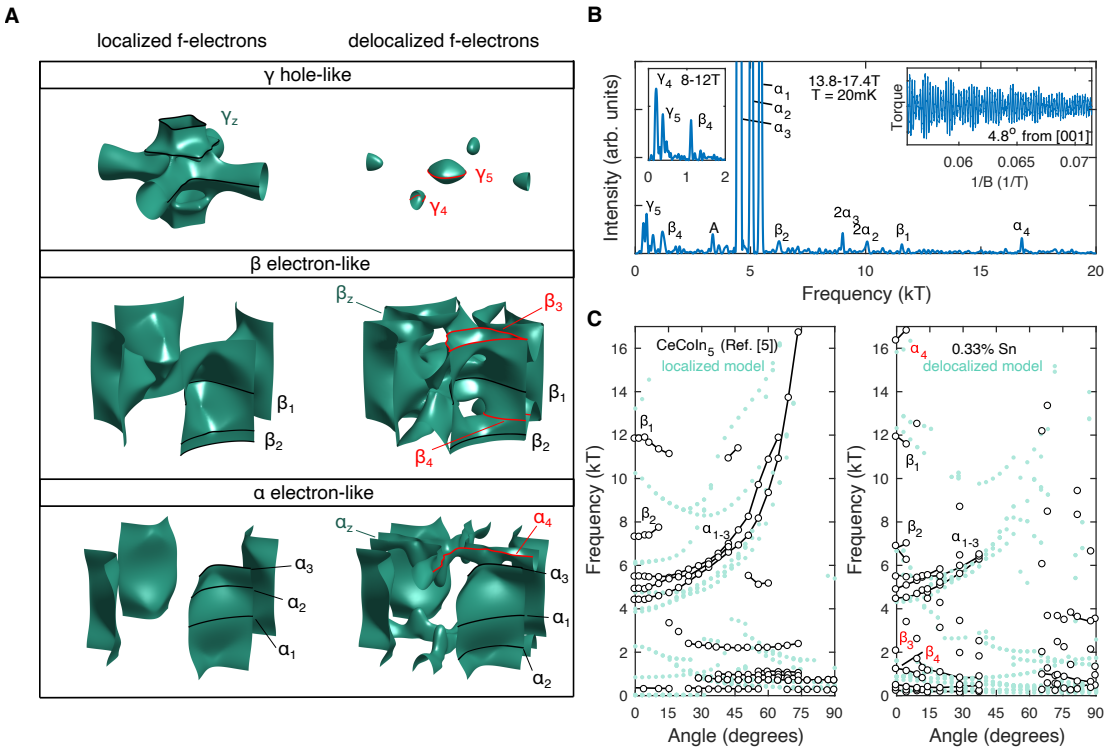

Figure 2.10: **de Haas-van Alphen oscillations in Sn-doped $CeCoIn_5$ and comparison to DFT calculations A** DFT calculated Fermi surface sheets of $CeCoIn_5$ with localized and delocalized f-electron models. Predicted dHvA orbits for $H \parallel [001]$ are drawn in black and red. Red orbits are unique to the delocalized f-electron model. **B** Characteristic dHvA spectrum with the magnetic field 4.8^o away from [001] of a crystal of 0.33% Sn-doped $CeCoIn_5$. The inset shows oscillations in the magnetic torque after background subtraction. **C** dHvA oscillation frequencies as a function of angle tilting the magnetic field from the crystallographic [001] to [100] directions in pure $CeCoIn_5$ (Ref. [178]) and 0.33% Sn-doped $CeCoIn_5$. Light green points are DFT calculated frequencies of the localized and delocalized f-electron models respectively.

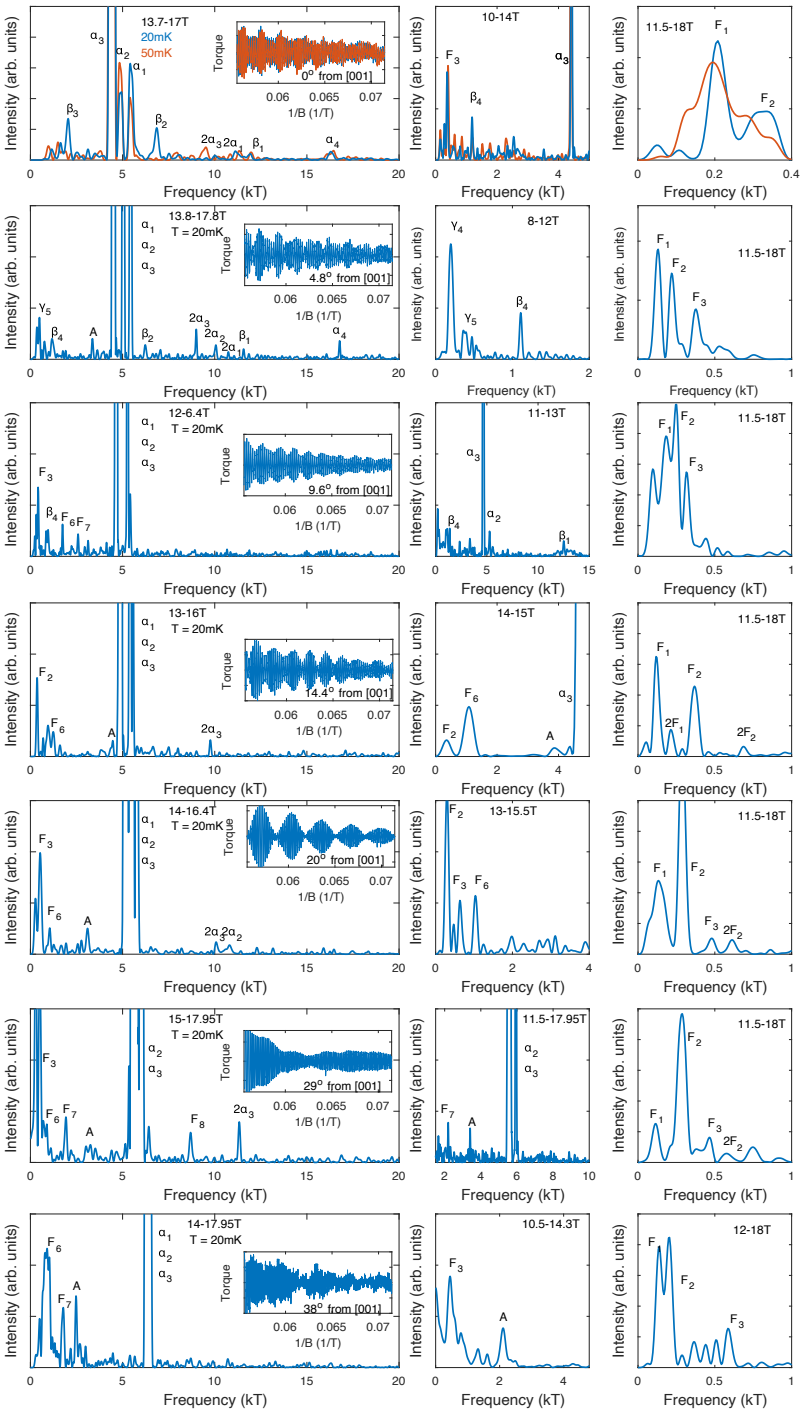

Figure 2.11: **Spectra taken as a function of field angle** Quantum oscillation spectra taken at different tilt angles and different field ranges.

Fermi surface	label	localized f-electron model	$CeCoIn_5$ Ref. [178]	0.33% Sn-doped $CeCoIn_5$	delocalized f-electron model
γ_Z	γ_1	0.8			
γ_Z	γ_2	2.3			
γ-cross	γ_3	13.2			
γ-ellipsoid	γ_4			(0.46)	0.7
γ-ellipsoid	γ_5		(0.24)	(0.2)	0.22
α-cylinder	α_1	4.8	5.6	5.4	5.6
α-cylinder	α_2	4.0	4.5	4.8	4.4
α-cylinder	α_3	3.9	4.2	4.4	4.3
α_Z	α_4			16.3	15.8
β-cylinder	β_1	10.3	12.0	11.9	12.3
β-cylinder	β_2	6.1	7.5	6.8	6.7
β_Z/cylinder	β_3			2.0	1.6
β_Z/cylinder	β_4			1.2	0.9

Table 2.1: **de Haas-van Alphen extremal orbit assignments** Units of kiloTesla, $H \parallel [001]$, from experiments and DFT calculations. Each orbit is labeled by the assigned Fermi surface sheet, which are visualized on the calculated Fermi surface sheets in Fig. 2.10A.

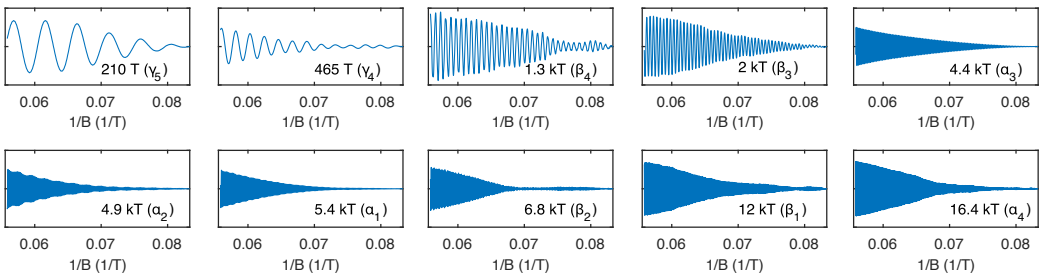

Figure 2.12: **Time-series filtered oscillation spectra over different frequency windows** Filtered time series data at 0 degree tilt angle for fundamental frequencies. Oscillation amplitudes are observed to increase as field increases.

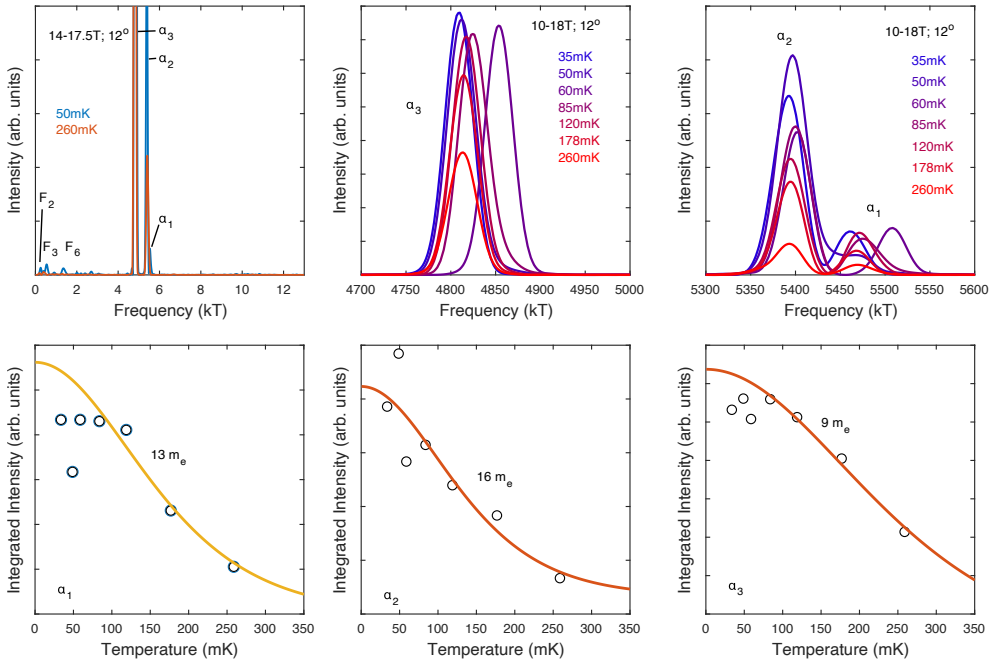

Figure 2.13: **Effective mass of main orbits and temperature-dependent frequency**

for the main orbits. First, the frequency seems to depend on temperature, peaking at about 60mK. For α_3 and α_1, the frequency changes by considerably more than the width of the spectral peak, suggesting this behavior is intrinsic to the sample. Second, the oscillations do not seem to obey (LK) theory in many instances. An attempted LK fit yields a comparable effective mass to that observed previously in the literature for the orbits which have been observed in pure $CeCoIn_5$ [178]. Over certain field ranges the oscillations get stronger with increasing temperature, peaking around 60mK, and decrease as temperature increases further. The deviations from Lifshitz-Kosevich seem to depend on the strength of the applied magnetic field (Fig. 2.14). This behavior cannot easily be attributed to an uncertainty in the temperature measurement or nonequilibrium sample temperature because over certain field windows α_3 follows LK theory rather well while over the same field window α_1 shows strong deviations, especially around the 60mK range where the frequency shift is strongest.

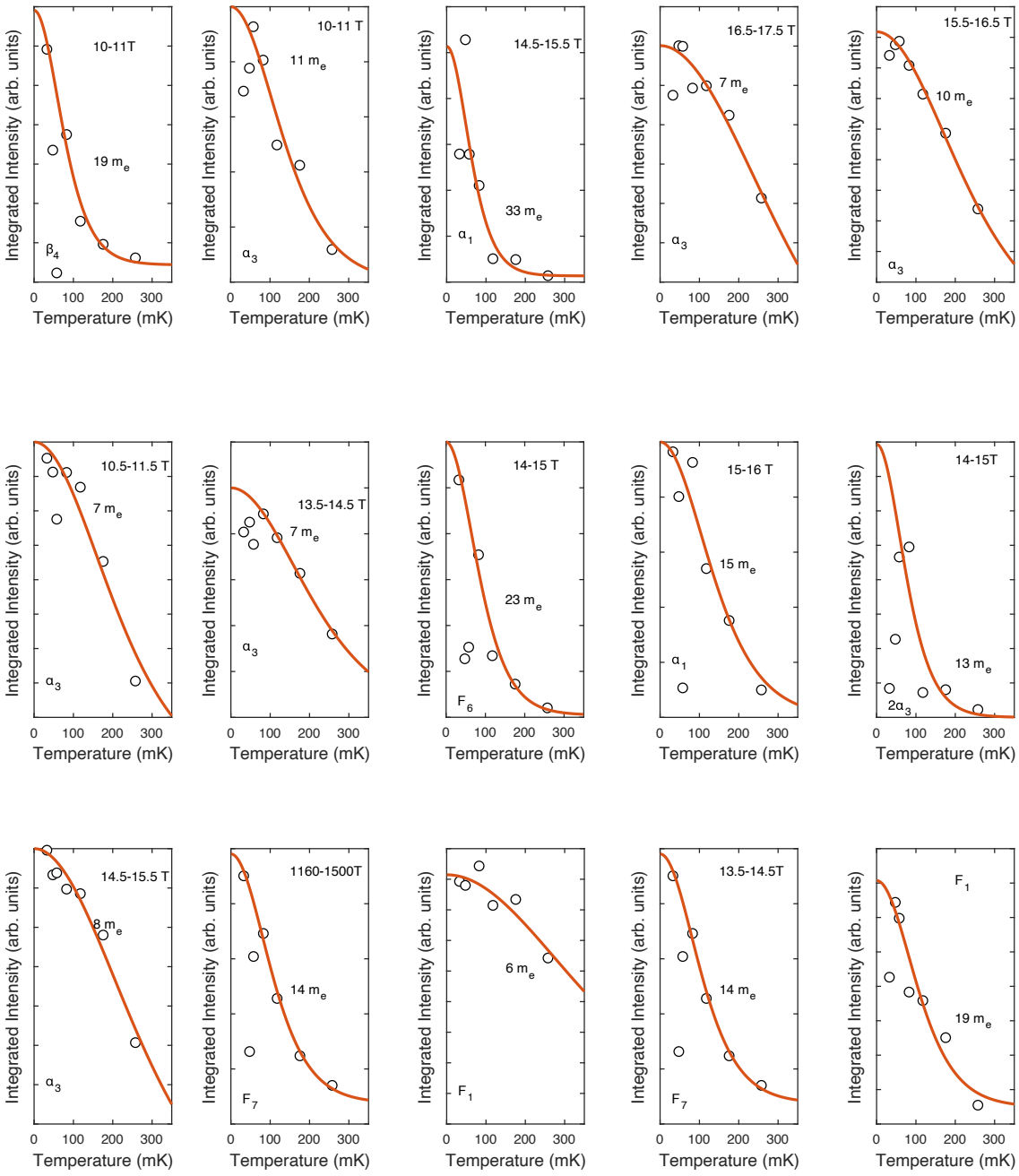

Figure 2.14: **Effective masses over different field windows where field is 12 degrees from [001]** Panels are labeled by the field window, estimated effective mass from attempted LK fit (red line), and frequency assignment. Deviations from LK are often observed near 60mK.

Angle-resolved photoemission measurements

"There may be time to measure your doped $CeCoIn_5$ samples if that could still be useful" — Danny Eilbott

Our ARPES measurements corroborate the dHvA evidence for a Fermi surface reconstruction. Fig. 2.15 compares Fermi surface maps at the Brillouin zone top in pure $CeCoIn_5$ and 3% Sn-substituted $CeCoIn_5$ at 10K. Our data on pure $CeCoIn_5$ agrees well with previous reports. The cylindrical Fermi surfaces centered at the zone corners are visible. Bright spots near the Z point are probably signatures of the γ_Z Fermi surface, as discussed in Refs. [86, 32].

In the 3% Sn-substituted sample, we observe enhanced intensity at the R point of the Brillouin zone relative to the pure material, as well as a qualitative change in structure near Z. Overall it appears that the electronic structure changes with Sn-substitution, with a sharp cross-shaped structure emerging in the RZA plane which resembles α_Z or β_Z of our delocalized model calculations (α and β bands nearly overlap along this cut, and as such they may be difficult to distinguish from one another in ARPES). Weak features appear at the R point in pure $CeCoIn_5$ as well, potentially indicating that incoherent states exist at the R point — these states may exist because of the partially delocalized f-electron character in the pure material.

It is important to note that these weak features in pure $CeCoIn_5$ at the R point are relatively temperature independent, in stark contrast to the behavior of the Sn-doped sample. In Fig. 2.15C, we explore the temperature-dependence of these Fermi surface sheets via the ARPES intensity at the R point. The relative intensity at R increases in the Sn-substituted sample upon decreasing temperature below about 90K with the onset of f/conduction hybridization (see also Fig. 2.16). In the pure material, the R point spectral weight is relatively constant down to 10K. This comparison suggests that the Fermi surface sheet in 3% Sn-doped $CeCoIn_5$ emerges, or is made relatively more coherent, because of enhanced f/conduction electron hybridization induced by Sn-substitution. By contrast no such coherent feature exists in the pure material at any measured temperature.

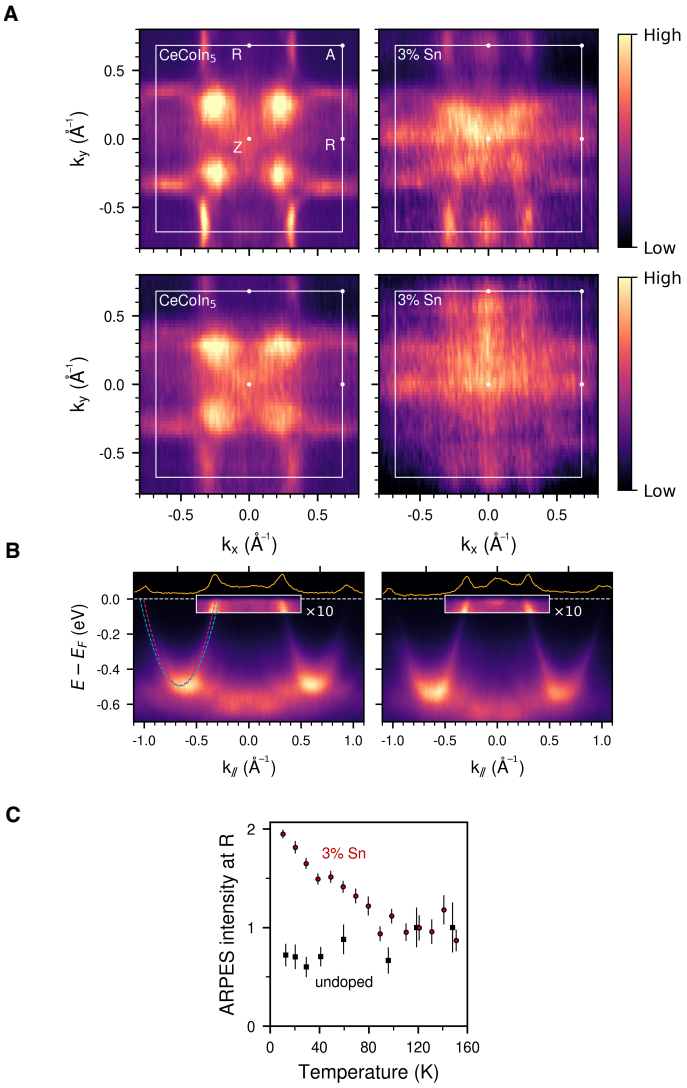

Figure 2.15: **ARPES measurements of $CeCoIn_5$ and Sn-doped $CeCoIn_5$ A** Fermi surface maps in pure and 3% Sn-substituted $CeCoIn_5$ at the Brillouin zone top (RZA plane). A new Fermi surface sheet appears at the zone top in the Sn-substituted sample. Each of the four subpanels represents measurements on a different cleave. **B** A-R-A dispersion cuts. Parabolic α and β bands are labeled by red and blue dotted lines. The new Fermi surface in the Sn-substituted sample is observed as an increase in spectral intensity at the Fermi level at R. The spectral intensity within the white box has been enhanced by a factor of ten for clarity. **C** Comparison of temperature-dependent intensity at the R point normalized to the average value between 120-160K.

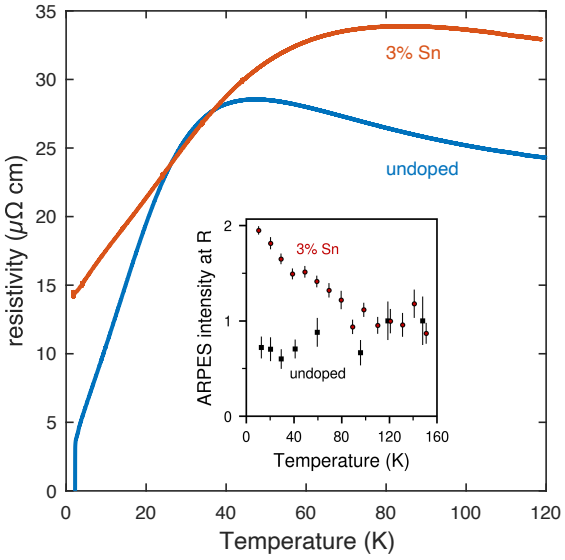

Figure 2.16: **ARPES intensity compared to resistivity coherence temperature** Coherence temperature appears as a peak in temperature-dependent resistivity, and can be correlated with the onset of f/conduction electron hybridization [86]. The coherence temperature in the 3% Sn-substituted sample is about 85K compared to about 45K in the pure material. The inset shows the ARPES intensity associated with a new Fermi surface which appears gradually below its coherence temperature. This Fermi surface is not present in the pure material even below its coherence temperature.

Recovery of Luttinger's theorem in a fractionalized Fermi liquid picture

The experimental data provides evidence that $CeCoIn_5$ exists near a quantum phase transition associated with the delocalization of f-electron charge. On one side of the quantum phase transition (represented by Sn-substituted $CeCoIn_5$), the Fermi volume includes the f-electrons. In contrast to the pure material, the net carrier density of Sn-substituted samples appears to include the f-electrons (Fig. 2.6). This change coincides with signatures of new Fermi surface sheets (Fig. 2.15, Table 2.5), which seem to agree well with predicted Fermi surfaces unique to the delocalized f-electron DFT model (Fig. 2.10A).

Presumably, the ground state of the strongly Sn-doped samples is a Fermi liquid which includes the f-electrons in the Fermi volume as a result of hybridization between the f and conduction electrons. Admittedly, aside from the carrier density and Fermi surface measurements being consistent with the full Luttinger count expected of a heavy Fermi liquid phase, we have not presented direct evidence that the ground state on this side of

the transition is a Fermi liquid. Such evidence could come in the form of, for example, a low-temperature T^2 resistivity in very heavily Sn-doped samples. Other evidence could come in the form of a low-temperature saturating magnetic susceptibility, or analysis of the Wiedemann-Franz coefficient, or Wilson ratio. If we take other heavy Fermi liquid materials as any indication, these signatures of a Fermi liquid ground state would probably be limited to temperatures below about 100mK [11].

On the other hand, in Cd-doped samples and pure $CeCoIn_5$, even the low temperature Fermi surface appears to exclude a considerable fraction of the f-electrons, and the bulk net carrier density is more consistent with localized f-electrons. On this side of the quantum phase transition, the Fermi volume is smaller than the expected Luttinger count. Taken together, these data suggest that Sn-substitution of $CeCoIn_5$ induces a Fermi volume changing transition between a phase with predominantly localized f-electrons to one with a delocalized character, i.e. a small-to-large Fermi surface transition. This transition could be attributed to an enhancement of the Kondo coupling induced by electron doping [61, 31, 169] — according to the typical view of f-electron metals, f-electron delocalization is a result of Kondo hybridization between the f level and conduction electrons. Although there are reports of such hybridization developing below about 45 Kelvin in pure $CeCoIn_5$ [86] and Cd-doped $CeCoIn_5$ [34] resulting in a detectable f-electron contribution to the Fermi surface, we find that the low-temperature carrier density of these materials is consistent with predominantly localized f-electrons (Fig. 2.6).

High magnetic fields may compete with the Kondo coupling by polarizing the f-electrons, but notably the Hall resistivity remains linear up to 73T (Fig. 2.6B), so it seems likely that higher fields are required to induce a complete breakdown of Kondo hybridization. In a 2% Cd-doped sample we did observe an ultra high field transition close to 70 Tesla. At present, we believe this transition is associated with the complete breakdown of the partial Kondo hybridization present in the material. Plans to explore this further include high field measurements on a series of Cd-doped samples.

A delocalization transition is a reasonable scenario from the perspective of doping-tuned Kondo coupling. Because of the constraints imposed by Luttinger's theorem, the reduction in Fermi volume in the more localized f-electron regime is expected to coincide with antiferromagnetic order where the Brillouin zone is reduced [186]. However, it is hard to reconcile this scenario with the data because the transition to antiferromagnetism is seen only around Cd doping of 0.6% [152], considerably removed from the suggested delocalization transition induced by Sn-substitution (Fig. 2.6C). Furthermore, magnetic order has never been observed in native $CeCoIn_5$ or Sn-substituted $CeCoIn_5$ [169, 31, 61, 97], and the ARPES and dHvA data suggest that the Brillouin zone is essentially unchanged by Sn-substitution.

At a high level, it then seems that the Fermi volume of the material expands as a result of a change of one of the interaction parameters — the Kondo hybridization scale. Such an observation is strictly at odds with Luttinger's theorem. An alternative possibility is that the Fermi volume doesn't change across this transition, but the volume of fermionic states that are *charged* does. This would require some of the charged fermion states in the large Fermi surface regime to transition into charge neutral fermion states in the small Fermi

surface regime in order to conserve total Fermi volume.

2.6 Possible spin-charge separation: effect of critical charge fluctuations on electrical conductivity

"I'm going through the calculation again carefully to make sure I didn't make a mistake" — Tessa Cookmeyer

A phase that preserves Fermi volume across such a localization transition has been theoretically predicted and is known as the fractionalized Fermi liquid [177]. The f-electron charge localizes to the cerium site, reducing the Fermi volume, while the spin excitations of the f moments remain itinerant and form a charge neutral Fermi surface [177]. Interestingly, the low-temperature specific heat of the samples is relatively independent of doping across this substitution series, even though the Fermi surface appears to increase in volume. We can speculate that the specific heat is constant as a function of doping (Fig. 2.6C) owing to the presence of a neutral Fermi surface, which conserves the fermionic degrees of freedom of the system even when the density of itinerant electrons appears to increase. One may also expect quantum fluctuations associated with a delocalization transition to enhance the specific heat coefficient. Such an enhancement has been observed as a function of decreasing temperature below 2K in pure $CeCoIn_5$ [23]. However, the confinement of these effects to <2K temperatures could explain why we do not detect singular behavior in C/T at 4K across the substitution series. Direct imaging of fractionalized particles is challenging. One option is ARPES measurements of two separate quasiparticle peaks associated with chargeons and spinons. Another is transport measurements in well-controlled and lithographically defined setups [193, 93]. In addition, there are possibilities for detecting spin-charge separation through comparison of thermal conductivity to electrical conductivity measurements [215].

All of these experimental techniques are made more challenging by the fact that, in the fractionalized Fermi liquid, the spinon and holon contributions coexist with a bath of regular conduction electrons from the non-f bands. Thus, at present we are largely limited to indirect signatures of fractionalized excitations. One possible signature is an unaccounted-for divergence in the low-field Hall effect at low temperatures. In the fractionalized Fermi liquid model, this arises from a depletion of the bosonic charge carriers at the critical point.

In particular, our calculations of the Hall conductivity of such a fractionalized phase capture several distinctive aspects of the low-field Hall coefficient in this material. In the simplest description of the fractionalized Fermi liquid, the f-electron separates into a fermionic spinon carrying its spin, and a gapped bosonic mode, in this case a valence fluctuation, carrying its charge. f-electron delocalization can be identified with the closing of the boson gap. Near this transition, the electrical conductivity has contributions from the fermionic spinons, the charged bosons and the conduction electrons. The spinon and the bosons should be added in series [83]. The boson's resistivity will then dominate owing to their much smaller number, and we therefore neglect the spinon contribution. Adding to this the resistivity of the

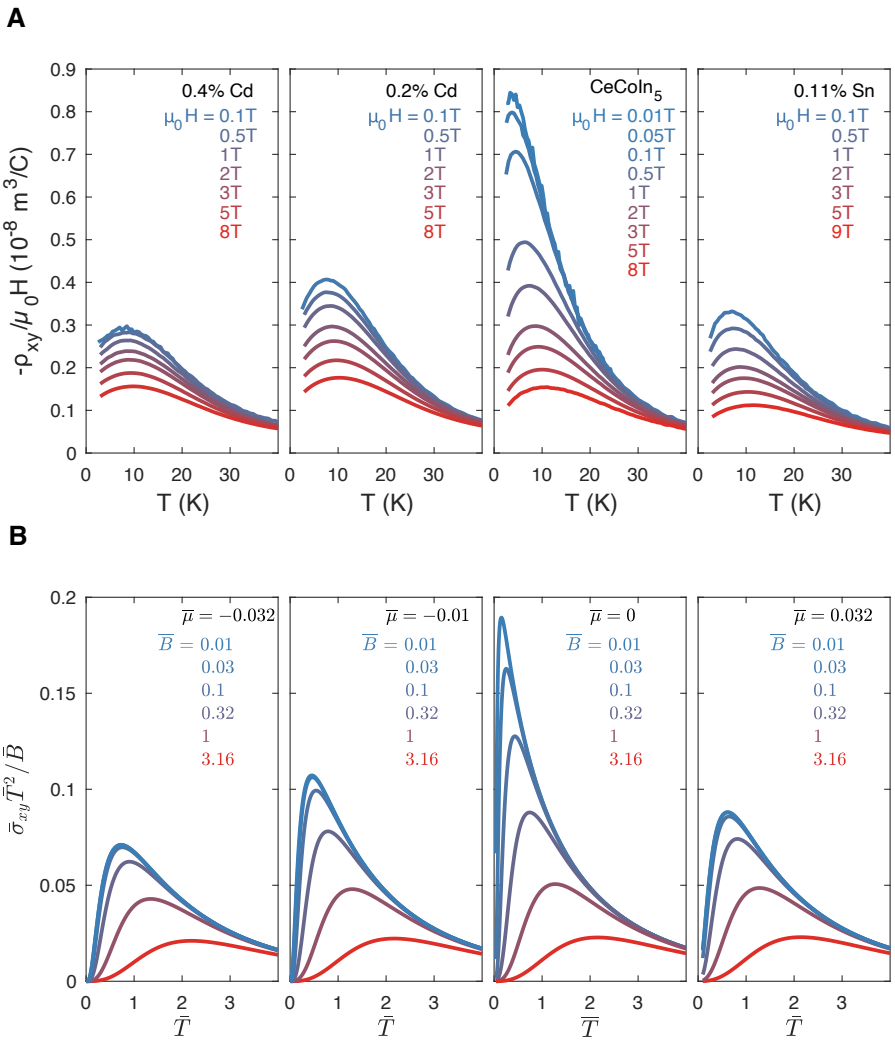

Figure 2.17: **Comparison of experimental data and theoretical calculations of the conductivity of critical valence fluctuations around an f-electron delocalization transition. A** Experimentally measured Hall resistivity, divided by the applied magnetic field, for samples with different compositions. **B** The theoretically predicted Hall effect from bosonic valence fluctuations of the fractionalized Fermi liquid model. Each panel is labeled by the chemical potential in the theory corresponding to the doping level in the experiment, where $\mu < 0$ corresponds to hole-doping and $\mu > 0$ corresponds to electron-doping. Curves are labeled by the normalized magnetic field value and all theory data includes a parametrization of impurity scattering, $\bar{C} = 4$. See Ref. [123] for the details of the calculation and relevant parameter normalizations.

conduction band in parallel gives:

$$R_H = R_H^c \frac{\sigma_c^2}{(\sigma_{\rm tot})^2} + \frac{1}{\mu_0 H} \frac{\sigma_{xy}^b}{(\sigma_{\rm tot})^2} \tag{2.10}$$

where σ_c and R_H^c are the longitudinal conductivity and Hall coefficient of the conduction electrons, respectively, and σ_{xy}^b is the Hall conductivity of the bosonic valence fluctuations. The total conductivity is $\sigma_{\rm tot}$. In our calculation, we consider two processes that contribute to the scattering rate of the valence fluctuations. One process is provided by the internal gauge field [177]. The other mechanism is scattering on the doped ions, which grows linearly with the doping level (see Fig. 2.18). One may expect an enhancement of the low-field Hall coefficient stemming from the second term in Eq. 2.10 caused by the singular behavior of the valence fluctuations when the boson gap closes. This expectation is corroborated by a semi-classical Boltzmann analysis, the details of which are given in Ref. [122]. As shown in Fig. 2.17, the results of the calculation of the conductivity in this model give good agreement with the measured Hall coefficient as a function of temperature, doping level, and magnetic field with the assumption that pure $CeCoIn_5$ is the sample closest to the delocalization transition. The results shown in Fig. 2.17B are obtained from a calculation of σ_{xy}^b, and converted to a Hall coefficient using the physical resistivity of the system $1/\sigma_{\rm tot} = \rho_{xx} \sim T$ as observed in the experiment over the relevant temperature range. A more complete description of the longitudinal resistivity in this model will be the subject of future work.

We emphasize that the experimental observations seen in Fig. 2.17A are difficult to reconcile with more conventional transport models. From the semiclassical transport point of view, the low-field R_H is proportional to the carrier density of the most mobile carriers [154], so it is surprising that R_H has such a strong temperature-dependence with a peak at finite temperature, and retains the same sign and uniformly decreases with either hole or electron doping. In addition, the observed symmetric-in-doping Hall coefficient cannot be readily attributed to disorder scattering induced by chemical substitution, as we find that disordering the material by other means, substituting lanthanum for cerium, has a relatively small effect on the low-field R_H (see Fig. 2.20). These key features of the experimental transport data are captured by the valence fluctuation model described above.

The absence of evidence for symmetry breaking around this transition opens the possibility for the fractionalization of f-electrons into separate spin and charge degrees of freedom. Although our conductivity calculations support this theoretical picture, direct evidence for such fractionalized electrons is desireable, and may be possible with inelastic neutron measurements [19] or Josephson tunneling experiments [176]. On a final note, recent experiments on cuprate high-temperature superconductors find evidence for a Fermi surface reconstruction where the localized charge of the Mott insulator gradually delocalizes over a certain oxygen doping range near the endpoint of the pseudogap phase (sometimes referred to as a p to $1+p$ transition [17]). We have presented evidence for an analogous transition in an f-electron metal. It is possible that such a quantum phase transition underlies some of the similarities between $CeCoIn_5$ and cuprate superconductors [144, 138, 178, 149, 97, 187,

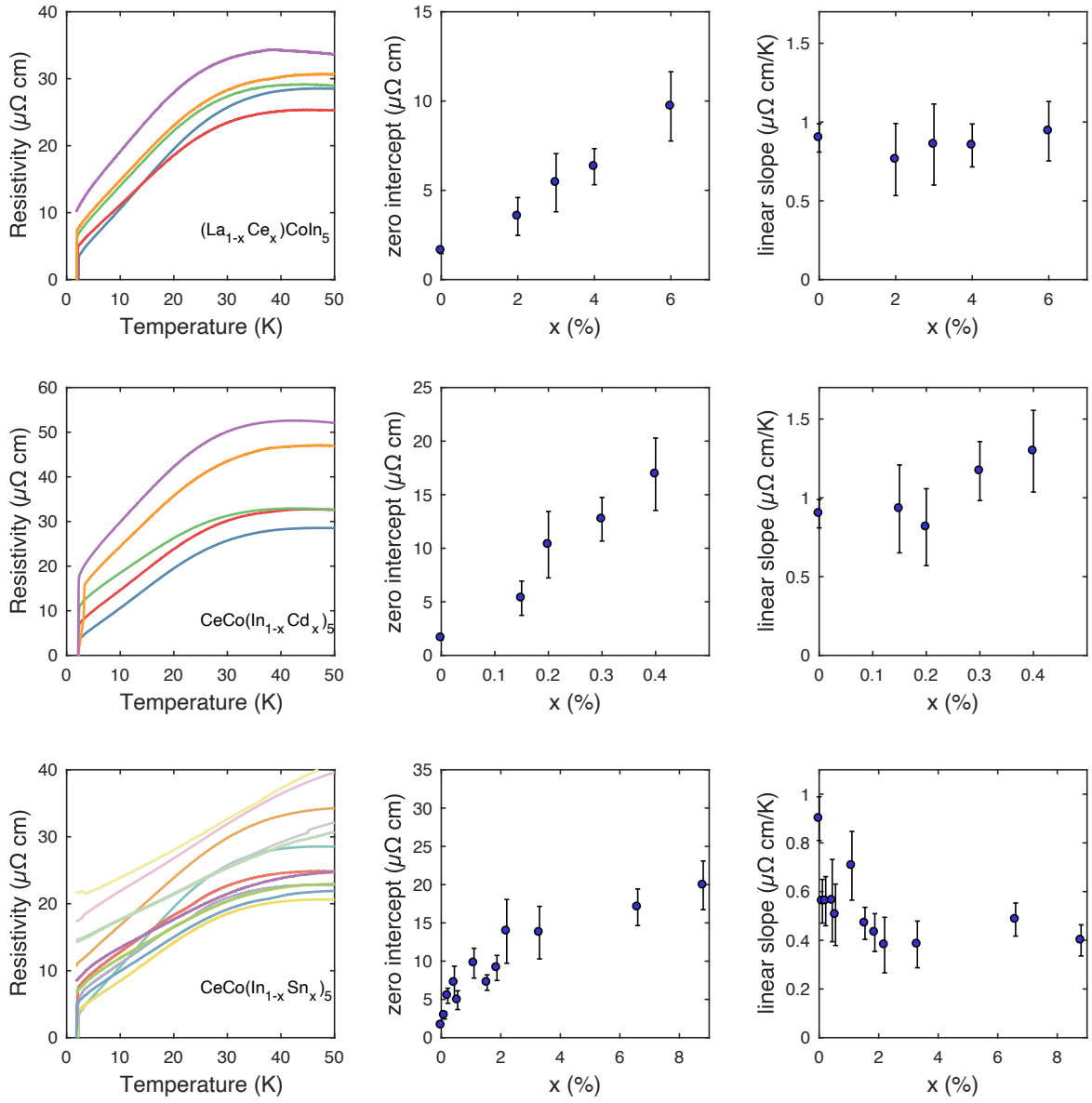

Figure 2.18: **Resistivity in doped $CeCoIn_5$** Each row shows the resistivity versus temperature traces for samples with different doping levels. (La $x = 0\%$, 0.2%, 0.3%, 0.4%, 0.6%, Cd $x = 0\%$, 0.15%, 40.2%,0.3%,0.4%, Sn $x = 0\%$, 0.11%, 0.22%, 0.44%, 0.55%, 1.1%, 1.54%, 1.87%, 2.2%, 3.3%, 6.6%, 8.8%. A linear fit to the resistivity was taken over the 8-15K temperature range. The slope and zero-temperature intercept versus doping level are plotted in the second two panels of each row.

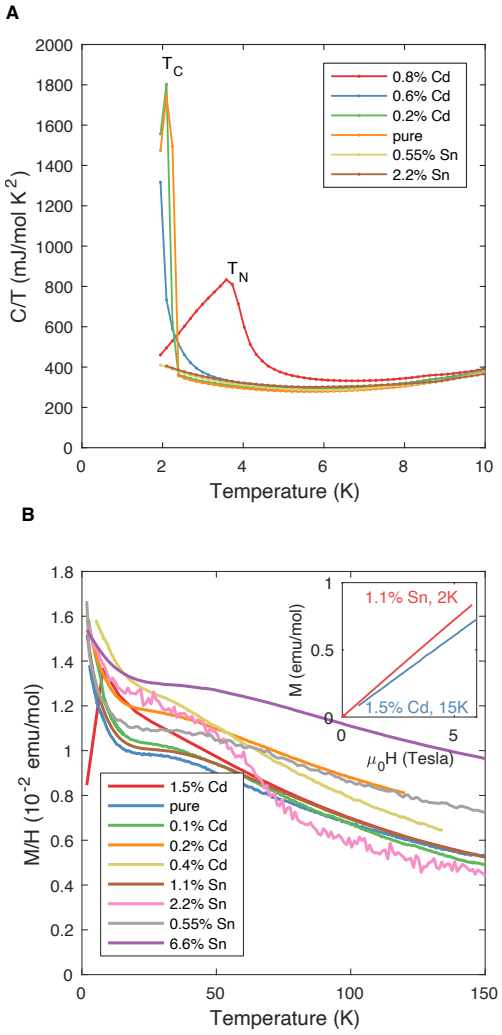

Figure 2.19: **Heat capacity and magnetization of doped $CeCoIn_5$ A** Heat capacity at different doping levels measured using a heat pulse technique with a 2% temperature rise. Each data point represents an average of three repeated measurements. Superconducting or Neel transitions are observed. **B** Magnetization measured by warming up the sample from low temperature in fixed fields between (0.1 and 1T). The inset shows that the field-dependent magnetization for two characteristic samples is linear in field. The temperature-dependent susceptibility is similar among all samples. The 1.5% Cd-doped sample shows a Neel transition.

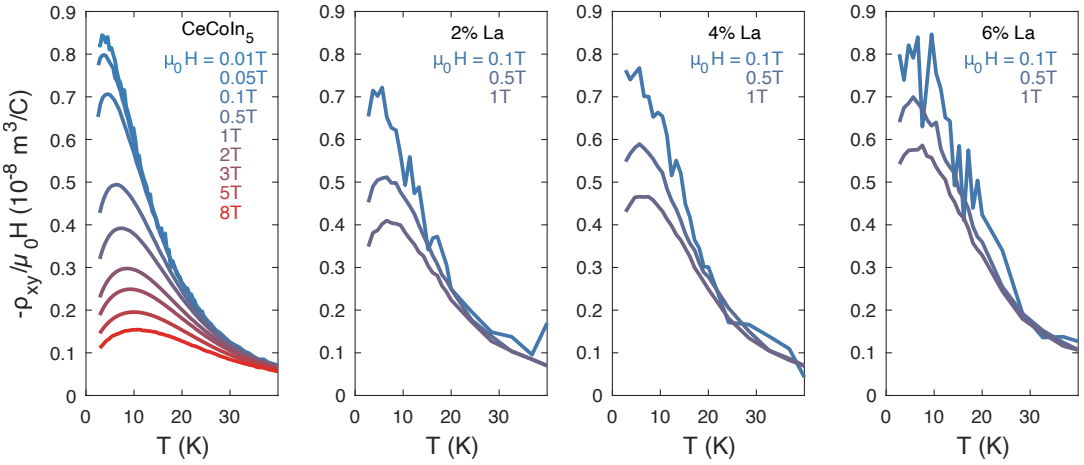

Figure 2.20: **Hall coefficient in $CeCoIn_5$ with lanthanum substitution of the cerium.** Doping with lanthanum induces a modest increase in the value of the low-field Hall coefficient. This can be contrasted with the rapid suppression of the low-field Hall coefficient induced by either Cd or Sn substitution of In, as seen in Fig. 2.17. Note that $CeCoIn_5$ was measured down to 0.01T, while the La-doped samples were only measured down to 0.1T.

225, 194, 23], and perhaps our work may help guide interpretation of these recent results on cuprates.

2.7 Crystal growth procedures and Hall effect measurement techniques

Crystal growth and characterization

$CeCoIn_5$ was grown by a well-established flux method [149]. Cerium, cobalt, and indium were combined in an alumina crucible in a ratio of (1:1:20). Cerium is a rapidly oxidizing metal, and as such it is typically packed in mineral oil. The oil was first washed off with a 3-step acetone, isopropynol, ethanol rinse. The outer oxide layer of the cerium chunks was stripped off with wire cutters and then discarded. The remaining shiny lump of cerium was placed directly into the alumina crucible, and then transferred to a glove box with an inert atmosphere while the other elements were weighed out. After combining the rest of the elements in the crucible, it was removed from the glovebox and sealed in an evacuated quartz tube and placed in a furnace. The furnace was first rapidly heated to 1150 degrees C, and maintained at this temperature for 10 hours. The cerium and cobalt dissolve in

this indium-rich melt. Then, the desired phase precipitates out of the melt upon slowly cooling the mixture to a temperature above the melting point of indium. After melting at 1150 C, the furnace was rapidly cooled to 750 degrees C over the course of 10 hours. This rapid quenching step serves to encourage crystal nucleation. Then the furnace was cooled to 400 degrees C over the course of 120 hours. The excess indium liquid was spun off with a centrifuge. Shiny platelette samples of $CeCoIn_5$ are obtained.

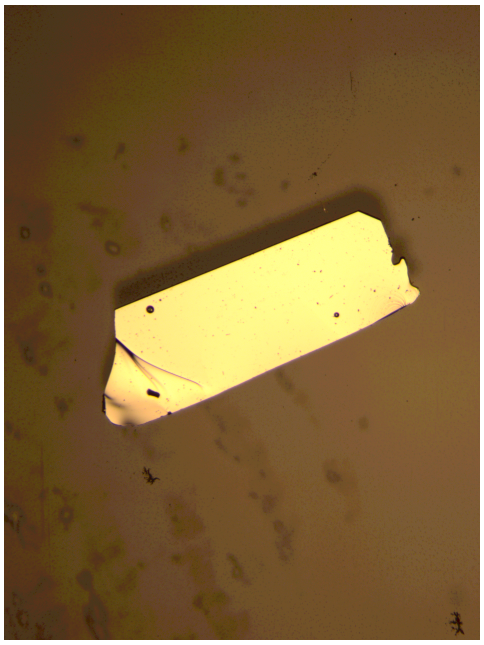

Figure 2.21: **Image of a crystal of $CeCoIn_5$** The long axis of the crystal is about 4mm.

We also grew $CeCoIn_5$ where a small amount of indium was substituted with other elements. Each chemical substitution level required a separate growth as described above, but with a nominal percentage of the indium flux replaced by cadmium or tin. The purpose of this substitution process is to dope electrons or holes into the metal, the motivation for which is described in the previous sections. In the crystals resulting from this process, the actual percentage of substituents incorporated into the sample turned out to be smaller than the nominal concentration. For both cadmium and tin alloying of $CeCoIn_5$, we generally observed a linear dependence of the true concentration on the nominal concentration in the growth. As shown in Fig. 2.22, this dependence was determined by measuring transition temperatures for magnetism or superconductivity, and comparing the temperatures to the published literature where previous authors have mapped out the dependence of transition temperature on chemical composition [31]. This comparison was supplemented by our own chemical analysis for samples with relatively high concentration levels (energy dispersive X-ray spectroscopy).

On the other hand, samples were also prepared in which cerium was replaced by lanthanum. The substitution process is analogous to that described above. In this case, the amount of lanthanum in the sample seems to coincide with the nominal concentration.

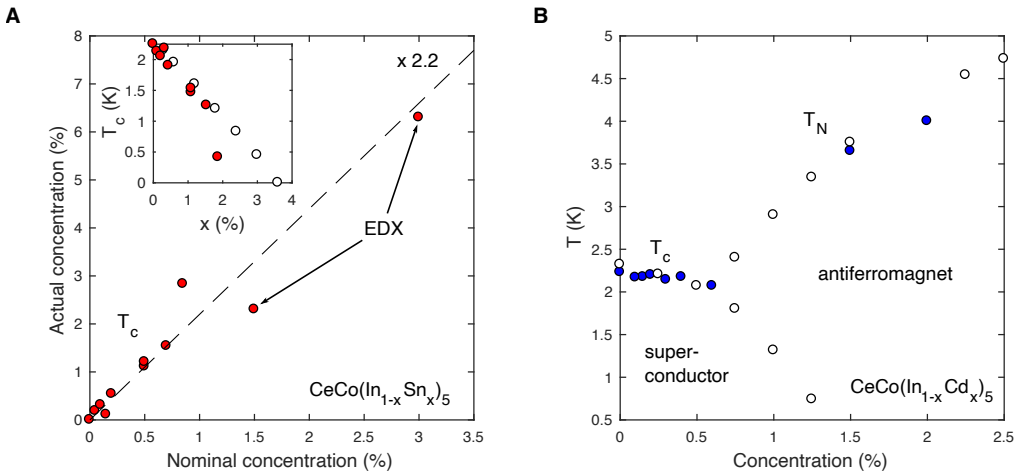

Figure 2.22: **$CeCoIn_5$ with cadmium or tin alloying A** Sn concentration, determined by comparison of superconducting transition temperature to literature for concentrations less than 1%, and energy dispersive x-ray (EDX) spectroscopy for concentrations greater than 1%. The dashed line shows the scaling factor ($\times 2.2$) for determining actual concentration from nominal using a linear fit to the combined data. The EDX points extrapolate the trend of the lower concentrations well. The inset shows the measured superconducting transition temperature versus the nominal concentration scaled by 2.2 in comparison to published data (open circles) [31]. **B** Phase diagram of Cd-doped $CeCoIn_5$. Open circles are reprinted from literature [31]. Blue circles are from the present study where the nominal concentration of Cd has been scaled by a factor of 0.1 to estimate the actual concentration.

Hall effect measurements in a ^{3}He refrigerator

"You can continue to use the turbo pump for now, as there is likely life left in it" — Eric Suter"

The size of the Hall voltage signal is inversely proportional to the thickness of the sample, and proportional to the drive current. At the requisite temperatures for the Hall coefficient experiments on $CeCoIn_5$, typically the drive current is limited by sample heating considerations given the limited cooling power afforded by ^{3}He circulation. Depending on the resistance of the electrode-sample contact, only 100-500 μA can be applied. Therefore, it is critically important that the sample thickness is reduced as much as possible for these experiments in order to maximize the signal-to-noise ratio. We found that rather high

signal-to-noise ratios are obtained when the sample is less than 20 μm thick. Acceptable signal-to-noise is obtained in the 20-50 μm range. Some of the platelet samples as-grown are on the order of 20 μm thickness or even less, and these can be directly contacted to. Otherwise, samples needed to be mechanically polished successively with 3-5 μm, and 1 μm grit polishing paper. Reducing the sample thicknesses has the added benefit of removing voids full of metallic indium flux that naturally form in single crystals during the growth process.

Electrical contact to $CeCoIn_5$ samples can be made by gold sputtering contact pads and attaching gold wires EE129 silver epoxy cured at 80^{o}C for two hours. For these samples the surface tends to oxidize when heated, and electrical contacts made to an as-grown surface or heated surfaces tend to have either high contact resistance or high interfacial capacitance. Gold sputtering contact pads does help as long as the sample isn't heated above about 100^{o}C. Once the contacts are attached with silver paint or epoxy, either to gold sputtered pads or an as grown surface, annealing with a relatively high current through the electrodes (10-20mA) for a split second can significantly improve the contact resistance, probably because the high current penetrates through the interfacial oxide layer between the electrode and the sample.

Thickness measurements were made using the high-contrast edge of the sample in an optical microscope. About half of the sample thickness measurements were calibrated using SEM images, where good agreement was found with the optical microscope measurements.

Focused ion beam device mounting and fabrication

In order to achieve measurable sample signals in pulsed magnetic fields, the samples needed to be thinned down to about 2μm thickness. For this, focused ion beam fabrication at the National Center for Electron Microscopy and Lawrence Berkeley National Lab was required. Several steps needed to be taken to ensure ease of fabrication in the focused ion beam. These samples generally cannot be fabricated into devices if they are thicker than about 10μm because material falls back into the trenches as its undergoing milling. Thus, the samples need to be roughly thinner than 5μm to begin with. Single crystals in fresh growths were selected which were determined to be around 5μm or less thickness. These crystals are fairly rare in growths, and are generally easier to find in freshly opened batches which have not undergone much handling. The crystals were then cut with a scalpel to about 50μm $\times$ 50μm lateral dimensions. The purpose of this step is to minimize the amount of time spent cutting out contacts in the sample itself.

For sample mounting, torr seal was mixed and left to dry for about ten minutes. A small dab of the torr seal was placed in the center of a glass substrate of 2mm$\times$2mm dimensions. The crystal was then mounted on the surface of the torr seal using a fine wooden stick. The torr seal was cured at 60^{o}C for two hours on a hot plate. Then a katpon tape mask was placed over the sample, and sputtered with gold for 40 seconds three times successively. After the mask is removed, the sample is ready for focused ion beam fabrication for milling of device dimensions and cutting contacts out of the gold on the glass substrate. Scanning electron micrograph images of fabricated samples are shown in Fig. 2.23.

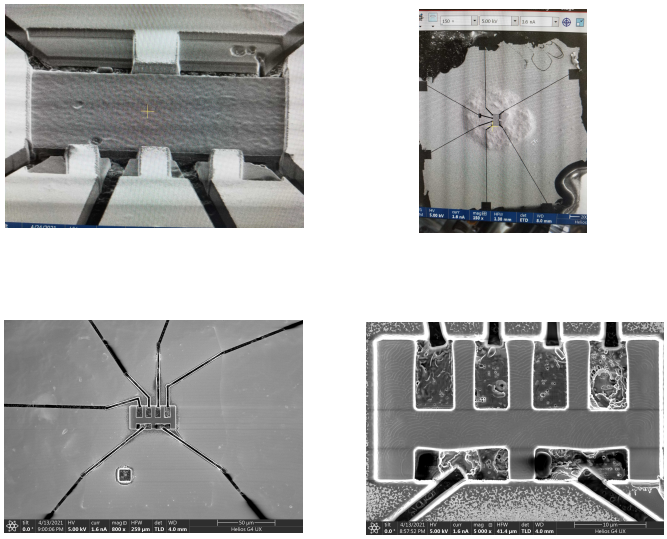

Figure 2.23: **Scanning electron micrograph images of focused ion beam fabricated Hall bar devices**

Chapter 3

Nearly-antiferromagnetic metals

The work in this chapter was based on previously published work in Ref. [123]. Sections 3.1, 3.2, 3.3, 3.5, 3.7, and 3.8 are original to this text. 3.7 contains some portions of text from Ref. [123]. The other sections were copied from Ref. [123] with certain parts rewritten to fit into the broader structure of this text. The present author performed transport measurements, sample preparation, and modeling of the data. Permission to include published data was obtained from the coauthors of Ref. [123].

Probably one of the most thoroughly studied examples of non-Fermi liquid behavior is in nearly-antiferromagnetic metals. The rare-earth-based alloy $CePd_2Si_2$ was one of the first such materials, being first discovered and experimentally studied at low temperature in the 1970s [192]. Clear deviations from Fermi liquid theory were observed, and attributed to the presence of very long-wavelength antiferromagnetic spin fluctuations that arise near the antiferromagnetic phase boundary. More recently, the discovery of iron-based superconductivity in the late 2000s drove renewed interest in the study of nearly-antiferromagnetic metals [168]. It is also widely believed that much of the physics of electron-doped cuprate superconductors can be explained by the proximity to an antiferromagnetic state [14]. Some believe that this is also the case for the hole-doped cuprates.

It is often the case that superconductivity develops at the endpoint of an antiferromagnetic phase at low temperature. Theoretically, it has been argued that antiferromagnetic fluctuations in two dimensional systems induce an attractive interaction between electrons that induces superconducting pairing [114, 134]. Experimentally, evidence exists for such a description. For example, a neutron resonance at the same momenta as that of the antiferromagnetic ordering vector have been observed in the superconducting state of many iron-based materials [44]. However, it is worth noting that the mechanism for superconductivity in most of these materials is still up for debate.

3.1 Non-Fermi liquid physics in nearly-antiferromagnetic metals

There is good reason to believe that many nearly-antiferromagnetic metals host an antiferromagnetic quantum critical point [70]. That is, the antiferromagnetic phase transition remains second-order and persists to zero temperature as the system is perturbed by a non-thermal parameter. This phenomenon has surprising effects on the metal at finite temperature. Proximity to an AFM quantum critical point manifests as fluctuations of the AFM order parameter that proliferate to longer and longer length scales as the critical point is approached [133, 129], either by decreasing temperature or by perturbing the system with a non-thermal parameter such as chemical composition or applied hydrostatic pressure. This process can lead to singularities in bulk thermodynamic properties like specific heat capacity, as discussed in the introduction of this text [174]. The thermodynamic properties of quantum critical antiferromagnets, for example a logarithmically diverging heat capacity which contradicts Fermi liquid theory, in many cases can be reasonably well-accounted for using a model in which the electrons are weakly coupled to a bath of critical antiferromagnetic modes [133, 41]. Certainly, some open questions remain in regards to dealing with the fact that the critical magnetic modes lie in the spin degrees of freedom of the same electrons to which they are coupled [41]. Perhaps most notably, a nearby antiferromagnetic quantum critical point appears to often have dramatic consequences on the electrical transport properties of metals, often inducing a resistance that scales with a power law less than quadratic at low temperature which indicates a breakdown of the adiabatic principle for Fermi liquids. The fact that these effects are observed in bulk transport measurements suggests that fluctuations are somehow coupling to most if not all of the electrons in the metal. This is surprising because the antiferromagnetic modes from the standpoint of the theories discussed above [129] should only be strongly coupled to a small fraction of electrons that overlap with the antiferromagnetic modes in momentum space.

Therefore, most of the outstanding problems in the study of nearly-antiferromagnetic metals reside in the non-superconducting state, where non-Fermi liquid physics is observed. Perhaps the most challenging property to accurately capture in these materials is the electrical transport — resistivity and Hall effect [72]. In this chapter, we will discuss how models of electrical transport were developed for $CePd_2Si_2$ — these models actually draw heavily from conventional transport models that are applied to Fermi liquid systems, but with some modifications [164, 165]. We will also discuss how models in similar spirit can be used to capture much of the observed electrical transport properties of iron-based superconductors, which have recently become a topic of intense study. Certain aspects of these transport models may transfer over to copper-oxide superconductors and other related materials.

3.2 Transport in nearly-antiferromagnetic metals

"Resistivity is the first thing you measure, and the last thing you understand" — Zlatko Tešanović

One of the 'hot topics' in the study of electronic materials during the 1950s-1970s was determining the Fermi surfaces of semiconductors and metals — materials like germanium, silicon, copper, aluminum, etc. Around this time experiments were actually realizing the concept of a Fermi surface beyond just an abstract theoretical construct — the various complicated contours of the Fermi surface of a metal where found to actually have an effect on its measurable physical properties. As it turns out the resistivity of a metal in an applied magnetic field is highly sensitive to the shape of the Fermi surface as well as the direction of the field and current with respect to the principle axes of the crystal. And, because resistivity experiments were fairly straightforward even with the technology of the time, there was a considerable drive to develop models to relate the results of resistivity experiments, especially resistivity in applied magnetic field (magnetoresistivity), to the shape of the Fermi surface of the metal. This was the original motivation for studying electronic magnetotransport in solids.

In many ways, transport coefficients of a metal are some of the most difficult physical properties to understand microscopically. One needs knowledge of the spectrum of the carriers, knowledge of the sources of transitions between different states, and knowledge of how these quantities change with temperature or with the application of a magnetic field. Even then, several approximations need to be made for there to be any hope of theoretical calculations making meaningful statements about experimental results. Due to the work of Pippard [154], Shockley [183], Chambers, and others, it was generally believed that we had a good understanding of the requisite approximations, and we developed a good understanding of the electrical transport properties of solids. These established transport theories are called 'semiclassical'. Quantum mechanics defines their statistics (Fermi-Dirac statistics), and potentially transition rates between states are based on solutions to Schrodinger's equation. The classical part comes in the motion of the particles, their trajectories, and the fact that transitions, happening with a certain probability based on the quantum calculation, are then considered to be instantaneous when they do happen. In this way, quantum entanglement or interference effects between quasiparticles or electrons are not considered. Based on the semiclassical description, the temperature-dependent resistivity was understood in most metals, and most importantly the magnetic field-dependent resistivity was understood well enough that people could actually to some extent determine the shape of a metal's Fermi surface using magnetoresistance measurements — one of the original goals of this line of work.

Lurking in the background, however, was the puzzling behavior of the temperature- and field-dependent resistivity of certain nearly-antiferromagnetic metals like $CePd_2Si_2$ [87]. These materials led to questions regarding the approximations going into the semiclassical theory of transport, and even the Fermi liquid description itself.

Fig. 3.1 shows the comparison of the temperature-dependent resistivity of $CePd_2Si_2$ un-

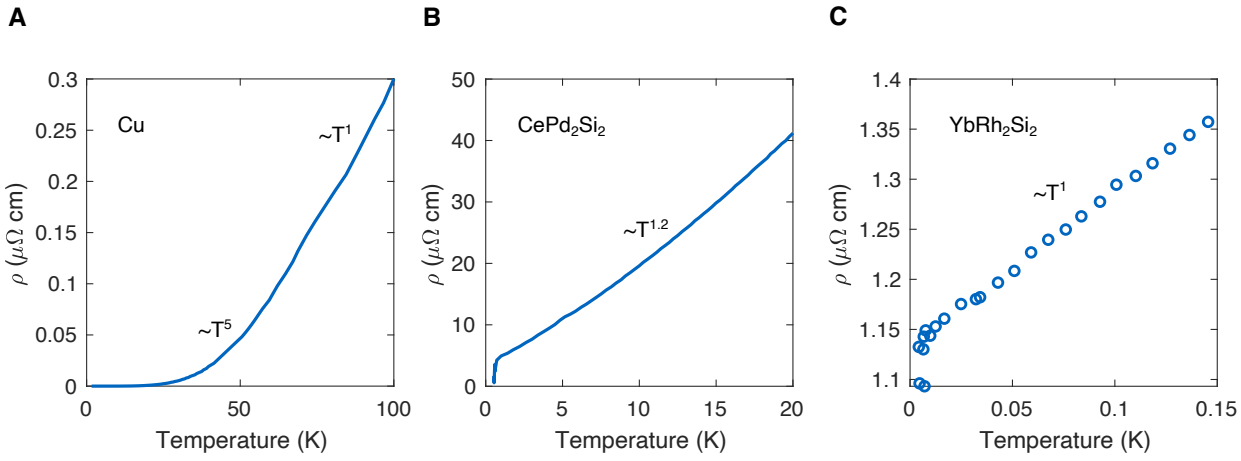

Figure 3.1: **Comparison of temperature-dependent resistivity in different metals at low temperatures A** Resistivity of copper at low temperatures as an example of a typical metal [89]. Phonon scattering induces a T^5 power law in bulk resistivity, which transitions to T-linear at higher temperature. At the lowest temperature, the resistivity saturates because of impurity scattering. **B** $CePd_2Si_2$ at a critical pressure of 28 kbar, near the zero-temperature endpoint of the antiferromagnetic phase. The resistivity varies as $T^{1.2}$, in stark contrast to the behavior observed in copper and other metals at low temperature [87]. **C** The resistivity of $YbRh_2Si_2$ under an applied field of 60mT along the crystallographic c-axis [141]. The resistivity varies linearly with temperature down to the lowest measurable temperatures. Both $CePd_2Si_2$ and $YbRh_2Si_2$ exhibit a bulk resistivity scaling, which, if interpreted as an electron-electron scattering rate, seems to violate the adiabatic principle central to the Fermi liquid description of metals.

der pressure, a nearly-antiferromagnetic metal, to that of elemental Cu. The temperature-dependent resistivity of Cu can be understood primarily from the perspective of charge carriers bouncing off of thermal vibrations of the lattice. At high-temperature the resistivity varies linearly with temperature because the number of available phonon states grown in proportion to temperature. At some lower temperature scale (known as the Debye temperature), phonon states start to depopulate, and the resistivity is found to vary as T^5. At a lower temperature, the resistivity saturates because of charge carriers losing momentum to impurities. The astute reader might wonder where the famous T^2 Fermi liquid electron-electron collision rate presents itself in the resistivity of elemental metals. It turns out that this contribution is usually tiny compared to the dominant role of electron-phonon contributions to the resistivity, so in normal metals the low-temperature T^5 behavior presents itself most prominently. And what's more, you would be hard-pressed to find a metal that deviates significantly from the resistivity curve shown in Fig. 3.1A, barring any phase transitions.

Phonons are present in every material, and the Debye temperature is more or less similar within about a factor of two for most metals. Most importantly from the perspective of Fermi liquid theory, the low-temperature resistivity of these metals varies with a power law greater than 2 at low temperature, thus we can be somewhat confident that the relaxation rate of electrons is not surpassing the limits imposed by the adiabatic principle central to Fermi liquid theory.

Compare the above behavior to the resistivity of $CePd_2Si_2$ (Fig. 3.1B). The resistivity of this material, when a pressure of 28 kbar is applied to it, varies as $T^{1.2}$ over an extended range in temperature, and down to relatively low temperatures — low enough that if it were a metal like copper, we would definitely expect the conventional T^5 dependence from phonons to present itself. For a long time, the unusual temperature-dependent resistivity of $CePd_2Si_2$ was attributed to the influence of antiferromagnetic fluctuations that were believed to be present in the system given its proximity to AFM and the presence of a putative AFM QCP. But there is a more concerning feature in the temperature-dependent resistivity of $CePd_2Si_2$. Fermi liquid theory apparently limits the quasiparticle relaxation rate to T^2, as discussed in the introduction. To reiterate: if the quasiparticle relaxation rate is faster than T^2 (and assuming that the resistivity is correlated with the quasiparticle relaxation rate), then the adiabatic approximation going into Fermi liquid theory is no longer valid, and it becomes unclear whether the fundamental description of the electrons as independent particles is valid at all. So, the resistivity in $CePd_2Si_2$ becomes more than a question about how antiferromagnetic fluctuations may dissipate the momentum of quasiparticles, but more about whether the system actually violates Fermi liquid theory from a more fundamental level. By analogy, imagine if the low-temperature specific heat capacity of a metal went as $T^{1/2}$ rather than T-linear — we would probably wonder what is going on in that metal, and whether its electrons can be described as independent fermions.

It was only by the late 90's that A. Rosch developed a rigorous theory of transport to describe the $T^{1.2}$ scaling with temperature seen in the experiments on $CePd_2Si_2$ [164, 165]. He did it by assuming the antiferromagnetic quantum critical scenario described in the introduction chapter of this text. Although an abnormally high relaxation rate may occur at 'hot spots' connected by the antiferromagnetic ordering vector, most of the Fermi surface is superficially not affected by this strong scattering rate, at least according to simplified versions of semiclassical transport theory. Rosch, however, re-examined some the assumptions going into the semiclassical transport theory developed in the 1950's, and noticed that the overall T-dependent resistivity is not directly correlated to the quasiparticle relaxation rate, and in principle scaling laws in the T-dependent resistivity faster than T^2 over substantial ranges in temperature even at very low temperature are admissible from the semiclassical transport perspective. This can be true even if the critical fluctuations which scatter electrons only affect very localized regions of momentum space. The source of the influence of such localized scattering on the majority of electrons is related to the nonlinear mixing of scattering from magnetic fluctuations and disorder scattering. The latter can 'smear' out the hot spots such that they have a dramatic influence on the overall transport properties.

The issues brought up by the $T^{1.2}$ scaling in the resistance of $CePd_2Si_2$ become more press-

ing with the discovery of the copper-oxide ceramic superconductors, certain heavy fermion metals, and to a certain extent iron-pnictide superconductors, many of which exhibit a linear temperature scaling of their resistances that *seems* to violate the criterion of T^2 quasiparticle relaxation in a Fermi liquid. An example of such a linear-in-temperature resistivity scaling down to essentially the lowest experimentally accessible temperatures is shown in Fig. 3.1C for the heavy fermion metal $YbRh_2Si_2$ under an applied field of 60mT — under these conditions the material is very close to antiferromagnetic order and potentially a charge delocalization transition. It has been a long standing puzzle to understand the electrical transport properties of such nearly-antiferromagnetic or nearly-charge localized systems at very low temperatures. Some argue that the concept of a Fermi liquid quasiparticle, and the conventional semiclassical approach to understanding electrical transport, needs to be overhauled completely to capture the behavior seen in Fig. 3.1C. The rationale here is that at such low temperatures, the resistivity is probably representative of only electron-electron scattering as it is difficult to imagine bosonic modes being excited at only a few mK above absolute zero, and thus the quasiparticle relaxation rate is faster than the adiabatic principle allows. On the other hand, as has been shown by the example of $CePd_2Si_2$, transport can be an un-intuitive measurement in the sense that the behavior of the resistivity is not necessarily a probe of the dynamics of individual quasiparticles, and in addition, the presence of bosonic modes even at low temperature is difficult to rule out (even in certain Fermi liquids a linear resistivity can persist to incredibly low temperature on the order of a few Kelvins as a result of low-energy phonons [81]). Moreover, the temperature regimes over which unexpected resistivity-temperature scaling is observed is of critical importance. $YbRh_2Si_2$ is one of the most rock solid examples of non-Fermi liquid transport, exhibiting a linear resistivity down to a few mK. Other situations like the copper-oxide superconductors, which exhibit linear resistivity down to the superconducting transition temperatures which are on the order of 10s of Kelvin, are less clear cut (lead for example, has a linear resistivity down to 10 kelvin or so because of the phonon contribution; in certain situations the phonon contribution can be extended well below the Debye temperature, even sometimes down to rather low temperatures like 100 mK depending on the dimensionality of the material, and the details of the phonon spectrum [220, 81]).

In the existing literature on the potential non-Fermi liquid properties of nearly antiferromagnetic metals and other types of quantum critical metals, a considerable weight is given to transport data. The purpose of this chapter is to critically evaluate which features in experimental data, primarily on iron-pnictide superconductors, can be understood from the semiclassical transport perspective, and which features are outstanding issues that may require transport models 'beyond the semiclassical picture'. This is a separate, but related, distinction than the one between Fermi liquid and non-Fermi liquid (as has been shown by $CePd_2Si_2$ where certain regions of the Fermi surface may have non-Fermi liquid properties, but the overall transport behavior can be reasonably well understood by a semiclassical transport model). In the later sections of this chapter, we will describe some experiments that can be done in order to determine to what extent the semiclassical theory of transport is applicable to different classes of non-Fermi liquid systems.

3.3 Semiclassical transport theory of solids

"If you are out to describe the truth, leave elegance to the tailor." — Ludwig Boltzmann

This text will primarily deal with transport, and the features in transport that can potentially be explained by semiclassical transport theory even in strongly interacting electron systems. Transport models beyond the semiclassical approach are being developed. These models will not be discussed in this text to any considerable degree, in part because at the present time such models are difficult to test experimentally using bulk transport measurements.

Upon application of an external electric field, the Fermi surface of a material will shift in k-space, populating excited electron states on one side (wherever $\mathbf{E} \cdot \mathbf{v} > 0$), and hole states on the other (wherever $\mathbf{E} \cdot \mathbf{v} < 0$). The action of the force is balanced by momentum relaxation in the form of electrons scattering off of impurities, temperature fluctuations, and other electrons. The competition between the external force supplied by the electric field, and the mechanisms for momentum dissipation to the lattice will lead to a steady-state current density flowing through the metal ($\mathbf{J}$). $\mathbf{E}$ and $\mathbf{J}$ are related to each other to first-order by the conductivity σ ($\mathbf{J} = \sigma\mathbf{E}$). In general the conductivity is a tensor quantity, because both the current density and electric field are vectors. A closely related property of metals is the resistivity $\rho = \sigma^{-1}$, the inverse of the conductivity tensor. The values of the ρ tensor, and how they change with temperature and external magnetic field, are determined by the specific details of momentum relaxation and energy spectrum of a material; the goal of transport theory in solids is to determine how these mechanisms lead to the observable ρ. This turns out to be a rather complicated problem in metals, even apparently 'simple' ones like aluminum and lead, because the electronic energy spectrum may have a rather complicated dependence on momentum in three dimensions, and the mechanisms for momentum relaxation could be equally complicated. A series of approximations are often employed to at least get a base-level understanding of the behavior of ρ as a function of temperature, magnetic field, and defect density of the sample. In nearly-magnetic metals, the sources of momentum relaxation may be even more complicated than in 'simple' metals like aluminum, and in these cases more comprehensive models are required. We will first describe the simplest transport models, and then build on that.

Drude Model

The most basic transport theory relies on the assumption of a 'scattering time'. After being accelerated by an electric field, a quasiparticle will travel along for some average amount of time, τ, until it scatters at which point its momentum is randomized completely. The Drude model uses the free electron approximation; electrons simply move in straight lines between collisions.

The system will reach an equilibrium where the force supplied by the electric field is counteracted by the average momentum relaxation due to scattering (exactly what the elec-

trons are scattering off of will be discussed later), which gives rise to a net resistance to current. This can be captured by a relatively straightforward force balance equation

$$\frac{d}{dt}\langle \mathbf{p}(t)\rangle = q\mathbf{E} - \frac{\langle \mathbf{p}(t)\rangle}{\tau}, \tag{3.1}$$

where $\langle \mathbf{p}(t)\rangle$ is the average momentum per electron. Here, the assumption made is that if the electric field were removed, the momentum of the particle distribution would decay exponentially — this is captured by the $\frac{\langle p(t)\rangle}{\tau}$ term. More intuitively, this term represents the fact that transitions caused by scattering from, for example lattice impurities or thermal vibrations, are momentum-randomizing, and thus a quasiparticle which suffers such a scattering event on average loses its momentum in the direction of the electric field. The steady-state solution, where the net variation of average momentum is set equal to zero ($\frac{d\langle p\rangle}{dt} = 0$), gives $\langle \mathbf{p}\rangle = nq\langle \mathbf{v}\rangle$. Substituting $\mathbf{J} = nqm\langle \mathbf{v}\rangle$, we arrive at an expression for the conductivity, σ in terms of the carrier density n, charge q, and electron mass m.

$$\mathbf{J} = \left(\frac{nq^2\tau}{m}\right)\mathbf{E} = \sigma\mathbf{E} \tag{3.2}$$

This is essentially a recreation of the phenomenological form of Ohm's law ($\mathbf{J} = \sigma\mathbf{E}$), but with a physical picture in mind. However, the Drude model assumes that all quasiparticle scattering randomizes momentum, and that all quasiparticles, either in real or momentum space, have the same average scattering rate. It also does not take into account momentum-space anisotropy in the distribution of quasiparticles (such an anisotropy is present in almost every metal). The Drude model is severely limited because of these approximations, and should generally only be applied as a tool for qualitatively understanding trends. For example, the Drude model can give us a sense of how the resistivity of a material will increase or decrease with effective mass, impurity concentration (i.e. scattering rate), or carrier density. However, properties like the temperature-dependent resistivity are very likely to contain effects which violate the approximations of the Drude model, as we will discuss in the following sections. Interpreting the resistivity as a measurement of the scattering rate, for example, is not justifiable given the approximations that go into deriving Eq. 3.2.

Drude originally used the classical Maxwell-Boltzmann distribution when deriving the results of this transport theory, but they turn out to be correct for a free electron gas with a Fermi-Dirac distribution. This is because the force balance equations central to this transport theory are independent of the statistical distribution of particles. Only results related to the speed of the particles are affected by this distinction, i.e. estimations of the 'mean free path' (the average distance between scattering events) will be completely wrong if the Maxwell-Boltzmann distribution is used.

For example, if we apply Eq. 3.2 to low-temperature copper, the calculated scattering rate is $\tau = 3.7 \times 10^{13}$ Hz — Drude assumed, and classically we expect, that electrons scatter off of the positively charged ions of the lattice (the average distance between ions in copper is 3.6Å in copper) giving us an average classical velocity of electrons in copper of 13000 m/s.

In reality, electrons in copper obey Fermi statistics, and their velocity is given by the Fermi velocity (1.57×10^6 m/s). Thus, the estimate given by Maxwell-Boltzmann statistics is completely wrong, as we know now, but Drude didn't know about Fermi statistics at the time. Moreover, the actual mean free path of pure copper taking into account the true Fermi velocity is 430Å, more than 100 times higher than the mean free path than expected from the classical calculation (i.e. the assumption that electrons scatter off of the ions in the lattice). The takeaway is that electrons do not scatter off of the ions that make up the lattice. This is because the electron Bloch states are itinerant wavefunctions that extend over the periodic potential induced by the ions, as discussed in Chapter 1. It turns out that the scattering time τ of the Drude equation, at least at very low temperature, is actually determined by the density of lattice defects in the material. The distance between defects, especially in pure samples of copper, is much further than between lattice ions, explaining the relatively large mean free path of electrons in copper. If the underlying lattice was perfectly uniform, the electrons would actually never scatter in the low temperature limit, and the resistance would be zero. This fact is a consequence of the quantum wave-like nature of the electrons in a metal. In fact, measuring the low-temperature resistivity of metals was the original motivation for liquifying helium, which ultimately led to the discovery of superconductivity in mercury in 1911. The addition of Fermi statistics to the Drude model, as described in this paragraph, is sometimes referred to as the Drude-Sommerfeld model.

Boltzmann equation

Consider cases now where either the particle distribution is anisotropic in momentum space, or there are sources of scattering that affect certain regions of momentum space more than other regions, or there are sources of scattering that change the electron momentum by a relatively small amount. In such cases, electrons may be more likely to be scattered to certain momenta over others, and their momentum isn't necessarily randomized by a single scattering event (a key assumption of the Drude model in the previous section). In this case, electrons can scatter multiple times before their net momentum in the direction of the electric field is reduced to zero. This is especially true if the majority of scattering is 'small-angle', in the sense that the total change in momentum after a scattering event is small; most electron-electron scattering mechanisms, for example, are small-angle. Almost all nearly-magnetic metals have scattering rates that are anisotropic, or complicated electronic structures. Therefore, while the Drude model is useful for a qualitative general understanding of the contributions to the resistivity of a material, more accurate descriptions require approaches beyond the Drude model.

In order to solve this problem, we cannot only use the average momentum per particle as was done in the Drude picture because particles at different momenta may have different scattering rates or velocities. The quasiparticle distribution function needs to be considered — that is, a probability density function that describes the density of particles at each position $\mathbf{r}$ in momentum state $\mathbf{k}$ at time t; $f(\mathbf{k}, \mathbf{r}, t)$. In the steady state, the distribution function is time-independent, and all sources of $\frac{\partial f}{\partial t}$ will sum to zero. We consider three

mechanisms that affect the distribution function: diffusion of particles into and out of volume element $\mathbf{r}$, external forces such as electric and magnetic fields, and scattering of electrons into and out of different $\mathbf{k}$ states.

$$\left(\frac{\partial f}{\partial t}\right)_{\text{diffusion}} + \left(\frac{\partial f}{\partial t}\right)_{\text{ext. forces}} + \left(\frac{\partial f}{\partial t}\right)_{\text{scattering}} = 0 \tag{3.3}$$

Diffusion

Diffusion takes into account the motion of particles between different spatial positions, i.e. volume elements $\mathbf{r}$. The velocity of particles in state $\mathbf{k}$ is v_k. In a time t, the particle will move $v_k t$. The concentration of particles at a position r after an infinitesimal time δt is equal to the concentration of particles at $r - v_k \delta t$ at a time of 0. Thus,

$$f(\mathbf{k}, \mathbf{r}, \delta t) = f(\mathbf{k}, \mathbf{r} - v_k \delta t, 0) \tag{3.4}$$

$$f(\mathbf{k}, \mathbf{r}, 0) + \frac{\partial f(\mathbf{k}, \mathbf{r}, t)}{\partial t}\delta t = f(\mathbf{k}, \mathbf{r}, 0) - \frac{\partial f(\mathbf{k}, \mathbf{r}, t)}{\partial \mathbf{r}} \cdot v_k \delta t \tag{3.5}$$

Therefore,

$$\left(\frac{\partial f}{\partial t}\right)_{diffusion} = -\nabla_r f \cdot v_k \tag{3.6}$$

External Forces

Newton's law straightforwardly gives the effect of external forces on the crystal momentum

$$\dot{\mathbf{k}} = \frac{e}{\hbar}\left[\mathbf{E} + \mathbf{v}_k \times \mathbf{B}\right] \tag{3.7}$$

Using the same logic as in the previous section on diffusion, we obtain:

$$\left(\frac{\partial f}{\partial t}\right)_{ext.forces} = -\frac{e}{\hbar}\nabla_k f \cdot \left[\mathbf{E} + \frac{\mathbf{v}_k \times \mathbf{B}}{c}\right] \tag{3.8}$$

Scattering

We consider the scattering of particles between state $\mathbf{k}$ and other states $\mathbf{k}'$ [1]. It is assumed that scattering happens instantaneously and does not change the position of the particle, i.e. $\mathbf{r}$ and t are the same before and after scattering-induced transition between states. Let the transition rate from state $\mathbf{k}$ to $\mathbf{k}'$ be $g(\mathbf{k}, \mathbf{k}')$. In essence, $g(\mathbf{k}, \mathbf{k}')$ captures all the microscopic details of scattering into a single rate. At the moment, we will just keep this as a general transition rate, which can be computed from more microscopic considerations later. Then,

$$\left(\frac{\partial f}{\partial t}\right)_{scattering} = \int\int\int \frac{d^3k'}{(2\pi)^3}\left[f_{k'}(1 - f_k)g(k', k) - f_k(1 - f_{k'})g(k, k')\right]. \tag{3.9}$$

The first term in the integrand describes transitions from a state $\mathbf{k}'$ into a state $\mathbf{k}$. The second term describes transitions in the other direction. Note that in general $g(k,k') \neq g(k',k)$! The kernel is integrated over all possible $\mathbf{k}'$ states in order to determine the rate of change of density of particles in the volume element $\mathbf{k}$ with respect to time. This term is essentially equivalent to a Fermi's golden rule argument.

Relaxation time approximation

Typically, the full Boltzmann equation for transport in solids is prohibitively difficult to solve. Either a numerical method must be used, or an approximation must be made to obtain analytical solutions. The most commonly applied approximation is called the 'relaxation time approximation' (RTA). In this approach, we assume that the distribution function is only weakly perturbed away from its equilibrium state.

$$f(k,r,t) \approx f_0(k,r,t) + f_A(k,r,t), \tag{3.10}$$

where $f_0(k,r,t)$ is the Fermi-Dirac distribution for the case of electrons in a metal. Then the term associated with scattering between states can be approximated by dropping terms associated with return scattering events, i.e. transitions that cause electrons to move between k and k' and back again [1].

$$\left(\frac{\partial f}{\partial t}\right)_{scattering} \approx -f_A(k) \int\int\int \frac{d^3k'}{(2\pi)^3} g(k,k') \left(1 - \frac{f_A(k')\cancel{g(k',k)}}{\cancel{f_A(k)}g(k,k')}\right) \approx -\frac{f_A(k)}{\tau(k)} \tag{3.11}$$

$$\approx -\frac{f(k,r,t) - f_0(k,r,t)}{\tau(k)}. \tag{3.12}$$

All scattering is lumped into a single timescale (τ_k), which may depend on momentum, but does not take into account multiple scattering events where the momentum of a particle in the distribution function can transition multiple times before relaxing. Essentially, in the relaxation time approximation all scattering is assumed to be completely momentum randomizing, much like scattering in the Drude equation. The main difference here compared to the Drude case is that here, the distribution function has a momentum, and potentially spatial, dependence, and the scattering rate can also depend on momentum.

It is important to note that the RTA is not only quantitatively incorrect, but qualitatively incorrect if the majority of scattering is small-angle (i.e. scattering events are not momentum randomizing), or if there is significant anisotropy in the scattering rate. Considerable care should be taken in interpreting conclusions drawn from the RTA. The transition rate term is an alteration to the quasiparticle distribution function depending on the scattering rate between states. There is a 'feedback' effect in which changes to the scattering rate on particular parts of the Fermi surface warp the distribution of quasiparticles. As a result, beyond the RTA the transport properties are no longer determined by the behavior of individual quasiparticles undergoing scattering events, but are instead determined by the collective properties of the whole Fermi surface.

3.4 Magnetotransport properties of nearly-antiferromagnetic metals and high-temperature superconductors: comparisons with other metals

"Doesn't look like anything to me" — Westworld

Armed with some knowledge of semiclassical transport theory, we can attempt to attack the problem of magnetotransport in nearly-antiferromagnetic metals. The introduction to this chapter primarily focused on the temperature-dependent transport properties of such materials. A more recent question has been brought up in their magnetotransport properties — that is, the variation of the resistivity in a magnetic field, typically measured at low temperatures. The original purpose of studying magnetotransport was to gain access to the normal state properties of high-T_c materials at very low temperatures. In this process, a number of puzzling phenomenological descriptions were developed, starting in the mid 2010s.

It has been found that a 'hyperbolic' magnetoresistance scaling form phenomenologically captures the interplay of field and temperature in many strongly correlated materials and nearly-antiferromagnetic metals:

$$\frac{\rho(T,H)-\rho_0}{\alpha k_B T} \sim \sqrt{1+\left(\frac{\eta H}{\alpha k_B T}\right)^2}, \tag{3.13}$$

where $\rho(T,H)$ is the field-dependent resistivity at temperature T, and η a parameter that plays a similar role for the field dependence as α does for the temperature dependence [71]. Eq. (3.13) was motivated by measurements of $BaFe_2(As_{1-x}P_x)_2$ near its antiferromagnetic quantum critical point. Since then, a growing number of putative quantum critical metals have shown qualitatively similar behavior [71, 171, 157, 116, 142, 137, 170, 36, 108, 60], albeit with notable deviations in the quantities α and η. The observation of H-linear magnetoresistance, as suggested by Eq. (3.13), is unusual but not unprecedented. There are multiple possible causes of this including the presence of Dirac quasiparticles [3, 145], sample heterogeneity [121, 158], guiding center diffusion in a smooth random potential [190], fluctuations from spin density waves [165, 106], or singular regions of the Fermi surface where the Fermi velocity changes discontinuously [154, 105]. However, Eq. (3.13) places further constraints on the origin of the MR, as it conflicts with the conventional Kohler's rule for classical magnetoresistance [154], which will be discussed further later on,

$$\frac{\rho(H)-\rho(0)}{\rho(0)} = f\left(\frac{H}{\rho(0)}\right), \tag{3.14}$$

where f is a smooth and usually positive function. Kohler's rule is satisfied in metals as long as the scattering rate changes uniformly when, for example, the temperature or disorder level are varied. Even if the scattering rate is anisotropic in momentum space, one expects

Kohler's rule to be satisfied so long as the 'pattern' of anisotropy is unchanged [191]. This constraint of Kohler's scaling is reflected in the denominator of Eq. (3.14), which takes into account both temperature-independent and temperature-dependent scattering contributions, $\rho(0) = \rho_0 + \rho_t$. By contrast, in Eq. (3.13), the disorder scattering is subtracted and the quantum critical MR scales only with the T-linear component of the resistivity ($\rho_t = \alpha k_B T$) in apparent violation of Kohler's rule. A realistic theory of magnetotransport in quantum critical metals must simultaneously capture the H-linear MR and the hyperbolic scaling with temperature dictated by Eq. (3.13). In this text, we describe such a theory and show that it captures the salient features of experimentally measured MR in $BaFe_2(As_{1-x}P_x)_2$.

As described above, the linear magnetoresistance phenomenon and scaling form with temperature proved to be quasi-universal, in the sense that a number of high-temperature superconductors, unconventional superconductors, and metals near a quantum critical point, were found to exhibit a linear magnetoresistance at low temperatures. Subsequently, a number of possible explanations were put forward, ranging from linear magnetortesistance induced by variations in the carrier density across a sample [189], to more exotic models based on the Sachdev-Ye-Kitaev Hamiltonian [148]. It is clear, that a mechanism for linear magnetoresistance in this broad class of materials needs to be readily generalizeable to a rather broad set of materials with possibly different electronic and magnetic structures and properties.

3.5 Models of orbital magnetoresistance in the presence of Fermi surface sinks: applications to nearly-antiferromagnetic metals

Orbital magnetoresistance theory

In order to understand why linear magnetoresistance may be considered unusual, it is first important to discuss the origin of magnetoresistance, and general predictions of conventional models of magnetoresistance.

Consider first a free Fermi gas, or, for the purposes of this demonstration, a metal with an isotropic Fermi surface and isotropic momentum relaxation rate. One can calculate the field-dependent conductivity using the force balance equation in the steady-state in analogy to the Drude formula, but in this case also including the effect of a transverse magnetic field which generates a Lorentz force [154]. We assume that the scattering rate is isotropic in the relaxation time approximation.

$$e\left(\mathbf{E} + \langle \mathbf{p}(t) \rangle \times \mathbf{B}\right) = \frac{\langle \mathbf{p}(t) \rangle}{\tau}. \tag{3.15}$$

Note that we could have gotten to the above starting from the Boltzmann equation as well. If we flow a current in a predefined orientation, and measure the resulting electric field in

the steady state (say along x), with a magnetic field applied perpendicular to the current direction (say along z), then we arrive at the following identities:

$$E_x = \frac{m^*}{ne^2\tau} J_x \tag{3.16}$$

$$E_y = \frac{1}{ne} B J_x \tag{3.17}$$

$$E_z = 0 \tag{3.18}$$

. Using the definition $\mathbf{E} = \rho\mathbf{J}$, we arrive at the conclusion that a gas of electrons without any anisotropy in either the scattering rate or distribution function has zero magnetoresistance. The resistance ρ_{xx}, although perhaps finite depending on the scattering time τ, does not change with the strength of the applied magnetic field.

Now on the other hand, suppose we had two different types of carriers, say electrons and holes, as is quite common in semiconductors or multiband metals. Then, we need to add their conductivities together to determine the total conductivity of the sample.

$$\sigma = \sigma_{electrons} + \sigma_{holes} \tag{3.19}$$

Assuming that each carrier type has it's own carrier density, scattering time, and effective mass (everything isotropic), we can calculate the resistance. For each gas, their resistivity components are given by the formula calculated above $\rho_{xx} = \frac{m^*}{ne^2\tau}$ and $\rho_{xy} = \frac{1}{ne}B$, summing their conductivities and inverting yields a finite magnetoresistance, as seen in simulations shown in Fig. 3.2. The addition of conductivities of carriers that have different mobilities or carrier densities yields a finite magnetoresistance. This property explains the finite magnetoresistance of almost all real metals, which may have scattering rate anisotropies that could be considered as different carriers with different scattering rates that add in parallel, or we might have anisotropies in effective mass, or we might have imbalances in the density of carriers of different species in a metal. All of these can give a finite magnetoresistance, but there are three important general features to note here. One, the magnetoresistance seems to always be proportional to B^2 at very low fields, regardless of any of the details. Two, except in very exceptional circumstances like perfect electron-hole carrier balance, the magnetoresistance saturates at high fields. We note here that some of the giant magnetoresistance metals are essentially simple metals with perfect electron-hole balance [180]. Three, there may be a very narrow range of B-linear magnetoresistance arising from semiclassical motion of electrons, but it is more accurately described as a crossover regime between B^2 behavior at low fields and saturation at high fields.

Shockley tube integrals

The previous discussion was focused on isotropic Fermi surfaces, where the scattering time, effective mass, or carrier density may vary between different Fermi surfaces. However, how do we deal with situations in which the Fermi surface itself is anisotropic? The curvature of

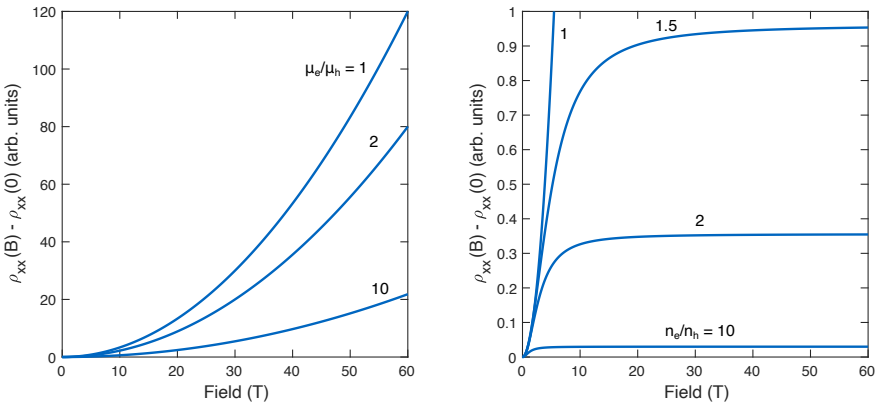

Figure 3.2: **Magnetoresistance of two carrier model varying relative mobilities and densities**

the Fermi surface, the effective mass, the local carrier density, and the scattering time can change as a function of momentum. After all, as we discussed earlier, one of the motivations for studying magnetotransport in metals was to experimentally determine the shape of the Fermi surface by measuring magnetoresistance and changing the direction of the magnetic field with respect to the crystallographic axes and current direction. To this end, the Shockley tube integral was developed [183].

Within the relaxation time approximation, the formula for magnetoconductivity can be expressed as a "tube integral", the form of which was originally derived by Shockley. When an electric field is applied to the Fermi surface, states parallel to the electric field are accelerated. The linear-order response of the distribution function is given by

$$-eV/\hbar^3 \frac{\partial f}{\partial \epsilon} \mathbf{E} \cdot \mathbf{v} d^3k = \frac{-eV}{h^3 k_B T} f(1-f) \mathbf{E} \cdot \mathbf{v} \frac{d^3k}{(2\pi)^3}. \tag{3.20}$$

Application of magnetic field produces flow along the Fermi surface. The current produced by the electric and magnetic fields can be calculated by integrating the expression above over angle across the constant energy contour of the Fermi surface in the relaxation time approximation. Thus the electric field and current are linearly related through an integral over the Fermi surface. This integration yields the Shockley tube integral formula [115]

$$\sigma_{\alpha\beta} = \frac{e^2}{4\pi^3\hbar^2} \int dk_H \frac{m_c}{\omega_c} \int_0^{2\pi} d\psi' \int_0^{\infty} v_\alpha(\psi', k_H) v_\beta(\psi' - \psi, k_H) e^{-\psi/\omega_c \tau(\psi)}, \tag{3.21}$$

where α and β are two orthogonal directions in the plane perpendicular to the magnetic field. Generally, they are chosen to correspond to crystallographic directions or appropriately

rotated crystallographic directions. k_H is the direction of momentum along the magnetic field vector. m_c is the effective mass, and ω_c is the cyclotron frequency of a given orbit. v in all cases is the velocity defined at the Fermi surface. ψ is the azimuthal angle in the plane perpendicular to the magnetic field vector. This equation essentially represents the solution of the Boltzmann equation in the presence of magnetic field and under the relaxation time approximation. Of course, here the scattering time may vary across the Fermi surface, but critically, the relaxation-time approximation is still used. That is, a scattering event is assumped to completely randomize the quasiparticle momentum. This need not be the case when scattering is anisotropic, so one needs to exercise caution in applying this formula where $\tau(\psi)$ is assumed to be a function of azimuthal angle.

Kohler's rule

One interesting observation that results from the arguments in the previous section is a simple scaling relation. Under the relaxation time approximation, the Shockley tube integral tells us that the changes in conductivity in a magnetic field essentially only depend on the quantity $\omega_c\tau$. So for example, if we were to take a piece of metal and measure the magnetoresistance $\Delta\rho(B)/\rho(0)$, which is defined to appropriately normalize out physical constants which affect the zero field resistivity, and then take another same piece of metal with slightly more disorder, the difference in magnetoresistance beteween the two could essentially be captured by taking into account the changes in scattering rate induced by the disorder. Essentially, when $\Delta\rho(B)/\rho(0)$ is plotted against $B/\rho(0)$ (an experimental proxy for $\omega_c\tau$), then the magnetoresistance curves of a metal with the same intrinsic properties but varying levels of disorder scattering will collapse onto one plot. This relation is known as Kohler's rule [191].

Strictly speaking, the intention of Kohler's rule is the above experiment, where one takes the same piece of metal and varies the disorder level in the metal. Often in the literature, Kohler's scaling attempts are made as a function of temperature (where it is assumed that temperature changes the scattering rate in a similar way to increasing the disorder level). There is no reason to assume that varying the temperature is equivalent to varying the disorder level from the point of view of quasiparticle scattering, as increasing the temperature could increase the scattering rate more on certain points on the Fermi surface than others. One can tell from the Shockley tube integral that if the angle-dependence of $\tau(\psi)$ changed, certainly this factor could not be normalized out into the simple Kohler's scaling relation. Thus, as described earlier, Kohler's rule only applies to situations where the scattering rate overall increases or decreases, but not to situations where the pattern of scattering anisotropy changes, or to cases where the relaxation-time approximation is invalid. While not rigorously true, the opposite is also often true — if a material's magnetoresistance obeys Kohler's rule when the scattering rate is isotropically varied, then we can be pretty confident that the magnetoresistance has an orbital origin within the relaxation time approximation, and its properties can very likely be described accurately by the Shockley tube integral.

Model of turning points in antiferromagnetic $BaFe_2(As_{1-x}P_x)_2$

Fermi surface in the antiferromagnetic state

With respect to the previous chapter, it is clear that a full understanding of electron transport, and particularly magnetotransport, requires knowledge of the Fermi surface structure. The Fermi surface of the non-magnetic phase of $BaFe_2(As_{1-x}P_x)_2$ has been well characterized in the literature. It is composed of quasi-cylindrical electron and hole Fermi surfaces, as depicted schematically in Fig. 3.3A [200, 182, 54, 52, 222, 151, 55]. In the AFM ordered phase (for phosphorous content $x < 0.31$), the Fermi surface reconstructs due to the interaction between the electrons or holes and spin-density wave fluctuations. One way to visualize this is to imagine that the electron and hole Fermi surfaces are displaced by the antiferromagnetic ordering vector, and due to the spin-density wave interaction, a gap opens at points on the points of overlap between the electron and hole Fermi surfaces. Following this logic, a simplified cartoon of the AFM reconstructed Fermi surface is shown in Fig. 3.3B. In fact, while the real Fermi surface of $BaFe_2(As_{1-x}P_x)_2$ in its AFM phase is somewhat more complicated than depicted in the cartoon in Fig. 3.3B due to the presence of multiple electron and hole pockets, the cartoon captures many of the salient features of the calculated and observed Fermi surface in AFM $BaFe_2(As_{1-x}P_x)_2$ [101, 139]. In particular, note that the reconstructed Fermi surface is composed of banana-shaped pockets, with regions of large Fermi surface curvature at the corners. This feature, which is also seen in calculations and experimental measurements of the Fermi surface, and will prove to be extremely meaningful with regards to the magnetotransport response of the material.

Finally, it is important to comment on the presence of the orthorhombic structural distortion which occurs at nearly the same temperature as the AFM transition in $BaFe_2(As_{1-x}P_x)_2$ [224, 94, 62]. Such a distortion should in principle reduce the symmetry of the material from 4-fold to 2-fold with a commensurate reduction in the symmetry of the Fermi surface. In bulk samples, however, the presence of twin domains will restore an average 4-fold symmetry to the sample [199, 217, 150]. In any case, many of the following arguments would apply to the properties of a single twin domain of AFM Ba-122 as well, which has a set of two (rather than 4) banana-shaped pockets in its Fermi surface [217, 150].

Shockley tube integral around the Fermi surface of AFM $BaFe_2(As_{1-x}P_x)_2$

The models for orbital magnetoresistance in the presence of anisotropic quasiparticle spectra, particularly in the iron-pnictide metals, were developed in Refs. [105, 106]. See also Ref. [123] for more details about this section. As discussed in the previous section, sharp 'turning points' in the Fermi surface, as seen in the banana-shaped pockets of the AFM state of Ba-122, can induce a linear-in-field magnetoresistance response. As a quasiparticle undergoes orbital motion in a magnetic field, the Fermi velocity is rapidly reversed at these turning points [105]. This mechanism produces an H^2 variation of the MR at low fields, which crosses over to linear variation at higher fields as the number of quasiparticles pushed through the turning point by the Lorentz force linearly increases with field [105, 154]. Note that this

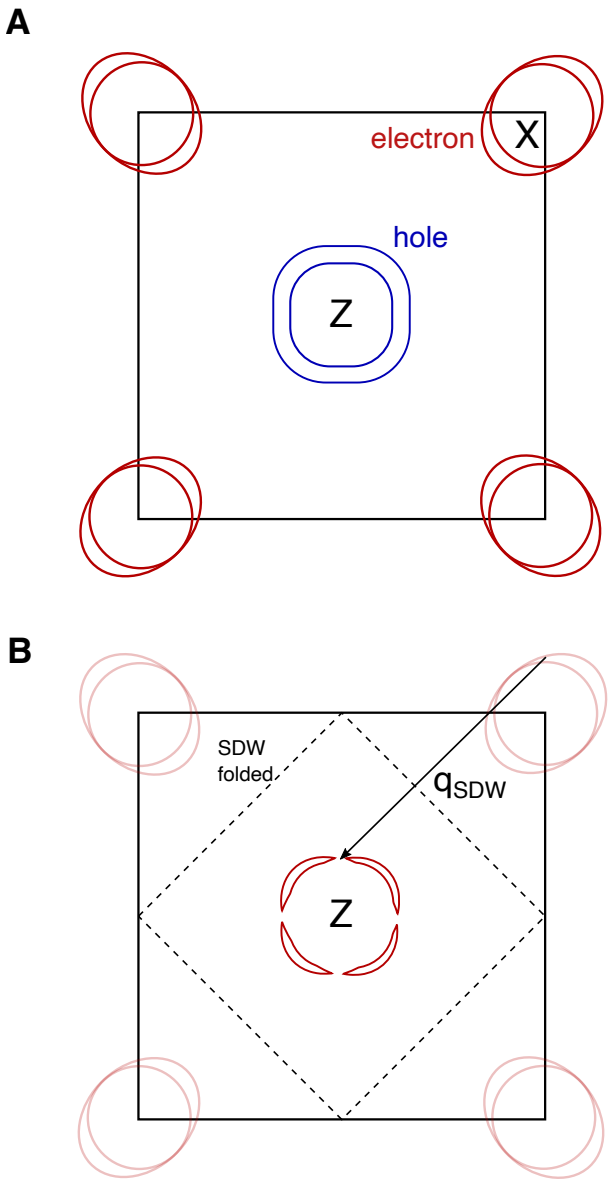

Figure 3.3: **Cartoon Fermi surface of Ba-122 through a characteristic k_z cut** (A) in the non-magnetic state. It is composed of two hole-like cylinders at the zone center, and two electron-like ones at the corner. (B) In the AFM SDW state, the Brillouin zone is folded perpendicular to the AFM ordering vector q_{SDW}, resulting in a nesting of the electron and hole cylinders. A gap opens due to the SDW interaction between the two, leading to banana-shaped pockets at the zone center, which can be electron- or hole- like (or have both) depending on the strength of the AFM interaction. In this example, it is shown what the electron-like reconstructed Fermi surfaces look like.

contribution coexists with the conventional MR of the rest of the Fermi surface, which is expected to be much smaller than the turning-point MR because of the relatively much lower Fermi surface curvature on the regions away from the turning-points.

This model was developed in Ref. [105]. The result is calculated within the relaxation time approximation for the Boltzmann equation. The calculation of the magnetoconductivity is carried out in the Shockley 'tube integral' representation. The α, β component ($\alpha, \beta = x$ or y) of the conductivity tensor is given by

$$\sigma_{\alpha\beta} = \frac{2e^2}{\hbar^2} \sum_{\text{bands}} \frac{dp_z}{(2\pi)^3} S_{\alpha\beta}(p_z), \tag{3.22}$$

where $S_{\alpha\beta}$ is a contribution from a single representative p_z slice of the Fermi surface, and

$$S_{\alpha\beta} = \frac{c}{\hbar e H} \int \frac{dp}{v} v_\beta \int_p \frac{dp'}{v'} v'_\alpha \exp\left(- \int_{p'}^{p''} \frac{dp''}{v''} \frac{c}{eH\tau} \right). \tag{3.23}$$

Here, v and p are Fermi velocities and momenta integrated along the Fermi surface, and τ is the scattering time. In general, τ may have a dependence on p, and in this case strictly speaking the relaxation time approximation and the Shockley tube integral Eq. 3.23 are both invalid — the full Boltzmann equation should be used. Nevertheless, some useful insights can be gained from the relaxation time model in the low temperature limit where the scattering time τ is isotropic. In particular, one important point that we are trying to get across is that resistivity can be H-linear as a result of only the shape of the Fermi surface, and need not arise from an anomalous scattering rate or other anomalous dynamical properties. Although, as we will see in the next section, an H-linear resistivity can also arise from an anomalously anisotropic scattering rate in the context of the full Boltzmann calculation.

Eq. 3.22 implies that a single slice in p_z is representative of the conductivity of the whole Fermi surface. This assumption would be exactly correct if the Fermi surfaces of $BaFe_2(As_{1-x}P_x)_2$ were perfectly two-dimensional cylinders extending along the z-direction of the Brillouin zone. The real calculated Fermi surfaces of AFM Ba-122 have significant dispersion and warping along the k_z direction, but at least for our purposes the two-dimensional approximation is useful for capturing qualitative features in the experimental magnetoresistance data.

The resulting reduced conductivity is given by the following formula

$$S_{xx}(H) - S_{xx}(0) = -\frac{8\left(v_{h,x} - v_{e,x}\right)^2 \tau_{\text{tp}} \Delta_{\text{tp}}}{\hbar v_h v_e \sin\theta_{\text{tp}}} \mathcal{B}(h), \tag{3.24}$$

where Δ_{tp} is the size of the AFM gap, τ_{tp} is the quasiparticle scattering time in the vicinity of the turning point, and

$$H_{\text{tp}} = \frac{2c\Delta_{\text{tp}}}{e\tau_{\text{tp}} v_h v_e \sin\theta_{\text{tp}}} \tag{3.25}$$

is the field scale. $\mathbf{v}_h$ and $\mathbf{v}_e$ are the Fermi velocities at the nesting points, and $\theta_{\rm tp}$ is the angle between them (nesting angle). $\mathcal{B}(h)$ is a dimensionless function of the reduced field parameter, $h = H/H_{\rm tp}$, given by

$$\mathcal{B}(h) = -\int_0^\infty dx \int_0^\infty dy \exp(-y) \times \left(\frac{x^2 - h^2 y^2/4}{\sqrt{(x+\frac{h}{2}y)^2+1}\sqrt{(x-\frac{h}{2}y)^2+1)}} - \frac{x^2}{x^2+1} \right). \tag{3.26}$$

with asymptotics $\mathcal{B}(h) \simeq \frac{3\pi}{16}h^2$ for $h \ll 1$ and $\simeq h - \frac{\pi}{2}$ for $h \gg 1$. This function is plotted in Fig. 3.4. It can be well approximated by a hyperbola function ($\mathcal{B}(h) \approx \sqrt{1+h^2} - 1$). Eqs. 3.22, 3.24, and 3.26 determine the behavior of the magnetoconductivity, $\sigma_{xx}(H) - \sigma_{xx}(0)$.

We consider the magnetoresistivity now. In the regime of small magnetoconductivity $|\sigma_{xx}(H) - \sigma_{xx}(0)|, \sigma_{xy}(H) \ll \sigma_{xx}(0)$, the magnetoresistivity is given by $\rho_{xx}(H) - \rho_{xx}(0) \approx -[\sigma_{xx}(H) - \sigma_{xx}(0)]/\left[\sigma_{xx}(0)\right]^2 - \left[\sigma_{xy}(H)\right]^2/\left[\sigma_{xx}(0)\right]^3$. Due to the large Fermi surface curvature, the turning-point term exceeds both conventional diagonal and Hall contributions. Combining Eqs. 3.22 and 3.24 for $\sigma_{xx}(H) - \sigma_{xx}(0)$ and using the multiple-band Drude formula $\sigma_{xx}(0) = e^2\tau(n_h/m_h + n_e/m_e)$, we obtain

$$\rho_{xx}(H) - \rho_{xx}(0) \approx r_{\rm tp}\mathcal{B}\left(H/H_{\rm tp}\right). \tag{3.27}$$

with the coefficients

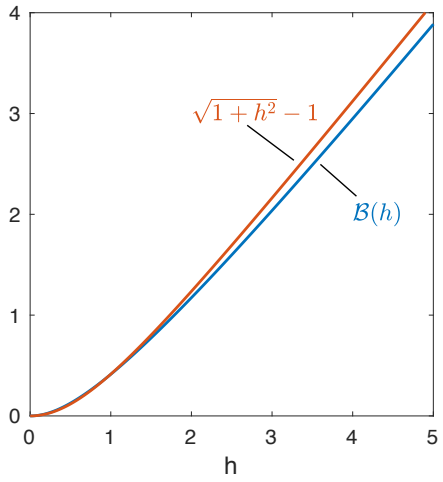

Figure 3.4: **Scaling magnetoresistance function ($\mathcal{B}(h)$) from turning-point model.** The blue line is the dimensionless function $\mathcal{B}(h)$ from the turning-point model. The orange line is a hyperbola, which provides a good approximation of the exact mathematical expression.

$$H_{\rm tp} = \frac{2c\Delta_{\rm tp}}{e\tau_{\rm tp}(v_h v_e \sin\theta_{\rm tp})}, \tag{3.28}$$

(in CGS units), and

$$r_{\rm tp} \approx \frac{4\left(v_{h,x}-v_{e,x}\right)^2 \tau_{\rm tp}\Delta_{\rm tp}}{\pi^2 e^2\hbar^2\tau_{\rm cold}^2 s v_h v_e \sin\theta_{\rm tp}\left(\frac{n_h}{m_h}+\frac{n_e}{m_e}\right)^2}. \tag{3.29}$$

$\Delta_{\rm tp}$ is the size of the AFM gap and $\tau_{\rm tp}$ and $\tau_{\rm cold}$ are the quasiparticle scattering rates in the vicinity of the turning point and in the background, $m_{e,h}$ are effective masses, which are approximately the same for the hole and electron bands [200, 182, 54, 52, 222], $n_{e,h}$ are the band carrier densities, and s is the c-axis lattice parameter. $\tau_{\rm tp}$ need not be equal to $\tau_{\rm cold}$ because the scattering rate can be anisotropic due to scattering on AFM fluctuations. $\mathbf{v}_{h,e}$ are the Fermi velocity on the hole and electron band, and $\theta_{\rm tp}$ is the nesting angle. The dimensionless function $\mathcal{B}(h)$ computed in Ref. [105] has asymptotics $\mathcal{B}(h) \simeq (3\pi/16)h^2$ for $h \ll 1$ and $\mathcal{B}(h) \simeq h$ for $h \gg 1$ This function is plotted in Fig. 3.4. Note that this contribution to the MR coexists with the conventional contribution from the rest of the Fermi surface, but is enhanced approximately by a factor of $\epsilon_f/\Delta_{\rm tp}$ due to the large curvature at the turning points [105].

Model of hot spots in nearly-antiferromagnetic $BaFe_2(As_{1-x}P_x)_2$

Here we discuss the possibility that orbital motion is interrupted, not by some sort of feature in the Fermi surface as in the previous case, but by an anomaly in the momentum-dependent scattering rate. In the phase diagram of P-substituted Ba-122, when the AFM phase is suppressed to zero temperature by P-substitution (as is the case for $x = 0.31$ $BaFe_2(As_{1-x}P_x)_2$) [79, 124, 181], quantum critical spin fluctuations produce strong quasiparticle scattering, and the turning points evolve into 'hot spots' [106, 162]. The concept of hot spots was first introduced in the physics of cuprate high-temperature superconductors, and found to capture a number of their properties [75, 195].

In this regime of Ba-122, quasiparticles experience scattering induced by incipient spin fluctuations at points where the electron and hole Fermi surfaces are nested by the antiferromagnetic ordering vector. In this scenario the quasiparticle scattering rate is, by the very nature of its localization to specific k-points, highly anisotropic. As discussed in the previous sections of this chapter, such an anisotropic scattering rate warrants consideration of the full Boltzmann equation without recourse to the relaxation time approximation.

In principle one should solve this equation numerically using finite element methods. However, useful insights can be gained by using an analytical solution with some approximations described in detail in Ref. [106]. First, it is assumed that the scattering rate due to the hot spot follows a Lorentzian lineshape as a function of momentum along the Fermi surface

$$\frac{1}{\tau_s^{\rm hs}(p_s)} \approx \gamma_{\rm hs}\frac{\hbar|v_s^{\rm hs}|w_s/\pi}{p_s^2+w_s^2}, \tag{3.30}$$

where s is the band index, and $\gamma_{\rm hs}$ and w_s are the strength and width of the hot spot

respectively, determined via microscopic spin susceptibility parameters

$$\gamma_{\rm hs} = \frac{3\pi g^2 \gamma (k_B T)^2}{32\hbar^3 |v_s||v_{\bar{s}}| \sqrt{\eta_t(\eta_s\eta_{\bar{s}} - \eta_{s\bar{s}}^2)\alpha_x}}, w_s = \hbar\sqrt{\frac{\alpha_x}{\tilde{\eta}_s}}. \tag{3.31}$$

Here, g is a coupling constant between the conduction electrons and spin fluctuations. α, η, and γ are parameters of the spin susceptibility defined in the following way assuming Gaussian spin fluctuations:

$$\chi_j(\mathbf{q},\omega) = \frac{1}{-i\gamma\omega + \alpha_j + \eta_i q_i^2} \tag{3.32}$$

$$\eta_t = \sum_i \eta_i n_{t,i}^2, \quad \eta_s = \sum_i \eta_i n_{s,i}^2, \text{ and } \eta_{s\bar{s}} = \sum_i \eta_i n_{s,i} n_{\bar{s},i} \tag{3.33}$$

$$\tilde{\eta_s} \equiv \frac{\eta_s\eta_{\bar{s}} - \eta_{s\bar{s}}^2}{\eta_{\bar{s}}} \tag{3.34}$$

The η parameters depend on the local orientation of the hot line. Here, $\mathbf{n}_t$ is the unit vector along the hot line and $\mathbf{n}_s$ are the unit vectors along the electron and hole Fermi surfaces satisfying the conditions $\sum_i \eta_i n_{t,i} n_{s,i} = 0$, which replace the orthogonality conditions in the isotropic case. For the simplest choice, the hot line is oriented along the z-axis with no in-plane anisotropy, and $\eta_x = \eta_y$. Then, $\eta_t = \eta_z$, $\eta_s = \eta_{\bar{s}} = \eta_x$. $\eta_{s\bar{s}} = \eta_x \cos\alpha_{\rm eh}$, and $\tilde{\eta_s} = \eta_x \sin^2\alpha_{\rm eh}$, where $\alpha_{\rm eh}$ is the angle between the electron and hole Fermi surfaces at the hot spot.

The calculation of conductivity at zero magnetic field yields the following results. The total conductivity is a sum of conductivity from the hot spot and the background conductivity:

$$S_{xx} = S_{xx}^{(0)} + S_{xx}^{\rm hs}. \tag{3.35}$$

These are given by

$$S_{xx}^{(0)} = \sum_s \int v_{s,\alpha}^2 \tau_s \frac{dp_s}{\hbar|v_s|}, \tag{3.36}$$

and

$$S_{xx}^{\rm hs} = -\gamma_{\rm hs} \frac{(v_{2,\alpha}^{\rm hs}\tau_2 - v_{1,\alpha}^{\rm hs}\tau_1)^2}{1/r_1 + 1/r_2}, \tag{3.37}$$

where

$$r_s = \frac{1}{\gamma_{\rm hs}} \int \frac{dp_s/\hbar|v_s|}{\tau_s + \tau_s^{\rm hs}(p_s)} \approx \sqrt{\frac{32\hbar^3\alpha_x|v_s||v_{\bar{s}}|\sqrt{\eta_t\eta_{\bar{s}}}}{3g^2\gamma(k_BT)^2|v_s^{\rm hs}|\tau_s}}. \tag{3.38}$$

$s = 1$ or 2 are labels of the nested electron and hole Fermi surfaces, and τ_s is the background scattering time, for example due to scattering from impurities, on each Fermi surface sheet.

The calculation of the conductivity in magnetic field yields the following results. We first introduce the reduced field scale

$$H_{\mathrm{hs},s} = \frac{\hbar c}{|e|}\gamma_{\mathrm{hs}} r_s = \frac{c}{|e|}\frac{\pi\sqrt{3\gamma}gk_BT}{\hbar\sqrt{32|v_s||v_{\bar{s}}||v_s^{\mathrm{hs}}\tau_s\tilde{\eta_s}\sqrt{\eta_t\eta_{\bar{s}}}}}. \tag{3.39}$$

Note the explicit dependence on temperature, T, and background scattering time, τ_s. Then the magnetoconductivity from the hot spot is given by

$$\begin{aligned} S_{xx}^{\mathrm{hs}}(H) - S_{xx}(0) \approx -\gamma_{\mathrm{hs}}(v_{1,\alpha}^{\mathrm{hs}}\tau_1 - v_{2,\alpha}^{\mathrm{hs}}\tau_2)r_1r_2 \\ \times\frac{v_{1,\alpha}^{\mathrm{hs}}\tau_1(1+\mathcal{G}_2)\mathcal{G}_1 - v_{2,\alpha}^{\mathrm{hs}}\tau_2(1+\mathcal{G}_1)\mathcal{G}_2}{r_1(1+\mathcal{G}_1)+r_2(1+\mathcal{G}_2)}, \end{aligned} \tag{3.40}$$

$$\mathcal{G}(h) \approx \frac{1}{\pi}\int_0^\infty dx\,\exp(-x)G\left(\frac{\pi hx}{4}\right) - 1 \tag{3.41}$$

$$G(a) = 4\sqrt{1+a^2}E\left(\frac{a^2}{1+a^2}\right) - \frac{2}{\sqrt{1+a^2}}K\left(\frac{a^2}{1+a^2}\right), \tag{3.42}$$

where E and K are complete elliptic integrals of the second and first kind respectively. $\mathcal{G}_s = \mathcal{G}(H/H_{\mathrm{hs},s})$. The dimensionless function $\mathcal{G}(h)$ follows an approximately hyperbolic dependence on h (Fig. 3.5). We plot $\mathcal{G}(h)$ in Fig. 3.5, and show the good approximation provided by the hyperbola $\sqrt{1+h^2}-1$. This justifies the approximation used in the main text that $\mathcal{G}(h) \sim \sqrt{1+h^2}-1$.

We assume that the electron and hole bands have comparable parameters. $w_1 \approx w_2$, and $|v_1^{\mathrm{hs}}|\tau_1 \approx |v_2^{\mathrm{hs}}|\tau_2$. In this case, we can drop band indices in $H_{\mathrm{hs},s}$ and r_s and arrive at a simplified formula for the magnetoconductivity from the hot spot

$$\delta S_{xx}^{\mathrm{hs}}(H) \approx \frac{-\gamma_{\mathrm{hs}}r}{2}(v_{1,\alpha}^{\mathrm{hs}}\tau_1 - v_{2,\alpha}^{\mathrm{hs}}\tau_2)^2\mathcal{G}(H/H_{\mathrm{hs}}). \tag{3.43}$$

Assuming that the hot-spot contribution dominates the magnetoresistanceand $\tau_1 \approx \tau_2$, we evaluate

$$\rho_{xx}(H) - \rho_{xx}(H=0) \approx r_{\mathrm{hs}}\,\mathcal{G}(H/H_{\mathrm{hs}}) \tag{3.44}$$

with the coefficient

$$\begin{aligned} r_{\mathrm{hs}} \approx& \frac{\gamma_{\mathrm{hs}}r\left(v_{1,x}^{\mathrm{hs}} - v_{2,x}^{\mathrm{hs}}\right)^2}{4\pi^2\hbar e^2 s\left(n_h/m_h + n_e/m_e\right)^2} \\ =& \frac{H_{\mathrm{hs}}\left(v_{1,x}^{\mathrm{hs}} - v_{2,x}^{\mathrm{hs}}\right)^2}{4\pi^2\hbar^2 s|e|c\left(n_h/m_h + n_e/m_e\right)^2}. \end{aligned} \tag{3.45}$$

Plugging in the explicit temperature dependences, H_{hs} is proportional to temperature, with constants of proportionality determined by the spin susceptibility parameters, and the background scattering rate, τ_{cold},

$$H_{\mathrm{hs}} \propto T/\sqrt{\tau_{cold}}. \tag{3.46}$$

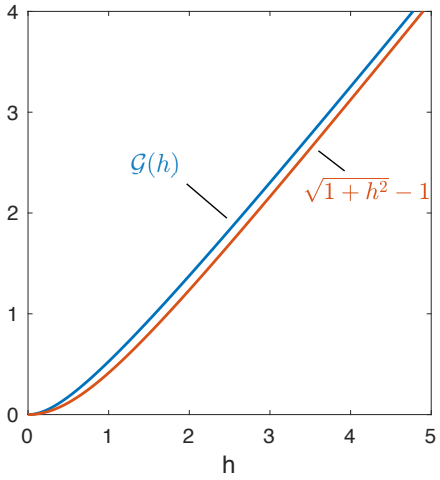

Figure 3.5: **Scaling magnetoresistance function ($\mathcal{G}(h)$) from the hot spot model.** The blue line is the dimensionless function $\mathcal{G}(h)$ from the hot spot model (see text). The orange line is a hyperbola, which provides a good approximation of the exact mathematical expression.

In a magnetic field, the effect of hot spots on orbital magnetoresistance is similar to that of the turning points [106, 165]

$$\rho^{\text{hs}}(H) - \rho(0) = r_{\text{hs}}\mathcal{G}\left(H/H_{\text{hs}}\right). \tag{3.47}$$

The parameters in the hot-spot model, r_{hs} and H_{hs}, are determined by critical spin fluctuations rather than an AFM gap. Both these parameters scale in the same way with temperature and background scattering time

$$H_{\text{hs}} = \Gamma_H \frac{T}{\sqrt{\tau_{\text{cold}}}},\ r_{\text{hs}} = \Gamma_r \frac{T}{\sqrt{\tau_{\text{cold}}}}. \tag{3.48}$$

The coefficients Γ_H and Γ_r depend on the spin-susceptibility and electronic-band parameters. $\mathcal{G}(h)$ is a dimensionless function with a slightly different exact form compared to the turning-point model in Eq. 3.27, but qualitatively similar behavior (Fig. 3.6). Note that, unlike in the turning-point model, the characteristic field scale H_{hs} is determined by the strength of scattering at the hot spot and its region of influence as compared to the background scattering rate, τ_{cold}. Thus, changes to this rate are expected to affect the characteristic field scale in the critical regime.

Finally, the scaling form of both the turning-point MR [Eq. 3.50] and the hot spot MR [Eq. 3.47] can be well-approximated by a hyperbola (Fig. 3.6)

$$\mathcal{B}(h), \mathcal{G}(h) \approx \sqrt{1+h^2} - 1 \tag{3.49}$$

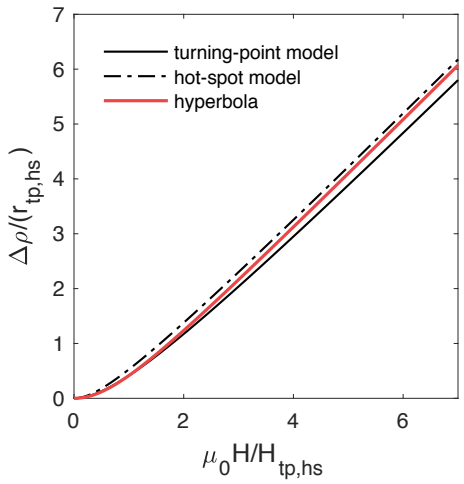

Figure 3.6: **Hot-spot and turning-point magnetoresistance scaling functions and comparison with hyperbola** The MR ($\Delta\rho = \rho(H) - \rho(H = 0)$) in both the turning-point and hot-spot models is controlled by two parameters ($r_{\mathrm{tp,hs}}$ and $H_{\mathrm{tp,hs}}$; tp and hs indicate turning-point and hot-spot respectively). The MR from the hot-spots or turning-points follows scaling functions (black lines) with exact expressions given in the previous sections. Note that both functions are well-approximated by a hyperbola $\Delta\rho/r_{\mathrm{tp,hs}} = \sqrt{1 + (H/H_{\mathrm{tp,hs}})} - 1$ (red line), a phenomenological model which has been previous used to analyze the magnetoresistance of several nearly-antiferromagnetic compounds.

This will prove useful when exploring the data in the context of hyperoblic MR scaling and its relation to these models.

3.6 Experimental magnetoresistance of $BaFe_2(As_{1-x}P_x)_2$ with applied theoretical model

"With four parameters I can fit an elephant, and with five I can make him wiggle his trunk!" — *Enrico Fermi*

Parent compound $BaFe_2As_2$

The parent compound $BaFe_2As_2$ is nonsuperconducting and has an antiferromagnetic transition at $T_N \approx 135$K [166]. Its fermiology is well established [200, 54, 52, 151], and previous measurements have reported H-linear MR in this compound [84]. Here, we explore the MR of an as-grown single crystal in the context of the turning-point model to show that the model reproduces the experimentally observed MR.

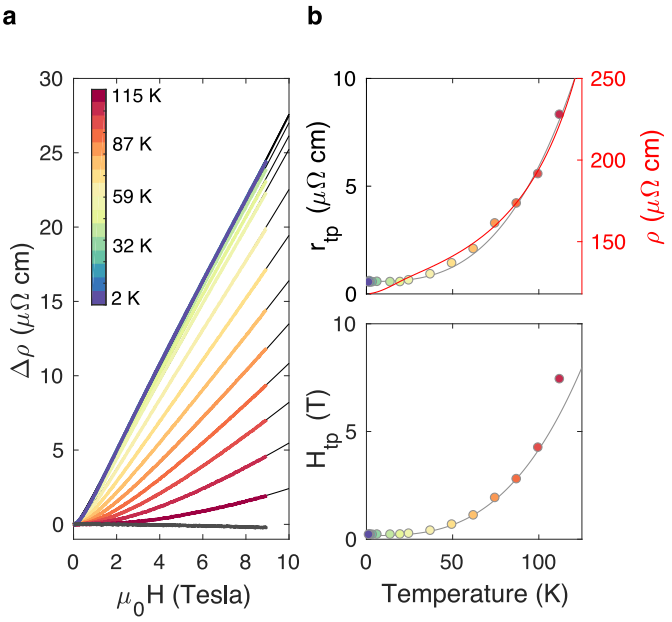

Figure 3.7: **Transport in $BaFe_2As_2$ and magnetoresistance model based on turning points** (a) Isothermal magnetoresistance at various temperatures. Black lines are fits to the turning-point model given by Eq. 3.27. (b) Model parameters extracted from the fits; error bars are smaller than the data points. The grey lines show that both parameters vary with T^3 with a finite offset. The red line shows that the zero-field resistivity similarly varies approximately with T^3, suggesting that the MR parameters vary with the scattering rate.

Fig. 3.7 shows the temperature-dependent MR of $BaFe_2As_2$. The MR is clearly H-linear at high fields, consistent with previous observations [84]. We see that the data are well-

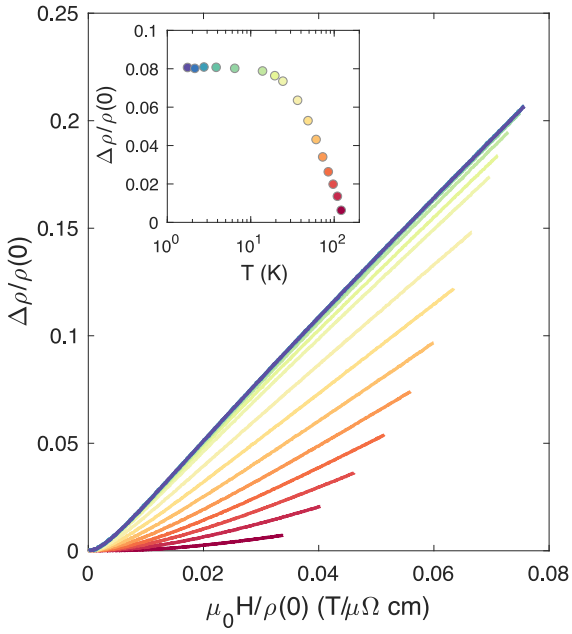

Figure 3.8: **Kohler's rule in $BaFe_2As_2$** Relative magnetoresistance versus reduced field for different temperatures. The inset shows the temperature dependence of the relative MR at a reduced field of $\mu_0 H/\rho(0) = 0.03T/\mu\Omega$ cm.

fitted by the turning-point model given by Eq. 3.27. The two parameters, $r_{\rm tp}$ and $H_{\rm tp}$, saturate at low temperature and grow with increasing temperature, mimicking the behavior of the resistivity at zero-field. This suggests that the changes to the MR coefficients r_{tp} and H_{tp} reflect the temperature-induced enhancement of the scattering rate as suggested by Eq. 3.28 and Eq. 3.29. At low temperature, both MR parameters saturate, suggesting a single dominant scattering rate which is independent of temperature, likely due to disorder. Indeed, in Fig. 3.8, we observe that the MR amplitude saturates below 10K. The failure of Kohler's rule as temperature increases can be attributed to temperature-induced anisotropic scattering due to spin-waves [205] in combination with a potentially temperature-dependent AFM gap.

The dominant role of isotropic disorder scattering at low temperature allows us to evaluate the plausibility of the model parameters. Using the known values of carrier density and effective mass ($n_e = 1.17 \times 10^{20} cm^{-3}$, $n_h = 1.23 \times 10^{20} cm^{-3}$, and $m \approx 2m_e$ for both electrons and holes) [200], the Drude estimate of the residual scattering time is $\tau = \tau_{\rm cold} = \tau_{\rm tp} = 3 \times 10^{-13} s$ ($\rho_0 \approx 100 \mu\Omega cm$). The previously quoted values of Fermi velocity vary between $0.5 \times 10^7 cm/s - 2.5 \times 10^7 cm/s$ [52, 6, 151]. With the Drude scattering time above, Eq. 3.28 gives an AFM gap of $\Delta \approx 1$ meV using the low-temperature $H_{\rm tp} \approx 0.2$T and a Fermi velocity of $v_F \approx 2 \times 10^7 cm/s$ [6]. This is considerably lower than the AFM gap $\Delta \approx 10 meV$

expected for the transition temperature of 135K, but at least consistent within an order of magnitude. Better agreement is found if the relevant scattering time is in fact lower than the Drude estimate ($\sim 10^{-12}s$), which is a possibility considering that the Drude estimate may be inaccurate for this multiband system. Alternatively, there may be a deeper reason for the relatively small effective gap at the turning point. Parity constraints cause the hybridization between hole and electron bands to vanish at $k_x = 0$ [55]; because the turning points are close to this axis, this could result in a suppression of the effective AFM gap near the turning point.

On a final note, while approximately H-linear MR can exist over a narrow range of field in compensated metals such as $BaFe_2As_2$ [154], this effect is only expected to occur close to the high-field limit when $\omega_c\tau = eH\tau/mc \approx 1$. From the above considerations, we estimate that $\omega_c\tau = 1$ at 40T in this sample. The experimental MR therefore becomes H-linear well below the conventional high-field limit.

Underdoped $BaFe_2(As_{1-x}P_x)_2$ with x = 0.19

Here, we examine a single crystal of $BaFe_2(As_{1-x}P_x)_2$ with $x = 0.19$, where the antiferromagnetic Néel transition temperature is $T_N \approx 95$K. In Fig. 3.9, transport data are shown for this crystal. Fig. 3.9a shows that the resistivity at zero applied field varies with T^2 over a broad range of temperature inside the AFM ordered state with a finite intercept at $T = 0$. At this composition, the resistivity is likely influenced by anisotropic quasiparticle scattering from diffuse spin fluctuations [213, 205].

Fig. 3.9b shows the MR inside the AFM state which displays H-linear behavior at high fields. Note that the measured relative MR just below T_N is a factor of 12 larger than the MR just above T_N, suggesting that the turning points again provide a dominant contribution to the measured MR. We therefore neglect the conventional MR contribution when modeling the data. The data are well fitted by the turning-point model given by Eq. 3.27 with the temperature-dependent parameters shown in Fig. 3.9c. Again, the MR parameters follow a similar temperature dependence to that of the zero-field resistivity, suggesting the MR parameters vary with the scattering time. The amplitude of the MR and characteristic field are slightly different in this composition than in $BaFe_2As_2$. This can likely be attributed to changes in the AFM gap or scattering time induced by P-substitution. Unfortunately, the fermiology is not well established at this composition, but assuming comparable parameters to the parent compound, these measurements are in the low-field limit of orbital MR (i.e. $\omega_c\tau \ll 1$).

We find that a hyperbolic MR scaling can be derived from our model at this composition. From Fig. 3.9c, we observe that the offsets of $H_{\text{tp}} = \gamma T^2 + \gamma_0$ and $r_{\text{tp}} = \beta T^2 + \beta_0$ are relatively small compared to the temperature dependence over the measured range, and can be neglected (at the lowest measured temperature 20K, $\beta_0/\beta T^2 \approx 0.3$, and $\gamma_0/\gamma T^2 \approx 0.1$). Plugging in $\rho(0) = \rho_0 + \alpha' T^2$, $H_{\text{tp}} \approx \gamma T^2$, and $r_{\text{tp}} \approx \beta T^2$ into a hyperbolic approximation of

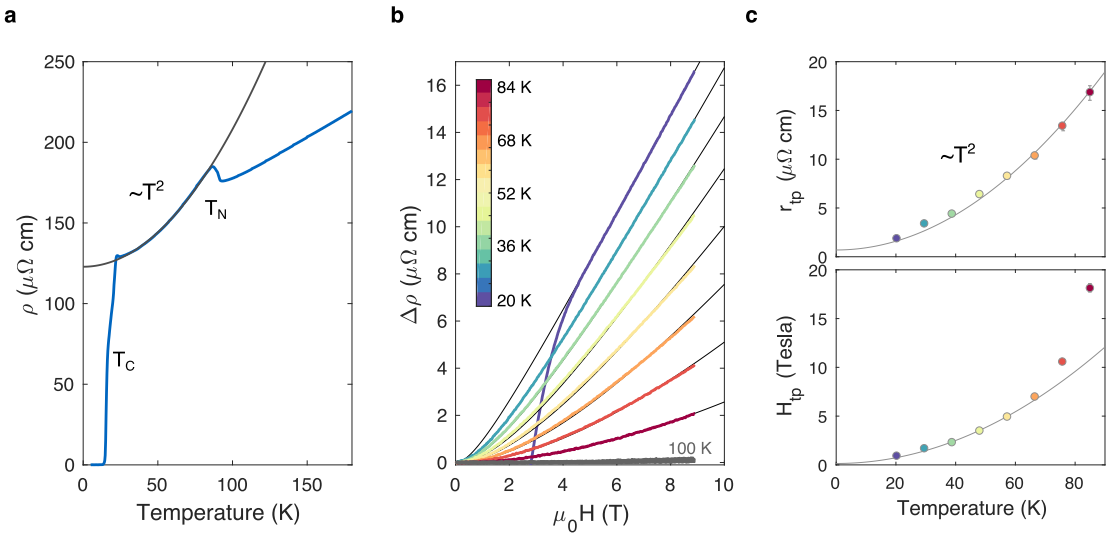

Figure 3.9: **Transport in $BaFe_2(As_{0.81}P_{0.19})_2$ and magnetoresistance model based on turning points** (a) Resistivity shows a transition to an AFM ordered state ($T_N \approx 95K$), and superconducting state beginning at $T_c = 22K$ with zero resistance at $15K$. Inside the AFM state, the resistivity varies with T^2, with a finite $T = 0$ intercept. The data are fitted well by $\rho(H = 0) = 122.8[\mu\Omega cm] + 0.0085[\mu\Omega cm/K^2] \times T^2$ (black line). (b) Magnetoresistance for different temperatures with fits to the turning-point MR model [Eq. 3.27] indicated by black lines. (c) The fit parameters of the model are plotted as a function of temperature, with a best fit line to the data below 70 K. $H_{\rm tp} = 0.098[T] + 0.0015[T/K^2] \times T^2$, and $r_{\rm tp} = 0.69[\mu\Omega cm] + 0.0023[\mu\Omega cm/K^2] \times T^2$.

the turning-point MR [Eq. 3.49], we obtain

$$\frac{\rho(H) - \rho_0}{T^2} \approx \beta \sqrt{1 + \left(\frac{\mu_0 H}{\gamma T^2}\right)^2} + \alpha' - \beta. \tag{3.50}$$

The applicability of this hyperbolic scaling relation to the MR of the x = 0.19 sample is shown in Fig. 3.10a. This is in contrast to the failure of conventional Kohler scaling shown in Fig. 3.10b. The MR scales only with the temperature-dependent scattering rate despite the rather large residual resistivity. The scaling shown in Fig. 3.10a is similar to the established phenomenology [Eq. 3.13] for the MR of quantum critical metals in the literature — the difference is that this is realised in the AFM ordered state rather than the quantum critical regime, and the temperature-dependent resistivity varies with T^2 rather than with T. This is reflected in the different temperature-dependence of the denominator in Eq. 3.50 compared to Eq. 3.13.

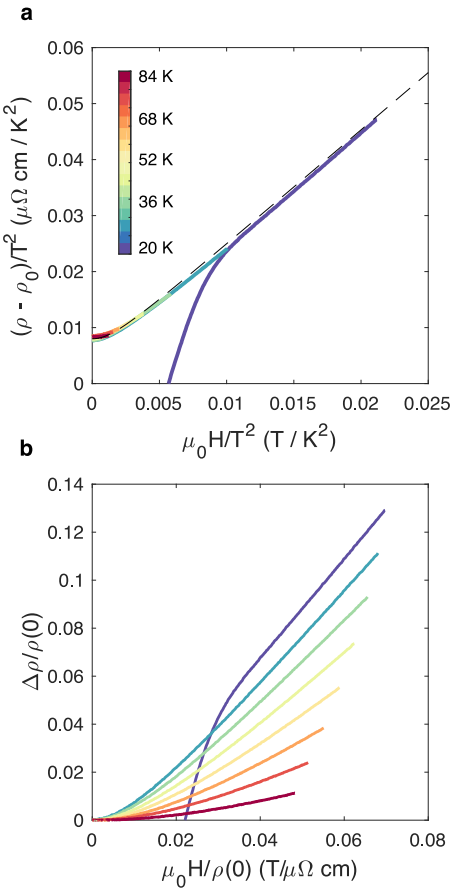

Figure 3.10: **Comparison of hyperbolic magnetoresistance scaling and Kohler's rule inside the AFM ordered state of $BaFe_2(As_{0.81}P_{0.19})_2$** (a) A simple hyperbolic scaling relation holds, where the residual resistivity $\rho_0 = 122\mu\Omega cm$ is first subtracted. The dashed black line is the expression given by Eq. 3.50 with $\beta = 0.0039[\mu\Omega cm/K^2]$, $\alpha' = 0.0085[\mu\Omega cm/K^2]$, and $\gamma = 0.0015[T/K^2]$. (b) Kohler's rule is violated as a function of temperature.

The validity of hyperbolic scaling described by Eq. 3.50, and the failure of Kohler's rule, are rooted in the apparent anisotropy of the scattering rate. In particular, the MR parameters are controlled by the scattering rate at the turning points, and the small offsets of $r_{\rm tp}(T)$ and $H_{\rm tp}(T)$ indicate that the temperature-dependent scattering rate at the turning point is much larger than the temperature-independent residual contribution over the measured range. Thus, the MR is primarily controlled by the temperature dependence independently of the residual resistivity. Quantitatively, we estimate that the inelastic T^2 scattering near the turning point is enhanced by a factor of $[\beta T^2/\beta_0]/[\alpha' T^2/\rho_0] \approx 100$ over the background scattering rate; this is in contrast to the relatively small changes in the overall resistivity $\rho(20K)/\rho_0 \approx 1.03$, which is sensitive to scattering on the whole Fermi surface. The presence of multiple scattering times, one of which is anisotropic, explains the violation of Kohler's rule observed in Fig. 3.10b [191]. It is not surprising that the scattering rate at the turning point is much higher than the background given the presence of diffuse spin fluctuations centered at turning points in underdoped $BaFe_2As_2$ [205]. This implies that the turning point is simultaneously a hot spot, where the turning point MR dominates as long as the region of hot spot scattering is much larger than the width of the turning point. At sufficiently low temperature, spin fluctuations should be damped and the isotropic disorder scattering contribution becomes dominant. We expect the hyperbolic scaling shown in Fig. 3.10 to fail and for Kohler's rule to be restored when $\beta_0/\beta T^2 < 1$ (i.e. at T < 10 K). Unfortunately, the superconducting critical field at this composition makes this temperature regime inaccessible in our measurement apparatus.

Quantum critical $BaFe_2(As_{1-x}P_x)_2$ with x = 0.31

In this sample, the AFM phase is suppressed to zero temperature, and the turning points evolve into hot spots characterized by scattering from critical spin fluctuations [79, 124, 181, 106]. The phenomenological H/T scaling given by Eq. 3.13 is known to describe the MR of this composition [71]. Here, we show that this behavior can be captured by the hot-spot MR model given by Eq. 3.47, as the characteristic parameters are predicted to have a linear variation with temperature. Moreover, as discussed in the theory section, an effective experimental method to test this model in the quantum critical regime is by varying the background scattering rate ($\tau_{\rm cold}$), for example by varying the concentration of defects in the underlying crystal lattice. This is expected to alter the characteristic field scale determining the crossover between H^2 to H-linear MR [Eq. 3.48]. We accomplish this experimentally with 3 MeV alpha particle irradiation of samples with $x = 0.31$ phosphorous substitution. This irradiation method produces isotropic defects with a distribution of radii (from pointlike to nm in radius) [48], which increase the residual resistivity at zero field and temperature. The temperature-dependent resistivity follows a T-linear dependence which is not significantly affected by irradiation (Fig. 3.17).

Fig. 3.11a shows the magnetoresistance for samples in the quantum critical regime with varying concentration of defects. The MR data for each sample across a range of temperatures can be well fitted by Eq. 3.47 and Eq. 3.48. Fig. 3.11b shows that each sample obeys

the hyperbolic H/T scaling form described in the introduction; this scaling is not qualitatively affected by a factor of three increase in the residual resistivity, but there is a notable change in the coefficients of the scaling function.

We show here that H/T MR scaling, and the disorder-dependence of the coefficients, are captured by our hot-spot MR model. As shown in Fig. 3.12, the hot-spot parameters extracted from the fits have the following temperature dependences: $H_{\rm hs} \approx \gamma T$, and $r_{\rm hs} \approx \beta T$, consistent with the theory predictions [Eq. 3.48]. We note that the offsets of $r_{\rm hs}$ and $H_{\rm hs}$ are essentially zero within the error bars, and can be neglected. Using the hyperbolic approximation of the hot-spot MR scaling function, Eq. 3.49, along with $H_{\rm hs} = \gamma T$, $r_{\rm hs} = \beta T$, and $\rho = \rho_0 + \alpha T$, we arrive at the hyperbolic H/T scaling relation

$$\frac{\rho(H) - \rho_0}{T} \approx \beta \sqrt{1 + \left(\frac{\mu_0 H}{\gamma T}\right)^2} - \beta + \alpha. \tag{3.51}$$

Fig. 3.11b shows the validity of this hyperbolic scaling relation. Note that Eq. 3.51 has a similar form to the phenomenological scaling established by Eq. 3.13. We emphasize that this scaling results from the T-linear dependence of hot-spot parameters, which is a direct prediction of our MR model [Eq. 3.48]. In addition, the small offset of $r_{\rm hs}$ manifests the dominant role of inelastic scattering over background disorder scattering at the hot spot over the measured range; this is similar to the situation at x = 0.19, and is an essential property for realizing the hyperbolic MR scaling.

Fig. 3.12 shows the T-linear dependence of the hot-spot parameters extracted from the experimental data in agreement with Eq. 3.48 of the theory. Notably, Fig. 3.12a shows that the characteristic field scale $H_{\rm hs}$ increases as the background scattering rate increases. The square root dependence of this field scale on the disorder scattering rate is consistent with the expectation of the hot-spot model (Eq. 3.48 where $\rho_0 \sim \tau_{\rm cold}^{-1}$). This dependence is reflected in the broadening of the hyperbolic MR as the disorder level increases as shown in Fig. 3.11b. We also observe that the gradient of $r_{\rm hs}(T)$ increases as the disorder level increases in agreement with Eq. 3.48, though the error bars from the fits are comparably larger for this parameter.

We also perform tests of Kohler's rule at fixed temperature where the scattering rate is varied by disorder to further verify the hot-spot model. In Fig. 3.13, we show that at a fixed temperature in $BaFe_2(As_{1-x}P_x)_2$ $(x = 0.31)$, Kohler's rule is violated in the high-field linear magnetoresistance regime, but satisfied in the low-field quadratic regime. The failure of Kohler's rule in the linear magnetoresistance regime at a fixed temperature reflects the fact that the background disorder scattering alters the pattern of scattering anisotropy as predicted by our hot-spot model in Eq. 3.48 and the text surrounding it. This is also consistent with the nontrivial dependence of the characteristic field $H_{\rm hs}$ on disorder (Fig. 3.12a). The validity of Kohler's rule in the low-field quadratic regime confirms the orbital origin of the MR in the quantum critical composition of $BaFe_2(As_{1-x}P_x)_2$. In the low-field limit, the majority of quasiparticles have not yet been pushed into the hot spot (a conservative

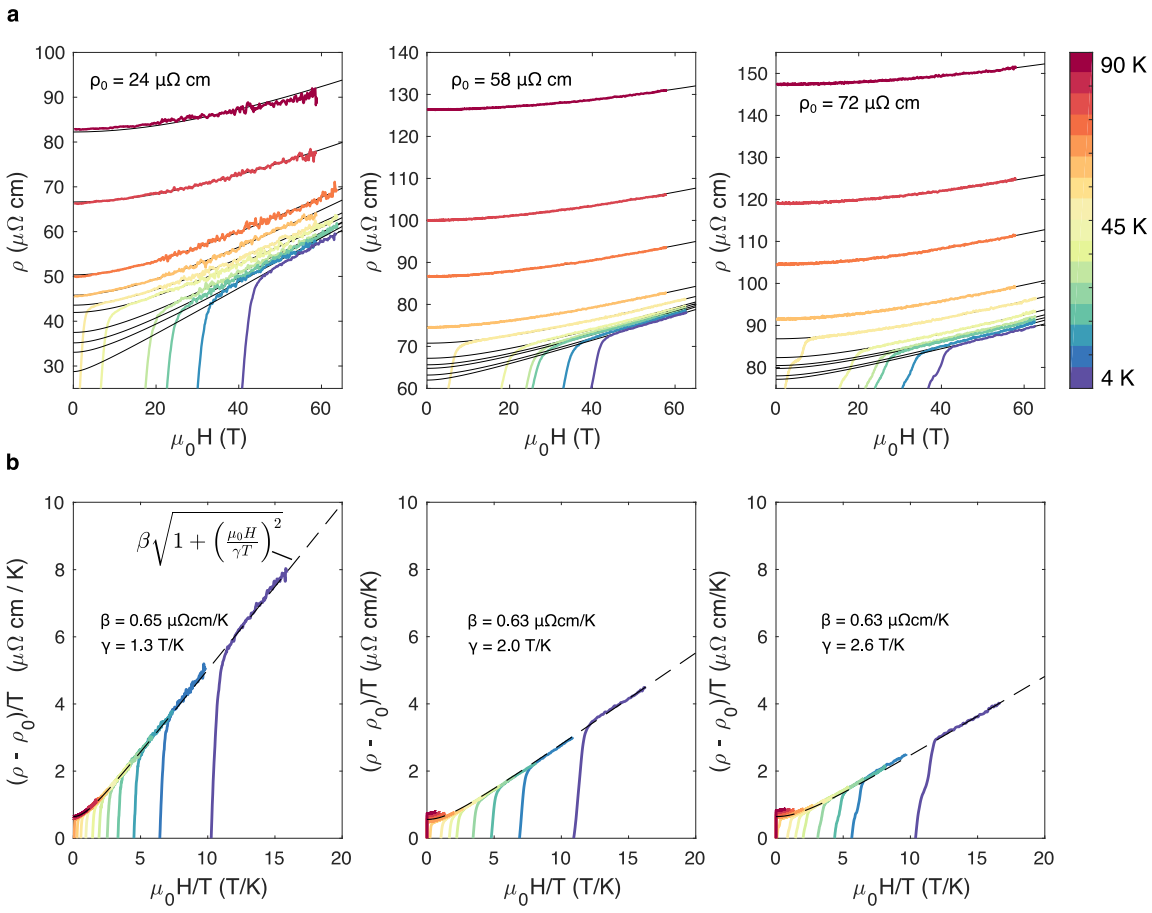

Figure 3.11: **Magnetoresistance, hot spot model, and hyperbolic scaling in $BaFe_2(As_{0.81}P_{0.31})_2$ with varying levels of disorder** (a) The samples show clear H-linear dependence at high fields. Black lines are fits to the hot spot MR model given by Eq. 3.47. Each panel is labeled by the extrapolated zero-temperature resistivity, which quantifies the level of disorder. (b) Hyperbolic scaling of MR for each respective sample. Dashed lines are hyperbolic functions with the parameters shown in each figure.

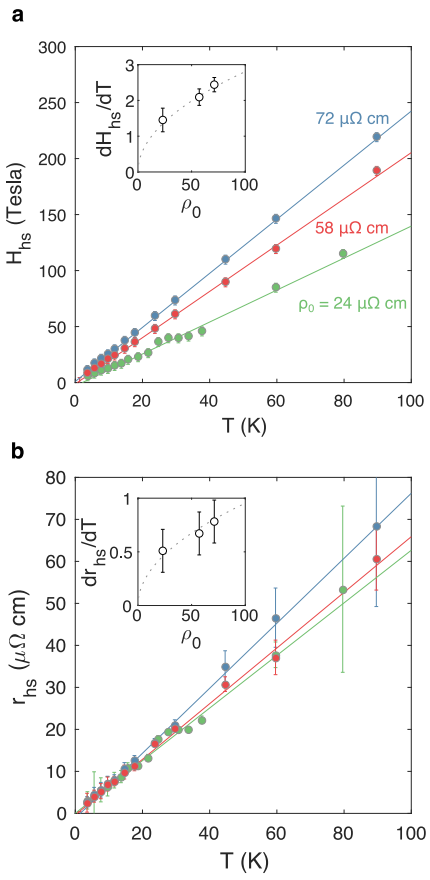

Figure 3.12: **Hot spot parameters in $BaFe_2(As_{1-x}P_x)_2$ with x=0.31** (a) Characteristic field $H_{\rm hs}$ as a function of temperature with a linear fit for each sample. Inset shows the slope of $H_{\rm hs}(T)$ versus the residual resistivity. The dotted line shows the expected $\rho_0^{1/2}$ dependence according to Eq. 3.48 of the hot-spot model. (b) Hot-spot MR amplitude. The inset shows the slope of $r_{\rm hs}(T)$ versus the residual resistivity with a fit to the expected $\rho_0^{1/2}$ dependence. Error bars are derived from the confidence intervals of the hot-spot fits and the linear fits in the present
figure.

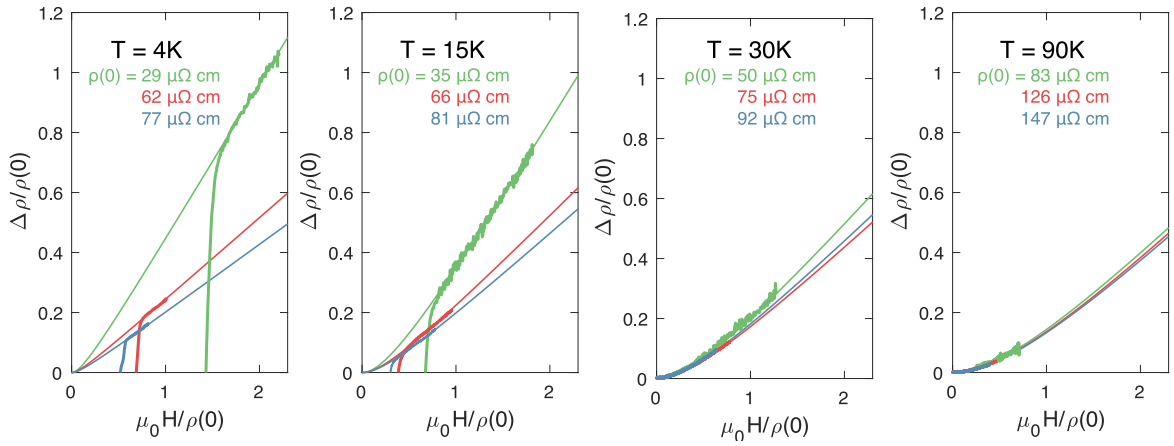

Figure 3.13: **Isothermal Kohler's rule in quantum critical $BaFe_2(As_{1-x}P_x)_2$ x=0.31** A comparison of the isothermal magnetoresistance of separate samples with varying doses of alpha particle irradiation. The violation of Kohler's rule in the linear MR regime suggests that disorder scattering alters the degree of scattering anisotropy in agreement with the hot-spot model. Solid lines are fits to Eq. 3.47, for which the zero-field resistivity is extracted from each trace. The curves are labeled by the resistivity of the sample at zero field at the given temperature. $\mu_0 H/\rho(0)$ is in units of Tesla/$\mu\Omega$cm.

estimate of $\omega_c\tau = 1$ is 100 Tesla), so only a small fraction of a cyclotron orbit has been completed.

The H-linear MR of $BaFe_2(As_{1-x}P_x)_2$ can be understood as a result of orbital motion which is impeded at particular points on the Fermi surface — either due to the presence of a gap (sharp cusp in the Fermi surface) or a hot spot (region of anomalously high scattering rate). In $BaFe_2(As_{1-x}P_x)_2$, both of the aforementioned phenomena are generally understood to arise as a result of the antiferromagnetic coupling between the hole- and electron-like bands, which in the AFM ordered state induce a gap in the single-particle spectrum, and in the paramagnetic state near antiferromagnetism induce quasiparticle scattering.

We have demonstrated this as a viable model of the MR in this material over a wide range of the phase diagram. In the critical regime, spin fluctuations result in a linear increase of the hot-spot scattering with temperature, which underlies the hyperbolic H/T scaling of MR at x = 0.31 [71]. Another important ingredient for realizing hyperoblic MR scaling is that the disorder scattering rate at the hot spot is comparably smaller than the inelastic spin-fluctuation scattering rate, and therefore the MR is primarily controlled by the temperature-dependent resistivity. This interpretation is confirmed by our observation of hyperbolic H/T^2 scaling in $BaFe_2(As_{1-x}P_x)_2$ with x = 0.19 in the AFM regime. Note that this does not imply that ρ_0 is small compared to ρ_t, only that the effect of disorder on the hot-spot scattering rate is small compared to its temperature dependence. Consequently, hyperbolic scaling is

expected to break down and give way to Kohler scaling at the lowest temperature where disorder scattering becomes dominant. We indeed observe a weak deviation from hyperbolic scaling in the most disordered x = 0.31 sample at 1.5 K (Fig. 3.14). Experiments at lower temperatures and sufficiently high magnetic fields to destroy superconductivity are necessary to explore the potential restoration of Kohler scaling in the low-temperature limit.

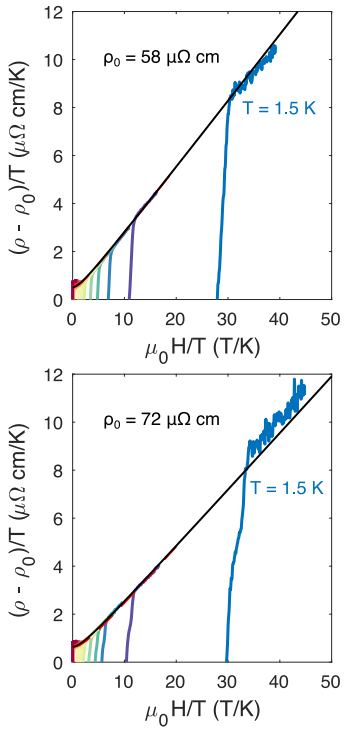

Figure 3.14: **H-T scaling plots from the two most heavily disordered samples of x = 0.31 $BaFe_2(As_{1-x}P_x)_2$** The curves labeled 1.5 K are from magentoresistance traces at the lowest temperature measured. A weak deviation from the H-T scaling function is observed at 1.5 K in the sample with a residual resistivity of 72 $\mu\Omega cm$.

Our study shows that the temperature dependence of the hot-spot or turning-point parameters is strongly influenced by the P-substitution level (Figs. 3.7b, 3.9c, and 3.12). For example, the temperature scaling of the characteristic field goes from T^3 to T^2 to T-linear, following a similar trend as the zero-field resistivity, as the P concentration tunes the system towards the critical point at $x = 0.31$. This may reflect the character of spin excitation scattering and AFM gap as a function of P-substitution. In particular, neutron scattering experiments show that the well-defined spin waves of $BaFe_2As_2$ become increasingly diffusive spin fluctuations as the material is doped [205]. It is likely that diffusive spin fluctuations result in a relatively high scattering rate at the hot-spots/turning-points at x = 0.19 and x = 0.31, which contributes to the onset of hyperbolic scaling at those composition. This is in

contrast to the parent compound $BaFe_2As_2$ where the spin waves are sharply-defined [205], and the hyperbolic scaling fails (see Fig. 3.15. Notably, it is thought that the diffusive spin fluctuations at moderate doping levels also provide a pairing mechanism for superconductivity [205, 216], and therefore it would be interesting to explore the possible correlation between hyperbolic MR scaling and superconductivity in $BaFe_2(As_{1-x}P_x)_2$ [171]. The present study shows that MR measurements may be useful for probing hot-spot properties across the P-substituted phase diagram. This could provide valuable quantitative information as to how spin excitations influence the resistivity and ultimately superconductivity in iron-based superconductors [216]. Note that compositions of $BaFe_2(As_{1-x}P_x)_2$ also undergo a tetragonal-to-orthorhombic distortion when cooling through T_N. The resulting twin boundaries in single crystals are expected to induce temperature-independent scattering, which can be parametrized by the disorder scattering rate in our model.

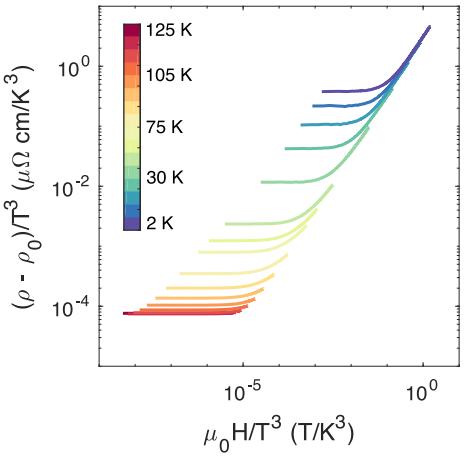

Figure 3.15: B/T^3 **scaling in $BaFe_2As_2$ magnetoresistance data** The simple scaling relation between field and temperature does not seem to describe the magnetoresistance data of the parent compound $BaFe_2As_2$

Experimental considerations and irradiation

"It sounds easy enough. When can we meet to discuss or do the irradiation?" — Yeonbae Lee

Monte Carlo (SRIM) calculations were performed using the material parameters of $BaFe_2(As_{1-x}P_x)_2$, and 3MeV alpha particles. The average penetration depth of 3MeV particles is about 7μm, as shown in Fig. 3.16C. For distances lower than 7μm, the distribution of collision events seems to be largely independent of distance. These simulations indicate that, by cleaving the samples to thicknesses smaller than 7μm, we can mitigate the risk of gross inhomogeneity in the samples after irradiation. In addition, we can ensure that a significant portion of the sample is disordered such that the bulk transport properties are intrinsically meaningful.

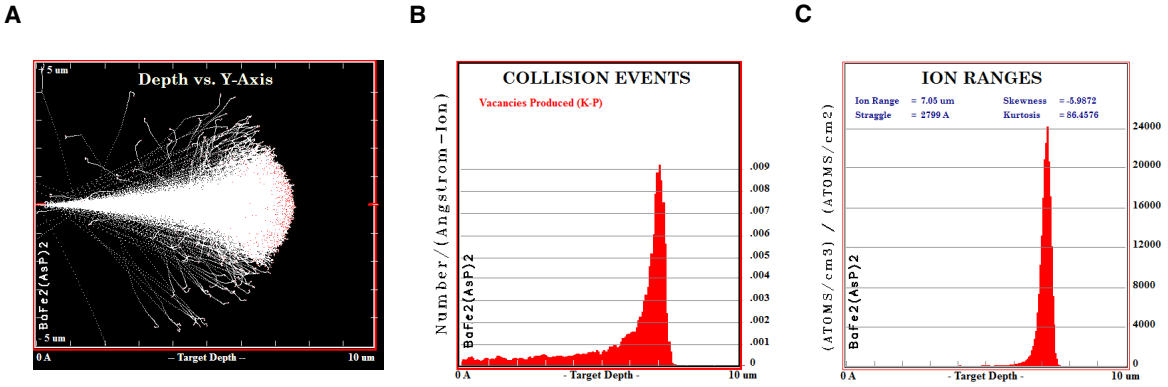

Figure 3.16: **Monte Carlo (SRIM) calculations of the penetration depth profile of 3 MeV alpha particles in $BaFe_2(As_{1-x}P_x)_2$ A** Simulated particle trajectories in a two-dimensional slice. **B** Collision event profile as a function of distance. **C** Profile of ion depth. Particles penetrate on average 7μm into $BaFe_2(As_{1-x}P_x)_2$.

Samples were super glued to a glass slide, and thin sheets were cleaved off with a scalpel blade. Electrical connections to the sheets were made by masking the samples with GE varnish, sputtering gold contact pads, removing the GE mask, and attaching gold wires to the gold pads with H20E silver epoxy. The thickness of the samples was checked using a confocal microscope, and samples with thickness significantly greater than 6 um were discarded. Overall about 20 devices were prepared and screened using this method. The resistance of several samples was then measured from 1.8K to 300K in a commercial QuantumDesign PPMS. In order to account for variation in the geometrical parameters between samples, a scaling factor was applied to each sample based on its un-irradiated room temperature resistance.

The samples were then taken to the Rutherford Backscattering Beamline at Lawrence Berkeley National Lab. The beam accelerates alpha particles with 3 MeV energy through a variable-radius aperture. An aperture diameter of 4mm was used for these experiments. The exposure time to the beam controls the total irradiated charge per unit area, measured in C/cm^2. Each sample was electrically grounded to a carbon tape-coated backing plate, and then exposed to the beam for between 0 and 200 seconds in 20 second intervals (to mitigate the heating effects of the beam). After this process, the resistance of the samples was measured again from 1.8K to 300K in the PPMS. Select samples were wired for pulsed field measurements, as described in Appendix A. Special care was taken to never heat the irradiated samples above room temperature in order to avoid annealing them.

Fig. 3.17a shows resistivity measurements of $BaFe_2(As_{1-x}P_x)_2$ with $x = 0.31$. Samples were homogeneously irradiated by alpha particles by varying exposure time to the alpha particle beam. A larger dose of alpha particles (in units of particles per centimeter squared; p/cm^2) increases the density of defects in the crystal. Notably, increasing the dose causes the resistivity of the sample to increase by a temperature-independent constant as shown in Fig. 3.17b, at least over the temperature range where resistance measurements are possible above the superconducting transition temperature. The average temperature-dependent slope of the resistivity is largely unaffected by the dosage.

In Fig. 3.17c, we show the effect of alpha particle irradiation on the superconducting transition temperature. The data is compared to a naive application of the Abrikosov-Gorkov model assuming an $s\pm$ pairing scenario [20], where only intraband disorder scattering is pair-breaking.

$$-\ln(t_c) = \psi\left(\frac{1}{2} + \frac{g}{2t_c}\right) - \psi\left(\frac{1}{2}\right), \tag{3.52}$$

where ψ is the digamma function, and

$$g = \frac{\Delta\rho_0}{C}\frac{\hbar}{2\pi k_B T_c^0 \mu_0 \lambda_0^2} \tag{3.53}$$

is a dimensionless scattering rate calculated from the irradiation-induced changes to the residual resistivity ρ_0, and penetration depth measurements, λ_0, taken from Refs. [70, 146]. The resistivity is proportional to the total scattering rate ($\Delta\rho_0$), while pair-breaking is only due to interband scattering, which constitutes a small fraction of the total scattering rate in general. Therefore, we introduce the coefficient C in Eq. (3.53), which takes into account the ratio of the interband scattering rate to the total scattering rate. We find that a constant of $C = 0.15$ gives a good fit to the data (Fig. 3.17c), suggesting that about 15% of the total scattering rate induced by disorder is interband scattering.

3.7 Experimental magnetoresistance of $FeSe_{1-x}S_x$

"I'll have a cruciferous legume — John Singleton"

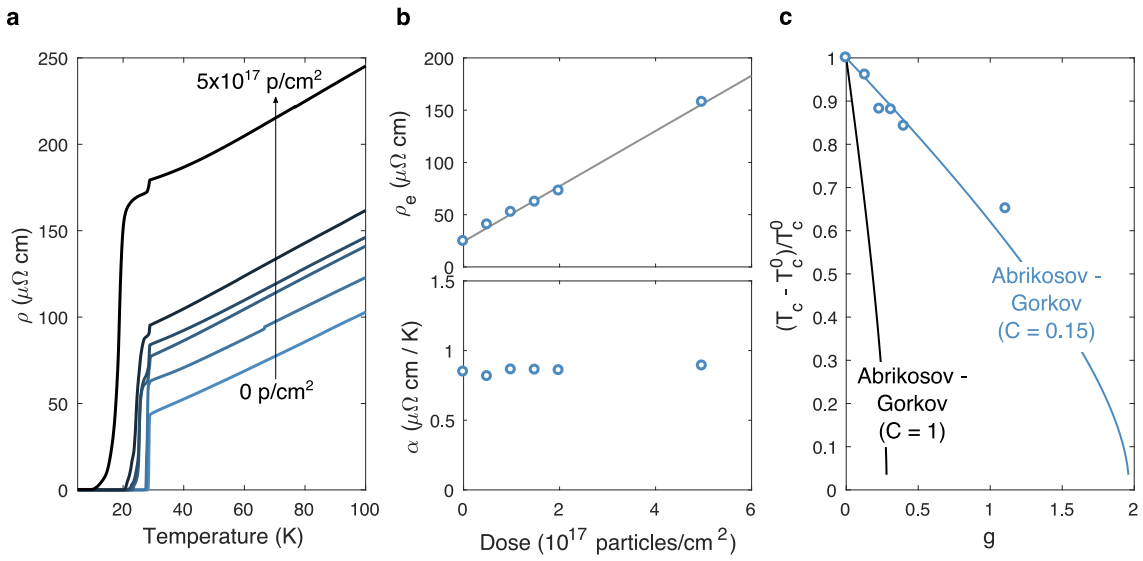

Figure 3.17: Transport and superconductivity in $BaFe_2(As_{0.69}P_{0.31})_2$ irradiated with 3 MeV α-particles (a) Resistance versus temperature in samples with varying doses of α-particle irradiation. The two-step feature in the superconducting transition likely arises from the regions under the measurement terminals, which are protected from the irradiation by gold leads, and therefore go superconducting before the irradiated part of the sample does [36]. (b) Residual resistivity ($\rho(T \to 0) = \rho_e$), evaluated from a linear fit to the resistance from T_c to 80 Kelvin. The solid grey line shows the linear increase of the residual resistivity with the irradiation dose. The slope of the resistivity versus temperature, $\alpha \approx 0.8$ $\mu\Omega$cm/K, is relatively constant as a function of irradiation dose. (c) Suppression of T_c (lower transition) plotted against the normalized scattering rate g (see main text). $T_c^0 = 28.8$ K is the superconducting transition temperature of the pristine sample. The black line shows the expectation of the Abrikosov-Gorkov model assuming all scattering is pair-breaking ($C = 1$). The blue line shows the result of Abrikosov-Gorkov where 15% of the induced scattering is pair-breaking ($C = 0.15$).

The mechanism proposed in the previous section, essentially that of impeded orbital motion — either through a sharp Fermi surface feature or a singularity in the scattering rate — seems to be rather general. One might wonder whether a similar result is obtained in systems which are not necessarily magnetic, but may have other sources of scattering anisotropy in their Fermi surfaces. Indeed, there are several non-Fermi liquid metals, or strongly correlated electron metals, which have been observed to exhibit B-linear magnetoresistance, and it might be useful to explore whether the behavior in such systems can be explained by a similar orbital mechanism to the one discussed in the previous sections. In this section, we address one such material which is nearly-nematic, rather than nearly-antiferromagnetic. In the next section we address other potential material systems where similar experimental magnetoresistance phenomenology is observed.

To give some more background, $BaFe_2(As_{1-x}P_x)_2$ is not only thought to be close to an antiferromagnetic quantum critical point, but also a 'nematic' quantum critical point. The proximity to a nematic quantum critical point [110] suggests nematic fluctuations could also affect the resistivity [112, 216, 37, 50, 51]. As a useful comparison for exploring this possibility, an excellent material to study is $FeSe_{1-x}S_x$. $FeSe_{1-x}S_x$ is not magnetic at any composition (though the material is certainly close to a magnetic phase, and exhibits evidence of magnetic fluctuations [25]). Nevertheless, the notion of non-Fermi liquid transport behavior is very well-established in this compound, and is believed to originate from a quantum critical point. In particular, pristine FeSe undergoes a tetragonal to orthorhombic structural transition when cooled below about 100 Kelvin. This is sometimes referred to as a "nematic" phase, because such a transition breaks the rotational symmetry of the tetragonal lattice without reducing the translational symmetry. When selenium is replaced by sulfur, the structural transition temperature is suppressed to zero temperature at a fractional sulfur concentration of about 0.18-0.19, and evidence of non-Fermi liquid physics is observed at this nearly-nematic phase boundary [38], where there is a putative quantum critical point of the nematic order parameter. A phase diagram as a function of chemical composition is shown in Fig. 3.18. Superconductivity is present at low temperature in all compositions.

Here we primarily focus on transport measurements of $FeSe_{1-x}S_x$, especially chemical compositions very close to the critical endpoint of $x \approx 0.18$. Crystals of $FeSe_{1-x}S_x$ were grown by a KCl flux growth technique. One of the complications of working with KCl as a flux is that the potassium will evaporate at high temperature and attack the quartz glass, causing it to rupture. A solution to this issue is to seal the crucible in a quartz tube of 0.75 mm radius, and then seal the ampoule in a secondary larger quartz tube. The outer ampoule contains the contents of the growth in the event that the inner ampoule ruptures. The rationale for using KCl is the very low melting temperature — Fe_7Se_8 tends to form when Fe and Se in roughly 1:1 ratio are together heated above about 770^{o}C. Fe and Se are both reasonably soluble in KCl. In the KCl growth process, the melting occurs at 840^{o}C, but after cooling, the crystals are annealed at 400^{o}C for 24 hours in order to stabilize the $FeSe_{1-x}S_x$ alloy.

The charge is first heated to 840 over 8 hours. Then it is held at 840^{o}C for 30 hours, cooled to 820^o over 1 hour, cooled to 770^o at 0.5^{o}C/hour, cooled to 400^{o}C over about 10

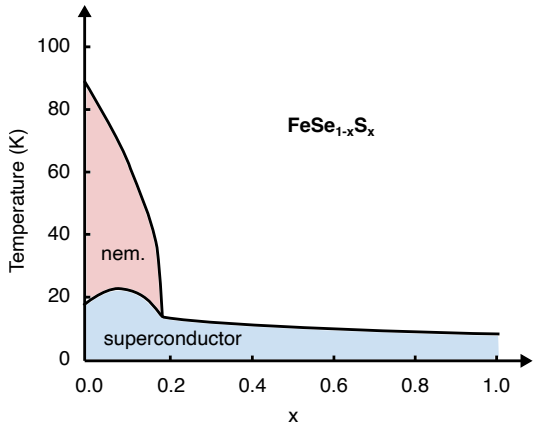

Figure 3.18: **Phase diagram of sulfur-substituted FeSe** The nematic phase ("nem."), which is really an orthorhombic structural distortion of the crystal lattice, is suppressed to zero temperature by substitution of sulfur for selenium. The phase diagram is reproduced from Ref. [38]. At the endpoint of $x \approx 0.18$, the nematic phase is fully suppressed to zero at a putative nematic quantum critical point. Note that superconductivity is present at low temperature in all compositions of this phase diagram.

hours, held at 400^{o}C for 24 hours, and cooled to room temperature over 2-3 hours. This recipe was adapted from the literature [119]. The crystals can be separated from the salt flux by hand, or the salt can be washed away with distilled water. Note that this growth recipe produces lower quality crystals (as measured by the residual resistivity) than the more prevalent $AlCl_3$/KCl eutectic melt technique [116].

We confirmed the chemical composition of growths produced using the above technique using energy dispersive X-ray spectroscopy. Transport results are shown here for the sample of $x = 0.18$ sulfur concentration, the one which is nominally closest to the zero-temperature endpoint of the nematic phase. As seen in Fig. 3.19A, at this composition, non-Fermi liquid transport behavior is observed at low temperatures just above the superconducting transition. The resistivity scales linearly with temperature over this range. This behavior is well-established in this compound. Motivated by the results in the previous sections of this chapter, we explored the magnetoresistance of this material to look for similarities with $BaFe_2(As_{1-x}P_x)_2$ and other putative quantum critical metals.

Samples were measured in pulsed magnetic fields up to 60 Tesla using techniques similar to those described in the other sections of this chapter. Fig. 3.19B shows that the magnetoresistance of $FeSe_{0.82}S_{0.18}$ at this putative nematic quantum critical point exhibits B-linear magnetoresistance at low temperature, which continuously crosses over to B^2 behavior at higher temperatures. This overall trend is extremely similar to that observed in $BaFe_2(As_{1-x}P_x)_2$ near a putative antiferromagnetic quantum critical point, but here we

are dealing with a nematic quantum critical point.

Finally, Fig. 3.19C shows that the magnetoresistance data in this sample obeys a qualitatively similar scaling form as the other samples explored in this chapter. This fairly definitively shows two things. One, the observation of linear magnetoresistance is not necessarily solely a consequence of antiferromagnetism, or antiferromagnetic fluctuations. Two, an explanation for the linear-in-B scaling behavior must be flexible enough to capture both the trend observed in $BaFe_2(As_{1-x}P_x)_2$ (an antiferromagnetic quantum critical point) and that observed in FeSe substituted with sulfur (a nematic quantum critical point).

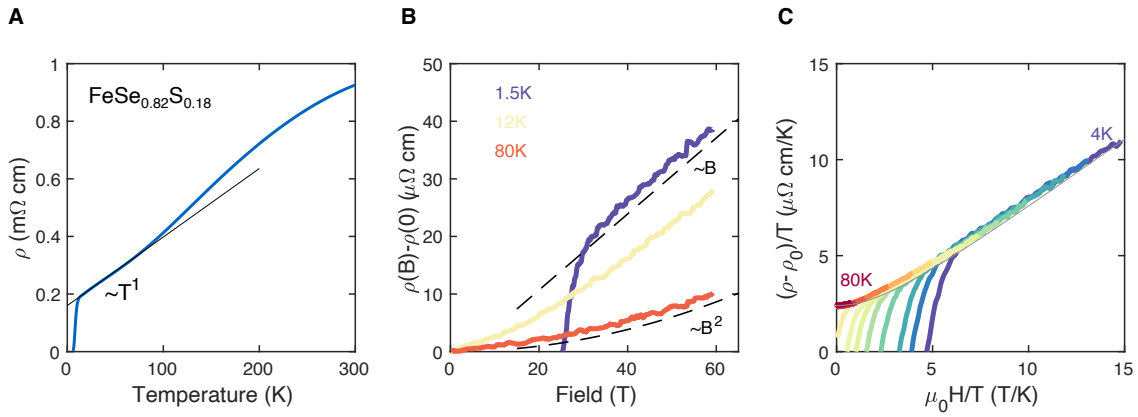

Figure 3.19: **Magnetotransport in $FeSe_{0.82}S_{0.18}$ near a nematic quantum critical point**
A Resistivity versus temperature at this composition exhibits non-Fermi liquid T-linear resistivity just above the superconducting transition temperature. **B** The high-field magnetoresistance ($\rho - \rho(0)$), where $\rho(0)$ is the measured or extrapolated resistivity at zero magnetic field at each temperature, is linear in field at low temperatures, and becomes more quadratic in field as temperature increases. The dashed lines illustrate the high-field limiting behavior. **C** The data obey a scaling relation between field and temperature. $\rho_0 = 181.6\mu\Omega cm$ is the zero-field, zero-temperature residual resistivity extrapolated from panel A. The scaling observed here, and the overall linear-in-field magnetoresistance at low temperatures, is extremely similar to that observed in $BaFe_2(As_{1-x}P_x)_2$.

While our $BaFe_2(As_{1-x}P_x)_2$ model naturally captures several features in the experimental MR over a wide range of the phase diagram, it seems that the influence of the nematic order on the MR can be neglected in that compound. On the other hand, as seen in this section, $FeSe_{1-x}S_x$ near a putative nematic QCP [78] shows very similar MR to that of $BaFe_2(As_{1-x}P_x)_2$ [116]. There are a few possibilities. It is possible that the nearby magnetism in $FeSe_{1-x}S_x$ has a strong influence on the MR and the present hot-spot model is applicable to that material [22, 57]. Another option is that nematic fluctuations effectively

create hot spots in $FeSe_{1-x}S_x$ [112]. One very interesting observation to note is that there appears to be a combination of B-linear and B^2 contributions to the MR in very clean samples of $Fe(Se_{1-x}S_x)$ [116]. A straightforward interpretation is that the orbital magnetoresistance associated with cold and hot spots on the Fermi surface add in parallel. The latter induces a hyperbolic dependence of the MR on H which survives even in the presence of relatively high rates of disorder scattering, as seen in the $BaFe_2(As_{1-x}P_x)_2$ samples in the previous sections and the $FeSe_{1-x}S_x$ sample measured in this section. The former, on the other hand, is a more conventional orbital contribution to the magnetoresistance, which is enhanced as the mobility (i.e. purity) of the samples is increased. This might explain why an apparent conventional B^2 contribution to the MR is observed in relatively pure samples of $FeSe_{1-x}S_x$. The sample used in the present study is rather dirty relative to those grown by other techniques, and so the B-linear term dominates in the presence of high disorder. However, the differences between $BaFe_2(As_{1-x}P_x)_2$ and $FeSe_{1-x}S_x$ should be explored further.

3.8 Possible generalizations

Given that the hot-spot model accurately captures the MR of $BaFe_2(As_{1-x}P_x)_2$ and the H/T scaling, it is likely that the AFM fluctuations are the source of the anomalous T-linear resistivity in the quantum critical regime of $BaFe_2(As_{1-x}P_x)_2$. However, while the hot-spot regions are expected to give a correction to the conductivity that is linear in T, at zero-field the cold parts of the Fermi surface are expected to dominate [75]. Within a nearly-antiferromagnetic Fermi-liquid framework, one option is that mixing of hot spot and disorder scattering leads to nontrivial behavior of the overall resistivity [164, 165]. Such a scenario is thought to describe the resistivity of $CePd_2Si_2$, as discussed in the earlier sections of this chapter. Our data on $BaFe_2(As_{1-x}P_x)_2$ is difficult to reconcile with such a mechanism for temperatures above T_c — disorder adds a temperature independent component to the resistivity consistent with Matthiessen's rule, which can only occur if the temperature-dependent scattering is independent of disorder. However, at such high temperatures it is possible that the hot spots are smeared out enough that they essentially cover the whole Fermi surface and lead to a more isotropic scattering rate. This possibility is consistent with the fact that the magnetoresistance at temperatures above about 30K, where T-linear resistivity at zero field is observed, is more or less B^2 in agreement with orbital motion in the presence of isotropic scattering. Moreover, Kohler's rule is obeyed in this relatively high temperature regime. In order to further explore the possibility that the T-linear resistivity in $BaFe_2(As_{1-x}P_x)_2$ arises from hot spot scattering, it would be necessary to examine the disorder-dependent resistivity at very low temperatures to see possible changes in the power law scaling as the disorder level is varied.

There are other possibilities as well. Other nearly-antiferromagnetic Fermi-liquid models show that magnetic fluctuations at hot spots can influence the overall resistivity through multiple scattering [26], or the so-called backflow effect [102]. A more recent revival of the hot-spot picture has shown that an unconventional two-particle scattering process connecting

hot and cold regions can render the entire Fermi surface a 'marginal' Fermi liquid with an overall T-linear resistivity [136]. A theory of orbital MR in a marginal Fermi liquid would be an interesting extension of the present study.

Finally, linear-in-B magnetoresistance has been observed in several classes of cuprate superconductors, including, but probably not limited to LCCO (electron-doped cuprate and nearly-antiferromagnetic metal) [171], and LSCO (hole-doped cuprate) [60].

In regards to LCCO, hot spots at the antinodal regions of the Brillouin zone of the electron-doped cuprates have been suggested as a source of anomalous behavior in transport and photoemission measurements for some time [13, 104], so in light of our results, the recent observations of H-linear magnetoresistance in electron-doped cuprate superconductors may be interpreted as a result of antiferromagnetic fluctuations at hot spots. The model pertaining to $BaFe_2(As_{1-x}P_x)_2$ can likely be readily adapted to the Fermi surface and scattering rate anisotropy present in electron-doped cuprates. This picture of an anisotropic scattering rate would also explain a long-standing question regarding the violation of Kohler's rule observed in the cuprates [69]. Moreover, scaling behavior with the cotangent of the Hall angle has been observed in many quantum critical metals, the so-called 'modified' Kohler's rule [103, 88], and we leave to future work whether this can be captured in the present hot-spot model.

In regards to LSCO, the hole-doped cuprate, it is not necessarily the case that antiferromagnetic hot spots are present in this compound. However, the material is close to a van Hove singularity, which could induce a higher quasiparticle scattering rate that is momentum-dependent — the van Hove points touch the Fermi level at certain parts of the Brillouin zone before others. From an orbital magnetoresistance point of view, such an ansiotropic scattering rate could in principle induce a B-linear contribution to the magnetoresistance in a qualitatively similar way as antiferromagnetic hot spots. In fact, such a picture of orbital motion was recently put forward to explain the linear magnetoresistance of LSCO [16].

All together, it seems plausible that the presence of B-linear magnetoresistance observed in many strongly correlated electron systems and putative quantum critical materials can be explained by the concept of interrupted orbital motion as described in this chapter [74, 27]. The origin of such interrupted orbital motion could arise through an anisotropic scattering rate, sharp features in the Fermi surface, or even other more exotic mechanisms [74]. While this theory does not explain all aspects of transport data in these materials (in particular, the temperature-dependent resistivity is still an open problem), it gives a satisfying description of the magnetoresistance phenomenology in many different materials from a general standpoint. In addition, perhaps this theory of orbital motion could give a starting point for analyzing magnetoresistance measurements as a probe of Fermi surface and scattering rate anisotropy in complex non-Fermi liquid metals [66], much like the way in which magnetoresistance was originally used to probe the Fermi surfaces of elemental metals in the 1970s.

Chapter 4

Nearly-ferromagnetic metals

We now consider a slightly different problem — that of nearly-ferromagnetic metals. Many of the same general topics that arose in the study of nearly-antiferromagnetic metals — including quantum criticality, breakdown of Fermi liquid theory, and unconventional superconductivity — are also prevalent in nearly-ferromagnetic metals. In some ways, it falls in the same category of problem, where superconductivity can also emerge near a magnetic phase boundary that persists close to zero temperature, and strong electron-electron interactions can destabilize the Fermi liquid. The only difference at face value is that the magnetic phase is ferromagnetic rather than antiferromagnetic.

However, this turns out to be quite an important distinction. The study of nearly-ferromagnetic superconductivity suffers from the problem that there are only a handful of materials where such a phase competition exists. A simple way to understand the rarity of such a phase competition is that superconductivity on general grounds is destroyed by magnetic field, either externally applied, or from magnetic impurities [125]. Antiferromagnetism isn't necessarily in direct opposition to superconductivity because the net magnetic moment in an antiferromagnet is zero when appropriately averaged over some length scale. On the other hand, the net moment in a ferromagnet is by definition nonzero, implying that there is a fundamental incompatibility between a ferromagnetic phase and a superconducting one. But, there are materials where such a coexistence does occur [12].

In addition to the consequences of nearly-ferromagnetic order on the electron fluid in a metal, there are notable consequences on the superconducting state itself. The ferromagnetic spin fluctuations tend to result in electron pairing in the equal-spin pairing channel [49]. That is, the Cooper pair wavefunction, rather than being composed of two electrons in a superposition $|\uparrow\downarrow\rangle - |\downarrow\uparrow\rangle$, which is typical for example in electron-phonon coupling superconductors, can be composed of equal spin states ($|\uparrow\uparrow\rangle$, $|\downarrow\downarrow\rangle$, $|\uparrow\downarrow\rangle + |\downarrow\uparrow\rangle$) [49]. Intuitively, if the Cooper pair spin quantum number is aligned along the magnetic moment of the sample, the pair-breaking effects of the magnetic moment could be significantly reduced compared to the opposite spin pairing scenario; this to some extent explains how this type of superconductivity can survive in the presence of ferromagnetism. Due to symmetry constraints imposed by Fermi statistics, the spatial wavefunction in the equal-spin pairing scenario must

be spatially antisymmetric. Both the finite angular momentum of the Cooper pairs, and the spatial asymmetry of their wavefunctions, have remarkable consequences for the properties of the superconducting state [130]. In addition to their interest as unprecedented phenomena from a physics point of view, some of these properties are considered highly desireable for novel quantum information processing platforms [53]. As a consequence, much of the modern research on this topic concerns itself with the discovery of materials where a phase competition between ferromagnetism and superconductivity is observed.

4.1 The role of weak itinerant ferromagnetism

Recall in the introduction to this text, we briefly mentioned that electron-electron interactions that are beneficial to superconductivity also have a propensity to induce electronic order that is not superconductivity (e.g. ferromagnetism, antiferromagnetism, charge density waves, etc). In certain nearly-ferromagnetic metals, superconductivity can occur as a result of pairing mediated by ferromagnetic fluctuations [49]. The mechanism for this is essentially based on the Coulomb interaction, not the dipole-dipole interaction between spins which is usually much weaker [172]. Equal spin electrons can have an attractive Coulomb interaction as a result of the symmetry constraints of the wavefunction between two electrons in equal or opposite spin states [49].

Ferromagnetic spin-fluctuation-mediated superconductivity like the situation described above has a few criteria. First, generally speaking the attractive interaction will be favorable if the same electrons that make up the Fermi surface are the ones that are ferromagnetic or nearly-ferromagnetic, i.e. the magnetic moment arises from an imbalance in the population of majority and minority spin electrons. As such, the ferromagnetism is considered 'itinerant', in the sense that the net moment comes from itinerant electrons. This scenario can be contrasted with the Heisenberg view of ferromagnetism, where the magnetic moments are largely localized, and develop spontaneous order through exchange interaction with other localized magnetic moments. Second, the strength of the equal-spin attractive interaction is proportional to the spin susceptibility [49]. It is therefore beneficial if the ordered magnetic moment is 'weak' or close to zero (as it could be in nearly-ferromagnetic metals), such that the spin susceptibility is high. Some of these arguments about itinerant magnetism can be put on more precise footing [132, 198, 161, 132]. But the above criteria are essentially consistent with what is observed in nearly-antiferromagnetic superconductors, like iron-based superconductors, where the antiferromagnetic moment is relatively fragile and strongly itinerant [223]. Experiments on U-based nearly-ferromagnetic superconductors also tend to show a correlation between superconductivity and a wewak itinerant magnetic moment [160].

One of the simplest experimental methods to determine 'how itinerant' a ferromagnet is is by measuring the value of the spontaneous moment. In itinerant ferromagnets, the value of the magnetic moment when the sample is fully saturated tends to be much smaller than that expected if the magnetization were to come from the magnetic ions [161]. For example, in an itinerant ferromagnetic containing nickel, we might see a saturated moment on the order

of 0.5 μ_B/Ni, whereas a nickel ion in its most common 2+ oxidation state would produce a magnetic moment closer to 2 μ_B/Ni. The decay of such spin waves at high temperature actually produces a Curie-Weiss susceptibility, even though strictly speaking the local moment picture is not applicable. Rather remarkably, the fluctuating magnetic moment extracted from Curie-Weiss analysis often corresponds well to the free-ion magnetic moment, even though the characteristic $1/T$ dependence of the susceptibility is not strictly speaking coming from local moments. In certain extreme cases, ferromagnetism can arise in metals even though there are naively no magnetic ions in the material (for example, $ZrZn_2$ [219]). The dichotomy between a small saturated magnetic moment, and relatively large high-temperature fluctuating moment, is one of the defining features of itinerant ferromagnetism.

4.2 A candidate for nearly-ferromagnetic superconductivity: magnetic characterization of $NiTa_4Se_8$

With the above arguments in mind, we present here an excellent candidate for nearly-ferromagnetic superconductivity, and then proceed to describe one method by which superconductivity can be induced in this system. The material is $NiTa_4Se_8$, a layered material with conducting $TaSe_2$ layers sandwiched by layers of nickel atoms in a triangular lattice. First, we will describe the basic characterization of this material, which suggest that it is a weak itinerant ferromagnet, making it a strong candidate for nearly-ferromagnetic superconductivity. Then, we will describe how superconductivity can be induced in single crystalline samples by reducing the nickel concentration.

Growth procedure and crystallography

Single crystals were grown by a two-step procedure. First, a precursor was prepared. The elements were combined in a ratio Ni:Ta:Se (0.4:1.0:2.0), loaded in an alumina crucible, and sealed in a quartz tube with 200 torr Argon gas. The tube was heated to 670^{o}C — the boiling point of selenium — for 12 hours, and then the temperature was raised to 900^{o}C and kept there for 5 days. The furnace was then shut off and allowed to cool naturally. This reaction yields a free-flowing black powder that was ground with a mortar and pestle.

Second, the precursor was loaded with 3 mg/cm^3 iodine in a 21 cm long quartz tube, evacuated, and placed in a horizontal two-zone furnace. The precursor and iodine were in zone 1 and the other end of the tube (the growth zone) were in zone 2. Both zones were heated to 850^{o}C for 3 hours to encourage nucleation. Then, zone 2 was kept at 850^{o}C while zone 1 was reduced to 700^{o}C. This condition was maintained for 12 hours to clean the growth zone. Finally, the temperature of zone 1 was raised to 850^{o}C and that of zone 2 was lowered to 700^{o}C. This growth condition was maintained for 5 days after which the furnace was shut

off. Hexagonal crystals up to 5 mm in lateral length were collected from the cold zone. They are easily exfoliated with a scalpel or scotch tape.

Energy dispersive X-ray spectroscopy detects an elemental ratio of 0.25:1.00:1.89 (Ni:Ta:Se), suggesting that the samples used in this study are about 5% selenium deficient. We believe that this deficiency arises due to the vaporization of selenium during the precursor reaction, which could potentially be adjusted for by adding 5-10% excess selenium to the first stage of the growth procedure.

The results of powder X-ray diffraction (PXRD) experiments suggest that $NiTa_4Se_8$ ($Ni_{1/4}TaSe_2$) crystallizes in the P63/mmc structure. These experiments are performed on precursor powder resulting from a solid-state reaction from which single crystals were grown using chemical vapor transport as described in the crystal growth section. The residual between the fitted PXRD pattern and the experimental one seems to mainly originate from an underestimation in the intensities of the peaks in the refinement as compared to the experiment (Fig. 4.1C). Thus, every significant peak of the experimental PXRD pattern can be accounted for using the crystal structures schematically shown in Fig. 4.1A and B. Based on these diffraction experiments, we conclude that the material is composed of layered basal planes of $TaSe_2$ in the 2H polymorphic form, and there are no significant side phases in the precursor powders. $NiTa_4Se_8$ appears to be isostructural to $Fe_{1/4}TaSe_2$ [135] and $MnTa_4S_8$ [209], other doped transition metal dichalcogenides. Between the sheets of $TaSe_2$, the nickel atoms sit between the tantalum atoms in the neighboring layers. The nickel atoms themselves form a trigonal layer with twice the a-axis periodicity of the tantalum atoms. The crystal structure parameters determined from powder X-ray diffraction refinement are $a = 6.878(6)\mathring{A}$ and $c = 12.506(5)\mathring{A}$.

Fig. 4.2 shows the results of low-temperature physical and magnetic properties characterization experiments on single crystal samples. A spontaneous magnetization develops below a Curie temperature of 58K (Fig. 4.2A), as indicated by the splitting of magnetization curves collected with field-cooled and zero field-cooled protocols. The susceptibility ($\chi = M/H$) appears to be slightly larger for magnetic field directed perpendicular to the basal planes — above 100K, the susceptibility anisotropy ratio is approximately independent of temperature $\chi_c/\chi_{ab} \approx 1.3$, indicating that the magnetic moments have a weak preference for the interplanar direction. In addition, a secondary feature appears in the M v T curve at a temperature of $T_{c2} = 36K$, both in the in plane and out of plane directions. This temperature is also associated with a change in curvature in the resistivity-temperature curve (Fig. 4.2B). While the main ferromagnetic-like transition at T_{c1} is clearly resolved in heat capacity measurements, the feature at T_{c2} is not, suggesting that the lower temperature anomaly coincides with a relatively small change in entropy. There more complicated features will be discussed in more detail later.

Because the secondary feature in magnetic susceptibility is rather broad (Fig. 4.2A), and does not seem to be associated with a significant heat capacity anomaly, it is important to address the possibility of possible magnetic impurity phases as a source of this anomaly. The most likely candidates are NiSe [208] and $NiSe_2$ [221] both of which have ferromagnetic ordering temperatures around 20K. However, the secondary feature in susceptibility data on our

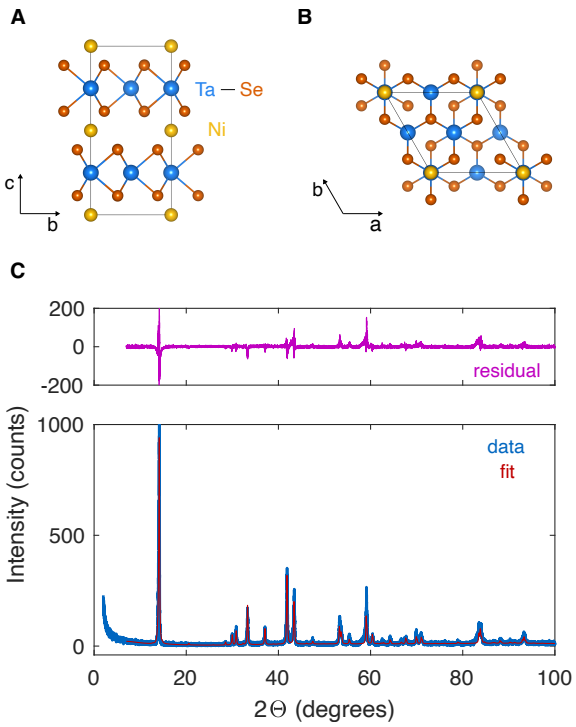

Figure 4.1: **Crystal structure of $NiTa_4Se_8$ A** Crystal structure as viewed along the crystallographic *a*-axis. The unit cell is outlined by black lines, and the crystallographic coordinates are shown in the bottom left. Nickel atoms sit between the $TaSe_2$ layers. **B** Crystal structure viewed along the crystallographic *c*-axis. The tantalum atoms form a triagonal lattice. The nickel atoms similarly form a triangular lattice with twice the periodicity of that of the tantalum atoms. **C** Powder X-ray diffraction data and refinement (fit shown in red) based on the P63/*mmc* space group. The residual (the difference between the data and fit) is shown in pink. The lattice parameters extracted from the PXRD refinement are stated in the text. Each prominent peak present in the PXRD data is captured by the refinement based on the crystal structure represented in panels A and B.

$NiTa_4Se_8$ crystal occurs closer to 35K. In addition, our PXRD data does not show evidence of peaks associated with either NiSe or $NiSe_2$, suggesting that any potential impurity phases constitute an undetectably small fraction of the samples. And, susceptibility measurements on this powder also show a main ferromagnetic transition at 58K and a secondary anomaly at about 36K in agreement with the data on single crystal samples (Fig. 4.3). In addition, the resistivity (Fig. 4.2B) of single crystal samples exhibits a broad crossover feature across 35K. For these reasons, we believe the 35K crossover is an intrinsic feature of $NiTa_4Se_8$, which certainly warrants further study.

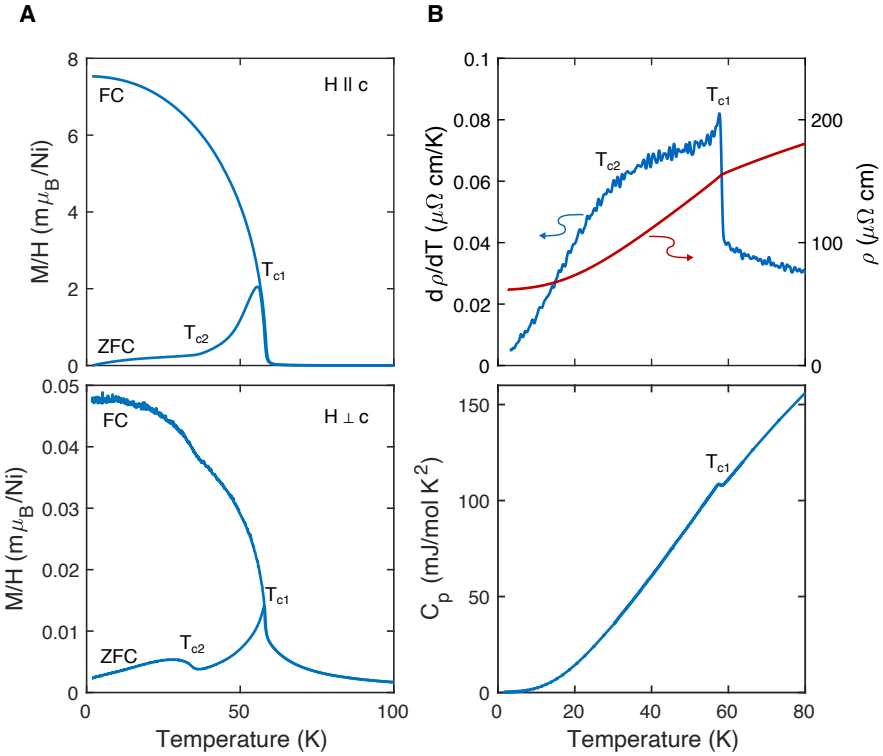

Figure 4.2: **Physical and magnetic properties of $NiTa_4Se_8$ A** Magnetization parallel and perpendicular to the crystallographic c-axis and ab-plane taken in the field-cooled (FC) and zero field-cooled (ZFC) protocols with a magnetic field of 100 Oe. A ferromagnetic-like transition is observed at $T_{c1} = 58K$, and a secondary feature, most prominently observed in ZFC traces, is observed at a lower $T_{c2} = 38K$. **B** Resistivity and heat capacity measurements. T_{c1} is associated with a prominent change in curvature in the resistivity (ρ) versus temperature. T_{c2} is associated with a change in the curvature of the temperature-dependent resistivity, most prominently observed in the derivative with respect to temperature. The specific heat capacity (C_p) exhibits a weak anomaly at T_{c1}. T_{c2} is not associated with a resolvable heat capacity anomaly.

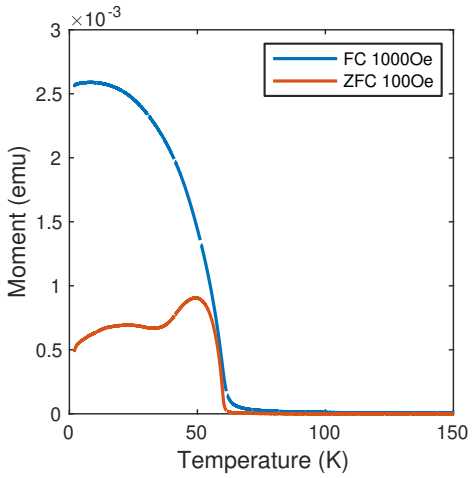

Figure 4.3: **Magnetization data on polycrystalline $NiTa_4Se_8$** Taken in field-cooled (FC) and zero field-cooled (ZFC) protocols. Two anomalies in the magnetization versus temperature trace are observed in agreement with the data on single crystal samples.

In regards to the original motivation, the magnetization data on single crystal samples strongly suggests that this material is a weak itinerant ferromagnet. Fig. 4.4A shows the inverse susceptibility with a fit to the Curie-Weiss law ($\chi = C/(T - \Theta)$), where Θ is the Curie temperature and C is a coefficient proportional to the effective moment ($C = N\frac{\mu_0 \mu_{\text{eff}}}{3k_B}$), where μ_{eff} is the effective moment, and N is the concentration of moments in the material. For field in both the in plane and out of plane configurations, a similar Curie temperature is found (54-55K), which agrees well with the observed ordering temperature. Assuming that the magnetism arises purely from the nickel ions, the fluctuating effective moments are 2.1 μ_B/Ni and 1.8 μ_B/Ni for the out of plane and in plane configurations, respectively, consistent with the magnetic moment associated with a nickel ion in the Ni^{2+} oxidation state. On the other hand, as shown in Fig. 4.4B, the saturated moment taken from low temperature isothermal magnetization field sweeps is found to be 0.69 and 0.85 μ_B per nickel for the out of plane and in plane directions, respectively. Thus, the saturated moment appears to be considerably smaller than the value of the effective Curie-Weiss moment for both crystallographic directions. Such a disparity is a hallmark of itinerant ferromagnetism [161, 198]. See also conductivity measurements up to 60T in Fig. 4.5, which confirm that a 3 Tesla field is sufficient to reach saturation in both the c and ab-plane measurements. Note that at higher temperatures, a secondary coercive field event associated with a tiny magnetic moment (0.02 μ_B) is observed in the hysteresis loops (Fig. 4.4B inset).

Altogether, the magnetization data suggests that the material is to first approximation, ferromagnetic, with an out of plane easy axis. There are a few reasons why this description is not complete though. First of all, a secondary feature is observed below the Curie

temperature (Fig. 4.2) — because this crossover appears most prominently in magnetic susceptibility measurements, it seems likely that it is associated with either secondary spin ordering or spin reorientation. Second, a spin flip transition is observed for magnetic field directed along the hard axis (Fig. 4.4 — this is inconsistent with pure uniaxial ferromagnetic order, where the magnetization would be expected to linearly rise until saturation. A spin flip transition indicates either antiferromagnetic exchange between layers, or perhaps the presence of a secondary magnetic subsystem with easy plane anisotropy. It seems probable that a description of the magnetism involves easy-axis nickel moments carrying a majority of the materials ordered magnetization, while a secondary magnetic subsystem, perhaps the tantalum moments, also spontaneously order with a smaller moment per ion, and are either antiferromagnetically coupled to the nickel moments or have easy plane anisotropy. A description of the seemingly complex magnetism in this material certainly warrants further study.

Finally, we note that the measured electronic contribution to the heat capacity in $NiTa_4Se_8$ is relatively large (62 ± 6 mJ/mol K^2). This value yields a density of states of 13 ± 1 eV^{-1}u.c.$^{-1}$. The Sommerfeld coefficient in this compound is close to that of heavy fermion metals. Moreover, the T^2 coefficient of the resistivity, A, in comparison to the Sommerfeld coefficient yields a relatively high Kadowaki-Woods ratio, comparable to that observed in f-electron metals and weak itinerant magnets with strong spin fluctuations [131, 28]. These results suggest that the electron-electron interactions in $NiTa_4Se_8$ are relatively strong, even when adjusted for the relatively high density of electronic states at the Fermi level.

All together, this layered compound seems to be a weak-moment itinerant ferromagnet with out of plane easy axis as a result of the nickel spins. In addition, there is potentially some more complicated magnetic texture with a much smaller moment — one possibility is that a more complex magnetic order is induced in the tantalum ions. The latter point is at present not critical to our criteria for nearly-magnetic superconductivity, but is nevertheless interesting and warrants further characterization. Finally, the itinerant ferromagnetic character also leads to apparently very strong electron-electron interactions. These features together motivate us to search for superconductivity in this material, potentially coexistent or on the border of ferromagnetism, and possibly mediated by ferromagnetic spin fluctuations.

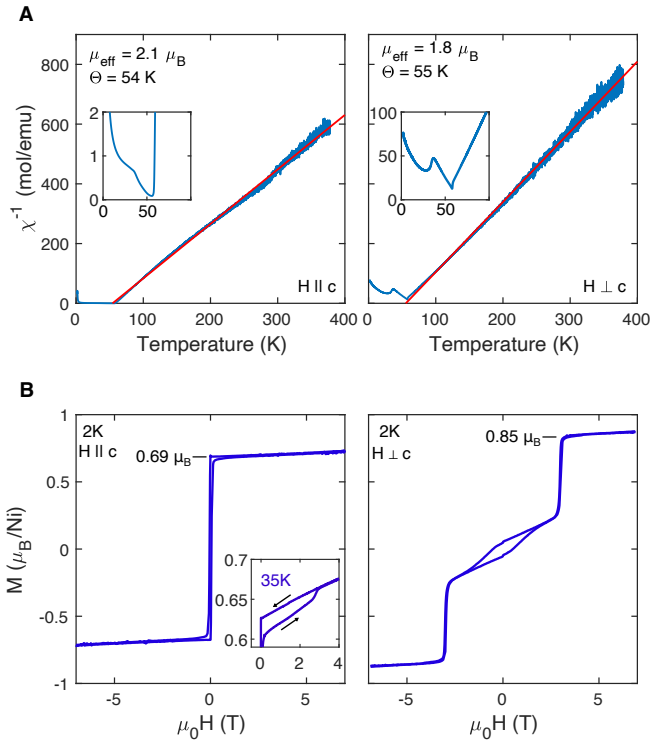

Figure 4.4: **Magnetic properties of $NiTa_4Se_8$ A** Inverse susceptibility versus temperature for the out of plane ($H \parallel c$) and in plane ($H \perp c$) directions. The effective fluctuating moment per nickel atom, μ_{eff}, extracted from a Curie-Weiss fit (red line) is shown in the panels, along with the Curie temperature Θ. The insets show a zoom in of the inverse susceptibility at low temperature, which shows a double-dip feature characteristic of ferrimagnetic order. **B** Magnetization versus field hysteresis loops for two crystallographic directions. The out of plane loop exhibits a sharp coercive field event, with a saturated magnetic moment of 0.69 bohr magneton per nickel atom. The inset shows that a smaller coercive field event is present at a higher field. For in-plane magnetic field, there is an apparent spin flip transition at a field of about 3 Tesla, and the saturated moment is about 0.85 bohr magneton per nickel.

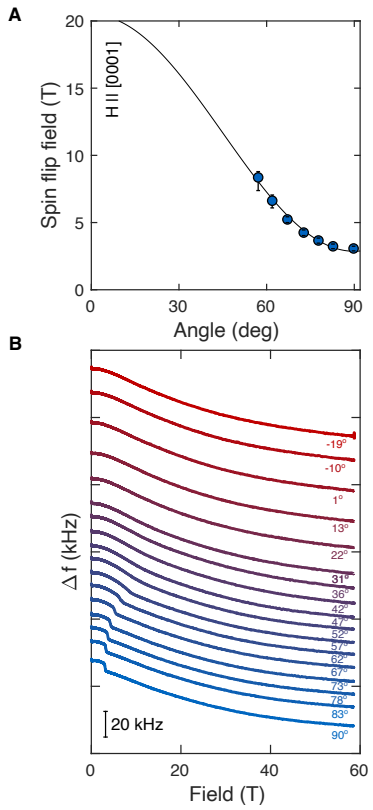

Figure 4.5: **High-field proximity detector oscillator (PDO) measurements as a function of angle tilting from out of plane to in-plane directions A** Transition field as a function of angle, extracted from derivatives of the field traces shown in panel B. The black line is $2.9 + 17.6\cos^2(\theta)$. **B** Field sweeps of the resonant frequency shift of a PDO circuit including the sample; curves are offset vertically for clarity. The shift of the resonant frequency is proportional to the conductivity of the sample [5]. A transition is observed when the field is in the plane of the crystal, consistent with the magnetization data in Fig. 4.4. The transition rapidly disperses to higher fields as the angle tilts out of plane, and disappears when the tilt angle is lower than about 60 degrees.

4.3 A first-order quantum phase transition

The presence of a spin flip transition at finite fields motivates us to study potential quantum critical physics at the zero-temperature endpoint of this phase. After all, much of the motivation in the introduction in this text focuses on destabilization of a Fermi liquid induced by symmetry-breaking at zero temperature. However, one of the particular issues with such transitions out of a ferromagnetic metal is that soft fermionic modes cause the transition to become first-order at finite temperature [95]. This means that rather than develop critical modes with long wavelength, the system tends to develop an inhomogeneous phase distribution at the quantum phase transition [212]. In fact, we will note here that the zero-temperature endpoint of the spin-flip transition in the magnetic field/temperature phase diagram of $NiTa_4Se_8$ does indeed exhibit characteristics of a first-order phase transition.

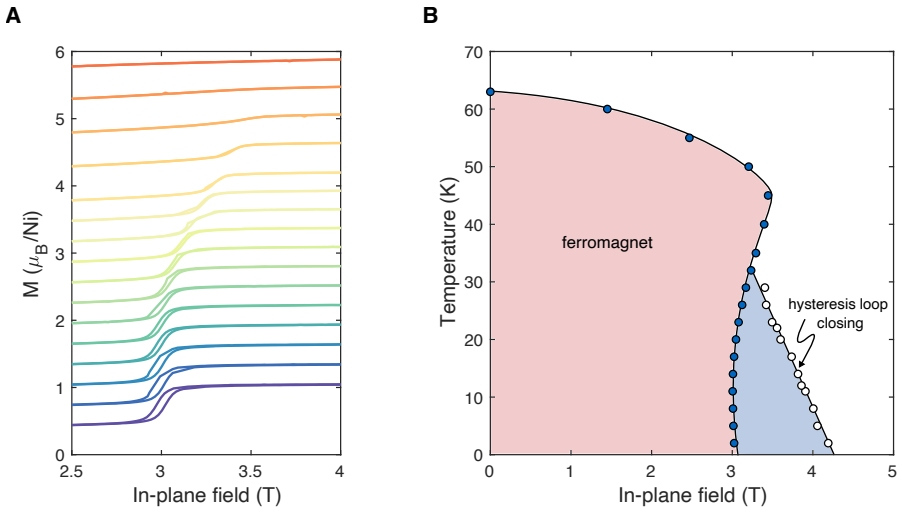

Figure 4.6: **Magnetic field-temperature phase diagram of the spin-flip transition in $NiTa_4Se_8$ A** Zoom-in of Magnetization versus field traces at different temperature (blue is low, red is high). Curves are offset for clarity. Hysteresis develops at low temperature around the transition, indicating that the transition is first-order. **B** The magnetic field-temperature phase diagram where solid blue points delineate the spin flip transition (maximum in $\partial M/\partial H$), while open circles show where the hysteresis loop around the transition closes fully.

Fig. 4.6 shows magnetization versus field measurements at different temperatures for determining the field of the spin-flip transition. The magnetic field-temperature phase diagram is shown in Fig. 4.6B. Most notably, the magnetization versus field trace becomes hysteretic around the spin-flip transition at low temperatures as seen in Fig. 4.6A. Hysteresis strongly indicates that the transition is first-order, i.e. it is discontinuous so that it involves the

formation of domains rather than long-range fluctuations. Fig. 4.6B shows that the high temperature spin-flip transition (which does not exhibit hysteresis) then develops hysteresis at lower temperatures at the same time that the phase boundary bends inwards. The shaded blue region indicates the width of the hysteresis loop in field in which presumably disordered domains form. One interpretation is that the second-order transition at high temperatures is driven first-order as temperature decreases. Such behavior is common among itinerant ferromagnetic quantum phase transitions [95]. In this interpretation, the point at which the transition develops hysteresis (around 34K and 3.3 Tesla) would be a multicritical point at which a second-order transition becomes a first-order transition.

Further measurements of magnetic susceptbility and heat capacity around the potential tricritical point and subsequent first-order quantum phase transition will shed further light on these questions. One interesting possibility has been suggested for stabilizing a second-order quantum phase transition out of the ferromagnet [167]. The basic idea is to apply pressure to the system to suppress the ferromagnetic order. At some pressure, the second-order transition is expected to become first-order at a tricritical point, much like the behavior observed in Fig. 4.6B. However, the second-order nature of the transition can be recovered by applying magnetic field to the material. Thus, under pressure and magnetic field it may be possible to realize a quantum critical point (a second-order phase transition at zero temperature).

4.4 Superconductivity in proximity or coexistent with ferromagnetism in $Ni_xTa_4Se_8$

This material can also be grown with varying degrees of nickel concentration between the layers of single crystal samples. Fig. 4.7 shows laue diffraction pattern images taken at the Advanced Light Source beamline 12.3.2 at Lawrence Berkeley National Lab. What we notice is that many of the samples have very sharp laue reflections, and therefore a high degree of crystallinity. The notable exception is $Ni_{0.6}TaSe_2$, which seems to have two different crystal orientations, perhaps suggesting phase inhomogeneity or twinning. In samples with reduced nickel content, there do not seem to be extra reflections in addition to those of $TaSe_2$. Therefore, it seems to be the case that when the nickel content is reduced substantially, the nickel atoms form an amorphous layer, in the sense that they do not exhibit long-range periodic structure, between the $TaSe_2$ planes. The chemical composition of these crystals was determined by EDX measurements.

Samples with substantially reduced nickel concentration (28%) exhibit superconductivity around 2.5K as seen in the resistivity comparison shown in Fig. 4.8. This sample does not seem to exhibit a ferromagnetic transition, at least certainly not one as prominent as in the $NiTa_4Se_8$ sample. This leads to the hypothesis that reducing the nickel concentration tunes between a weak itinerant ferromagnetic phase (as characterized in the preceding section) and a superconducting phase.

Indeed, for a sample with a slightly higher nickel concentration (60%), a ferromagnetic transition is observed at about 31K, and a superconducting transition is observed at about 2K (Fig. 4.9). The ferromagnetism is detected in transport measurements as the onset of hysteresis in the measured Hall signal as a function of applied magnetic field (Fig. 4.9B), while the superconductivity is associated with a drop in the resistivity close to zero (Fig. 4.9A). Note, however, that the resistance does not drop fully to zero. This could indicate that the ferromagnetism and superconductivity are spatially separated within the single crystalline samples. Indeed the Laue pattern on these crystals suggests two different orientations associated with possible phase inhomogeneity (Fig. 4.7). On the other hand, the presence of superimposed hysteresis and superconducting transitions at 2K below the onset of superconductivity suggests that there is a substantial interaction between the superconductivity and ferromagnetism. Whether this is an interfacial interaction between segregated phases within the crystal, or a more microscopic coexistence of superconductivity and ferromagnetism, remains to be seen. It is worth noting that even if superconductivity and ferromagnetism are phase separated spatially, the superconductivity needs to be 'robust' to ferromagnetism in some sense. This is possible through either a triplet superconducting order parameter, or because of the possibility of spatial separation, a more conventional order parameter that is spatially modulated as seen in $ErRh_4B_4$ [120], for example.

At even lower concentrations of nickel, a bulk superconducting phase is observed without ferromagnetic order. Fig. 4.10 shows magnetic and thermodynamic characterization of the superconductivity in $Ni_{0.28}Ta_4Se_8$ with $T_c \approx 2$K. The electronic contribution to the

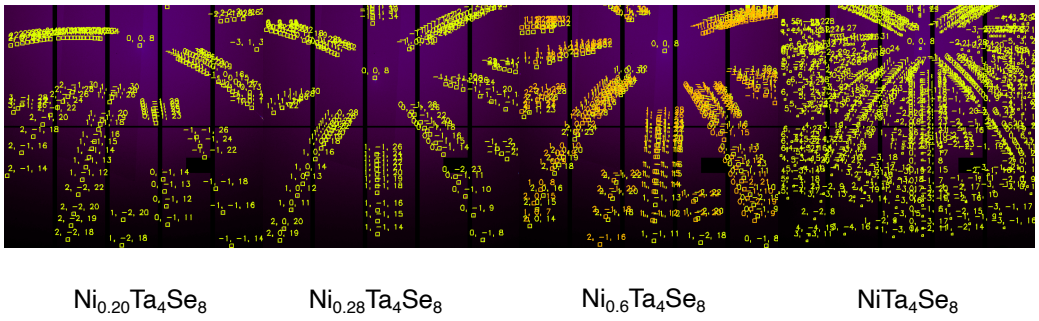

Figure 4.7: **Laue diffraction patterns of single crystals with various nickel concentrations** $NiTa_4Se_8$ shows sharp peaks, which can be indexed to $TaSe_2$ with a doubled unit cell, in agreement with the powder X-ray diffraction data. In crystals grown with lower nickel content (0.2-0.28), very sharp reflections demonstrate the high quality of the crystals. In the 60% nickel sample, there seems to be two separate crystal orientations within the crystal, suggesting possible twinning or phase inhomogeneity.

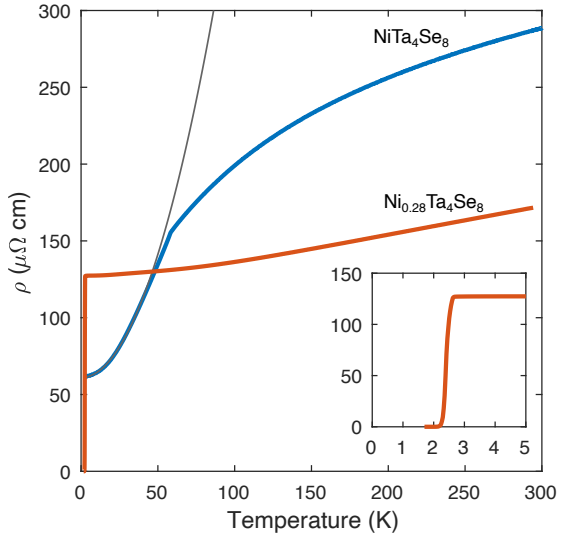

Figure 4.8: **Comparison of resistivity in $NiTa_4Se_8$ and a crystal with reduced nickel concentration** The ferromagnetic transition is not readily visible in the $Ni_{0.28}TaSe_2$ sample, and superconductivity is observed at about 2.5K where the measured resistance drops below the noise floor.

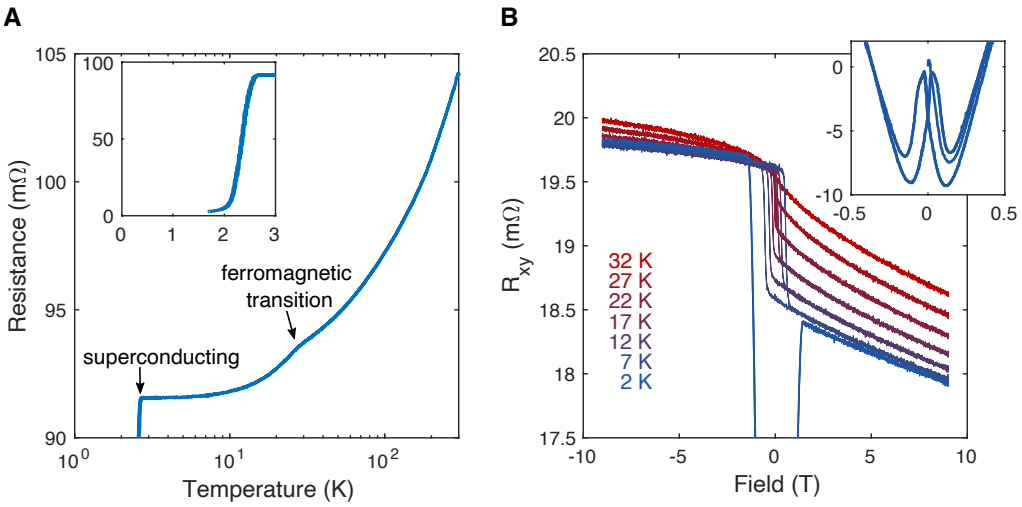

Figure 4.9: **Coexistence of ferromagnetism and superconductivity in $Ni_{0.6}TaSe_2$** **A** The resistance shows two prominent features. The higher temperature anomaly is associated with the onset of ferromagnetic order, as indicated by the onset of hysteresis in Hall effect measurements. The lower temperature transition is superconductivity where the resistance drops to a value close to, but not quite, zero (inset). **B** Hysteresis in Hall effect measurements onsets below 30K, coincident with the anomaly shown in panel A. At 2K, a superconducting critical field transition is observed superimposed on a hysteresis loop. This leads to the 'butterfly' structure in the hysteresis loop as shown in the inset.

heat capacity reaches around 45 mJ/molK^2, slightly lower than in $NiTa_4Se_8$. A significant heat capacity anomaly is observed at the superconducting transition temperature. Interestingly, there appears to be a residual contribution to the specific heat at low temperature (Fig. 4.10B). Such behavior has been observed in other nearly-ferromagnetic superconductors [160], but at present it is difficult to determine the origin of this residual entropy contribution.

Figs. 4.10C and D show magnetization measurements near the superconducting transition. A considerable diamagnetic signal is observed in the superconducting state, giving evidence for bulk superconductivity. Notably, the diamagnetic signal in the in-plane field configuration is much lower than in the out-of-plane field configuration. And, for in-plane field, a spike in the paramagnetic susceptibility is observed right above the superconducting transition (Fig. 4.10D inset). At present, it is difficult to say whether these characteristics originate in the largely two-dimensional structure of the crystal, and the presumably quasi two-dimensional electronic structure, or whether they are associated with some sort of anisotropy in the superconducting order parameter. Nuclear magnetic resonance measurements of the superconducting state would help answer these questions.

Nevertheless, this material clearly presents many directions for the exploration of nearly-ferromagnetic superconductivity, and its interplay with a nontrivial ferromagnetic state. The capacity for this platform to host superconductivity that survives proximity to ferromagnetism (Fig. 4.9) provides a host of opportunities to build platforms for superconducting spin transport as well. It is worth noting that, although the material is a nearly-ferromagnetic metal, and can indeed be driven to a quantum phase transition by magnetic field (Fig. 4.6, we have not detected evidence for non-Fermi liquid behavior either in thermodynamic or transport measurements (Fig. 4.8). Part of the reason for this is that the ferromagnetic transition apparently becomes first-order at sufficiently low temperature (Fig. 4.6). However, as suggested in Chapter 4.4, there may be opportunities to drive the system to a ferromagnetic quantum critical point, where non-Fermi liquid behavior is certainly expected to manifest, with pressure and magnetic field in tandem. We may even speculate on the possibility of realizing superconductivity at this zero-temperature second-order phase transition given the overall apparent propensity of this material to host superconductivity.

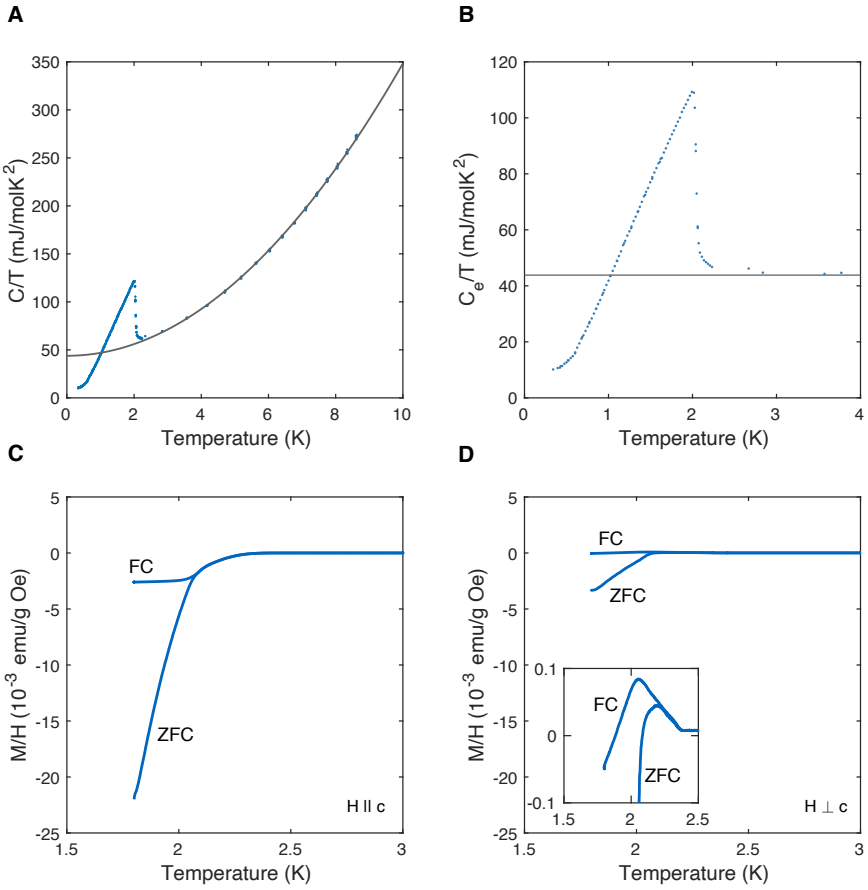

Figure 4.10: **Bulk superconductivity in $Ni_{0.28}Ta_4Se_8$ A** Heat capacity with a fit to the model $AT + BT^3$ (grey line). A superconducting anomaly is clearly observed around 2K. **B** Electronic contribution to the heat capacity at low temperature (subtracted BT^3 phonon contribution). **C,D** Magnetic susceptibility measured at 10Oe in field-cooled (FC) and zero field-cooled (ZFC) protocols for out of plane and in plane field.

Bibliography

[1] URL: http://web.mit.edu/6.730/www/ST04/Lectures/Lecture32.pdf.

[2] A. Abanov, A.V. Chubukov, and J. Schmalian. "Quantum-critical theory of the spin-fermion model and its application to cuprates: Normal state analysis". In: *Advances in Physics* 52.3 (2003), pp. 119–218.

[3] A. A. Abrikosov. "Quantum linear magnetoresistance". In: *Europhysics Letters* 49.6 (2000), p. 789. ISSN: 0295-5075.

[4] G. Aeppli et al. "Nearly singular magnetic fluctuations in the normal state of a high-T_c cuprate superconductor". In: *Science* 278.5342 (1997), pp. 1432–1435.

[5] M.M. Altarawneh, C.H. Mielke, and J.S. Brooks. "Proximity detector circuits: An alternative to tunnel diode oscillators for contactless measurements in pulsed magnetic field environments". In: *Review of Scientific Instruments* 80.6 (2009), p. 066104.

[6] J. G. Analytis et al. "Enhanced fermi-surface nesting in superconducting $BaFe_2(As_{1-x}P_x)_2$ revealed by the de Haas-van alphen effect". In: *Physical Review Letters* 105.20 (Nov. 2010), p. 207004.

[7] P. W. Anderson. "Hall effect in the two-dimensional Luttinger liquid". In: *Physical review letters* 67.15 (1991), p. 2092.

[8] P.W. Anderson. "Antiferromagnetism. Theory of superexchange interaction". In: *Physical Review* 79.2 (1950), p. 350.

[9] P.W. Anderson. "New approach to the theory of superexchange interactions". In: *Physical Review* 115.1 (1959), p. 2.

[10] P.W. Anderson. "The resonating valence bond state in La_2CuO_4 and superconductivity". In: *science* 235.4793 (1987), pp. 1196–1198.

[11] K. Andres, J.E. Graebner, and H.R. Ott. "4f-Virtual-Bound-State Formation in $CeAl_3$ at Low Temperatures". In: *Physical Review Letters* 35.26 (1975), p. 1779.

[12] D. Aoki, K. Ishida, and J. Flouquet. "Review of U-based ferromagnetic superconductors: Comparison between UGe_2, URhGe, and UCoGe". In: *Journal of the Physical Society of Japan* 88.2 (2019), p. 022001.

[13] N. P. Armitage et al. "Doping dependence of an n-type cuprate superconductor investigated by angle-resolved photoemission spectroscopy". In: *Physical Review Letters* 88.25 (June 2002), p. 4. ISSN: 10797114.

[14] N.P. Armitage, P. Fournier, and R.L. Greene. "Progress and perspectives on electron-doped cuprates". In: *Reviews of Modern Physics* 82.3 (2010), p. 2421.

[15] N. W. Ashcroft and N. D. Mermin. *Solid State Physics*. Holt-Saunders, 1976.

[16] A. Ataei et al. "Electrons with Planckian scattering obey standard orbital motion in a magnetic field". In: *arXiv preprint arXiv:2203.05035* (2022).

[17] S. Badoux et al. "Change of carrier density at the pseudogap critical point of a cuprate superconductor". In: *Nature* 531.7593 (Mar. 2016), pp. 210–214.

[18] P. Baňack and J. Noga. "Aspects of strong electron-phonon coupling in superconductivity of compressed metal hydrides MH_6 (M= Mg, Ca, Sc, Y) with Im-3m structure". In: *Journal of Applied Physics* 130.18 (2021), p. 183902.

[19] A. Banerjee et al. "Excitations in the field-induced quantum spin liquid state of α-$RuCl_3$". In: *NPJ Quantum Materials* 3.1 (Dec. 2018), pp. 1–7.

[20] Y. Bang and G. R. Stewart. "Superconducting properties of the s±-wave state: Fe-based superconductors". In: *Journal of Physics: Condensed Matter* 29 (Feb. 2017), p. 123003.

[21] J. Bardeen, L.N. Cooper, and J.R. Schrieffer. "Theory of superconductivity". In: *Physical Review* 108.5 (1957), p. 1175.

[22] A. Baum et al. "Frustrated spin order and stripe fluctuations in FeSe". In: *Nature Communications* 2.1 (Feb. 2019), pp. 1–7. ISSN: 2399-3650. (Visited on 06/13/2020).

[23] A. Bianchi et al. "Avoided antiferromagnetic order and quantum critical point in $CeCoIn_5$". In: *Physical Review Letters* 91.25 (Dec. 2003), p. 257001. ISSN: 0031-9007.

[24] D.W. Bloom, D.H. Lowndes Jr, and L. Finegold. "Low temperature specific heat of copper: Comparison of two samples of high purity". In: *Review of Scientific Instruments* 41.5 (1970), pp. 690–695.

[25] Anna E Böhmer and Andreas Kreisel. "Nematicity, magnetism and superconductivity in FeSe". In: *Journal of Physics: Condensed Matter* 30.2 (2017), p. 023001.

[26] M. Breitkreiz, P. M. R. Brydon, and C. Timm. "Transport in multiband systems with hot spots on the Fermi surface: Forward-scattering corrections". In: *Physical Review B* 89.24 (June 2014), p. 245106.

[27] M. Breitkreiz, P.M.R. Brydon, and C. Timm. "Interrupted orbital motion in density-wave systems". In: *Physical Review B* 94.20 (2016), p. 205103.

[28] W. F. Brinkman and S. Engelsberg. "Spin-fluctuation contributions to the specific heat". In: *Physical Review* 169.2 (1968), p. 417.

[29] J.R. Bumby. *Superconducting rotating electrical machines*. Vol. 15. Oxford University Press, USA, 1983.

[30] M Buttiker. "Symmetry of electrical conduction". In: *IBM Journal of Research and Development* 32.3 (1988), pp. 317–334.

[31] K. Chen et al. "Evolution of ground-state wave function in $CeCoIn_5$ upon Cd or Sn doping". In: *Physical Review B* 97.4 (Jan. 2018), p. 045134. ISSN: 2469-9950.

[32] Q. Y. Chen et al. "Direct observation of how the heavy fermion state develops in $CeCoIn_5$". In: *Physical Review B* 96.4 (July 2017), p. 045107.

[33] Q. Y. Chen et al. "Electronic structure study of $LaCoIn_5$ and its comparison with $CeCoIn_5$". In: *Physical Review B* 100.3 (July 2019), p. 035117.

[34] Q. Y. Chen et al. "Suppression of hybridization by Cd doping in $CeCoIn_5$". In: *Physical Review B* 100.23 (Dec. 2019), p. 235148. ISSN: 24699969. DOI: 10.1103/PhysRevB.100.235148.

[35] J.-H. Chu et al. "Determination of the phase diagram of the electron-doped superconductor $Ba(Fe_{1-x}Co_x)_2As_2$". In: *Physical Review B* 79.1 (2009), p. 014506.

[36] J.-H. Chu et al. "Possible scale invariant linear magnetoresistance in pyrochlore iridates $Bi_2Ir_2O_7$". In: *New Journal of Physics* 21.11 (Nov. 2019), p. 113041.

[37] A. V. Chubukov, R. M. Fernandes, and J. Schmalian. "Origin of nematic order in FeSe". In: *Physical Review B* 91.20 (May 2015), p. 201105. (Visited on 06/13/2020).

[38] A.I. Coldea. "Electronic nematic states tuned by isoelectronic substitution in bulk $FeSe_{1-x}S_x$". In: *Frontiers in Physics* (2021), p. 528.

[39] P. Coleman. *Introduction to many-body physics*. Cambridge University Press, 2015.

[40] P. Coleman. "Theories of non-Fermi liquid behavior in heavy fermions". In: *Physica B* 259-261 (Jan. 1999), pp. 353–358.

[41] P. Coleman and A. J. Schofield. "Quantum criticality". In: *Nature* 433.7023 (Jan. 2005), pp. 226–229.

[42] R. Comin et al. "Charge order driven by Fermi-arc instability in $Bi_2Sr_{2-x}La_xCuO_{6+\delta}$". In: *Science* 343.6169 (2014), pp. 390–392.

[43] N. J. Curro et al. "Anomalous NMR magnetic shifts in $CeCoIn_5$". In: *Physical Review B* 64.18 (2001).

[44] P. Dai. "Antiferromagnetic order and spin dynamics in iron-based superconductors". In: *Reviews of Modern Physics* 87.3 (2015), p. 855.

[45] *Data and Materials*. doi: 10.17605/OSF.IO/DFM7X. DOI: 10.17605. URL: http://10.17605/OSF.IO/DFM7X.

[46] K.B. Dave, P.W. Phillips, and C.L. Kane. "Absence of Luttinger's theorem due to zeros in the single-particle Green function". In: *Physical review letters* 110.9 (2013), p. 090403.

[47] A.P. Drozdov et al. "Superconductivity at 250 K in lanthanum hydride under high pressures". In: *Nature* 569.7757 (2019), pp. 528–531.

[48] M. Eisterer. "Radiation effects on iron-based superconductors". In: *Superconductor Science and Technology* 31.1 (Dec. 2018), p. 013001.

[49] D. Fay and J. Appel. "Coexistence of p-state superconductivity and itinerant ferromagnetism". In: *Physical Review B* 22.7 (1980), p. 3173.

[50] R. M. Fernandes, E. Abrahams, and J. Schmalian. "Anisotropic in-plane resistivity in the nematic phase of the iron-pnictides". In: *Physical Review Letters* 107.21 (Nov. 2011), p. 217002. (Visited on 06/13/2020).

[51] R. M. Fernandes et al. "Preemptive nematic order, pseudogap, and orbital order in the iron pnictides". In: *Physical Review B* 85.2 (Jan. 2012), p. 024534. DOI: 10.1103/PhysRevB.85.024534. URL: https://link.aps.org/doi/10.1103/PhysRevB.85.024534 (visited on 06/13/2020).

[52] J. Fink et al. "Electronic structure studies of $BaFe_2As_2$ by angle-resolved photoemission spectroscopy". In: *Physical Review B* 79 (15 Apr. 2009), p. 155118.

[53] M. Freedman et al. "Topological quantum computation". In: *Bulletin of the American Mathematical Society* 40.1 (2003), pp. 31–38.

[54] M. Fuglsang Jensen et al. "Angle-resolved photoemission study of the role of nesting and orbital orderings in the antiferromagnetic phase of $BaFe_2As_2$". In: *Physical Review B* 84 (1 July 2011), p. 014509.

[55] M. Fuglsang Jensen et al. "Angle-resolved photoemission study of the role of nesting and orbital orderings in the antiferromagnetic phase of $BaFe_2As_2$". In: *Physical Review B* 84.1 (2011), p. 014509.

[56] S. I. Fujimori. "Band structures of $4f$ and $5f$ materials studied by angle-resolved photoelectron spectroscopy". In: *J. Phys. Condens. Matter* 28.15 (Mar. 2016), p. 153002.

[57] E. Gati et al. "Bulk Superconductivity and role of fluctuations in the iron-based superconductor FeSe at high pressures". In: *Physical Review Letters* 123.16 (Oct. 2019), p. 167002.

[58] N. Gauthier et al. "Quantum-well states in fractured crystals of the heavy-fermion material $CeCoIn_5$". In: *Physical Review B* 102.12 (Sept. 2020), p. 125111.

[59] G. Ghiringhelli et al. "Long-range incommensurate charge fluctuations in (Y, Nd) $Ba_2Cu_3O_{6+x}$". In: *Science* 337.6096 (2012), pp. 821–825.

[60] P. Giraldo-Gallo et al. "Scale-invariant magnetoresistance in a cuprate superconductor." In: *Science* 361.6401 (Aug. 2018), pp. 479–481. ISSN: 1095-9203. DOI: 10.1126/science.aan3178.

[61] K. Gofryk et al. "Electronic Tuning and Uniform Superconductivity in $CeCoIn_5$". In: *Physical Review Letters* 109.18 (Oct. 2012), p. 186402. ISSN: 0031-9007.

[62] AI Goldman et al. "Lattice and magnetic instabilities in $CaFe_2As_2$: A single-crystal neutron diffraction study". In: *Physical Review B* 78.10 (2008), p. 100506.

[63] J.B. Goodenough. "Theory of the role of covalence in the perovskite-type manganites [La,M(II)] MnO_3". In: *Physical Review* 100.2 (1955), p. 564.

[64] P.M. Grant. "The Energy Super Grid". In: *Proc. World Energy Conference (Shanghai)*. 2004, pp. 109–112.

[65] David J Griffiths. *Introduction to Electrodynamics*. Pearson, 2013.

[66] G. Grissonnanche et al. "Linear-in temperature resistivity from an isotropic Planckian scattering rate". In: *Nature* 595.7869 (2021), pp. 667–672.

[67] F.M. Grosche et al. "Superconductivity on the threshold of magnetism in $CePd_2Si_2$ and $CeIn_3$". In: *Journal of Physics: Condensed Matter* 13.12 (2001), p. 2845.

[68] T. Hanaguri et al. "A 'checkerboard' electronic crystal state in lightly hole-doped $Ca_{2-x}Na_xCuO_2Cl_2$". In: *Nature* 430.7003 (2004), pp. 1001–1005.

[69] J. M. Harris et al. "Violation of Kohler's Rule in the Normal-State Magnetoresistance of $YBa_2Cu_3O_{7-\delta}$ and $(La_{1-x}Sr_x)_2CuO_4$". In: *Physical Review Letters* 75.7 (Aug. 1995), pp. 1391–1394. ISSN: 0031-9007. DOI: 10.1103/PhysRevLett.75.1391.

[70] K. Hashimoto et al. "A sharp peak of the zero-temperature penetration depth at optimal composition in $BaFe_2(As_{1-x}P_x)_2$". In: *Science* 336.6088 (June 2012), pp. 1554–1557.

[71] I. M. Hayes et al. "Scaling between magnetic field and temperature in the high-temperature superconductor $BaFe_2(As_{1-x}P_x)_2$". In: *Nature Physics* 12.10 (Oct. 2016), pp. 916–919. ISSN: 1745-2473.

[72] I.M. Hayes et al. "Superconductivity and quantum criticality linked by the Hall effect in a strange metal". In: *Nature Physics* 17.1 (2021), pp. 58–62.

[73] J.L. He, D.M. Rote, and H.T. Coffey. *Study of Japanese electrodynamic-suspension maglev systems*. Tech. rep. Argonne National Lab., IL (United States). Energy Systems Div., 1994.

[74] R.D.H. Hinlopen et al. "B^2 to B-linear magnetoresistance due to impeded orbital motion". In: *arXiv preprint arXiv:2201.03292* (2022).

[75] R. Hlubina and T. M. Rice. "Resistivity as a function of temperature for models with hot spots on the Fermi surface". In: *Physical Review B* 51.14 (Apr. 1995), pp. 9253–9260.

[76] J.E. Hoffman et al. "A four unit cell periodic pattern of quasi-particle states surrounding vortex cores in $Bi_2Sr_2CaCu_2O_{8+\delta}$". In: *Science* 295.5554 (2002), pp. 466–469.

[77] T. Holstein, R.E. Norton, and P. Pincus. "de Haas-van Alphen effect and the specific heat of an electron gas". In: *Physical Review B* 8.6 (1973), p. 2649.

[78] S. Hosoi et al. "Nematic quantum critical point without magnetism in $FeSe_{1-x}S_x$ superconductors". In: *Proceedings of the National Academy of Sciences of the United States of America* 113.29 (July 2016), pp. 8139–8143. URL: www.pnas.org/cgi/doi/10.1073/pnas.

[79] D. Hu et al. "Spin excitations in optimally P-doped $BaFe_2(As_{0.7}P_{0.3})_2$ superconductor". In: *Physical Review B* 94.9 (Sept. 2016), p. 094504.

[80] M. Huecker et al. "Competing charge, spin, and superconducting orders in underdoped $YBa_2Cu_3O_y$". In: *Physical Review B* 90.5 (2014), p. 054514.

[81] E.H. Hwang and S.D. Sarma. "Linear-in-T resistivity in dilute metals: A Fermi liquid perspective". In: *Physical Review B* 99.8 (2019), p. 085105.

[82] H. Ibach and H. Lüth. *Solid-state physics: an introduction to principles of materials science*. Springer Science & Business Media, 2009.

[83] L. B. Ioffe and A. I. Larkin. "Gapless fermions and gauge fields in dielectrics". In: *Phys. Rev. B* 39 (13 May 1989), pp. 8988–8999.

[84] S. Ishida et al. "Manifestations of multiple-carrier charge transport in the magnetostructurally ordered phase of $BaFe_2As_2$". In: *Physical Review B* 84.18 (Nov. 2011), p. 184514. (Visited on 06/26/2020).

[85] H. Ishii et al. "Direct observation of Tomonaga–Luttinger-liquid state in carbon nanotubes at low temperatures". In: *Nature* 426.6966 (2003), pp. 540–544.

[86] S. Jang et al. "Evolution of the Kondo lattice electronic structure above the transport coherence temperature". In: *Proceedings of the National Academy of Sciences* 117.38 (Sept. 2020), pp. 23467–23476.

[87] S.R. Julian et al. "The normal states of magnetic d and f transition metals". In: *Journal of Physics: Condensed Matter* 8.48 (1996), p. 9675.

[88] S. Kasahara et al. "Evolution from non-Fermi- to Fermi-liquid transport via isovalent doping in $BaFe_2(As_{1-x}P_x)_2$ superconductors". In: *Physical Review B* 81.18 (May 2010), p. 184519.

[89] S. Kasap, C. Koughia, and H.E. Ruda. "Electrical conduction in metals and semiconductors". In: *Springer handbook of electronic and photonic materials*. Springer, 2017, pp. 1–1.

[90] T. Kato. "On the adiabatic theorem of quantum mechanics". In: *Journal of the Physical Society of Japan* 5.6 (1950), pp. 435–439.

[91] B. Keimer et al. "From quantum matter to high-temperature superconductivity in copper oxides". In: *Nature* 518.7538 (2015), pp. 179–186.

[92] B.J. Kim et al. "Distinct spinon and holon dispersions in photoemission spectral functions from one-dimensional $SrCuO_2$". In: *Nature Physics* 2.6 (2006), pp. 397–401.

[93] C Kim et al. "Separation of spin and charge excitations in one-dimensional SrCuO 2". In: *Physical Review B* 56.24 (1997), p. 15589.

[94] Simon AJ Kimber et al. "Similarities between structural distortions under pressure and chemical doping in superconducting $BaFe_2As_2$". In: *Nature materials* 8.6 (2009), pp. 471–475.

[95] T.R. Kirkpatrick and D. Belitz. "Ferromagnetic quantum critical point in noncentrosymmetric systems". In: *Physical Review Letters* 124.14 (2020), p. 147201.

[96] G. Knebel et al. "The quantum critical point in $CeRhIn_5$: A resistivity study". In: *Journal of the Physical Society of Japan* 77.11 (2008), pp. 114704–114704.

[97] Y. Kohori et al. "NMR and NQR studies of the heavy fermion superconductors $CeTIn_5$ (T = Co and Ir)". In: *Physical Review B* 64.13 (Sept. 2001), p. 134526.

[98] A. Koitzsch et al. "Hybridization effects in $CeCoIn_5$ observed by angle-resolved photoemission". In: *Physical Review B* 77.15 (Apr. 2008), p. 155128.

[99] J. Kondo. "g-shift and anomalous Hall effect in gadolinium metals". In: *Progress of Theoretical Physics* 28.5 (1962), pp. 846–856.

[100] J. Kondo. "Resistance minimum in dilute magnetic alloys". In: *Progress of theoretical physics* 32.1 (1964), pp. 37–49.

[101] Takeshi Kondo et al. "Unexpected Fermi-surface nesting in the pnictide parent compounds $BaFe_2As_2$ and $CaFe_2As_2$ revealed by angle-resolved photoemission spectroscopy". In: *Physical Review B* 81.6 (2010), p. 060507.

[102] H. Kontani. "Anomalous transport phenomena in Fermi liquids with strong magnetic fluctuations". In: *Reports on Progress in Physics* 71.2 (Jan. 2008), p. 026501.

[103] H. Kontani. "Theory of magnetoresistance in correlated electron systems: Modified Kohler rule in high-T_c superconductors". In: *Physica B* 312-313 (Mar. 2002), pp. 25–27.

[104] H. Kontani, K. Kanki, and K. Ueda. "Hall effect and resistivity in high-T_c superconductors: The conserving approximation". In: *Physical Review B* 59.22 (June 1999), pp. 14723–14739. ISSN: 1550235X.

[105] A. E. Koshelev. "Linear magnetoconductivity in multiband spin-density-wave metals with nonideal nesting". In: *Physical Review B* 88.6 (Aug. 2013), p. 060412.

[106] A. E. Koshelev. "Magnetotransport of multiple-band nearly antiferromagnetic metals due to hot-spot scattering". In: *Physical Review B* 94.12 (Sept. 2016), p. 125154.

[107] H.A. Kramers. "L'interaction entre les atomes magnétogènes dans un cristal paramagnétique". In: *Physica* 1.1-6 (1934), pp. 182–192.

[108] R. Kumar, S. Singh, and S. Nair. "High temperature linear magnetoresistance and scaling behavior in the $Ba(Fe_{1-x}Co_x)_2As_2$ series". In: (2018). arXiv: 1801.03768v1.

[109] J.E. Kunzler et al. "Superconductivity in Nb_3Sn at high current density in a magnetic field of 88 kgauss". In: *Physical review letters* 6.3 (1961), p. 89.

[110] H. H. Kuo et al. "Ubiquitous signatures of nematic quantum criticality in optimally doped Fe-based superconductors". In: *Science* 352.6288 (May 2016), pp. 958–962. ISSN: 10959203.

[111] B. Lake et al. "Spins in the vortices of a high-temperature superconductor". In: *Science* 291.5509 (2001), pp. 1759–1762.

[112] S. Lederer et al. "Superconductivity and non-Fermi liquid behavior near a nematic quantum critical point". In: *PNAS* 114.19 (May 2017), pp. 4905–4910. ISSN: 1091-6490.

[113] P.A. Lee. "Low-temperature T-linear resistivity due to umklapp scattering from a critical mode". In: *Physical Review B* 104.3 (2021), p. 035140.

[114] P.A. Lee, N. Nagaosa, and X.-G. Wen. "Doping a Mott insulator: Physics of high-temperature superconductivity". In: *Reviews of modern physics* 78.1 (2006), p. 17.

[115] S.K. Lewin and J.G. Analytis. "Angle-dependent magnetoresistance as a probe of Fermi surface warping in $HgBa_2CuO_{4+}\delta$". In: *Physical Review B* 98.7 (2018), p. 075116.

[116] S. Licciardello et al. " Coexistence of orbital and quantum critical magnetoresistance in $FeSe_{1-x}S_x$". In: *Physical Review Research* 1.2 (Sept. 2019), p. 023011.

[117] F. London. "The λ-phenomenon of liquid helium and the Bose-Einstein degeneracy". In: *Nature* 141.3571 (1938), pp. 643–644.

[118] J.M. Luttinger and J.C. Ward. "Ground-state energy of a many-fermion system. II". In: *Physical Review* 118.5 (1960), p. 1417.

[119] M.W. Ma et al. "Crystal growth of iron-based superconductor $FeSe_{0.94}$ by KCl flux method". In: *Physica C: Superconductivity and its Applications* 506 (2014), pp. 154–157.

[120] K. Machida. "A Theory of Ferromagnetic Superconductors–An Analysis of Experiments on $ErRh_4B_4$ and $HoMo_6S_8$–". In: *Journal of the Physical Society of Japan* 51.11 (1982), pp. 3462–3468.

[121] P. Majumdar and P. B. Littlewood. "Dependence of magnetoresistivity on charge-carrier density in metallic ferromagnets and doped magnetic semiconductors". In: *Nature* 395.6701 (Oct. 1998), pp. 479–481.

[122] N. Maksimovic et al. "Evidence for a delocalization quantum phase transition without symmetry breaking in $CeCoIn_5$". In: *Science* (2022), eaaz4566.

[123] N. Maksimovic et al. "Magnetoresistance scaling and the origin of H-linear resistivity in $BaFe_2(As_{1-x}P_x)_2$". In: *Physical Review X* 10.4 (2020), p. 041062.

[124] K. Matan et al. "Anisotropic itinerant magnetism and spin fluctuations in $BaFe_2As_2$: A neutron scattering study". In: *Physical Review B* 79.5 (Feb. 2009), p. 054526. ISSN: 1098-0121. DOI: 10.1103/PhysRevB.79.054526. URL: https://link.aps.org/doi/10.1103/PhysRevB.79.054526.

[125] T. Matsuura. "The effects of impurities on superconductors with Kondo effect". In: *Progress of Theoretical Physics* 57.6 (1977), pp. 1823–1835.

[126] D.C. Mattis and E.H. Lieb. "Exact solution of a many-fermion system and its associated boson field". In: *Bosonization*. World Scientific, 1994, pp. 98–106.

[127] H.V. McIntosh. "Symmetry and degeneracy". In: *Group theory and its applications*. Elsevier, 1971, pp. 75–144.

[128] E. Merzbacher. *Quantum mechanics*. Jones & Bartlett Publishers, 1961.

[129] A.J. Millis. "Effect of a nonzero temperature on quantum critical points in itinerant fermion systems". In: *Physical Review B* 48.10 (1993), p. 7183.

[130] V.P. Mineev. "Superconductivity in ferromagnetic metals and in compounds without inversion centre". In: *International Journal of Modern Physics B* 18.22 (2004), pp. 2963–2990.

[131] A. K. Mishra et al. "Spin fluctuations in Cr doped MnSi". In: *Journal of Magnetism and Magnetic Materials* 448 (2018), pp. 130–134.

[132] T. Moriya. "Theory of itinerant electron magnetism". In: *Journal of Magnetism and Magnetic Materials* 100.1-3 (1991), pp. 261–271.

[133] T. Moriya and A. Kawabata. "Effect of spin fluctuations on itinerant electron ferromagnetism". In: *Journal of the Physical Society of Japan* 34.3 (1973), pp. 639–651.

[134] T. Moriya and K. Ueda. "Antiferromagnetic spin fluctuation and superconductivity". In: *Reports on Progress in Physics* 66.8 (2003), p. 1299.

[135] E. Morosan et al. "Sharp switching of the magnetization in $Fe_{1/4}TaS_2$". In: *Physical Review B* 75.10 (2007), p. 104401.

[136] C. H. Mousatov, E. Berg, and S. A. Hartnoll. "Theory of the strange metal $Sr_3Ru_2O_7$". In: *PNAS* 117.6 (Feb. 2020), pp. 2852–2857. ISSN: 10916490.

[137] Y. Nakajima et al. "Quantum-critical scale invariance in a transition metal alloy". In: *Communications Physics* 3.1 (Dec. 2020), p. 181.

[138] Y. Nakajima et al. "Unusual Hall effect in quasi two-dimensional strongly correlated metal $CeCoIn_5$". In: *Physica C* 460-462 (Sept. 2007), pp. 680–681. ISSN: 0921-4534. DOI: 10.1016/J.PHYSC.2007.03.082.

[139] Y Nakashima et al. "Fermi-surface reconstruction involving two van Hove singularities across the antiferromagnetic transition in $BaFe_2As_2$". In: *Solid State Communications* 157 (2013), pp. 16–20.

[140] S. Nakatsuji, D. Pines, and Z. Fisk. "Two fluid description of the Kondo lattice". In: *Physical Review Letters* 92.1 (2004), p. 016401.

[141] D.H. Nguyen et al. "Superconductivity in an extreme strange metal". In: *Nature Communications* 12.1 (2021), pp. 1–8.

[142] Q. Niu et al. "Quasilinear quantum magnetoresistance in pressure-induced nonsymmorphic superconductor chromium arsenide". In: *Nature Communications* 8.1 (June 2017), pp. 1–6. ISSN: 20411723.

[143] M. Oshikawa. "Topological approach to Luttinger's theorem and the fermi surface of a kondo lattice". In: *Physical Review Letters* 84.15 (2000), p. 3370.

[144] J. Paglione et al. "Field-induced quantum critical point in $CeCoIn_5$". In: *Physical Review Letters* 91.24 (Dec. 2003), p. 246405. ISSN: 0031-9007.

[145] H. K. Pal and D. L. Maslov. "Linear magnetoresistance from Dirac-like fermions in graphite". In: *Physical Review B* 88.3 (July 2013), p. 035403. ISSN: 10980121.

[146] A. Park et al. "Quasiparticle scattering in 3 MeV proton irradiated $BaFe_2(As_{0.67}P_{0.33})_2$". In: *Physical Review B* 98.5 (Aug. 2018), p. 054512.

[147] S. Paschen et al. "Hall effect evolution across a heavy fermion quantum critical point". In: *Nature* 432.7019 (Dec. 2004), pp. 881–885. ISSN: 0028-0836.

[148] A. A. Patel et al. "Magnetotransport in a Model of a Disordered Strange Metal". In: *Physical Review X* 8.2 (May 2018), p. 021049. ISSN: 2160-3308. DOI: 10.1103/PhysRevX.8.021049. URL: https://link.aps.org/doi/10.1103/PhysRevX.8.021049.

[149] C. Petrovic et al. "Heavy fermion superconductivity in $CeCoIn_5$ at 2.3 K". In: *J. Phys. Condens. Matter* 13 (2001), pp. 337–342.

[150] H Pfau et al. "Detailed band structure of twinned and detwinned $BaFe_2As_2$ studied with angle-resolved photoemission spectroscopy". In: *Physical Review B* 99.3 (2019), p. 035118.

[151] H. Pfau et al. "Detailed band structure of twinned and detwinned $BaFe_2As_2$ studied with angle-resolved photoemission spectroscopy". In: *Physical Review B* 99.3 (Jan. 2019), p. 035118.

[152] L. D. Pham et al. "Reversible tuning of the heavy fermion ground state in $CeCoIn_5$". In: *Phys. Rev. Lett.* 97.5 (Aug. 2006), p. 056404. ISSN: 0031-9007.

[153] A. Piel. *Plasma physics: an introduction to laboratory, space, and fusion plasmas*. Springer, 2017.

[154] A. B. Pippard. *Magnetoresistance in metals*. Cambridge University Press, 2009.

[155] N.M. Plakida. *High T_c Superconductivity*. 1995.

[156] J. Polchinski. "Effective field theory and the Fermi surface". In: (1992).

[157] R. Prozorov et al. "Effect of Electron Irradiation on Superconductivity in Single Crystals of $Ba(Fe_{1-x}Ru_x)_2As_2$ (x = 0.24)". In: *Physical Review X* 4 (2014), p. 041032. URL: https://journals.aps.org/prx/pdf/10.1103/PhysRevX.4.041032.

[158] N. Ramakrishnan et al. "Equivalence of effective medium and random resistor network models for disorder-induced unsaturating linear magnetoresistance". In: *Physical Review B* 96.22 (Dec. 2017), p. 224203.

[159] B.J. Ramshaw et al. "Quasiparticle mass enhancement approaching optimal doping in a high-T_c superconductor". In: *Science* 348.6232 (2015), pp. 317–320.

[160] S. Ran et al. "Nearly ferromagnetic spin-triplet superconductivity". In: *Science* 365.6454 (2019), pp. 684–687.

[161] P. Rhodes and E. P. Wohlfarth. "The effective Curie-Weiss constant of ferromagnetic metals and alloys". In: *Proceedings of the Royal Society of London. Series A. Mathematical and Physical Sciences* 273.1353 (1963), pp. 247–258.

[162] P. Richard et al. "Fe-based superconductors: an angle-resolved photoemission spectroscopy perspective". In: *Reports on Progress in Physics* 74.12 (Nov. 2011), p. 124512.

[163] R. Ritz et al. "Formation of a topological non-Fermi liquid in MnSi". In: *Nature* 497.7448 (2013), pp. 231–234.

[164] A. Rosch. "Interplay of disorder and spin fluctuations in the resistivity near a quantum critical point". In: *Physical Review Letters* 82.21 (May 1999), pp. 4280–4283.

[165] A. Rosch. "Magnetotransport in nearly antiferromagnetic metals". In: *Physical Review B* 62.8 (Aug. 2000), pp. 4945–4962.

[166] M. Rotter et al. "Spin-density-wave anomaly at 140 K in the ternary iron arsenide $BaFe_2As_2$". In: *Physical Review B* 78.2 (July 2008), p. 020503. DOI: 10.1103/PhysRevB.78.020503.

[167] S. Rowley et al. "Ferromagnetic and ferroelectric quantum phase transitions". In: *physica status solidi (b)* 247.3 (2010), pp. 469–475.

[168] M.V. Sadovskii. "High-temperature superconductivity in iron-based layered iron compounds". In: *Physics-Uspekhi* 51.12 (2008), p. 1201.

[169] H. Sakai et al. "Microscopic investigation of electronic inhomogeneity induced by substitutions in a quantum critical metal $CeCoIn_5$". In: *Physical Review B* 92.12 (Sept. 2015), p. 121105. ISSN: 1098-0121.

[170] B. C. Sales et al. "Quantum Critical Behavior in a Concentrated Ternary Solid Solution". In: *Scientific Reports* 6.1 (May 2016), pp. 1–8. ISSN: 20452322. DOI: 10.1038/srep26179.

[171] T. Sarkar et al. "Correlation between scale-invariant normal-state resistivity and superconductivity in an electron-doped cuprate". In: *Science Advances* 5.5 (May 2019), eaav6753. ISSN: 23752548.

[172] S.S. Saxena et al. "Superconductivity on the border of itinerant-electron ferromagnetism in UGe2". In: *Nature* 406.6796 (2000), pp. 587–592.

[173] D. Schoerling and A.V. Zlobin. *Nb_3Sn Accelerator Magnets: Designs, Technologies and Performance*. Springer Nature, 2019.

[174] A.J. Schofield. "Non-fermi liquids". In: *Contemporary Physics* 40.2 (1999), pp. 95–115.

[175] S.E. Sebastian et al. "Heavy holes as a precursor to superconductivity in antiferromagnetic $CeIn_3$". In: *Proceedings of the National Academy of Sciences* 106.19 (2009), pp. 7741–7744.

[176] T. Senthil and M. P. A. Fisher. "Detecting fractions of electrons in the high-T_c cuprates". In: *Physical Review B* 64.21 (Nov. 2001), p. 214511.

[177] T. Senthil, M. Vojta, and S. Sachdev. "Weak magnetism and non-Fermi liquids near heavy fermion critical points". In: *Physical Review B* 69 (3 Jan. 2004), p. 035111.

[178] R. Settai et al. "Quasi-two-dimensional Fermi surfaces and the de Haas-van Alphen oscillation in both the normal and superconducting mixed states of $CeCoIn_5$". In: *J. Phys. Condens. Matter* 13 (2001), pp. 627–634.

[179] V.R. Shaginyan, K. G. Popov, and S.A. Artamonov. "Hall coefficient in heavy fermion metals". In: *Journal of Experimental and Theoretical Physics Letters* 82.4 (2005), pp. 215–219.

[180] C. Shekhar et al. "Extremely large magnetoresistance and ultrahigh mobility in the topological Weyl semimetal candidate NbP". In: *Nature Physics* 11.8 (2015), pp. 645–649.

[181] T. Shibauchi, A. Carrington, and Y. Matsuda. "A quantum critical point lying beneath the superconducting dome in iron pnictides". In: *Annual Review of Condensed Matter Physics* 5.1 (Mar. 2014), pp. 113–135. ISSN: 1947-5454. DOI: 10.1146/annurev-conmatphys-031113-133921.

[182] H. Shishido et al. "Evolution of the Fermi surface of $BaFe_2(As_{1-x}P_x)_2$ on entering the superconducting dome". In: *Physical Review Letters* 104.5 (Feb. 2010), p. 057008.

[183] W Shockley. "Effect of Magnetic Fields on Conduction—"Tube Integrals"". In: *Physical Review* 79.1 (1950), p. 191.

[184] D. Shoenberg. *Magnetic oscillations in metals*. Cambridge university press, 2009.

[185] Q. Si and F. Steglich. "Heavy fermions and quantum phase transitions". In: *Science* 329.5996 (2010), pp. 1161–1166.

[186] Q. Si and F. Steglich. "Heavy fermions and quantum phase transitions." In: *Science* 329.5996 (Sept. 2010), pp. 1161–1166. ISSN: 1095-9203.

[187] V. A. Sidorov et al. "Superconductivity and quantum criticality in $CeCoIn_5$". In: *Phys. Rev. Lett.* 89.15 (Sept. 2002), p. 157004. ISSN: 0031-9007.

[188] S. Singh et al. "Probing the quantum critical behavior of $CeCoIn_5$ via Hall effect measurements". In: *Physical Review Letters* 98.5 (2007), p. 057001.

[189] J. Singleton. "Temperature scaling behavior of the linear magnetoresistance observed in high-temperature superconductors". In: *Physical Review Materials* 4.6 (2020), p. 061801.

[190] J. C. W. Song, G. Refael, and P. A. Lee. "Linear magnetoresistance in metals: Guiding center diffusion in a smooth random potential". In: *Physical Review B* 92.18 (Nov. 2015), p. 180204. URL: https://journals.aps.org/prb/abstract/10.1103/PhysRevB.92.180204.

[191] R. S. Sorbello. "Effects of anisotropic scattering on electronic transport properties". In: *Physics of condensed matter* 19.1 (Mar. 1975), pp. 303–316. (Visited on 06/12/2020).

[192] F. Steglich et al. "Superconductivity in the presence of strong pauli paramagnetism: $CeCu_2Si_2$". In: *Physical Review Letters* 43.25 (1979), p. 1892.

[193] H. Steinberg et al. "Charge fractionalization in quantum wires". In: *Nature Physics* 4.2 (2008), pp. 116–119.

[194] C. Stock et al. "Spin resonance in the d-wave superconductor $CeCoIn_5$". In: *Physical Review Letters* 100.8 (Feb. 2008), p. 087001.

[195] B. P. Stojković and D. Pines. "Theory of the longitudinal and Hall conductivities of the cuprate superconductors". In: *Physical Review B* 55 (13 Apr. 1997), pp. 8576–8595.

[196] M. Sundermann et al. "Orientation of the ground-state orbital in $CeCoIn_5$ and $CeRhIn_5$". In: *Physical Review B* 99.23 (2019), p. 235143.

[197] L. Taillefer. "Scattering and pairing in cuprate superconductors". In: *Annu. Rev. Condens. Matter Phys.* 1.1 (2010), pp. 51–70.

[198] Y. Takahashi. *Spin fluctuation theory of itinerant electron magnetism*. Vol. 9. Springer, 2013.

[199] MA Tanatar et al. "Uniaxial strain detwinning of $CaFe_2As_2$ and $BaFe_2As_2$: optical and transport study". In: *arXiv preprint arXiv:1002.3801* (2010).

[200] T. Terashima et al. "Complete Fermi surface in $BaFe_2As_2$ observed via Shubnikov-de Haas oscillation measurements on detwinned single crystals". In: *Physical Review Letters* 107.17 (Oct. 2011), p. 176402. ISSN: 00319007.

[201] Pascal Tixador. "Superconducting magnetic energy storage (SMES) systems". In: *Electricity transmission, distribution and storage systems*. Elsevier, 2013, pp. 442–477.

[202] Y. Tokiwa, E.D. Bauer, and P. Gegenwart. "Zero-field quantum critical point in $CeCoIn_5$". In: *Physical Review Letters* 111.10 (2013), p. 107003.

[203] Y. Tokiwa et al. "Quantum bicriticality in the heavy-fermion metamagnet YbAgGe". In: *Physical review letters* 111.11 (2013), p. 116401.

[204] O. Trovarelli, C. Geibel, and F. Steglich. "Low-temperature properties of $YbRh_2Si_2$". In: *Physica B: Condensed Matter* 284 (2000), pp. 1507–1508.

[205] G. S. Tucker et al. "Crossover from spin waves to diffusive spin excitations in underdoped $Ba(Fe_{1-x}Co_x)_2As_2$". In: *Physical Review B* 89.18 (May 2014), p. 180503.

[206] J.C. Tully. "Perspective on "zur quantentheorie der molekeln"". In: *Theoretical Chemistry Accounts* 103.3 (2000), pp. 173–176.

[207] YJ Uemura et al. "Universal correlations between T_c and n_s/m^* (carrier density over effective mass) in high-T_c cuprate superconductors". In: *Physical review letters* 62.19 (1989), p. 2317.

[208] N. Umeyama et al. "Synthesis and magnetic properties of NiSe, NiTe, CoSe, and CoTe". In: *Japanese Journal of Applied Physics* 51.5R (2012), p. 053001.

[209] B. Van Laar, H. M. Rietveld, and D. J. W. Ijdo. "Magnetic and crystallographic structures of Me_xNbS_2 and Me_xTaS_2". In: *Journal of Solid State Chemistry* 3.2 (1971), pp. 154–160.

[210] C.M. Varma, Z. Nussinov, and W. Van Saarloos. "Singular or non-Fermi liquids". In: *Physics Reports* 361.5-6 (2002), pp. 267–417.

[211] M. Vershinin et al. "Local ordering in the pseudogap state of the high-T c superconductor $Bi_2Sr_2CaCu_2O_{8+\delta}$". In: *Science* 303.5666 (2004), pp. 1995–1998.

[212] M. Vojta. "Quantum phase transitions". In: *Reports on Progress in Physics* 66.12 (2003), p. 2069.

[213] N. V. Volkenshtein, V. P. Dyakina, and V. E. Startsev. "Scattering mechanisms of conduction electrons in transition metals at low temperatures". In: *Physica Status Solidi B* 57.1 (May 1973), pp. 9–42.

[214] G.E. Volovik. "Quantum phase transitions from topology in momentum space". In: *Quantum analogues: from phase transitions to black holes and cosmology*. Springer, 2007, pp. 31–73.

[215] N. Wakeham et al. "Gross violation of the Wiedemann–Franz law in a quasi-one-dimensional conductor". In: *Nature communications* 2.1 (2011), pp. 1–6.

[216] X. Wang et al. "Superconductivity mediated by quantum critical antiferromagnetic fluctuations: The rise and fall of hot spots". In: *Physical Review B* 95 (17 May 2017), p. 174520. URL: https://link.aps.org/doi/10.1103/PhysRevB.95.174520.

[217] Matthew D Watson et al. "Probing the reconstructed Fermi surface of antiferromagnetic $BaFe_2As_2$ in one domain". In: *npj Quantum Materials* 4.1 (2019), pp. 1–9.

[218] R.H. White and T.H. Geballe. *Long Range Order in Solids. Chap. VII*. 1979.

[219] E.P. Wohlfarth. "Very weak itinerant ferromagnets; Application to $ZrZn_2$". In: *Journal of Applied Physics* 39.2 (1968), pp. 1061–1066.

[220] F. Wu, E. Hwang, and S.D. Sarma. "Phonon-induced giant linear-in-T resistivity in magic angle twisted bilayer graphene: Ordinary strangeness and exotic superconductivity". In: *Physical Review B* 99.16 (2019), p. 165112.

[221] S. Yano et al. "Magnetic structure of $NiS_{2-x}Se_x$". In: *Physical Review B* 93.2 (2016), p. 024409.

[222] T. Yoshida et al. "Two-Dimensional and Three-Dimensional Fermi Surfaces of Superconducting $BaFe_2(As_{1-x}P_x)_2$ and Their Nesting Properties Revealed by Angle-Resolved Photoemission Spectroscopy". In: *Physical Review Letters* 106 (11 Mar. 2011), p. 117001.

[223] Y.-Z. Zhang et al. "Itinerant nature of magnetism in iron pnictides: A first-principles study". In: *Physical Review B* 81.9 (2010), p. 094505.

[224] Jun Zhao et al. "Spin and lattice structures of single-crystalline $SrFe_2As_2$". In: *Physical Review B* 78.14 (2008), p. 140504.

[225] B. B. Zhou et al. "Visualizing nodal heavy fermion superconductivity in $CeCoIn_5$". In: *Nat. Phys.* 9.8 (Aug. 2013), pp. 474–479.

Appendix A

Measurements of electrical transport in extreme environments

The resistance to first-order determines the linear response of a material to an applied electric field. More microscopic insight is given elsewhere in this thesis, but for now we are concerned with these phenomenological equations.

$$V = IR, \tag{A.1}$$

or equivalently

$$I = GV, \tag{A.2}$$

where $G = R^{-1}$ is the conductance. V is the applied voltage, and I is the current generated. Or, as is usually the case in practical measurements, I is the applied current, and V is the voltage drop generated by it.

R, V, I, and G are extrinsic quantities, in that their values are dependent on the specific geometry of the sample under test — if a sample is particularly thin, V may have a larger value for a given I than if the sample is particularly thick, even though it is the exact same material. More material-specific insight can be gained by normalizing out geometrical factors. Then, $R \to \rho$, $I \to J$, and $V \to E$, and $G \to \sigma$. ρ is the resistivity, σ is the conductivity, J is the current density, and E is the electric field. Ohm's law in this language becomes

$$\begin{aligned} J &= \sigma E \\ E &= \rho J, \end{aligned} \tag{A.3}$$

where $\sigma = \rho^{-1}$. Of course, real measurements are carried out on samples of finite dimensions such that measurements give values of V and I. Then the intrinsic values of ρ and σ can be backed out by the experimentalist by taking into account the sample dimensions (distance between voltage terminals, thickness, cross-sectional area, etc). This process will be discussed

later, but first we will determine some fundamental symmetry-based constraints, which apply equally well to either ρ or R tensors.

In general, the voltage drop across a sample, V (generally understood as a voltage difference between two points on the sample), and I are three-dimensional vectors because current can be applied along any direction in 3-space inducing a corresponding voltage difference that can be decomposed into its x, y, and z components. Therefore, R and G are both 3×3 tensors, and the inverse of R should be understood as a matrix inverse.

$$\begin{pmatrix} V_x \\ V_y \\ V_z \end{pmatrix} = \begin{pmatrix} R_{xx} & R_{xy} & R_{xz} \\ R_{yx} & R_{yy} & R_{yz} \\ R_{zx} & R_{zy} & R_{zz} \end{pmatrix} \begin{pmatrix} I_x \\ I_y \\ I_z \end{pmatrix} \tag{A.4}$$

At first glance, it appears very challenging to determine any one component of the resistivity tensor, given that each induced voltage drop is the result of a linear combination of three unknown terms. Luckily, there are symmetry-based constraints on the resistivity tensor which make this process considerably easier. The Onsager-Casimir relations tell us about the reciprocity of the conductivity tensor components in an applied magnetic field [30].

$$\begin{aligned} G_{ij}(H) &= G_{ji}(-H) \\ R_{ij}(H) &= R_{ji}(-H). \end{aligned} \tag{A.5}$$

Longitudinal resistivities

Eq. A.5 directly implies that, in the absence of a magnetic field, the off-diagonal components of the resistivity tensor are all zero. Eq. A.6 in zero magnetic field becomes

$$\begin{pmatrix} V_x \\ V_y \\ V_z \end{pmatrix} = \begin{pmatrix} R_{xx} & 0 & 0 \\ 0 & R_{yy} & 0 \\ 0 & 0 & R_{zz} \end{pmatrix} \begin{pmatrix} I_x \\ I_y \\ I_z \end{pmatrix}. \tag{A.6}$$

To determine the values of R_{xx}, R_{yy}, and R_{zz} at zero field, one needs to only send the current along a specific direction of the material, for example along one of the crystallographic a, b, and c axes, and measure the induced voltage. Fig. A.1 shows the typical measurement setup.

Now, if the sample has a rectangular geometry, the resistance of the sample for example measured along x ($R_{xx} = V_x/I_x$) can be converted to a resistivity through the geometrical factors [15, 65].

$$R_i = \frac{\rho_i l_i}{t_k w_j}, \tag{A.7}$$

where i indicates the coordinate axis (x, y, or z) along which the current and voltage are measured. $A = t_k w_j$ is the cross sectional area of the rectangular sample (t_k is the thickness along k and w_j is the width along j; $t_k w_j$ is the area perpendicular to the direction along

which the current is run), and l_i is the distance between the measurement terminals along the direction that current is being run.

Hall (transverse) resistivities

Likewise, Eq. A.5 suggests that the off-diagonal components of the resistivity tensor can be nonzero when a magnetic field is applied. By carefully aligning the direction of the magnetic field and measurement terminals, we can isolate different off-diagonal resistivity components. As an example, consider a current applied only along the x direction of a crystal, then

$$\begin{aligned} R_{xx} &= \frac{V_x}{I_x} \\ R_{yx} &= \frac{V_y}{I_x}. \\ R_{zx} &= \frac{V_z}{I_x} \end{aligned} \tag{A.8}$$

Note that for measurements of, let's say R_{yx}, a voltage perpendicular to the current direction needs to be generated. Application of a magnetic field can lead to such a voltage due to the action of the Lorentz force $\mathbf{F}_{lorentz} \propto \mathbf{I} \times \mathbf{B}$. In the steady state, charges will build up to generate a voltage that counteracts the Lorentz force ($qV_{transverse} = -\mathbf{F}_{lorentz}$). This is simply because of the constraints of the experiment — I_y and I_z must both equal zero — there is nowhere for charges to go if they were to flow in either of these directions. If $\mathbf{B}$ is only directed along the z direction, then a Lorentz force and corresponding voltage are generated along V_y. If $\mathbf{B}$ is only directed along y, then a voltage is generated along z. Fig. A.1 shows how the orientation of the magnetic field determines which voltages are nonzero, and how the transverse voltages could be measured to determine the off-diagonal resistance tensor components.

Once the transverse resistances have been measured, they need to be converted to resistivities by normalizing out the length-scales associated with the sample geometry. This is captured by the following formula [15],

$$\rho_{ij} = t_k R_{ij}, \tag{A.9}$$

where t_k is the length of the sample along the k direction (perpendicular to both i and j).

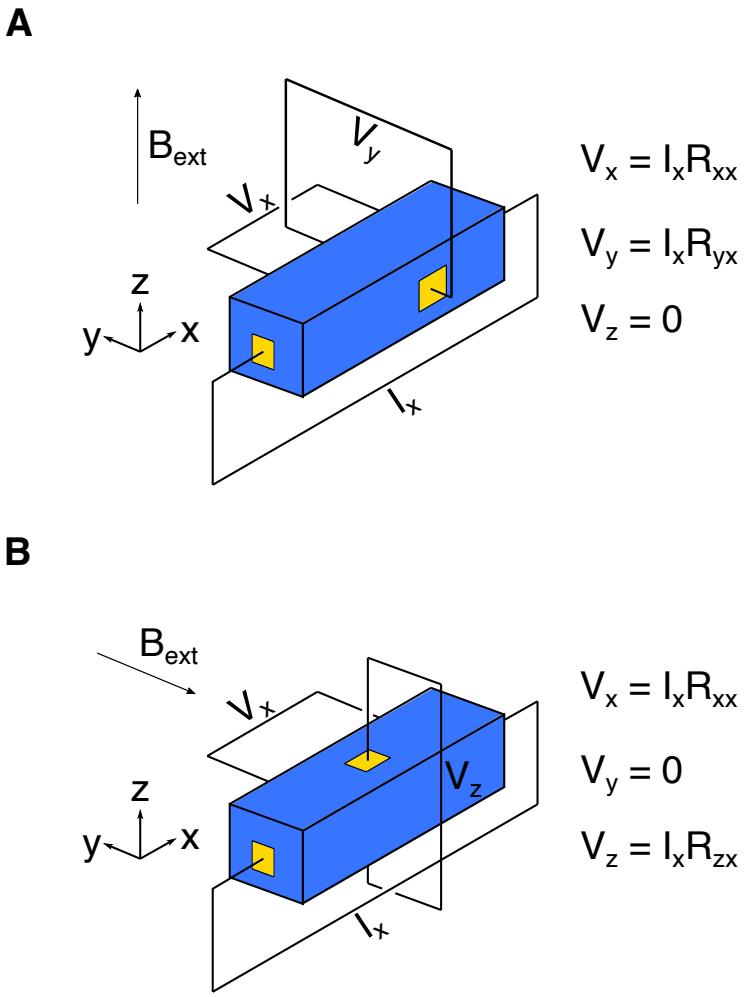

Figure A.1: **Four-terminal measurement scheme A** Measurement of the transverse resistivity V_y in an external magnetic field B_{ext} directed along z and current directed along x. **B** Measurement of the transverse resistivity V_z in an external magnetic field directed along y.

Experimental contact alignment and (anti)symmetrizing with respect to magnetic field

In general, all components of the resistance tensor may depend on magnetic field. The above arguments for isolating R_{xx}, R_{xy}, R_{xz} work as long as the measurement terminals are perfectly aligned. That is, when a voltage generated by a magnetic field is measured, each corresponding measurement terminal picks up only the voltage drop along x, y, and z. In reality, there might be some misalignment, such that the actual voltage drop seen by a given set of measurement terminals contains some linear combination of V_x, V_y, and V_z.

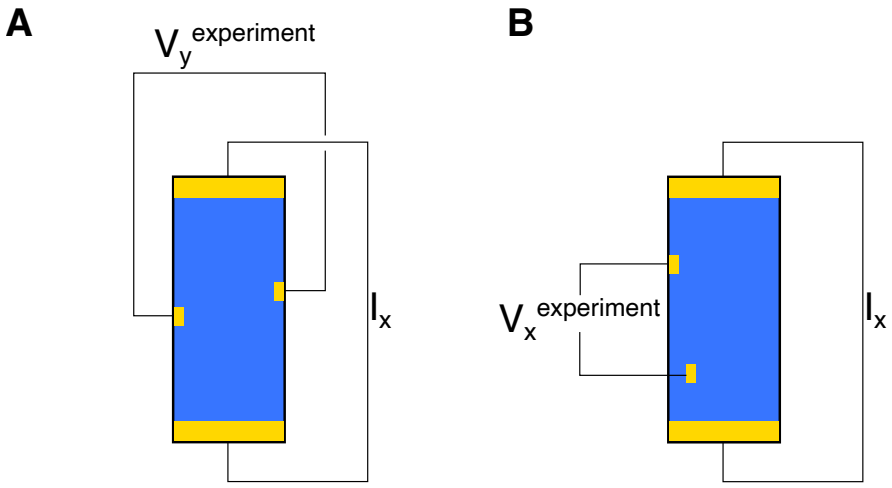

Figure A.2: **Cartoons of experimental contact misalignment which can lead to A** spurious V_x component in the $V_y^{experiment}$ contacts, and **B** spurious V_y voltage in the $V_x^{experiment}$ contacts.

For the sake of argument, suppose we are interested in measuring R_{xx} and R_{xy}. Measurement terminals are placed on one face of the sample in the V_x and V_y directions. It is relatively straightforward to minimize the amount of V_z voltage drop in these measurement terminals. One needs to polish or cleave a sample along the z direction so that the xy plane has a flat face (this argument also applies to measurements in the xz or yz planes of a crystal, but for this example we are considering xy). On the other hand, experimentally the measurement terminals for $V_x^{experimental}$ and $V_y^{experimental}$ are likely to contain some amount of voltage drop from both the x and y directions, which we can quantify by the 'degree of misalignment' of the contacts, p. These types of misalignments are shown schematically in the exaggerated cartoon Fig. A.2. Note that even with lithographically defined contacts, their finite width and uncertainty in metal deposition is bound to generate some amount of contact misalignment. It is experimentally unfeasible to generate contacts with $p = 0$. Then, the experimentally measured voltage drops in the real measurement terminals are

$$\begin{aligned} V_x^{experiment} &= V_x + V_y p \\ V_y^{experiment} &= V_x p + V_y. \end{aligned} \tag{A.10}$$

At zero field, $V_y = 0$, so while the $V_y^{experiment}$ contacts may pick up a spurious nonzero voltage at zero applied magnetic field, the $V_x^{experiment}$ contacts still give a reliable measurement of the V_x signal. On the other hand, in magnetic field, V_y becomes nonzero and both experimentally measured voltages contain some component of V_x and V_y. We can still isolate the real voltage drops along x and y directions in magnetic field, $V_x(B)$ and $V_y(B)$, from the experimentally measured voltage drops by employing the constraints imposed by the Onsager-Casimir symmetry relations. In particular, the reciprocity relations Eq. A.5 [30] imply that

$$\begin{aligned} R_{xx}(H) &= R_{xx}(-H) \\ R_{xy}(H) &= -R_{yx}(-H) = -R_{xy}(-H), \end{aligned} \tag{A.11}$$

and, simply plugging in the relations A.8, we find that

$$\begin{aligned} V_x(H) &= V_x(-H) \\ V_y(H) &= -V_y(-H) \end{aligned} \tag{A.12}$$

In simple terms, for a current driven along x and field along z, V_x is even in field, while V_y is odd in field. This means that even though the there may be some mixing between the intrinsic V_x and V_y in the experimentally measured voltage differences, we can isolate them using the parity relations Eqs. A.12 — the intrinsic field-dependence of V_x and V_y can be obtained by measuring the voltage difference in a positive and negative magnetic field, and then adding or subtracting the results of the two measurements.

$$\begin{aligned} \frac{V_x^{experiment}(H) + V_x^{experiment}(-H)}{2} &= V_x(H) \\ \frac{V_y^{experiment}(H) - V_y^{experiment}(-H)}{2} &= V_y(H) \end{aligned} \tag{A.13}$$

Measuring the voltage

Given the conclusions of the previous section, different linear-response resistivity components of a material can be obtained by sourcing a current and measuring a voltage, sometimes in an applied magnetic field. Sourcing a current is simple enough with a commercial current source, but how do we measure the voltage generated in such a configuration? This section gives an overview of the techniques use to perform precision measurements of the voltage (either longitudinal and transverse) produced by a current applied to a sample in extreme environments, i.e. at cryogenic temperatures and high magnetic fields. These sections describe the measurement circuits and apparatuses, considerations about desired sample properties, and considerations about optimizing measurement conditions in resistance measurements. Generally, all of the following considerations apply whether we are interested in measuring a longitudinal or transverse (Hall) voltage. We will not differentiate between the two in the following sections, as the voltage measurements are conducted in essentially the same way in either case.

Measurement circuit

This section describes the four- and two-terminal measurement circuits, and gives motivation for why the four-terminal measurement circuit is preferred for resistivity measurements in cryogenic setups.

Two-terminal measurements

Fig. A.3 shows a diagram of an electrical resistivity experiment using the two-terminal measurement scheme. The measurement apparatuses are kept at room temperature on a measurement rack with cabling that leads to the cryostat, and wires that run down the cryostat to the sample chamber. The sample temperature can then be manipulated by the cryostat while the resistance of the sample is monitored. In reality, the cabling leading to the cryostat, the cabling inside the cryostat, and the sample's measurement terminals all have their own resistances, as depicted schematically in Fig. A.3.

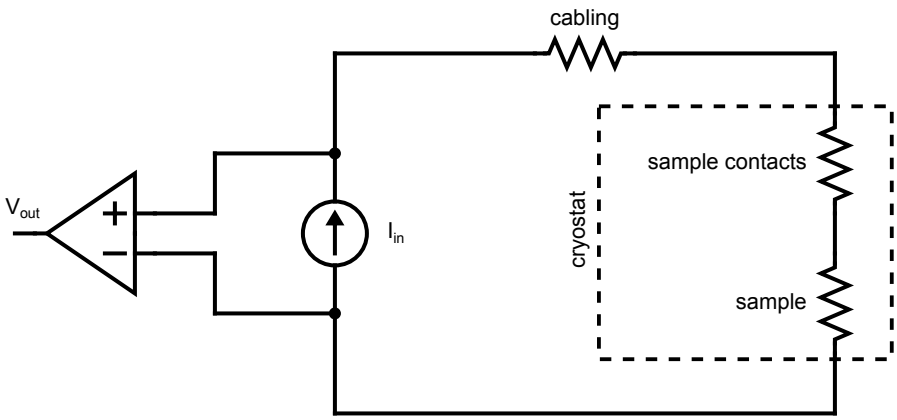

Figure A.3: **Two-terminal measurement scheme** The force and sense leads are the same. The measured voltage V_{out} includes the resistance of the sample, the cabling, and the sample contacts. The latter two can have a rather large temperature dependence, which complicates the determination of the sample resistance.

While this scheme is simple, the issue with the two-terminal measurement technique is that the voltage drop is measured over the resistance of all of the cabling and contacts leading up to the sample.

$$V_{out} = I_{in} \left(R_{cabling} + R_{contacts} + R_{sample} \right) \tag{A.14}$$

This is problematic, especially because the resistances of the samples measured in such conditions can be on the order of hundreds or even tens of milliOhms, while the cabling and wires leading to the sample is usually on the order of tens of Ohms, and will therefore completely swamp the signal from the sample. A further complication is that the resistance of the cabling inside the cryostat and the sample contacts may depend on temperature. As a consequence, it is very difficult to isolate the sample resistance in this scenario.

Four-terminal measurements

A better scheme is the so-called "4-terminal" measurement technique (depicted schematically in Fig. A.4A), where the force and sense terminals are all placed on the sample itself. In this scheme, the output voltage reflects only the voltage drop across the sample between the sense leads, and the resistance of the sample can be determined straightforwardly by measuring the voltage generated using a fixed source current.

$$V_{out} = I_{in} R_{sample} \tag{A.15}$$

A photograph of a real sample prepared for this technique is shown in Fig. A.4B; it is of course critical that the force and sense leads are electrically isolated from each other apart from the current path through the sample itself. If they are connected together through a relatively low-resistance 'short', a parallel conductance path with the sample is generated. In this case, current runs directly between the force and sense terminals rather than the sample, inducing a spurious voltage on the output.

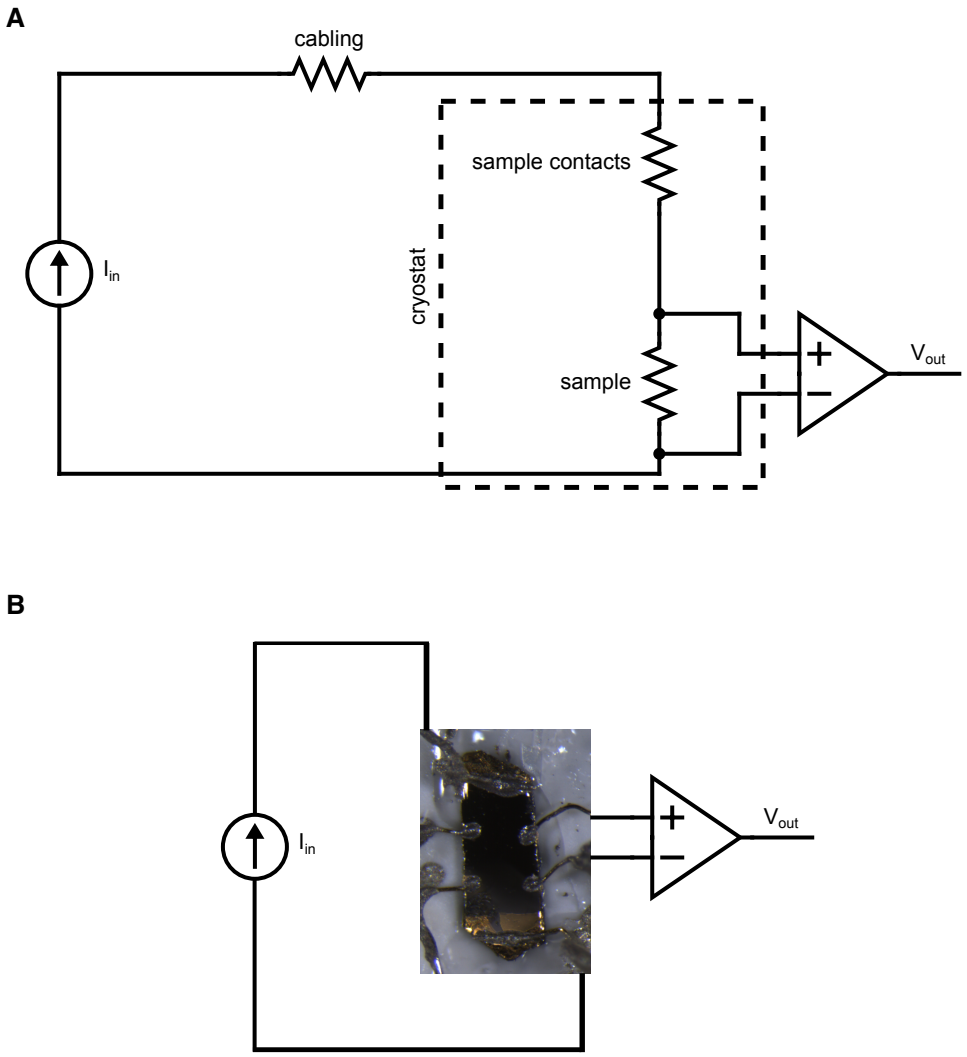

Figure A.4: **Four-terminal measurement scheme** (A) Shows a circuit diagram. The sense leads are attached to the sample between the force leads. The measured voltage V_{out} includes the only the resistance of the sample. (B) Shows a diagram including a photograph of a real sample taken under an optical microscope. The black rectangle is the sample, and the force and sense leads are attached to different regions of the sample for a four-terminal measurement.

Linear response regime: limitations on the amplitude of the source current

Ohm's law (A.2) implies that the voltage drop across the sample is directly proportional to the current, with a constant of proportionality determined by the resistance. While there may be higher-order resistivity terms that are intrinsic to the sample that lead to non-Ohmic behavior, i.e. terms which are proportional to I^3, I^5, etc, it is more often the case that the dominant source of non-Ohmic behavior is extrinsic to the sample. In addition, for the most part we are interested in the linear response in resistivity measurements. Typically, the linear response regime occurs in the limit of small drive currents. Nonlinear response at higher drive currents often results from Joule heating, which effectively places an upper limit on the operating drive current of resistance measurements. A characteristic example illustrating this principle is given below.

Test resistor example: linear response at low currents and nonlinearity from Joule heating

As an illustrative example, the current-voltage characteristics of a 1.5 Ω carbon test resistor at room temperature are shown in Fig. A.5. As expected, at low currents the measured voltage obeys Ohm's law and is almost perfectly proportional to the applied current, with a constant of proportionality of 1.488 Ω, giving a measured resistance that is well within the manufacturer's 5% tolerance. At higher levels of current, the characteristics become severely nonlinear, deviating from Ohm's law. Based on these measurements, if one were to apply too large of a measurement current, the value of V/I would severely underestimate the actual resistance of the sample as highlighted in Fig. A.5B. These measurements illustrate the fact that the resistance of a sample can only be accurately determined when the source current is sufficiently low such that V is linear in I.

Using a simple model, we can attribute the non-Ohmic nonlinearity at higher values of applied current to current-induced heating of the sample. An applied current will Joule heat the sample by inducing a power of $P = I^2R$. Assuming that all of this power goes into the sample itself (a rough approximation), this will cause the temperature of the sample to rise by $\Delta T = P/C$, where C is the heat capacity of the sample. Because the resistance of any material is temperature-dependent, this temperature rise in turn induces a change in the resistance of the sample. For this example, a carbon resistor, i.e. an insulator, the resistance has a characteristic temperature dependence of the form $R(T) = Ae^{B/T}$, where A, B are material-specific constants of proportionality. As a result of Joule heating, the voltage-current relationship becomes

$$V = IR = I\left[A\exp\left(\frac{B}{T_0 + I^2R_0/C}\right)\right], \tag{A.16}$$

where T_0 and R_0 are the nominal temperature and resistance of the sample without an applied current. In Fig. A.5, we see that Eq. A.16 qualitatively captures the nonlinear behavior of V

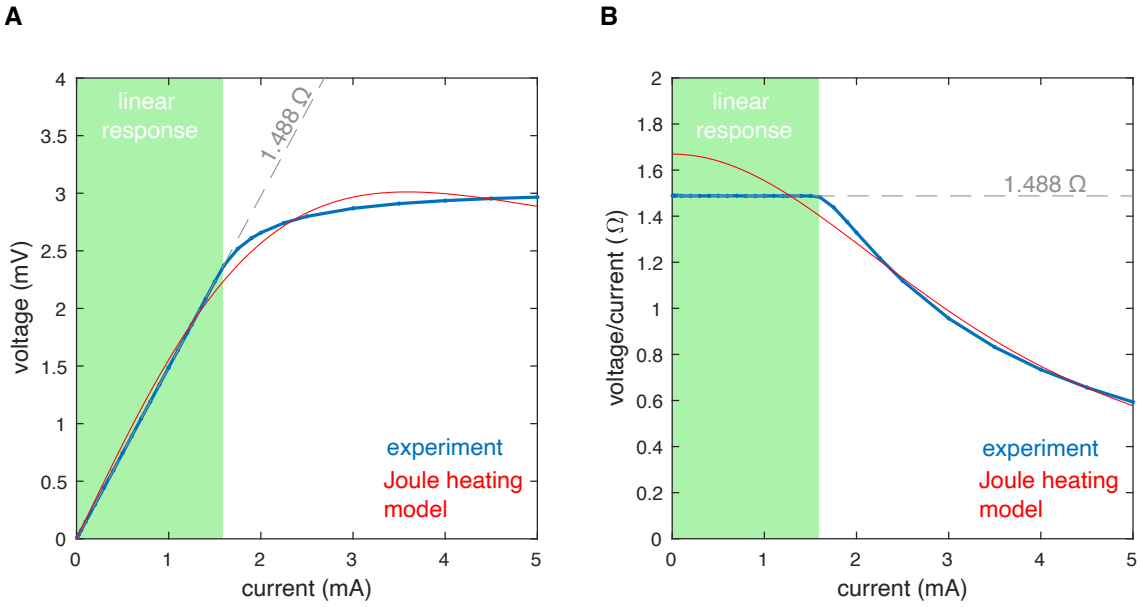

Figure A.5: **Representative current-voltage characteristics of a 1.5 Ω (±5%) test resistor A** Shows the measured voltage drop across the resistor as a function of drive current. The blue line is experimental data. At low currents, Ohm's law is well-obeyed and the voltage is almost perfectly linear in current with a constant of proportionality of 1.488 Ω, a measured resistance that is within 1% of the nominal resistance value of the test resistor, as illustrated by the gray dashed line. Considerable nonlinearity onsets at higher current levels. The overall behavior seen in the experiment across both regimes is reasonably well-described by considering the effects of Joule heating, which induce nonlinearity primarily at higher current levels (see text). **B** Same as panel A, but the y-axis is current divided by voltage. The plateau behavior at low current levels highlights the almost perfect linear response of voltage versus current at low currents, which gives the actual resistance of the sample. In the nonlinear regime at higher current levels, the value of current/voltage severely undershoots the actual resistance of the sample. Resistance measurements on this sample should be conducted in the green region, where the effects of Joule heating are minimized.

vs I at high drive currents; the curves shown in the figure are fits to the data where A, B, C are free parameters. More intuition about the effect of heating can be gained by expanding Eq. A.16 in orders of current.

$$V = IR_0 - I^3 \left[\frac{BR_0^2}{CT_0^2}\right] + \mathcal{O}(I^5). \tag{A.17}$$

The addition of heating results in higher-order terms that reduce the voltage relative to the expectations of straightforward Ohm's law without heating ($V = IR_0$). This type of sublinearity is observed in the experiment as seen in Fig. A.5.

The example shown above is essentially representative of almost all resistance measurements of real samples. Specific details may change (for example the overall behavior of the non-linear regime) depending on whether the sample is metallic or insulating, but overall most samples have the following features. They show linear, Ohmic current-voltage characteristics in the limit of zero current (where the proportionality is determined by the actual sample resistance), which transitions to a non-Ohmic regime at high values of current (where extrinsic effects such as Joule heating come into play). Resistance measurements should be carried out in the Ohmic regime at sufficiently low values of current, where the measured resistance is independent of the drive current (the green regions of Fig. A.5).

In principle, the threshold current between the linear and nonlinear regimes may change during the course of a measurement, let's say at different temperature or magnetic fields. The current-voltage characteristics should in theory be determined at each specified measurement condition. In practice, this process is too slow, and typically the current-voltage characteristics are only checked at the start of the measurement and a sufficiently low drive current well within the Ohmic regime is selected. The current-voltage characteristics can be periodically checked over the course of the measurement to ensure a low enough current is being used throughout.

Measuring the voltage induced by a drive current using lock-in amplification

Finally, we address the issue of actually measuring the voltage drop across the sample induced by the drive current. The most straightforward method is to source a DC current, and measure the voltage drop with a voltmeter (for example a Keithley 2100 digital multimeter). The issue with DC measurements is that the DC voltages of different nodes in the circuit may drift relative to one another due to, for example, ground loops or an imperfect ground reference. In addition, these measurements generally have relatively low sensitivity, and are unsuitable for measurement of low signal samples. The next best method is to use some sort of 'effective' AC method, where a negative and positive DC current pulse are applied to the sample in quick succession, and the DC voltage drop across the sample is measured in each case and averaged (such a setup is possible with a Keithley 6221 current source in conjunction with a Keithley 2182A nanovoltmeter).

However, the state-of-the-art, highest sensitivity method to measure the voltage induced by a drive current across a sample is by using lock-in amplification techniques. In this setup, a relatively low-frequency drive current, in the range of 1 Hz - 1 MHz is sourced through the current leads, and the output voltage on the sense leads is demodulated with a reference oscillator at the same frequency of the drive current. The demodulated voltage may have components that are in-phase and out-of-phase with the drive current — each of these can be separately demodulated in modern lock-in amplifiers. In a purely resistive measurement, the demodulated voltage only has an in-phase component (as we will discuss later), which can be used to recover the resistance of the sample ($R = V_{in-phase}/I$). In this case, what is meant by low-frequency drive current is that the frequency is low with respect to the characteristic timescale of the electronic response of a material (which is typically in the THz regime — electrons move very fast!). Thus, this technique gives effectively a measurement of the electrical response of the sample in the zero frequency limit. There are two main reason that a low, but finite frequency excitation is used in these measurements. First, sources of pesky DC offsets in the measurement circuit do not need to be corrected for. Second, low-frequency demodulation typically results in very high signal-to-noise ratios — on general grounds much higher than any sort of DC measurement technique.

Limitations on drive frequency

There is one main limitation to using the AC modulation/lock-in amplification technique to measure the resistance of a sample. In particular, the drive frequency must be carefully selected to be in a regime where the demodulated voltage is independent of drive frequency over an extended range. This is because, at least over the relatively low frequency ranges of these measurements, we do not expect resistive samples to have an intrinsic frequency-dependence to the conductivity. Frequency-dependence generally comes from extrinsic sources of reactive components in the measurement circuit, which obscure the actual resistance measurement of the sample itself.

We can understand the above condition by considering the measurement circuit using a lumped-element model. Assuming we are using the 4-terminal technique, the resistance (R) is the sample. The cabling leading to the sample and the electrical contacts on the sample (the joint where the electrode is in electrical contact with the sample surface), induce an inductance (L) and capacitance (C) in the circuit. The capacitance might represent, for example, the interface between the sense terminal and the sample itself, where sometimes the oxidized surface of the sample creates a dielectric barrier. The inductor in the lumped element circuit describes features like the self-inductance of the cabling and connectors leading up to the sample platform.

The total impedance of this lumped element circuit is

$$Z = R + i\omega L - i\frac{1}{\omega C}, \tag{A.18}$$

where ω is the frequency at which the circuit is driven. Two things are fairly apparent from this. The imaginary components which lead to an out-of-phase response in the detected signal, are primarily determined by the inductive and capacitive elements in the circuit. If the sample resistance is the only impedance present in the circuit, the response will be completely in-phase with the drive current. Finally, inductive and capactive components are responsible for the frequency-dependence of the signal in this model. The resistance should have a completely frequency-independent response.

Resistance measurements should therefore be carried out in a frequency regime where the out of phase signal is close to zero. Typically, this occurs in a frequency window in which the detected signal is independent of frequency. When the phase is significant, or the out-of-phase voltage is comparable to the in-phase voltage signal, the capacitance and inductance of circuit elements extrinsic to the sample are present in both the in phase and out of phase responses, and the resistance can not be recovered from either the in-phase or out-of-phase signals without a priori knowledge about the values of L and C. The bottom line is that if the phase is not close to zero, the results of the measurement do not reflect the resistance of the sample.

Transport measurements in pulsed magnetic fields

Shown in Fig. A.7 is the circuit diagram of the 4-point resistance measurement in pulsed magnetic fields. An AC voltage of 2V is supplied by a digital source, and sent through a resistor of variable value to generate the desired current. This current is DC isolated from the rest of the circuit by a transformer. A 10Ω resistor at room temperature is wired in series with the rest of the circuit, and the voltage over this element is measured separately during the course of the pulse to monitor the current level. The current is fed through the sample, at which point the resulting voltage drop across the sample is measured by the standard 4-point technique. The samples wired for pulsed field measurement look quite similar to the samples described in the previous sections. The one difference is, because the change in flux around the cabling and sample is so large, it is beneficial to decrease the loop area of the circuit which is exposed to the magnetic field to minimize inductive pickup during the field pulse. Therefore, twisted pair wires are attached as close to the sample as possible (Fig. A.6.

The resulting sample signal is digitized at about a 16 MHz clock rate, and lock-in detection is done in post processing. In order to get sufficient density of data points during the 100 ms field pulse to perform demodulation, the frequency of the drive current needs to be relatively high, on the order of 100 kHz to 1 MHz. At these frequencies, parasitic inductance becomes problematic, so it is rather important that the sample contacts have a low contact resistance (ideally less than 100Ω).

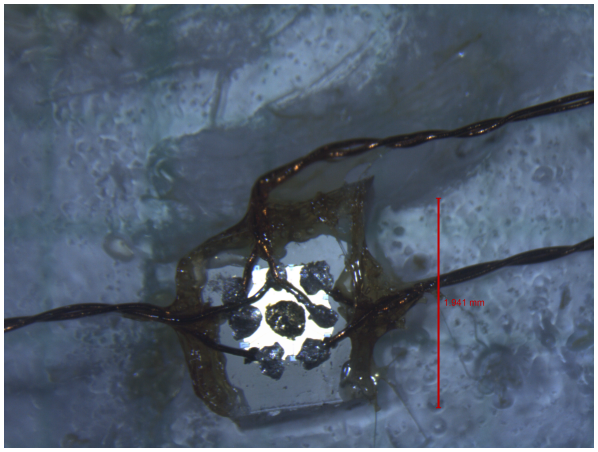

Figure A.6: **Image of a sample mounted on a substrate wired with twisted pair for pulsed field measurements** The device sits at the center of the gold square with contacts lithographically defined by the focused ion beam. Insulated copper wires of 0.001 inch diameter are twisted by hand. The insulation is stripped off at the ends, and electrical connection is made to the subtrate with silver epoxy. GE varnish (orange) provides structural stability so that the wires can be manipulated into position freely without damaging the sample contacts.

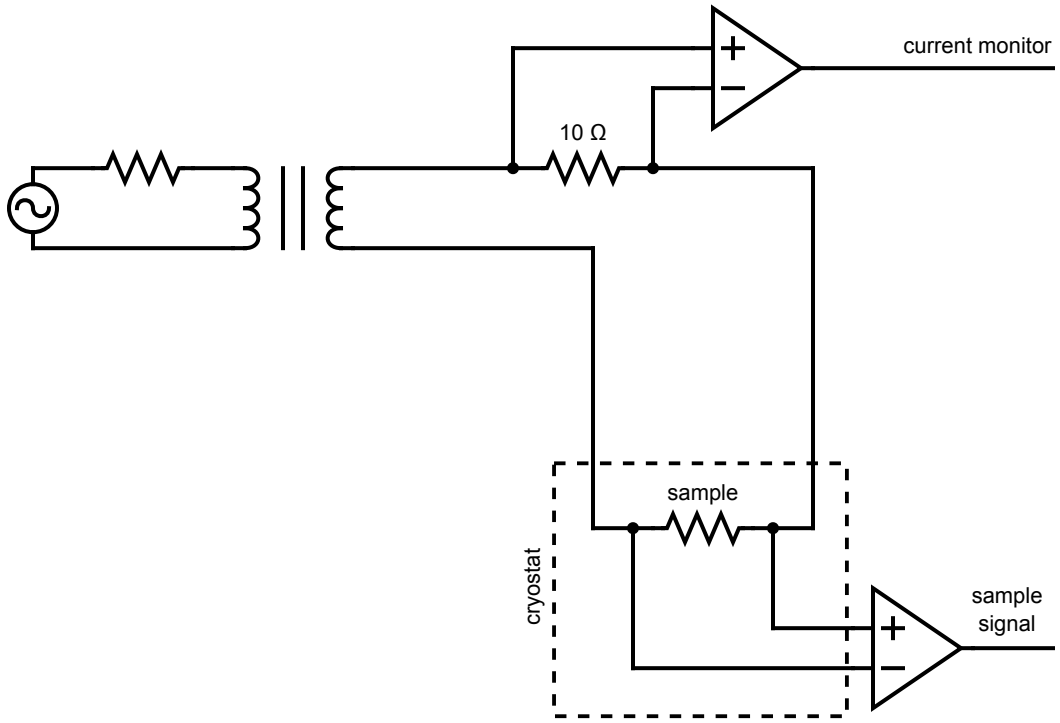

Figure A.7: **Pulsed field measurements** A diagram of the circuit during pulsed field measurements. All wiring is done with twisted pairs in order to minimize inductive pickup during the field pulse.